2014

Shallow Flow Instabilities: Effects of Gravity Standing Wave Coupling

Burak A. Tuna
Lehigh University

SHALLOW FLOW INSTABILITIES:

EFFECTS OF GRAVITY STANDING WAVE COUPLING

by

Burak Ahmet Tuna

Presented to the Graduate and Research Committee

of Lehigh University

in Candidacy for the Degree of

Doctor of Philosophy

in

Mechanical Engineering

Lehigh University

May 2014

Approved and recommended for acceptance as a dissertation in partial fulfillment of the requirements for the degree of Doctor of Philosophy.

_____

Date

_____

Dissertation Director

_____

Accepted Date

Committee Members:

_____

Professor D. O. Rockwell

_____

Professor X. Huang

_____

Professor J. Kazakia

_____

Professor A. Oztekin

To my Mother, Father,
and
My Brother,

ACKNOWLEDGEMENTS

Above all, I would like to express my deepest gratitude to my esteemed advisor, Professor Donald Rockwell. Not only has he given me the expert guidance, as he always has to all of his students, but he continually stimulated my analytical thinking and greatly assisted me with scientific writing. His perpetual energy and enthusiasm in research helped me a lot whenever I needed motivation. He was always accessible and willing to help for anything I need. I feel very lucky to have the opportunity to work with one of the best professors in the area of fluid mechanics. His efforts are invaluable and will never be paid back.

I am also very grateful for having an exceptional doctoral committee, and wish to thank Professor Alparslan Oztekin, Professor Jacob Y. Kazakia, and Professor Xiaolei Huang, for their precious time, support, and encouragement throughout this process.

I would like to extend my thanks to Professor Sadik Kakac, Professor Selin Aradag, Professor Sitki Uslu, Professor Emrah Kilic, Professor Yucel Ercan, Mr. Caglor Oluk, and Mr. Ilker Yalcin for supporting and encouraging me throughout my undergraduate study.

Many thanks to my colleagues and friends, Dr. Egemen Tinar, Mr. Okan Ilhan, Dr. Duygu Saydam, Mr. Mert Ozkaynak, Dr. Turgut Yilmaz, Dr. Cem Alper Ozen, Mr. Matthew Bross, Mr. Max Wolfinger, and many others for their valuable contributions, moral support and friendship.

I extend my appreciation to Mrs. JoAnn Casciano for her dedicated work, administrative assistance, and her kindness.

I also extend my appreciation to assistance of Mr. Richard Towne and Mr. James Bunderla for their extraordinary craftsmanship. Without their advices and practical solutions to the technical problems, this study could take one decade to be accomplished.

I owe many apologies to my always friends, Mr. Muhammet Kizil, Mr. Omer Malli, and Mr. Burak Terzi, who feel neglected during my graduate years. Even though we are at different parts of the world, I always feel that you are always there for me. I hope to spend time more frequently with you for the rest of my life.

And finally, this work is dedicated for my great family, without their support, enthusiasm, and encourage my whole education would have not been possible. I could not have achieved this without your presence. Thanks my mother, father, and brother for everything.

TABLE OF CONTENTS

Page

LIST OF FIGURES

Page

NOMENCLATURE

BL^+	Positive bifurcation line
BL^-	Negative bifurcation line
c_f	Bed friction coefficient
c_τ	Constant denoting error for centroid estimation
c_v	Propagation (or phase) speed
C	Speed of disturbance
C_r	Phase speed
d	Cylinder diameter
d_p	Particle diameter
d_τ	Particle diameter in image plane
D	Characteristic diameter of a large-scale vortical structure
DFT	Discrete Fourier Transform
DNS	Direct numerical simulation
E	Exchange velocity
$\bar{E}$	Time-averaged exchange velocity
$f^\#$	Aperture number of camera
f_s	Frequency of inherent instability of separated shear layer
f_n	Eigenfrequency of gravity standing wave within cavity
F	Focus
F_d	Dissipation term
Fr	Froude number
Fr_{cr}	Critical Froude number
g	Gravitational acceleration
h	Water depth
h_a	Height of acrylic components

h_c	Height of cylinder
h_d	Oscillation amplitude of gravity standing wave
h_p	Elevation of pressure transducer above bed
h_w	Shallow water depth
k	Complex wavenumber of instability
k	Mass exchange coefficient
k_i	Spatial amplification rate
k_r	Wavenumber of the disturbance
KH	Kelvin-Helmholtz instability
$\vec{l}$	Integration path in Stokes theorem
L	Streamwise length of cavity
L_c	Critical streamwise length
L_e	Streamwise length of channel located downstream of contraction
L_i	Distance between leading edge of acrylic plate (raised plate) to leading corner of cavity
L_T	Characteristic length scale of the turbulence
M	Mach number
M	Number of images used to calculate phase-averaged parameters
M_0	Magnification of experimental arrangement
n	Mode of gravity standing wave
N	Number of images used to calculate time-averaged parameters
p	Pressure
P	Production term
PCA	Planar concentration analysis
PIV	Particle image velocimetry
Q	Number of images used to employ spectral analysis
Q	Mass flux between cavity and main stream
R	Radius of curvature
$R_{xx}(\tau)$	Auto-spectral density
$R_{xy}(\tau)$	Cross-spectral density
Re	Reynolds number
Re_{hw}	Reynolds number based on shallow water depth
Re_W	Reynolds number based on width of channel
$\vec{s}$	Stokes theorem surface

S	Stability parameter or bed friction number
S_{cr}	Critical stability parameter
S_f	Flux bed friction number
$S_p(f)$	Spectral peak of the pressure oscillation
S_v	Spectra of transverse component of velocity fluctuation
SP	Saddle point
t	Time
T_D	Flushing time of fluid from cavity
T_w	Period of oscillation of the gravity standing wave
u	Streamwise velocity
u'	Streamwise velocity fluctuation
U	Free stream velocity
U_r	Depth-averaged inflow velocity at fully-coupled state
$\overline{U}$	Average velocity across the mixing layer
U/f_nL	Reduced inflow velocity (inverse of Strouhal number)
v	Transverse velocity
v'	Transverse velocity fluctuation
v_z	Vertical velocity
V	Velocity Magnitude
W	Width of cavity
W_d	Dimensionless channel width
W_e	Width of the channel located downstream of contraction
y	Cross-stream direction
x	Streamwise direction
z_L/h_w	Elevation of laser sheet above bottom surface (bed)

Greek Symbols

$\forall_{cav}$	Volume of cavity
$\forall_w$	Volume of exchanged water
δ	Width of transverse shear flow
δ_z	Depth of field
Δt	Time difference between PIV image pairs
ε	Gap between cylinder and upstream wall of cavity
ϵ_h	Horizontal eddy diffusivity

ξ	Effect of local friction
κ	Kinetic energy of large-scale transverse motions
Γ	Circulation
λ	Laser wavelength
λ	Wavelength of an instability
ρ	Density
σ	Smoothing parameter
$\sigma_{\Delta x}$	RMS displacement error in flow plane
$\sigma_{\Delta X}$	RMS displacement error in image plane
ϕ	Phase angle
$\Phi(y)$	Complex amplitude
$(\Phi_v)_0$	Phase angle at the separation corner
$\Phi_v(x)$	Streamwise phase variation of transverse velocity
ω	Complex frequency
ω_r	Frequency of disturbance
ω_i	Temporal amplification rate
ω	Vorticity
ψ	Stream function
γ	Compression ratio

Indices

max	Maximum value
rms	Root-mean-square value

Operators

$'$	Differentiation
$< >$	Time-averaging
$< >_p$	Phase-averaging
∂	Partial derivation
Δ	Difference
∇^2	Laplace operator

ABSTRACT

Shallow turbulent shear flows such as shallow mixing layers, jets, or wakes, can exist in environmental flows, e.g., flows in rivers, lakes, estuaries, and coastal regions. These flows frequently have large-scale, highly-coherent, vortical structures with length scales that are much larger than the flow depth. Such vortical structures can arise from either a convective or an absolute instability. Fully turbulent shallow flow past a cavity can lead to highly coherent oscillations, which arise from coupling between the inherent instability of the separated shear layer along the cavity opening and a gravity standing wave within the cavity.

The ultimate objectives of this investigation are to: (i) determine the effect of shear layer-gravity standing wave coupling on the flow structure and exchange processes; (ii) control the oscillations and exchange processes; (iii) reveal flow features for different cavity configurations and relate the flow patterns to the characteristics of exchange processes. Techniques of unsteady pointwise pressure measurements and particle image velocimetry (PIV) are used to assess the coherence and basic flow physics of oscillations over the flow domain along both a single cavity and successive cavities. The basic flow features observed for the

oscillations were either a transverse or longitudinal gravity standing wave within the cavity, downstream propagation of an organized disturbance or large-scale vortex along the cavity opening, and its impingement on the trailing corner of the cavity.

The amplitude of free surface oscillation within the cavity is characterized as a function of inflow velocity via unsteady pressure measurements. Coupled oscillation of the shear layer and the gravity standing wave yields large increases in the time-averaged entrainment and mass exchange coefficients between the cavity and the main flow. Such increases are due to substantial enhancement of turbulent stresses in the separated shear layer during the coupled oscillation, relative to the stresses associated with no coupling.

Patterns of the flow structure have been characterized as a function of elevation above the bed (bottom surface) of the shallow flow. At elevations close to the bed, the time-averaged streamlines are deflected inwards towards their center of curvature. This streamline deflection is due to radial migration of flow along the bed, which arises from a radial pressure gradient; this deflection causes skewing of the velocity vectors over the depth and creates streamwise vorticity. In addition, patterns of normal and shear Reynolds stresses are substantially altered as the bed is approached. These changes of stresses with depth are, in turn, associated with degradation of coherent, phase-averaged patterns of vortex formation in the separated shear layer.

Coupled oscillations of the shear layer and the gravity standing wave can be attenuated by a single geometric perturbation (cylinder) on the bed (bottom surface), which is located near the leading corner of the cavity. Reduced amplitude of the coupled oscillation can be attained for values of cylinder diameter and height nearly an order of magnitude smaller than the water depth. The reduction of oscillation amplitude is associated with an increased width of the separated shear layer along the opening of the cavity, even at elevations above the bed much larger than the height of the cylinder. Near the bed, a vorticity defect in the separated shear layer and deflection of the vorticity layer away from the cavity opening are evident. Attenuation of the oscillation amplitude is associated with: a major decrease in the peak values of the normal and shear Reynolds stresses in the separated shear layer; degradation of coherent, phase-averaged patterns of vortex formation; and decreased scale of the coherent vortical structures that propagate downstream along the cavity opening. These changes in the stresses and the flow structure are, in turn, directly correlated with lower values of exchange velocity along the opening of the cavity due to the decreased entrainment demand of the separated shear layer and, as a result, reduction of the value of mass exchange coefficient in presence of passive control device (cylinder).

In addition to shear layer-gravity standing wave coupling for a single cavity, shallow flow past successive cavities can also give rise to self-sustained oscillations, due to coupling between: the inherent instability of the separated shear layer along the opening of each cavity; and a gravity standing wave mode within

the cavity. As the flow velocity is varied, this coupling is associated with different orientations of the gravity standing wave, i.e., it can occur in either the transverse or the streamwise direction. Correspondingly, a defined phase shift exists between the coupled oscillations of adjacent cavities; the flow structure and mass exchange process along each of the sequential cavities can be altered depending on the orientation of the gravity standing wave within each cavity, that is, a streamwise-oriented versus a transversely-oriented gravity standing wave, as well as the phase shift between the standing waves in adjacent cavities. In presence of the transversely-oriented gravity standing wave, the oscillation amplitude of the coupled shear layer instability-cavity mode is larger, as indicated by the amplitude of deflection of the free-surface, and enhanced coherence and scale of the phase-averaged vortex formation occurs in the separated shear layer along the opening of each cavity. This coherent vortex formation results in a large increase in the magnitude of the turbulent shear stress in the separated shear layer and, as a consequence, an increase of the time-averaged exchange velocity and mass exchange coefficient along the opening of each cavity.

CHAPTER 1

INTRODUCTION

Shallow turbulent flow is ubiquitous in nature. Flows in wide lowland rivers, in stratified lakes, along ocean coastlines, and in estuaries are typical examples. This type of flow also occurs on a geophysical scale in the stratified atmosphere or the upper ocean. Free shear flows in shallow water can lead to vortex formation, and therefore give rise to self-sustained oscillations in the shallow flow domain. Two-dimensional flows such as planar mixing layer flows, planar jets, and planar wakes are prominent examples (Figure 1.1), as reviewed by Pope (2000). In all of these flows, the onset and development of vortex systems have a strong influence on transport, dispersion, and exchange of pollutants and dissolved matter, growth of flora and fauna, aquatic environment of marine life, erosion, and transport of sediment.

Shallow flows of finite streamwise length scale, for example, past cavity-like configurations, exist in many forms in our environment (Figures 1.2 and 1.3), such as: a series of cavities formed by multiple groynes (dead-water zones) along a river bank; a sequence of spur dikes along an ocean coastline; embayments exposed

to tidal rivers/flows; an embayment in the bank of river; harbors in ocean coastal regions; and inlet-lake systems. The unsteady and quasi-steady flow patterns in these configurations will be studied in this investigation.

1.1 SHALLOW FLOWS: AN OVERVIEW

Shallow flows are characterized as predominantly horizontal flows in a fluid domain in which the horizontal length scales greatly exceed the flow depth. In hydro-environmental applications, the flow depth corresponds to the water depth, which is aligned with the gravitational acceleration. A schematic of a typical shallow flow domain is shown in Figure 1.4. Shallow flows have a free surface and a shear-supporting bottom surface (bed). As shown in the plan view in Figure 1.4, the wavelength λ of an instability or the characteristic diameter D of a large-scale vortical structure is much larger than the water depth h_w, that is, $\lambda / h_w >> 1$ and $D / h_w >> 1$.

Turbulent flow is mainly governed by three-dimensional wall turbulence, produced by shear effect at the solid bottom. The boundaries, i.e., the free surface and the bed, suppress vertical motions and restrict the characteristic length scale of the turbulence L_T. Some types of coherent turbulent structures can be present in shallow flows, but the length scale of these structures is of the order or less than the water depth $L_T \leq h_w$, as reviewed by Nezu and Nakagawa (1993). These structures grow through instabilities of the base shear flow and decay due to stabilization by the bottom bed friction. These instabilities result in large vortex structures, which

are defined as two-dimensional coherent structures by Jirka and Uijttewaal (2004). The reader is referred to the works of Yalin (1992), Nezu and Nakagawa (1993), and Roy et al. (2004) for a comprehensive review of large-scale coherent structures. According to Jirka (1998, 1999, 2001), the generation mechanisms of these structures are classified as below:

Type A: Topographic Forcing. This is the most severe generation mechanism in which topographic forcing effects of a full range of rapidly-varying submerged and extending structures such as headlands, islands, jetties, and groynes (Figure 1.5). These features can generate strong transverse shear leading to local flow separation, and are sometimes accompanied by return flow (feedback) in the lee of the structure. This mechanism is a trigger for spatially growing instabilities, which lead to organized motions in the form of shallow wakes (Figure 1.6a-c) and shallow mixing layers (Figure 1.6d).

Type B: Internal Transverse Shear Instabilities. For this mechanism, velocity variations in the transverse direction exist in the shallow flow domain and give rise to spatial growth of two-dimensional coherent structures. Flows such as shallow jets (Figure 1.7a-b), shallow mixing layers and shallow wakes (Figure 1.7c) can be induced by: (i) source flow fluxes of momentum excess or deficit; (ii) gradual topographic changes (channels with flood plains, Figure 1.7d); and (iii) roughness variations of the bottom surface (bed).

Type C: Secondary Instabilities of Base Flow. This is the weakest type of generating mechanism. As explained earlier, the base flow is vertically sheared and contains three-dimensional turbulence structure with coherent features. The turbulence production and dissipation are in balance in the flow field; however, any imbalances in the equilibrium of turbulence production and dissipation can lead to a redistribution of the momentum exchange at the bed. These imbalances of the momentum exchange process can result in distortion of vortex lines and lead to generation of two-dimensional vortical structures.

1.2 SHALLOW SHEAR FLOWS

The shallow wake, shallow jet, and shallow mixing layer are the basic classes of shallow turbulent shear flows shown in Figure 1.1. These profiles contain inflection points and are susceptible instability, which forms from the mean transverse shear. As mentioned previously, the water depth h_w in shallow water flow prevents the development of three-dimensional instabilities, and the growth of a perturbation, i.e., the formation of the instability, is suppressed by the friction at the bottom (bed). The effect of bed friction on the instabilities of shallow turbulent shear flows is addressed by Chu et al. (1983, 1991) and later Chen and Jirka (1997, 1998).

Shallow wakes. The unstable wake dynamics in shallow flows have been investigated extensively via field and laboratory experiments, numerical simulations, as well as stability analyses. The experimental studies of Ingram and

Chu (1987), Chen and Jirka (1995), Carmer et al. (2001, 2003), and Uijttewaal and Jirka (2003) determined the essential features of near-wake instability. Chen and Jirka (1995) indicated three different types of shallow wakes: vortex shedding, unsteady bubble, and steady bubble. The typical example of 'vortex shedding' and 'steady bubble' wakes was visualized behind Islands in Rupert Bay, as described by Ingram and Chu (1987). In addition, in the recent investigations by Sadeque et al. (2009), Liang et al. (2012), and Sukhodolov and Sukhodolova (2013), the flow patterns in shallow wakes are characterized in environmental applications. Their measurements and visualizations showed a contradiction between stability criteria and experimental results in terms of the type of the wake. Moreover, numerical studies of Kawamura et al. (2002) and Yu et al. (2008) showed that the waves developing at the free surface strongly affect the flow features of shallow wakes. Three-dimensional DNS computations by Zhang et al. (1995) and Thompson et al. (1996) revealed the existence of different wavelengths of instabilities within the near wakes.

In addition to the aforementioned numerical and experimental studies, stability analyses have been conducted to explore the stability of shallow wake flows based on linear stability theory by Tennekes and Lumley (1977), Schar and Smith (1993), Grubišic et al. (1995), Williamson (1996), Chen and Jirka (1997), Chan et al. (2006), and Ghidaoui et al. (2006). Tennekes & Lumley (1977) obtained analytical expressions for transverse velocity profiles for unbounded (free) wakes. Following closely the route of Tennekes and Lumley (1977) for unbounded wakes,

Huerre and Monkewitz (1990), Williamson (1996), Socolofsky and Jirka (2004) describe an analytical solution for shallow wakes which can also be used as a suitable basis for stability analysis. Chen and Jirka (1997) interpreted the basic types of shallow wakes dependent on the stability parameter *S* and related the presence of absolute (or global) and convective instabilities (Huerre and Monkewitz, 1990) to the formation or absence of large-scale rollers in the near wake in a shallow water layer.

Shallow jets. The spatial development of instabilities and large-scale vortex formation in shallow jets have been examined by Giger at al. (1991), Dracos et al. (1992), Jirka (1994), Chen and Jirka (1993, 1998, 1999), Rowland et al. (2009), and Biggs et al. (2010). Giger at al. (1991) and Dracos et al. (1992) measured the turbulence and entrainment characteristics of jets in a shallow water layer. They noted that the water depth is an appropriate length scale to normalize the results. Chen and Jirka (1993, 1999) and Jirka (1994) experimentally investigated the mixing characteristics of shallow water jets by using a laser-induced fluorescence technique. Chen and Jirka (1998) addressed theoretically the instability characteristics of the shallow jet and reported the possibility of stabilizing the shallow jet, i.e., "relaminarization". Moreover, Rowland et al. (2009) mimic an environmental jet in the laboratory and compare the flow characteristics with previous studies of planar jets. They reported that, beyond distances greater than nine channel widths from the jet outlet, the jet is assumed to be self-similar and have mean properties consistent with other studies. More recently, the laboratory

study of Biggs et al. (2010) revealed the dynamics of a turbulent jet in the shallow flow domain; they conducted linear stability analyses to determine the spatial development of instabilities.

Shallow mixing layers. Shallow mixing layers occur due to transverse variations of bottom (bed) friction, water depth, or velocity. Experimental investigations of a shallow mixing layer were conducted by Chu and Babarutsi (1988), Uijttewaal and Tukker (1998), and Uijttewaal and Booij (2000). Uijttewaal and Tukker (1998) reported that turbulence in shallow mixing layers is anisotropic and can be considered as quasi two-dimensional. An established point of all these studies is the important role of bottom (bed) friction in suppressing perturbations. Linear stability analysis of shallow mixing layers was performed by Alavian and Chu (1985), Chu et al. (1991), Chen and Jirka (1998), Ghidaoui and Kolyshkin (1999), Kolyshkin and Ghidaoui (2002), and van Prooijen and Uijtewaal (2002). In addition, Babarutsi and Chu (1993, 1998), Booij and Tukker (2001), Biron et al. (2004), and van Prooijen and Uijttewaal (2009) established different models to understand and simulate the physics of shallow mixing layers. The aforementioned stability analysis and model studies of shallow mixing layers showed that the bed friction stabilizes the flow and reduces the rate of the growth of the mixing layer.

The foregoing investigations have substantially advanced our understanding of the flow structure and instabilities in shallow jets, wakes, and mixing layers. Since the main objective of this study is to investigate instabilities due to shallow

flow past a cavity, we will limit the discussion to a shallow mixing layer having a finite streamwise extent.

Vortex formation in a shallow mixing layer having a finite streamwise length scale, i.e., shallow flow past a cavity configuration, has been investigated experimentally by Wallast et al. (1999), Uijttewaal et al. (2001), Weitbrecht and Jirka (2001), Mizumura and Yamasaka (2002), Uijttewaal (2005), Riviere et al. (2010), and computationally by McCoy et al. (2006, 2007, 2008) and Constantinescu et al. (2009). These studies aimed to analyze the effect of the cavity (groin field, embayment, or dead zone) geometry on the vortex formation, shear layer along the cavity opening, flow structure, and mass/momentum exchange processes. The insightful advances described in the foregoing have provided a basis for further assessment of shallow mixing layers, which will be described thoroughly in the following sections.

1.3 ONSET AND DEVELOPMENT OF INSTABILITIES IN SHALLOW SHEAR FLOWS

Hydrodynamic stability of certain spatially developing free-shear shallow flows can be used to determine the onset of self-sustained oscillations. The behavior of a free-shear layer in shallow flow can be investigated by means of a linear stability analysis of two-dimensional, depth-averaged equations of motion with bottom friction and viscosity terms. As illustrated by Chu et al. (1991), Chen and Jirka (1997), Socolofsky and Jirka (2004), the depth-averaged equations of

motion for unidirectional flow, i.e., flow without curvature effects and free of Coriolis force, with two-dimensional (*x, y*) velocity field (*U+u, v*) are as follows:

$$\frac{\partial u}{\partial x} + \frac{\partial v}{\partial y} = 0 \tag{1.1}$$

$$\frac{\partial u}{\partial t} + U\frac{\partial u}{\partial x} + v\frac{\partial U}{\partial y} = -\frac{1}{\rho}\frac{\partial p}{\partial x} - \frac{c_f U}{h}u + \epsilon_h \nabla^2 u \tag{1.2}$$

$$\frac{\partial v}{\partial t} + U\frac{\partial v}{\partial x} = -\frac{1}{\rho}\frac{\partial p}{\partial y} - \frac{c_f U}{2h}v + \epsilon_h \nabla^2 v \tag{1.3}$$

in which ρ is the density, c_f is the bed friction coefficient (0.005-0.01), *U(y)* is the base velocity, *u(x,y,t)* and *v(x,y,t)* are the disturbance velocities, *p* is the pressure, and ϵ_h is the horizontal eddy diffusivity.

Linear stability theory of parallel shear flow is concerned with the development in space and time of perturbations around a basic flow *U(y)*. Fluctuations are typically decomposed into elementary instability waves and are given by the disturbance stream function $\psi(x, y, t)$:

$$\psi(x, y, t) = \Phi(y)e^{i(kx-\omega t)} \tag{1.4}$$

where *k* is complex wavenumber, ω is complex frequency, and $\Phi(y)$ is complex amplitudes. By using the definition of disturbances in Equation 1.4, small-amplitude velocity disturbances *(u, v)* are expressed as:

$$u = \Phi_u(y)e^{i(kx-\omega t)} \tag{1.5}$$

$$v = \Phi_v(y)e^{i(kx-\omega t)} \tag{1.6}$$

where Φ_u and Φ_v are the complex amplitudes. $k = k_r + ik_i$, k_r is the wavenumber of the disturbance, $-k_i$ is the spatial amplification rate for modes that propagate $x > 0$ direction, while $+k_i$ is the spatial amplification rate for modes that propagate $x < 0$ direction. Moreover, $\omega = \omega_r + i\omega_i$, in which ω_r is the frequency of the disturbance, and ω_i is the temporal amplification rate. By substituting these terms into Equations 1.1-1.3, and eliminating the pressure p and Φ_u, the shallow flow stability equation with a bottom friction term is as:

$$\begin{aligned}(U(y) - C + \xi)(\Phi_v'' - k^2\Phi_v) + \xi\frac{U'}{U}\Phi_v' - U'' - \Phi_v \\ = \epsilon_h(\Phi_v'''' - 2k^2\Phi_v'' + k^4\Phi_v)\end{aligned} \tag{1.7}$$

in which the prime denotes differentiation in the y direction, $\xi = c_f U/ikh$ is a parameter measuring the effect of local friction, $C = \omega/k = C_r + iC_i$, and C_r is the phase speed. Equation 1.7 is a modified form of Orr-Sommerfeld equation with the added effect of bottom (bed) friction. In order to determine the absolute and convective instabilities, the response of an impulse input in this equation can be investigated. The velocity profile is said to be absolutely unstable if transient disturbances spread upstream and downstream, and contaminate the entire flow as they amplify. On the other hand, the velocity profile is said to be convectively unstable if disturbances swept away as they amplify and eventually leave the basic

flow undisturbed. The reader is referred to the works of Huerre and Monkewitz (1985, 1990), Monkewitz (1990), Oertel (1990), and Couairon and Chomaz (1997) for absolute and convective instability analysis.

Chu et al. (1991) investigated the bed friction effect on transverse shear flows by using the energy equation as follows:

$$\left(\frac{\partial \kappa}{\partial t} + U\frac{\partial \kappa}{\partial x}\right) = -\langle u\frac{\partial p}{\partial x} + v\frac{\partial p}{\partial y}\rangle - \langle uv\rangle\frac{dU}{dy} - \frac{c_f U}{2h}(2\langle u^2\rangle + \langle v^2\rangle) \qquad (1.8)$$

in which h is the water depth, $\kappa = (< u^2 > + < v^2 >)/2$ is the kinetic energy of large-scale transverse motions, and '< >' denotes the long-time averaging operation. In Equation 1.8, the production term is given by:

$$P = -\langle uv\rangle\frac{dU}{dy} \qquad (1.9)$$

which shows that the energy transfer from the main flow to the transverse motion occurs via the action of Reynolds stresses $< uv >$. On the other hand, the dissipation due to bottom friction is equal to the negative work done by the large-scale transverse motions against the bed-friction force:

$$F_d = -\frac{c_f U}{2h}(2\langle u^2\rangle + \langle v^2\rangle) \qquad (1.10)$$

The ratio of the bed-friction dissipation term to the production term defines the flux bed friction number:

$$S_f = \frac{F_d}{P} = \frac{2\langle u^2 \rangle + \langle v^2 \rangle}{\langle uv \rangle}\left(\frac{c_f}{2h}\right)\left(\frac{U}{U_y}\right) \tag{1.11}$$

The flux bed friction number has been defined as the stability parameter S for shallow mixing layers by Chu and Babarutsi (1988), Babarutsi et al. (1989), and Babarutsi and Chu (1991a, 1991b):

$$S = \frac{\overline{c_f}\delta\overline{U}}{2h_w\Delta U} \tag{1.12}$$

where $\overline{c_f}$ is the bed friction coefficient, δ is the width of the transverse shear flow, $\overline{U}$ denotes the average velocity across the mixing layer, ΔU is the corresponding velocity difference across the mixing layer, and h_w is the water depth. The bed friction coefficient $\overline{c_f}$ is adapted from ASCE Task Force (1963) and modified as follows (Chu & Babarutsi, 1988):

$$\frac{1}{\sqrt{\overline{c_f}}} = -4log\left(\frac{1.25}{Re\sqrt{\overline{c_f}}}\right) \tag{1.13}$$

in which Re is the Reynolds number.

In Equation 1.12, the velocity difference ΔU imposes a destabilizing influence, whereas the friction coefficient $\overline{c_f}$ tends to retard the onset of the instability. The large-scale transverse motion will be suppressed if the stability parameter S is equal to or larger than the critical stability parameter value S_{cr} where dissipation exceeds production, i.e., $F_d > P$.

1.4 OSCILLATING CAVITY FLOW

Self-excited, unstable and oscillating cavity flow can occur in practical applications such as: flow over sunroofs and windows in automobiles; cavities in hulls of submarines; weapon bays in aircrafts; musical instruments; and groyne fields and embayments in rivers. Rockwell and Naudascher (1987) divided flow induced cavity oscillations into three categories: (i) fluid-dynamic oscillations due to cavity shear-layer instability, which are enhanced through a feedback mechanism; (ii) fluid-elastic oscillations, where the interaction with elastic displacement of the boundary leads to the shear-layer instability and its amplification; (iii) fluid-resonant oscillations, where shear-layer instability occurs due to either fluid compressibility or free surface gravity wave phenomena.

Oscillations of a free-surface in cavity-like configurations in the environment, such as groyne fields (dead-zones), river embayments, and harbors, are observed in the studies of Kimura and Hosoda (1997), Ikeda et al. (1999), Muto et al. (2000), Nezu and Onitsuka (2002), USACE (2002), Wirtz (2004), Ohomoto et al. (2005), and Uijttewaal (2005). These studies addressed the importance of these cavity-like geometries on the pollutant transport phenomena, navigation, sedimentation of groyne fields, and mass/momentum exchange between cavity region and main flow.

Free surface oscillation due to shallow water flow past a cavity-like geometry is associated with the fluid-resonant type cavity oscillation, which

involves coupling of the inherent instability of the unstable separated shear layer along the cavity opening with one or more modes of gravity standing wave within the cavity. This coupling occurs when the inherent instability frequency f_s of the separated shear layer coincides with an eigenfrequency f_n of the longitudinal- or transverse-oriented gravity standing wave within the cavity. Locked-on oscillations develop, leading to large amplitude fluctuations of the free water surface enclosed within the cavity. The change in orientation of the gravity standing wave within the cavity is due to variation of the free stream velocity, which results in a change of the frequency f_s associated with the unstable shear; in turn, the new value of f_s aligns with a different eigenmode of the cavity. The reader is referred to the works of Kuo and Yang (2004) and Wolfinger et al. (2012) for insightful reviews on lock-on phenomena in cavity flows.

Heller and Bliss (1975) stated that free surface oscillations inside a cavity can alter the underlying physics of the exchange processes. Mass exchange between the cavity-like geometries (groyne fields, dead-zones, or embayments) and the main stream has been studied by Uijttewaal (1999), Wallast et al. (1999), Kurzke et al. (2002), Engelhardt et al. (2004), Brevis et al. (2006), Le Coz et al. (2006), Jamieson and Gaskin (2007), McCoy et al. (2008), and Weitbrecht et al. (2008). The preceding investigations stated the importance of large-scale coherent structures and cavity geometry on the mass exchange process without considering free surface oscillations. It is therefore necessary to investigate the effect of

oscillations on the flow physics and the mass exchange process in presence of shallow flow past a cavity, which is the focus of present investigation.

1.5 OVERVIEW OF ATTENUATION TECHNIQUES

Shallow flow systems involving open channels, embayments, groynes, spur dykes, and harbors, which have a finite-length mixing layer along their openings, are highly prone to undergoing one or more modes of gravity standing waves inside the cavity. As mentioned in the foregoing sections, periodic oscillations of a gravity standing wave within the cavity can dramatically alter the flow physics and exchange processes. An important, yet relatively unexplored aspect of all of the foregoing configurations is the manner in which attenuation of the the degree of flow-resonant coupling and thereby the amplitude of the oscillationcan be achieved. To this end, several techniques have been attempted and are classified as active and passive control by Cattafesta et al. (2008). In the category of active control techniques, there is an external energy input to the system; while there is no such energy input for passive control.

In this study, passive control techniques are of interest; they have been successfully implemented via geometric modifications or steady fluid injection. Studies of passive control techniques include fences, spoilers, ramps, and a cylinder or a rod at a location close to the leading edge of the cavity.

Sarno and Franke (1994) comparatively studied effectiveness of a fence on suppressing cavity oscillations under subsonic and supersonic flows. They

concluded that a static fence was more effective than the fluid injection method. Similarly, Ukeiley et al. (2004) employed a leading-edge fence at different locations in the boundary layer. Their experiments showed that the fence could attenuate self-sustained oscillations due to increased shear layer thickness.

Mongeau et al. (1999) used a spoiler to control pressure fluctuations inside a vehicle due to grazing flow over a sunroof, and they succeeded in cancelling the noise. Moreover, Zhang et al. (1999) and Celik et al. (2007) experimentally investigated the effect of an upstream ramp on suppression of cavity oscillations. A ramp of sufficient size creates a separation bubble that can prevent self-sustained oscillations.

McGrath and Shaw (1996) attained reduction of tones and broadband noise with a cylinder located in the upstream boundary layer. They hypothesized that reduction of noise is related to the interaction of shed vortices with the shear layer instability. Also, Stanek et al. (2003) investigated the effectiveness of a rod in a crossflow for suppressing acoustic resonance in high speed cavity flows. They suggested optimal rod configurations for transonic and supersonic conditions.

In the present investigation, a cylinder, which is located at a location just upstream of the leading corner of the cavity, will be employed to suppress the fluid-resonant oscillations due to shallow flow past a cavity. In contrast to the aforementioned studies, the height of the cylinder will be much smaller than the

extent of the shallow water layer. Furthermore, different heights and configurations will be investigated to minimize the spanwise extent of the cylinder.

1.6 UNRESOLVED ISSUES

In view of the foregoing investigations of instabilities in shallow flows, it is evident that a number of issues remain unclarified and unexplored. Brief summaries of the unresolved issues as follows:

(i) Shear layer instability and vortex formation in a shallow flow of finite length scale. Shallow flow past a cavity having a finite streamwise length L can lead to fundamental changes of an instability and vortex formation in the separated shear layer along the cavity opening. The most unstable disturbance in the shear flow at a critical streamwise length L_c can give rise to development of large-scale coherent structures along the cavity opening. The sensitivity to inflow Reynolds number of the separating shear layer, the onset and the development of large-scale vortical structures, and the recirculating flow patterns within the cavity should be pursued.

(ii) Coupling of unsteady shear layer with a gravity standing wave resonant mode(s) of a cavity. Shallow flow configurations of finite streamwise length scale such as river embayments, spur dikes along an ocean coastline, groyne fields, and other cavity-like systems are highly prone to gravity standing wave resonance in one or more modes. The origin and physics for existence of this shear layer-gravity standing wave coupling have remained unclarified. Moreover, optimal

coupling, which can result in very large-scale, highly coherent vortex patterns in the separated shear layer, remains to be determined.

(iii) Mass exchange across unsteady shear layer. The aforementioned destabilizing influences defined in (i) and (ii) can drastically alter the exchange processes across unstable shear layer. The mass exchange between the cavity and the main stream is a function of the turbulence characteristics of the separated shear layer along the cavity opening. In order to attain a complete understanding of the physics, one should consider the flow physics and its relation to the effectiveness of flushing of fluid within an adjacent cavity during non-coupled and fully-coupled states of the oscillation. This aspect has not yet been pursued.

(iv) Depthwise variations of structure of shallow mixing layer. Due to the fundamentally different boundary conditions at the bed (bottom surface) and the free-surface above the bed, it is anticipated that the flow structure with and without gravity standing wave coupling will exhibit variations with depth. The nature of, and correlation between, the flow patterns along the bed and the free-surface regions, as well as the regions between them, have not been addressed. The manner in which the structure of the separated layer varies with elevation above the bed, and its relation to the effectiveness of the mass exchange between the cavity and the main stream, has not yet been characterized.

(v) Control techniques for coupling between shear layer instability and gravity standing wave mode(s). Impingement of an unstable shear layer on the

downstream corner of a cavity is known to be an important source for highly coherent, self-sustained oscillations. Stabilization, i.e., elimination of the instability, can be accomplished by using passive control techniques and, if so, the principal features of the flow structure at partially or fully attenuated states should be characterized. The effects of passive control techniques on both the frequency and amplitude of the self-excited, purely hydrodynamic instabilities within the shallow flow domain have not yet been addressed.

1.7 RESEARCH OBJECTIVES

The present investigation aims to address the issues described in the foregoing. The ultimate goal of the present research is to characterize the alterations of the flow structure that are associated with a shallow mixing layer having a finite streamwise extent. A technique of high image density, particle image velocimetry (PIV) will be employed, in conjunction with unsteady pressure measurements, to interpret the physics of flow in terms of pressure, velocity components, streamline topology, turbulence characteristics and vorticity, in conjunction with time- and phase-averaged patterns, with emphasis on the effects of coupling between the separated shear layer and a gravity standing wave mode of the cavity. This knowledge of the flow structure can lead to insight into the patterns of the mass exchange between the cavity and the main stream, as well as control of the oscillations. In doing so, the overall objectives of this investigation are to:

- Determine the optimal coupling between the instability/vortex formation in the shallow mixing layer and the modes of the gravity standing wave resonance via measuring the unsteady pressure response with respect to varying inflow velocity. Locked-on oscillations can occur when the inherent vortex formation frequency f_s matches with the resonant frequency of the f_n of the gravity standing wave mode of the cavity. Optimal coupling corresponds to the peak spectral amplitude of the oscillation at a defined inflow velocity in the region of lock-on, represented by $f_s / f_n = 1$.

- To control/attenuate the self-sustained oscillations, a cylinder having a height less than the shallow water layer will be placed upstream of the cavity, which may either deflect the shear layer away from the cavity opening or excite drive the instability of the unsteady shear layer to a higher frequency than the resonant frequency of the f_n of the gravity standing wave mode of the cavity.

- For cases of non-coupled and fully-coupled oscillations of an unstable shear layer with a gravity standing wave, as well as for partially or fully attenuated states, the following types of post processing will be employed for the mixing layer along the cavity opening and the recirculation flow within the cavity: (i) instantaneous and phase-referenced patterns of vorticity, which will identify small- and large-scale vortical structures; (ii) patterns of instantaneous, time-averaged, and phase-referenced streamline topology will be classified and interpreted using critical point theory (Perry

& Chong, 1987), allowing identification of focus, saddle points, and bifurcation lines; (iii) patterns of instantaneous and averaged turbulence characteristics of the unsteady shear layer, e.g., root-mean-square velocity fluctuations and Reynolds stresses, which allow global comparisons with the aforementioned patterns of vorticity and patterns of streamline topology; (iv) patterns of amplitudes of peaks of predominant spectral components and phase shifts, obtained from global spectral and cross-spectral analysis, will allow identification of the dimensionless frequencies at which the predominant fluctuating energy is concentrated, as well as the phase speeds of each of the spectral components in the separated shear layer(s) and recirculation zone(s).

- The quantitative results from previous studies have been concentrated on measurements at mid-depth or at the free-surface of the shallow water layer. Flow patterns and topological structures at successive elevations above the bed have not been investigated. Since, the boundary conditions at the bottom surface (bed) and the free-surface are different from each other, the possible sensitivity of flow structures and turbulence to elevation will be accounted for by translating the plane of observation to different elevations extending from the bed to the free surface of the shallow water layer.

- The mass flux between the cavity and the mainstream is considered to occur through an imaginary surface extending from the separation (upstream) corner and impingement (downstream) corner of the cavity. This imaginary

surface will be scanned along the cavity opening at successive elevations above the bed to obtain the variation of the profile of mass flux. A method that uses the velocity vector field determined with quantitative imaging, rather than marker fluid, will be used to determine the mass flux and formulate the dimensionless mass exchange coefficient.

- Previous studies have revealed that the structure of the separated shear layer is altered when a series of groynes, i.e., series of cavities, are present. Convection of vortical structures along the openings of successive cavities alters the development of the shear layer and the exchange processes along a given cavity. Moreover, existence of successive cavities can vary the coupling mechanism between the separated shear layer and a gravity wave mode for a given cavity. Therefore, an understanding of the underlying physical phenomena for vortex formation and phase shifts between successive cavities will be explored.

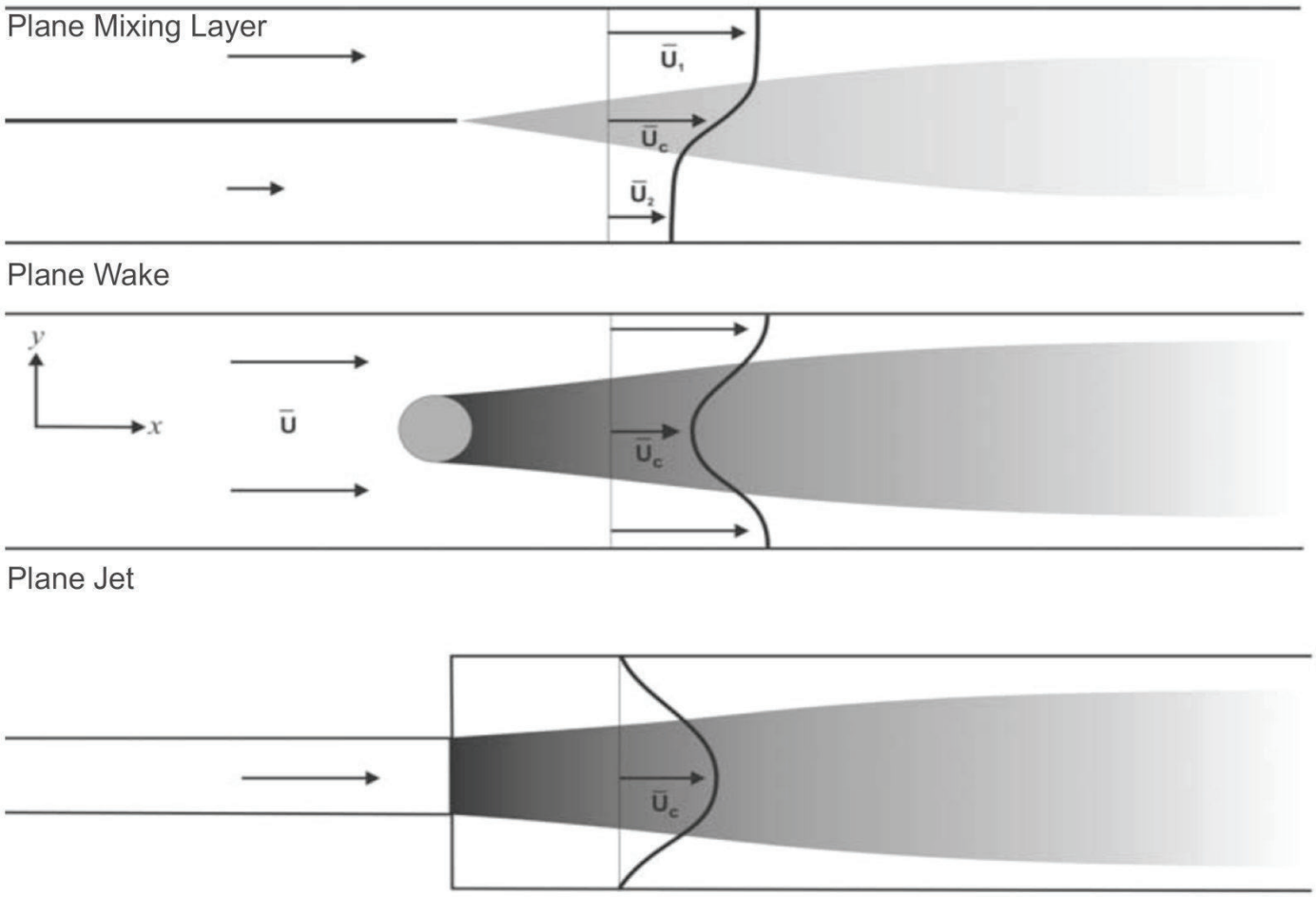

Figure 1.1: Sketch of two-dimensional shear flows (After Rhoads & Sukhodolov, 2008).

(a) (b)

(c)

(d)

Figure 1.2: (a) Spur dikes along River Lek in the Netherlands. **(b)** Groyne fields on the River Rhine in the Netherlands (Jirka & Uijttewall, 2004). **(c)** Spur dikes along Long Beach, NY. **(d)** Spur dikes along Long Branch Beach, NJ.

(a)

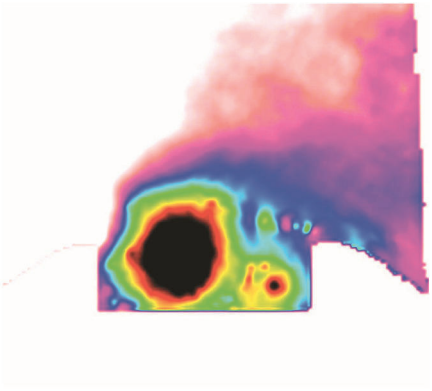

(b)

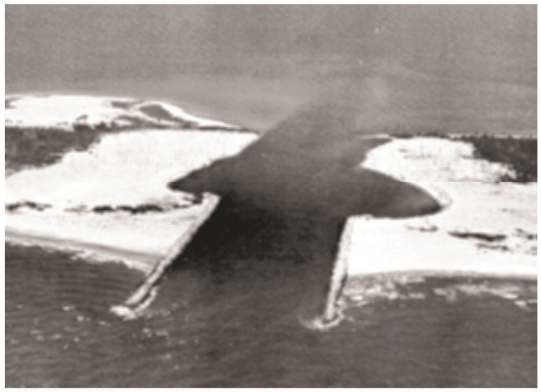

(c)

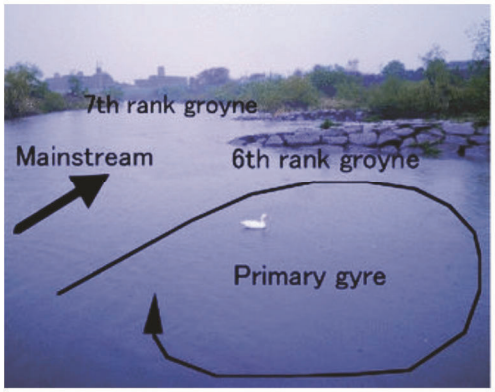

(d)

(e)

Figure 1.3: (a, b) Coastal embayment of Blackpool Sands in Devon, UK and visualization of vortex systems due to tidal flow past a flushing embayment (Elwell, 2004). **(c)** Cavities due to jetties at an inlet (Seabergh, 2002). **(d)** Consecutive groyne field on Katsuro River in Kyoto, Japan (Sanjou & Nezu, 2013). **(e)** Mckeller river wetlands project (near Lake Superior) showing two embayments containing habitat.

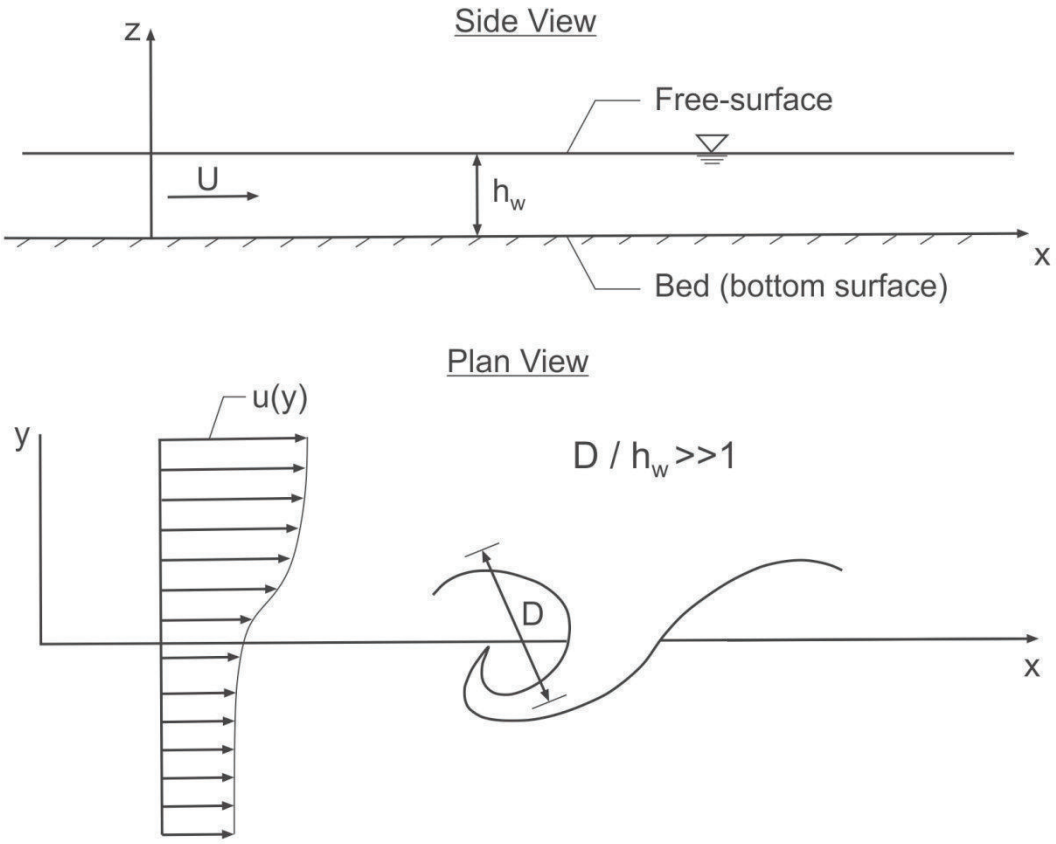

Figure 1.4: Schematic of shallow flow domain (After Jirka & Uijttewaal, 2004).

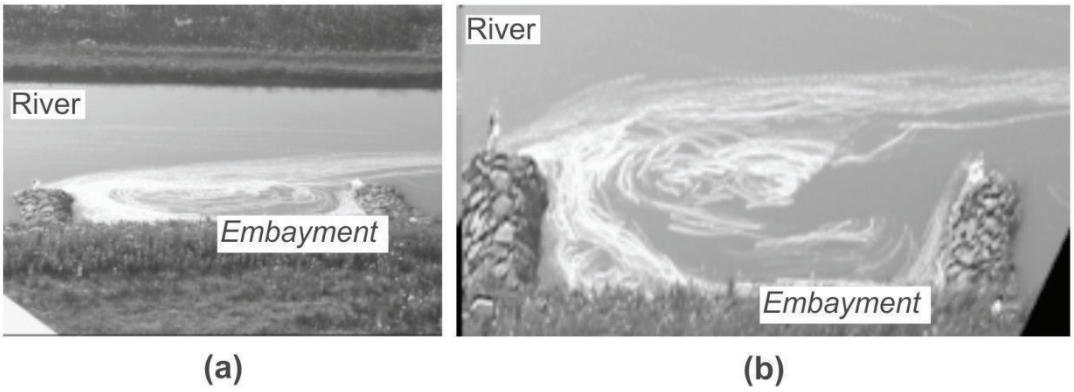

Figure 1.5: (a) Embayment (cavity) formed by groynes along Yodo River in Japan. **(b)** Aerial view of embayment showing vortex formation in the cavity shear layer and recirculation eddy within the cavity (Muto et al., 2002).

Figure 1.6: Top view (instantaneous photographs) of different wake patterns in shallow flows visualized by dye injected at the upstream of cylinder shoulders. **(a)** Vortex-street like wake. **(b)** Unsteady bubble wake. **(c)** Steady bubble wake. **(d)** Confluence of River Inn (light brown), River Danube (dark brown), and River Ilz (black)in Passau, Germany showing large vortical structures in the transverse shear layer (Adapted from Carmer, 2005).

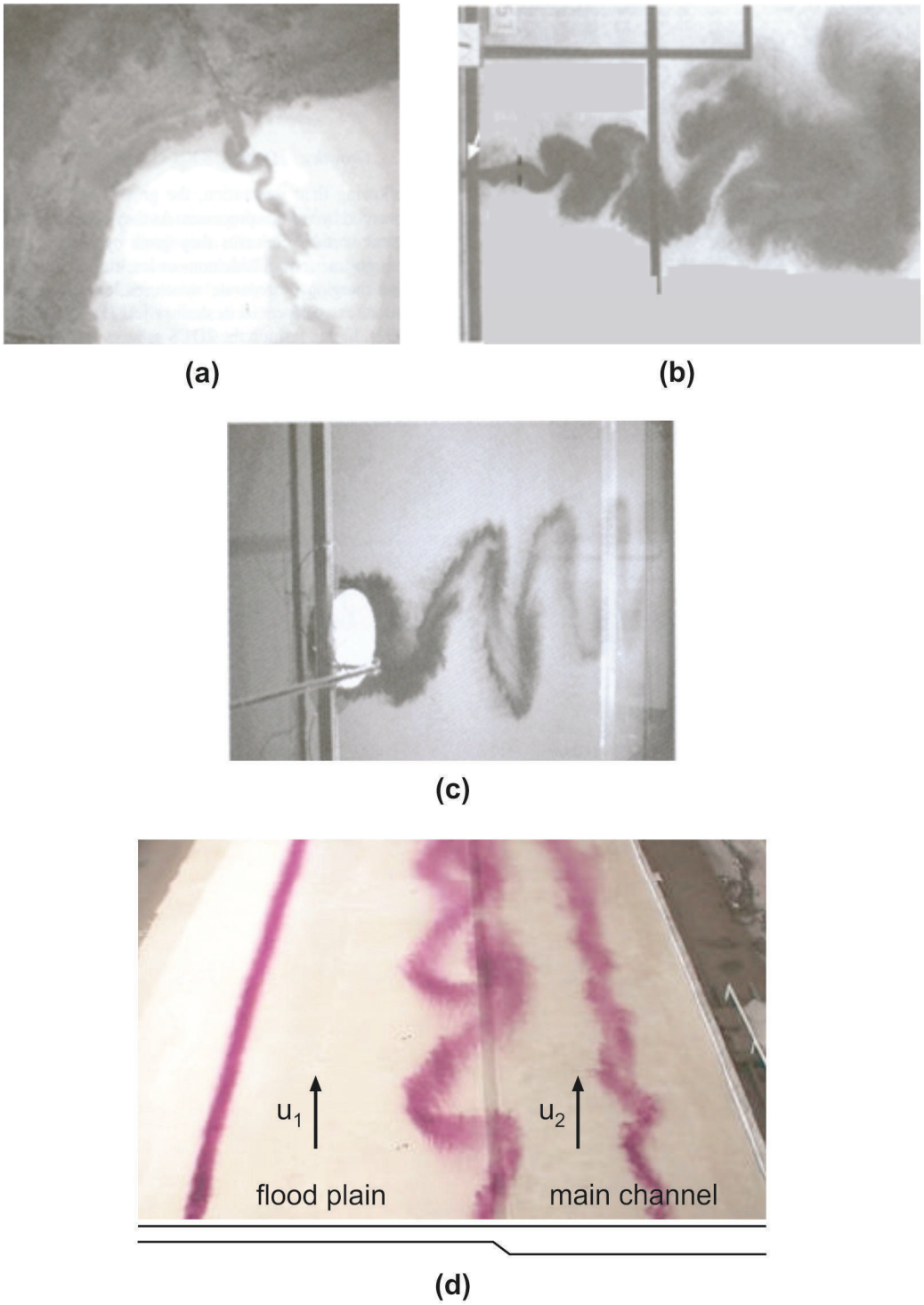

Figure 1.7: (a) Shallow jet (Re = 10^7) into Lake Balaton, Hungary (Jirka & Uijttewaal, 2004). **(b)** Shallow jet (Re = 10^4) entering a water table (Dracos et al., 1992). **(c)** Top view of shallow wake (Jirka & Uijttewaal, 2004). **(d)** Large coherent structures in mixing layer in a compound channel visualized by dye injection (van Prooijen et al., 2000).

CHAPTER 2

EXPERIMENTAL SYSTEM AND TECHNIQUES

The aim of this study is to: (i) determine the structure of a shallow, unsteady separated shear layer along a mouth of a cavity for non-coupled and fully-coupled oscillations; (ii) investigate passive control methods including a geometric perturbation on the bed (bottom surface), which is located near the leading corner of the cavity; and (iii) understand the underlying physics of the highly coherent oscillations due to shallow flow past successive cavities.

The intent of this chapter is to provide an overview of the system, the models, and the quantitative visualization and pressure measurement techniques employed during the experimental investigation of different cases. The experimental and the pressure measurement systems are introduced in Sections 2.1 and 2.2. Then, details of digital particle image velocimetry (PIV) and its components, are provided in Section 2.3. Next, processing of images and phase referencing technique will be described in Sections 2.4 and 2.5. Finally, evaluation of the flow features will be discussed in Section 2.6.

2.1 FLOW SYSTEMS

2.1.1 Water Channel

For all phases of this study, experiments are performed in a large-scale recirculating, low-turbulence, free-surface water channel located in the Fluids Research Laboratory at Lehigh University. An overview of experimental flow system is shown in Figure 2.1; and plan and side views of the test section are included in Figure 2.2. The experimental flow system consists of two reservoirs, a system of honeycombs and screens, a main test section, a test-section insert, and a computer controlled axial circulation pump. The main test section is made of transparent Plexiglas material and has an adjustable depth of 610 mm, a length of 4,877 mm, and a width of 927 mm. Large PVC (polyvinyl chloride) reservoirs are located at both ends of the water channel, and the free-stream velocity is maintained in the test section by pumping water from the downstream reservoir to the upstream reservoir, then through the honeycomb-screen arrangement. The speed of the axial pump is controlled by a unit that adjusts the RPM of the pump motor, and the honeycomb-screen arrangement involves two honeycombs and five screens. The honeycombs are a 6 inch thick honeycomb with 1/4 inch cells and a 3 inch thick honeycomb with 1/8 inch cells; these are followed by 5 screens spaced 7 inches apart. The honeycomb-screen arrangement quiets the flow ahead of the contraction and test section. The turbulence intensity in the test section is estimated below 0.2%, and the maximum depth-averaged flow velocity is 570 mm/s at the cavity location.

2.1.2 Test-Section Insert

A test-section insert was designed to control the depth of the shallow water layer, the flow velocity, and the cavity dimensions. The shallow water flow is generated along the upper surface of the raised plate as shown in Figures 2.1 and 2.2. This transparent plate is made of acrylic having a thickness of 12.7 mm, and it elevates the floor of the water channel to a height of 165 mm. The streamwise length of the shallow water layer, that is, the distance between the leading edge of the acrylic plate (raised plate) to the leading corner of the cavity is L_i = 1,907.5 mm. Boundary layer trips of 1.6 mm thickness and 13 mm width are located at the positions indicated in Figure 2.2. This arrangement allows rapid onset of turbulence and attainment of a turbulent boundary layer at the leading corner of the cavity.

In order to create the cavity geometry, acrylic components having a height of h_a = 102 mm are located on one side of the water channel along the upper surface of the raised plate. A contraction is placed upstream of the leading corner of the cavity, as indicated in the plan view of Figure 2.2. This contraction reduces the width of the test section from 927 mm to 470 mm; the width and streamwise length of the channel located downstream of the contraction are respectively W_e = 470 mm and L_e = 1,384 mm. The dimensions of the cavity are varied to investigate underlying flow physics; the specific dimensions of the cavity will be provided in the following chapters. For all experiments in this study, the depth of the shallow water layer is maintained at a value of h_w = 38.1 mm; the temperature of the water is 24 °C.

2.1.3 Inflow Conditions

Inflow conditions are determined experimentally by using PIV imaging, which will be thoroughly described in Section 2.3. The incoming flow is a fully developed turbulent shallow water flow, and the streamwise length of the shallow water layer is L_i. The criteria for a fully developed turbulent flow is given in the study of Uijttewaal et al. (2001) as $L_i / h_w > 50$, which corresponds to the ratio of inflow length L_i to the water depth h_w. This ratio is $L_i / h_w > 50.1$ in all experiments held in this study.

For all experiments herein, the depth-averaged inflow velocity is varied between U = 233 and 570 mm/s. Throughout the experimental investigations, the Reynolds number based on the water depth is maintained at $Re_{hw} > 4.5\text{x}10^3$. The value of Reynolds number Re, based on the width W_e of the inflow channel is in the range of $Re_W = 1.1\text{x}10^5$ to $2.7\text{x}10^5$; based on the water depth h_w, $Re_{hw} = 8.8\ \text{x}10^3$ to $2.2\ \text{x}10^4$.

In order to conduct experiments free of gravitational instabilities, the Froude number $Fr = U/\sqrt{gh_w}$ in the free stream is maintained within a specific range determined by Ghidaoui and Kolyshkin (1999). They revealed that an open channel flow is free of the gravitational instabilities below the critical Froude number, i.e., $Fr_{cr} < 1$. The range of Froude number in this study is Fr = 0.38 to 0.93, which is in the subcritical region. Therefore, the experiments are performed in absence of free-surface effects (gravitational instabilities) in the free stream.

2.2 PRESSURE MEASUREMENT SYSTEM AND TECHNIQUES

High sensitivity PCB piezoelectric pressure transducers (model number 106B50) are employed for all unsteady pressure measurements. This series of transducers has a nominal sensitivity of 72.5 mV/kPa and a resolution of 0.00048 kPa. The outputs from the transducers are connected to a PCB Piezotronics Signal Conditioner (Model number 480E09), which is used both to filter and amplify the pressure signal. Adjustments of the signal gains are performed by using the amplifier unit of the conditioner in order to ensure desired input voltage levels for the data acquisition board, and a low pass analog filter is employed at a cutoff frequency of 10Hz, which is well above the predicted frequency of the fluid-resonant oscillations.

The preconditioned analog pressure signals are transmitted to ports on a National Instrument Data Acquisition Board (Model: PCI-MIO-16E-4), which has a maximum sampling rate of 250,000 samples per second. For the final acquisition of experimental pressure data, the sampling rate is set to 20 samples per second, corresponding to a Nyquist frequency of 10 Hz. The maximum frequency for the present research is estimated to be 2.0 Hz, and the Nyquist criterion is thereby satisfied. In order to attain acceptable frequency resolution during spectral analysis, 2,048 samples are acquired for each record, i.e., the time span of each record is 102.4 seconds, and this resulted in a step size of 9.76×10^{-3} Hz. Ten of these time records are acquired for each inflow velocity.

In order to have consistent, repeatable results in the spectral analysis, it is important to use an effective window function for signal processing. The simple Hanning window function was employed. Calculation of pressure spectra involves transformation from the time domain to the frequency domain. The calculation of spectral magnitudes is done via built-in MATLAB function, which uses the fast Fourier transform algorithm by Cooley and Tukey (1965).

2.3 QUANTITATIVE IMAGING: PARTICLE IMAGE VELOCIMETRY

Particle image velocimetry (PIV) is used to determine the instantaneous fields of velocity vectors by imaging patterns of particle images. It has various names/forms, that is, pulsed light velocimetry (Adrian, 1984), digital PIV (Willert & Gharib, 1991), and particle tracking velocimetry (Adamczyk & Rimai, 1988). In a general sense, it involves seeding of the flow with small, reflective particles, and illumination of these particles over a plane of the flow by a pulsed laser sheet. Then, patterns of particle images within the laser sheet are acquired by a camera that is oriented perpendicular to the laser sheet, and effective computational methods lead to determination of the velocity vectors at each grid point.

In this study, a technique of high-image-density digital particle image velocimetry (Adrian, 1991) is employed to characterize the quantitative flow patterns during the oscillation cycle of fluid-resonant coupling. The purpose of particle image velocimetry is to acquire the velocity field, which includes velocity vectors at many grid points in the two-dimensional plane. An overview of this

imaging system, in relation to the cavity configuration, is given in Figures 2.2 and 2.3.

A New Wave Gemini 30 Hz double pulsed Nd:YAG laser system, having a maximum energy output of 90 mJ/pulse, is mounted on a traverse mechanism adjacent to the channel. By using an array of cylindrical and spherical lens, it is possible to transform the laser beam to a laser sheet. The cylindrical lens diverges the laser beam in only one direction, thereby generating a laser sheet; a spherical lens controls the thickness of the laser sheet, which is approximately 1 mm in the field of view shown in Figure 2.3. The maximum repetition rate is 15 Hz, which corresponds to acquisition of 15 image pairs per second.

Images are recorded by using a digital charge-coupled device (CCD) sensor POWERVIEW Plus 2MP camera, which has a 50 mm lens, with an array of 1,600 pixels × 1,192 pixels. It has a dynamic range of 12 bits, and the effective magnification of the camera provides a resolution in the field of view of 4.2 pixels/mm. During the PIV experiments, the image is first recorded on a CCD array. Then, the frame grabber reads the camera image from the CCD array and stores it in the computer as a digital image. The time it takes to read out the image from the CCD to the computer determines the framing rate. The camera is capable of operating at a maximum of 32 frames per second, which corresponds to 16 image pairs per second.

The model 610035 LASERPULSE TSI synchronizer is used as a control module for the PIV system. It is connected to the computer, digital camera, laser unit, frame grabber, external trigger, and external devices; the control is employed through the INSIGHT 4G software from TSI.

The water is filtered with a one micron filter system and subsequently seeded with metallic coated, hollow, plastic spheres having a diameter of 12 μm. To ensure high density seeding, a minimum 15 to 20 particles per interrogation window of 32 pixels x 32 pixels is employed.

During the PIV experiments, the repetition rate of the laser is set at 15 Hz, and the laser sheet is oriented horizontally and aligned with the direction of the free stream. The camera is placed below the water channel orthogonal to the horizontal plane as shown in the side view of Figure 2.2, and operated at 30 frames per second. The aforementioned double-pulsed laser and camera are triggered by a synchronizer, which supplies 15 sets of image pairs per second, i.e., the sampling frequency of the flow is 15 Hz. The plane of the laser sheet is displaced using the traverse mechanism in order to investigate the flow structure at different elevations of the shallow water layer. In order to avoid a large number of spurious vectors and to allow optimal evaluation of the particle image patterns, the time delay between the two pulses of the laser is varied from 2,500 μsecond to 3,500 μsecond depending on the inflow velocity at different elevations within the shallow water layer. For each set of PIV experiments, 200 pairs of images are recorded, and 15 sets of experiments are conducted, which leads to 3,000 sets of images at each

elevation above the bed. In order to define the phase of the oscillation at which PIV images are recorded, the signal transmitted from the synchronizer to fire the laser is recorded simultaneously with the pressure signal. This phase-referencing technique will be discussed subsequently.

2.4 PROCESSING OF IMAGES

Insight 4G software from TSI was employed in pre-processing, processing, and post-processing of images.

2.4.1 Pre-Processing

Pre-processing of the PIV images is the first step after the acquisition of images. There are different kinds of pre-processing, such as background image processing and spot masking. In this study the technique of background image subtraction is employed to enhance the image quality for processing.

The background image subtraction process includes two steps: (i) generation of a background image from a sequence of images by calculating the minimum intensity at each pixel of these images; and (ii) subtraction of the background image from each image. The use of minimum intensity makes possible enhancement of particle images without elimination of any illuminated particle due to the subtraction. This process is conducted for each set of images, i.e., the background image is calculated and subtracted from 200 images. As a result of this process, the signal to noise ratio is enhanced.

2.4.2 Processing

Processing of the patterns of particle images includes a frame-to-frame cross-correlation technique. At first, a processing mask can be defined, to limit the area of interest, which will exclude the regions outside of the flow field. In this study, a processing mask is used in order to avoid a large number of spurious vectors close to the cavity walls, which can occur due to the region outside the flow field. The processing mask that is used in this study is shown with a dashed-red line in Figure 2.3.

By using the aforementioned processing mask, the Nyquist grid generation method is employed for the grid generation and results in 32 pixel x 32 pixel interrogation windows with an effective overlap of 50% in both directions. The processing of the PIV images is accomplished by breaking the pre-processed images up into smaller regions, which are also called as interrogation windows. Basically, this method sets vectors with the x-axis spacing equal to half of the width of the interrogation window and the y-axis spacing equal to half of the height of the interrogation window. No interrogation window offsets are used and the process uses only a single pass. This method gives a vector grid with 50% interrogation window overlap fitting the Nyquist sampling criteria.

After the interrogation process is completed, the Hart correlation (Hart, 1998) is used for processing the PIV images. This method is a direct cross-correlation method that processes only the most significant pixels in order to

decrease total computation time. To do this, a compression ratio γ is used to set how many pixels are used in the computation. A value of $\gamma = 0.8$ is employed, i.e., 80% of pixels with the least significance are excluded, and 20% of the interrogation window pixels that are most significant are used in computations. Also, the Hart correlation method may increase the signal to background noise ratio, in addition to high speed computation.

The Hart correlation creates a correlation map, which is used to determine the location of the particle image displacement peak. A bilinear peak method is employed for peak detection, which is recommended for the Hart correlation. This method locates the correlation peak with sub-pixel accuracy by fitting a set of linear functions to the highest pixel and its 4 nearest neighbors. Two three-point fits are done: one in the x direction with the peak pixel and the pixels to the left and right of the peak; and one in the y direction with the peak pixel and the pixels above and below the peak.

2.4.3 Post-Processing

Keane and Adrian (1990) stated that the processing of PIV images can produce up to 95% valid velocity measurements. Lost pairs due to out-of-plane motion, or low seeding density can lead to spurious vectors. Therefore, it is necessary to remove bad vectors and replace them with the interpolated vectors calculated from surrounding grid points.

First of all, a validation process is conducted to remove bad vectors. A local median test method is used with a velocity tolerance "2" in the x and y directions for validation of the vectors. Basically, a given vector is compared against the median, which is computed using neighborhood vectors, which are in the range of a window size 3 pixels x 3 pixels, without including the vector at the center. Vectors that vary from the neighborhood median more than the user-defined tolerance are removed. Then, the removed vectors are filled by using the local mean via a recursive filling method. The recursive filling procedure sorts the holes by the number of valid neighbors found initially. It first fills the holes with the most valid neighbors since they have the best chance to be filled; it then fills the holes with the second most valid neighbors, in which the holes filled in the previous pass are also treated as valid neighbors; the same process is repeated until all holes in the flow field are filled.

Finally, by using Gaussian low-pass filtering, smoothing of data is performed. This last step is critical to remove the pseudo-white noise (Landreth & Adrian, 1988) due to the finite grid spacing of PIV data. The Gaussian low-pass filter uses a rotationally symmetric kernel of size n (filter size), which is set to 5 pixels x 5 pixels in this study, and a smoothing parameter σ, which has a value of $\sigma = 0.8$.

The aforementioned processing steps resulted in 7,227 vectors (99 x 73) with an effective grid size of 3.7 mm for each image pair, and a total of 3,000

randomly acquired velocity vector fields are used to calculate flow patterns. The estimated uncertainties of these velocity measurements are calculated by using the scheme given by Adrian and Westerweel (2010).

The RMS error in velocity measurements is given by:

$$\sigma_u = \frac{\sigma_{\Delta x}}{\Delta t} = \frac{\sigma_{\Delta X}}{M_0 \Delta t} \tag{2.1}$$

in which $\sigma_{\Delta x}$ is the RMS displacement error in flow plane, $\sigma_{\Delta X}$ is the RMS displacement error in image plane, $\Delta t = t_2 - t_1$ is the time difference between PIV image pairs, and M_0 is the magnification of the experimental arrangement. The RMS displacement error given in Equation 2.1 can be approximated as:

$$\sigma_{\Delta X} \cong c_\tau \,.\, d_\tau \tag{2.2}$$

where c_τ is constant denoting error for the centroid estimation and d_τ is the particle diameter in image plane. The value of c_τ is given by Adrian (1988) in the range of $c_\tau = 0.01 - 0.1$, and a value of $c_\tau = 0.06$ is employed in this study. Moreover, the finite value of particle diameter in the image plane is given approximately by:

$$d_\tau \cong M_0 \left[1.5\delta_z \lambda + {d_p}^2\right]^{0.5} \tag{2.3}$$

where δ_z is the depth of field, λ is the laser wavelength, and d_p is the particle diameter. In this study, the particle diameter is $d_p = 12$ μm, the laser wavelength is

λ = 0.532 μm, and the magnification is M_0 = 7.4 / 233 = 0.032. The value of the depth of field δ_z is given approximately by:

$$\delta_z \cong 4\left[1+\frac{1}{M_0}\right]^2 \lambda f^{\#2} \tag{2.4}$$

where $f^{\#}$ is the aperture number of the camera, which has a value of $f^{\#}$ = 8, in this study. By using Equations 2.1–2.4, the estimated uncertainties of the streamwise and transverse velocity measurements are 2% of the depth-averaged free stream velocity U throughout the experiments performed herein.

2.5 PHASE REFERENCING TECHNIQUE

In order to obtain accurate flow patterns during the oscillation cycle of the flow-resonator coupling, it is necessary to acquire the pressure signal simultaneously with the PIV data. As mentioned in Section 2.3, the flow is sampled at 15 Hz in this study, which results in acquisition of between 14 to 16 velocity fields per oscillation cycle of the gravity standing wave. The time-dependent flow structure, i.e., phase-averaged flow patterns, is calculated from the 3,000 randomly acquired velocity fields by using a technique called phase referencing.

The challenging part of this technique is that the pressure signals and PIV images are acquired using different host computers. To overcome this issue, the Q-Switch Synch Out signal of the laser is sampled together with the unsteady pressure fluctuation inside the cavity, which serves as the phase reference. The timing

diagram of a sample case is given in Figure 2.4. The Q-Switch Synch Out signal lasts less than 100 μs; for this reason, it is important to sample pressure signal at high rates. During the PIV experiments, a sampling rate of 20 kS/s (20kHz) is selected, and at this rate it is possible to get 4 to 6 pressure data points in the region of square pulse. The delay between Q-Switch Synch Out signal and laser pulse is less than 0.2 μs, and this delay is negligible when it is compared to the time difference, which is 2,500 μsecond to 3,500 μsecond, between PIV image pairs.

A sample case is given in Figure 2.5 involving the pressure signal in the cavity, indicated with blue line, for one oscillation period with the synchronization signal, represented with red line. As shown in Figure 2.5, 14 image pairs are recorded in one oscillation period (≅ 1 second). Determination of the phase of each image involves a phase referencing window, which has a span of ±5° phase *(ϕ)* of the oscillation. For instance, a window having a range of ϕ = 85° to 95° is employed to determine velocity fields for ϕ = 90°. The calculation of the phase of the pressure oscillation with the corresponding velocity field is performed by using an in-house code in MATLAB.

2.6 EVALUATION OF FLOW FEATURES

Once the processing and post-processing of PIV images are accomplished; the final form of the instantaneous velocity fields is determined. By using these velocity fields, it is possible to calculate time-averaged and phase-averaged flow patterns, as well as the turbulence statistics. Also, spectral analysis can be

employed at each point in the flow filed, since a time record of each point is acquired at each set of PIV experiments.

2.6.1 Time-Averaged Patterns

The time-averaged parameters are calculated by using N = 3,000 image pairs, i.e., 3,000 velocity fields. First of all, calculation of vorticity from the velocity data will be explained; then the definition of time-averaged parameters will be given.

Vorticity ω can be evaluated from each velocity field that is acquired by PIV measurements. In order to avoid possible errors due to noise, two different methods are used for the interior flow domain and for boundaries of the flow domain. First of all, the vorticity in the interior flow domain is calculated by using the circulation method, in which Stokes theorem is employed. The Stokes theorem on an integration path $\vec{l}$ enclosing the surface $\vec{s}$ is given as (Young et al., 2010):

$$\Gamma = \oint \vec{V} \,.\, d\vec{l} = \iint (\nabla x \vec{V}).\, d\vec{s} = \iint \vec{\omega}.\, d\vec{s} \tag{2.5}$$

By using the definition of the rectangular path including the grid points (*i,j*), the vorticity $\omega_z(i,j)$ within an enclosed area can be defined as:

$$\omega_z(i,j) = \frac{\Gamma(\mathrm{i},\mathrm{j})}{4\delta x \delta y} = \oint_{l(x,y)} \oint \vec{V} \,.\, d\vec{l} \tag{2.6}$$

where Γ is the circulation around the rectangular path calculated from numerical integration by using the trapezoid rule (Cheney & Kincaid, 2012).

Second, for the boundaries of the flow domain, finite difference methods are employed to calculate the vorticity. For two-dimensional, incompressible flow, the out-of-plane vorticity is defined as (Young et al., 2010):

$$\omega_z = \frac{\partial v}{\partial x} - \frac{\partial u}{\partial y} \tag{2.7}$$

Equation 2.7 is the approximation of vorticity by second order differentiation formulas. If the boundary is on the right side of the flow domain, a second order finite difference is employed to the partial derivatives as follows:

$$\frac{\partial v}{\partial x} = \frac{3v(i,j) - 4v(i-1,j) + v(i-2,j)}{2\Delta x} \tag{2.8}$$

$$\frac{\partial u}{\partial y} = \frac{3u(i,j) - 4v(i,j-1) + v(i,j-2)}{2\Delta y} \tag{2.9}$$

On the other hand, when the boundary is on the left, a forward difference formula is applied as:

$$\frac{\partial v}{\partial x} = \frac{-3v(i,j) + 4v(i+1,j) - v(i+2,j)}{2\Delta x} \tag{2.10}$$

$$\frac{\partial u}{\partial y} = \frac{-3u(i,j) + 4u(i,j+1) - u(i,j+2)}{2\Delta y} \tag{2.11}$$

Vorticity in the flow domain is calculated by using the aforementioned Equations 2.5 to 2.11 with the in-house MATLAB code.

Additional representations of the flow field are given in the following.

Time-averaged velocity magnitude:

$$< V(x,y) > = \frac{1}{N}\sum_{n=1}^{N} V_n(x,y) \tag{2.12}$$

Time-averaged streamwise component of the velocity:

$$< u(x,y) > = \frac{1}{N}\sum_{n=1}^{N} u_n(x,y) \tag{2.13}$$

Time-averaged cross-stream (transverse) component of the velocity:

$$< v(x,y) > = \frac{1}{N}\sum_{n=1}^{N} v_n(x,y) \tag{2.14}$$

Time-averaged vorticity:

$$< \omega(x,y) > = \frac{1}{N}\sum_{n=1}^{N} \omega_n(x,y) \tag{2.15}$$

Time-averaged exchange velocity:

$$\bar{E} = \frac{1}{N}\sum_{n=1}^{N}\frac{1}{L}\int_{0}^{L}|v_n(x, y=0)|dx \tag{2.16}$$

where $v_n\ (x,y = 0)$ corresponds to the cross-stream velocity along the cavity opening.

2.6.2 Phase-Averaged Patterns

In order to determine phase-averaged flow patterns, the phase referencing technique of Section 2.5 is used. This method led to a total of 60 images per phase window, i.e., there are $M = 60$ velocity fields for a defined phase ϕ in the phase-averaged flow patterns.

Phase-averaged representations are defined in the following.

Phase-averaged velocity magnitude:

$$< V^{\phi}(x,y) >_p = \frac{1}{M}\sum_{m=1}^{M} {V_m}^{\phi}(x,y) \tag{2.17}$$

Phase-averaged streamwise component of the velocity:

$$< u^{\phi}(x,y) >_p = \frac{1}{M}\sum_{m=1}^{M} {u_m}^{\phi}(x,y) \tag{2.18}$$

Phase-averaged cross-stream (transverse) component of the velocity:

$$< v^{\phi}(x,y) >_p = \frac{1}{M}\sum_{m=1}^{M} {v_m}^{\phi}(x,y) \tag{2.19}$$

Phase-averaged vorticity:

$$< \omega^{\phi}(x,y) >_p = \frac{1}{M}\sum_{m=1}^{M} {\omega_m}^{\phi}(x,y) \tag{2.20}$$

2.6.3 Turbulence Statistics

Calculation of the root-mean-square of the streamwise (longitudinal) velocity fluctuation u_{rms}, root-mean-square of the transverse (vertical) velocity fluctuation v_{rms}, as well as the Reynolds shear stress $<u'v'>$ are employed by using the time-averaged flow field data from Equations 2.13 and 2.14 as follows:

Root-mean-square of the streamwise (longitudinal) velocity component:

$$u_{rms}(x,y) = \sqrt{\frac{1}{N}\sum_{n=1}^{N}[u_n(x,y) - < u(x,y) >]^2} \tag{2.21}$$

Root-mean-square of the transverse (vertical) velocity component:

$$v_{rms}(x,y) = \sqrt{\frac{1}{N}\sum_{n=1}^{N}[v_n(x,y) - < v(x,y) >]^2} \tag{2.22}$$

Reynolds shear stress:

$$< u'v' > = \frac{1}{N}\sum_{n=1}^{N}[u_n(x,y) - < u(x,y) >].[v_n(x,y) - < v(x,y) >] \quad (2.23)$$

2.6.4 Spectral Analysis

Cross-spectral analysis in conjunction with PIV provides detailed distributions of temporal and spatial-temporal flow features. In this study, two capabilities are employed. First of all, the magnitudes of the auto-spectral density of the cross-stream (transverse) velocity along the cavity opening are used to determine the coherence and strength of the fluid-resonant oscillations.

Second, the cross-spectrum of the transverse (cross-stream) velocity with respect to the transvers (cross-stream) velocity at the leading edge of the cavity or the cross-spectrum of the transverse (cross-stream) velocity with respect to the pressure signal are evaluated, in order to determine the distribution of phase angle throughout the flow field at a given frequency, i.e., at the resonant frequency.

As a result of the PIV measurements, the time history of the cross-stream velocity at 7,227 points, with an array size of 99 (streamwise) and 73 (transverse), is acquired. Spectral analysis is employed by using a randomly selected set of images (Q = 200) having a total record time of t_{total} = 200 / 15 = 13.33 seconds, which results in a frequency resolution of 0.075 Hz.

Newland (1993) defined the auto- and cross-spectral density of $R_{xx}(\tau)$ and $R_{xy}(\tau)$, which are auto- and cross-correlation functions, as follows:

$$S_{xx}(\varpi) = \frac{1}{2\pi}\int_{-\infty}^{\infty} R_{xx}(\tau)e^{-i\varpi t\tau}d\tau \tag{2.24}$$

$$S_{xy}(\varpi) = \frac{1}{2\pi}\int_{-\infty}^{\infty} R_{xy}(\tau)e^{-i\varpi t\tau}d\tau \tag{2.25}$$

in which the correlation functions $R_{xx}(\tau)$ and $R_{xy}(\tau)$ defined as:

$$R_{xx}(\tau) = \frac{1}{Q}\sum_{q=1}^{Q} x_q(t).x_q(t+\tau) \tag{2.26}$$

$$R_{xy}(\tau) = \frac{1}{Q}\sum_{q=1}^{Q} x_q(t).y_q(t+\tau) \tag{2.27}$$

where Q is the discrete number of samples in the signal, which is Q = 200 in this study. Calculations of auto-spectral density of transverse velocity via Discrete Fourier Transforms (DFT's) are conducted by using in-house MATLAB codes. Details of these analyses by DFT's are given in the study of Bendat and Piersol (1980).

Discrete Fourier Transform (DFT) of the data series, i.e., transverse velocity v_1 and v_2 can be calculated according to:

$$X_k = \sum_{q=1}^{Q} (v_1)_q e^{-i(\frac{2\pi kq}{Q})} \ , k = 1,2, \dots, Q \tag{2.28}$$

$$Y_k = \sum_{q=1}^{Q} (v_2)_q e^{-i(\frac{2\pi kq}{Q})} \ , k = 1,2, \dots, Q \tag{2.29}$$

Then, the spectral densities are calculated by complex conjugate multiplication of X_k and Y_k.

Auto-spectral density:

$$S_{k_{xx}} = X_k^* X_k = A(\varpi) \tag{2.30}$$

Cross-spectral density:

$$S_{k_{xy}} = X_k^* Y_k \ = A(\varpi) + iB(\varpi) \tag{2.31}$$

where X_k* corresponds to the complex conjugate of X_k. Then, the normalized auto-spectral density and the phase variation of the point within the flow field are calculated as:

$$\overline{S_{k_{xx,xy}}} = \frac{2\sqrt{S_{k_{xx,xy}}}}{Q} \tag{2.32}$$

$$\Phi = tan^{-1} \frac{A(\varpi)}{B(\varpi)} \tag{2.33}$$

The phase Φ information of the transverse velocity is used to identify the phase variation of the separated shear layer along the cavity opening.

Details of normalization of all parameters are defined in subsequent Chapters. After calculation of time-averaged and phase-averaged parameters, turbulence statistics, spectral analysis of transverse (cross-stream) velocity, as well as pressure data, TECPLOT 360 and MATLAB programs are used to prepare final forms of the data. Then final image layouts are prepared by using the CorelDraw X5 program.

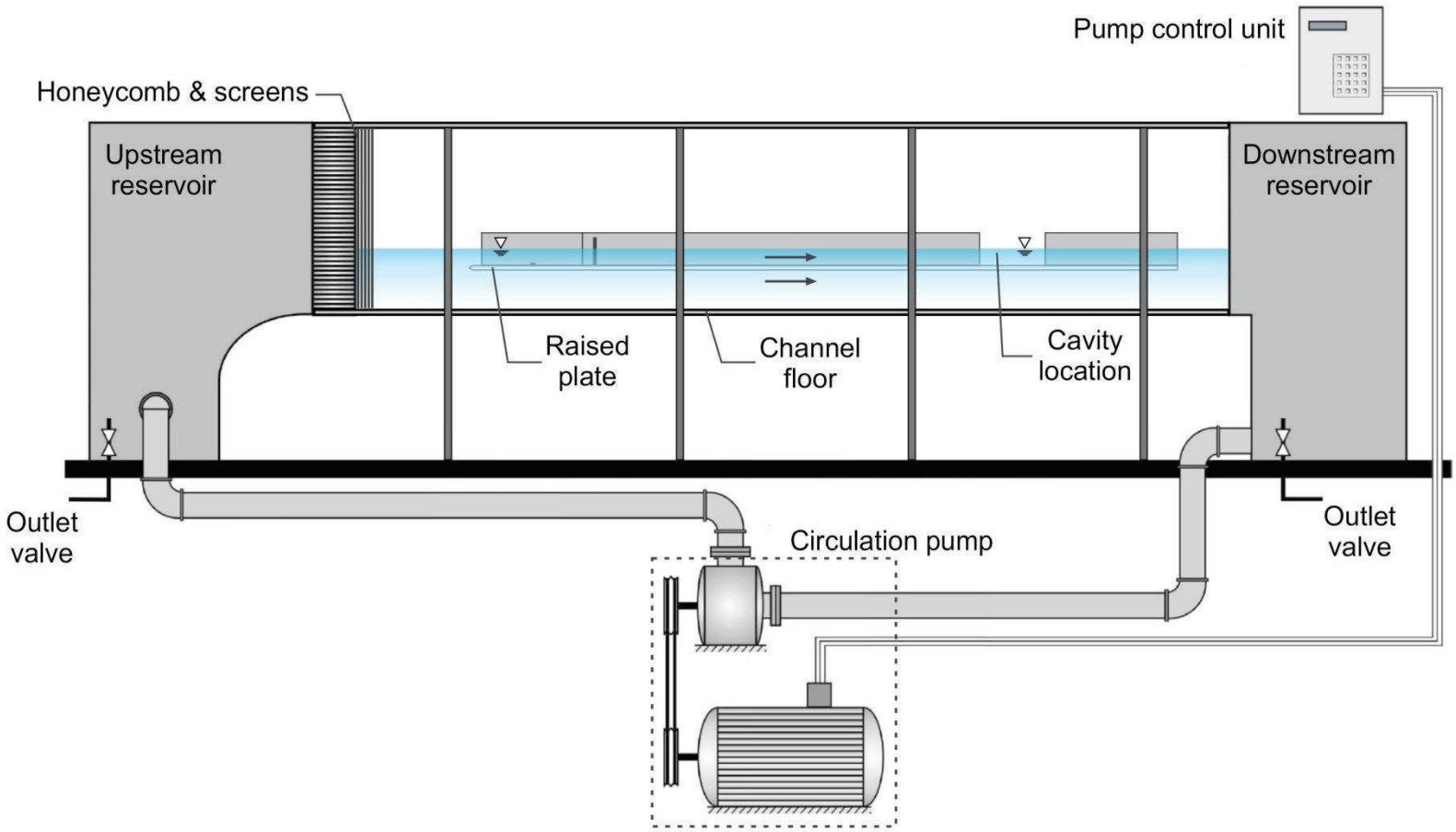

Figure 2.1: Overview of recirculating, free-surface water channel facility with the raised plate and acrylic components.

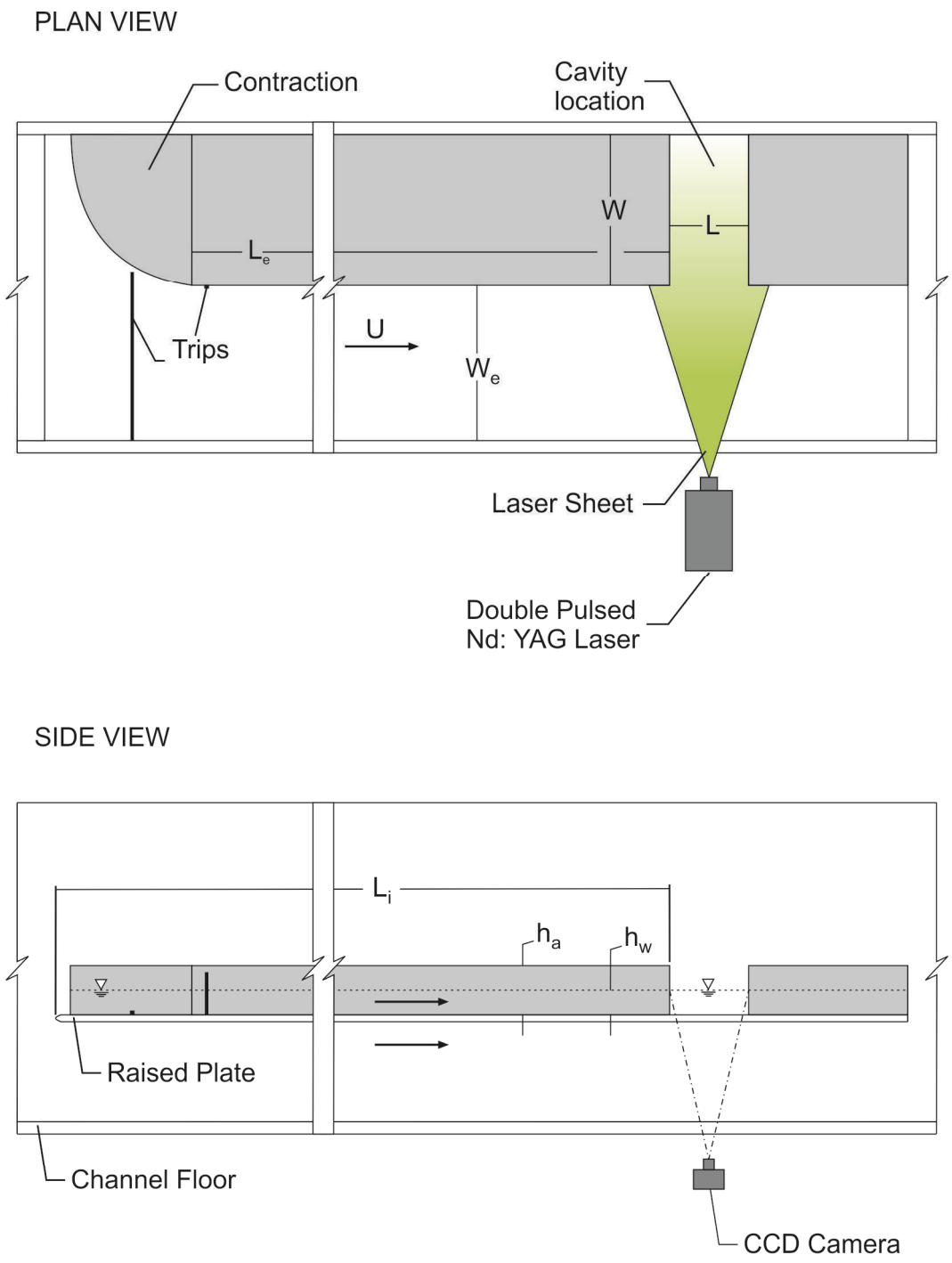

Figure 2.2: Schematic of experimental facility. (after Tuna et al., 2013)

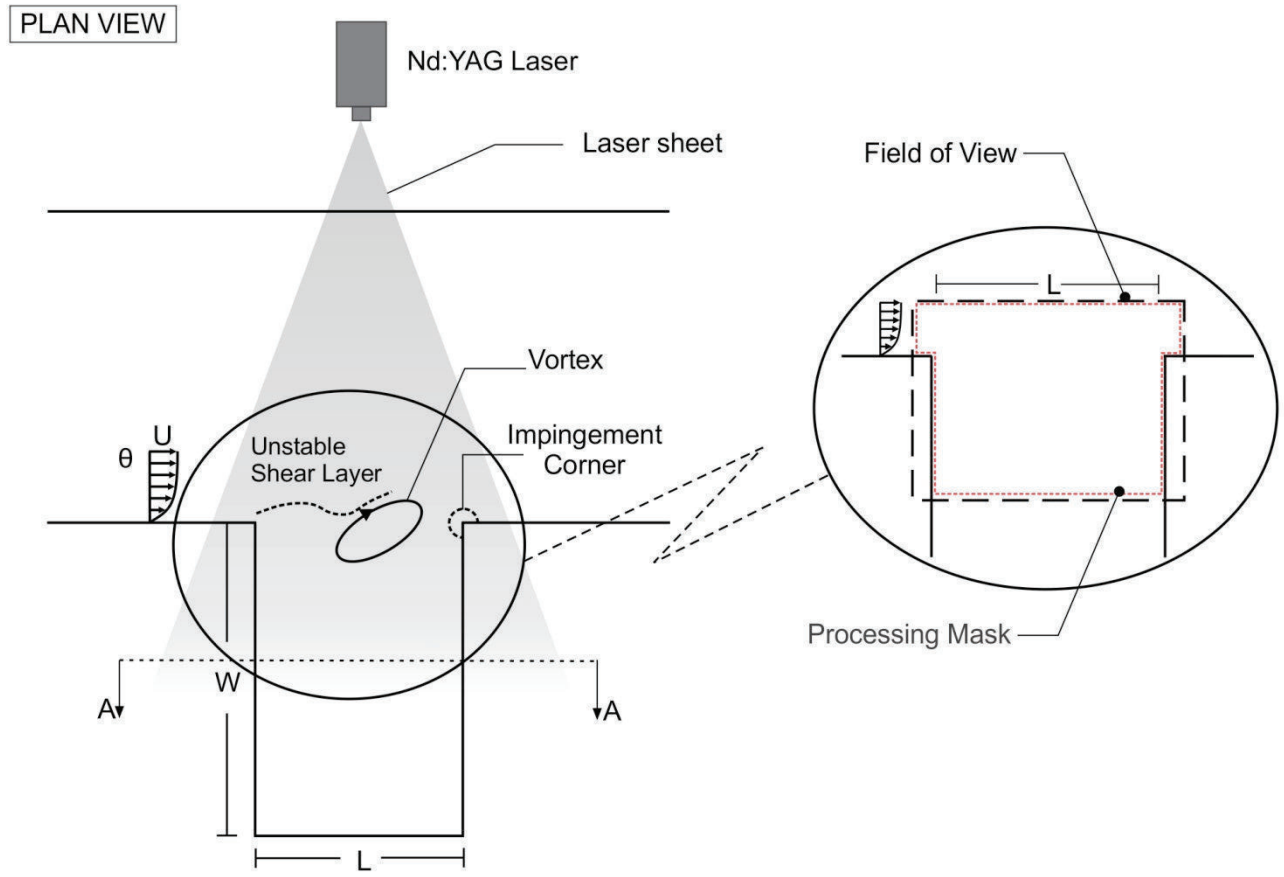

Figure 2.3: Schematic of experimental test section with quantitative imaging system. Also illustrated are unstable shear layer along opening of cavity, field of view and processing mask of particle image velocimetry.

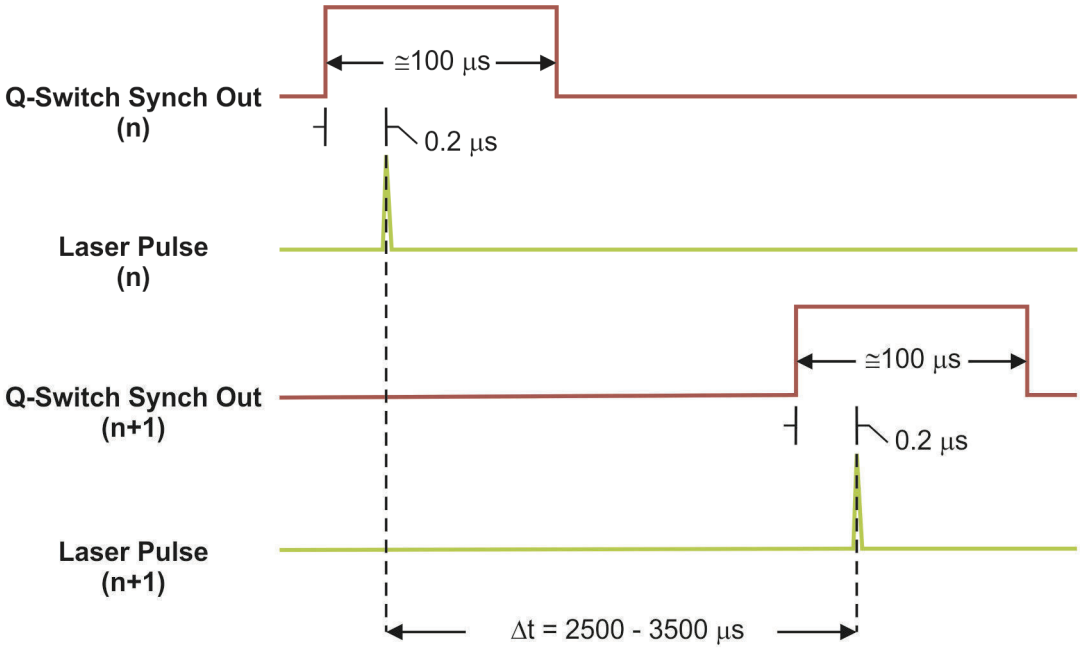

Figure 2.4: Timing diagram for synchronization of pressure data and PIV data. (not to scale for representation purposes).

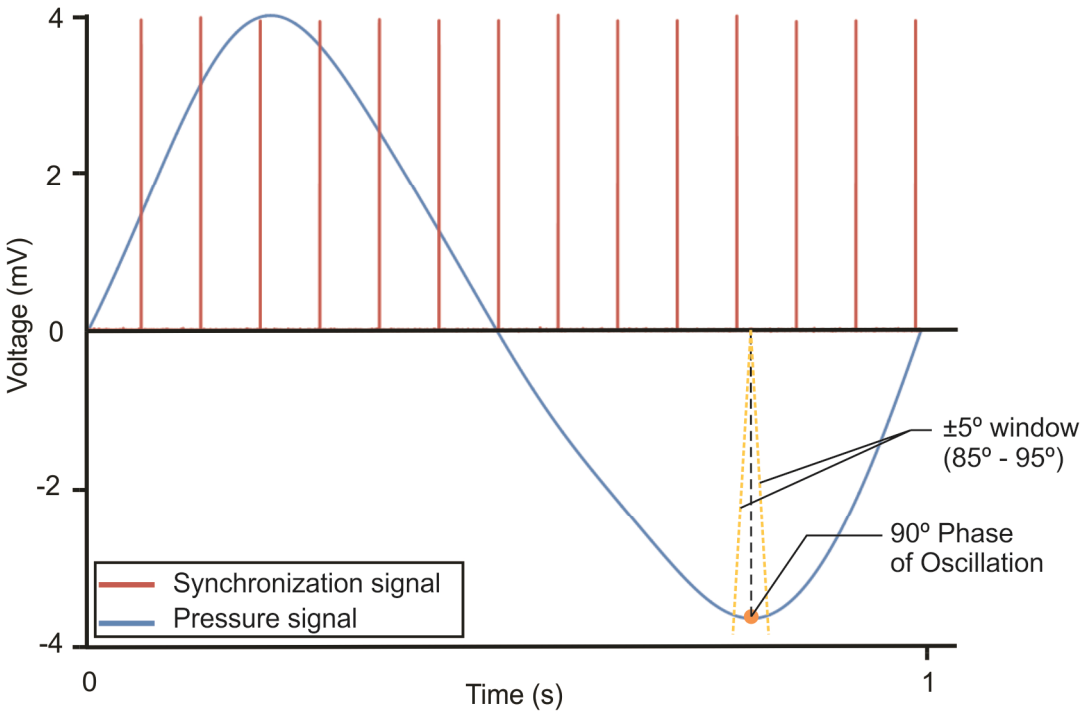

Figure 2.5: A representative sample experimental data showing pressure signal (blue line) for one oscillation period together with simultaneously acquired synchronization signal (red line). Also illustrated phase referencing window for 90° phase of the fluid-resonant oscillation.

CHAPTER 3

GLOBALLY COUPLED OSCILLATIONS AS A FUNCTION OF DEPTH

In the present chapter, the structure of shallow flow past a cavity is characterized as a function of: inflow Reynolds number; elevation above the bed (bottom surface); and the degree of coupling between the separated shear layer along the opening of the cavity and a gravity wave mode within the cavity. A technique of particle image velocimetry is employed simultaneously with unsteady pressure measurements to characterize the flow structure and degree of the coupling. Coherent patterns of vorticity along the cavity opening and at the trailing (impingement) edge of the cavity are related to the streamline topology and associated critical points as a function of elevation above the bed. Associated patterns of normal and shear Reynolds stresses are defined, and related to the exchange velocity and mass exchange coefficient along the cavity opening. Substantial increase of mass exchange between the cavity and the main flow occurs in presence of shear layer-gravity wave coupling for all elevations above the bed.

3.1 BACKGROUND

Shallow flows exist in many forms in our environment, including inland rivers, as well as coastal flows. Such flows have a free surface and a bed (bottom surface), and their horizontal dimensions are much larger than their depth h_w. As was mentioned in Section 2.1.3, these flows are usually fully turbulent and, in most cases, satisfy the criterion for a fully developed turbulent flow $L_i / h_w > 50$ (Uijttewaal et al., 2001), where L_i is the distance from the origin of the flow. Such a fully developed condition refers to the small-scale, three-dimensional turbulence between the free surface and the bottom surface (bed); this turbulence has a characteristic length scale L_T less than or equal to the water depth $L_T < h_w$. It is, however, typically considered to have an insignificant influence on the onset and the development of large-scale instabilities, which are considered to be quasi-two-dimensional, and vortex formation in the horizontal plane.

Basic classes of separated shallow flows in the horizontal plane include shallow jets, mixing-layers and wakes, which often have large, or practically infinite, streamwise length. A dimensionless stability parameter S determines if a flow instability develops in the horizontal plane, thereby leading to development of a vortex (ices). As mentioned previously in Section 1.3, stability parameter S is defined as $S = \overline{c_f}\delta\,\overline{U}/2h_w\Delta U$, where $\overline{c_f}$ is the bed friction coefficient, δ is the width of the transverse shear flow, $\overline{U}$ denotes the average velocity across the shear layer, ΔU is the corresponding velocity difference across the layer, and h_w is the water depth (Chu & Babarutsi, 1988). The velocity difference ΔU imposes a

destabilizing influence that promotes the onset of instability, whereas the friction coefficient $\overline{c_f}$ tends to retard the onset of the instability, i.e., it has a stabilizing effect. In essence, the onset of the instability and the associated vortex formation can therefore occur only when the magnitude of the stability parameter S is less than the critical stability parameter value S_{cr}.

3.1.1 Shallow wakes, mixing layers, jets of infinite streamwise extent

In recent decades, major contributions have been made to our understanding of shallow wakes, mixing layers and jets, involving experiments, theoretical developments, and numerical simulations. The primary emphasis has been on these classes of shallow flows having infinite streamwise extent. Representative investigations of instabilities and vortex formation in shallow wakes include: the studies of Ingram and Chu (1987), Chen and Jirka (1995), and Ghidaoui et al. (2006); in shallow mixing layers by Chu and Babarutsi (1988), Chen and Jirka (1998), and van Prooijen and Uijttewaal (2002); and in shallow jets by Giger et al. (1991), Dracos et al. (1992), and Jirka (1994). Theoretical analyses and numerical simulations of the possible convective and absolute instabilities of shallow wakes, mixing layers and jets, and the relationship of these instabilities to eventual development of large-scale vortical structures, have been undertaken in a range of studies, including those of Chu et al. (1991), Chen and Jirka (1997), van Prooijen and Uijttewaal (2002), Socolofsky and Jirka (2004), Chan et al. (2006), and Ghidaoui et al. (2006). Kolyshkin and Ghidaoui (2003) also characterized the effects of the rigid lid assumption. Ghidaoui and Kolyshkin (1999) and Kolyshkin

and Ghidaoui (2002) extensively assessed gravitational and shear instabilities of shallow flow in open channels.

3.1.2 Shallow mixing layers of finite length

All of the foregoing studies involve shallow flows of infinite streamwise extent. An obstacle or corner in a mixing layer produces a finite length scale in the streamwise direction. As a consequence, development of the mixing layer is influenced by the finite length scale of the instability as well as the upstream influence from the region of the impingement upon the obstacle or corner. A representative example of a shallow mixing layer having a finite length scale in the streamwise direction is the shallow flow past a cavity, which has been investigated experimentally by Weitbrecht and Jirka (2001), Kurzke et al. (2002), Wallast et al. (1999), Uijttewaal et al. (2001), and computationally by McCoy et al. (2008).

Shallow flow past a cavity can potentially give rise to excitation of an eigenmode of a gravity standing wave within the cavity, due to coupling with an inherent instability of the separated shear layer along the cavity opening. Kimura and Hosoda (1997) qualitatively visualized the formation of vortical structures along the opening of a cavity and computed the velocity field. Meile et al. (2011) experimentally determined the frequency and amplitude of periodic oscillations of the free surface in rectangular cavities along both walls of a channel. For a cavity configuration analogous to an organ pipe in air, Ekmekci and Rockwell (2007)

related the coherence of vortex formation along the cavity opening to the degree of coupling with a longitudinal gravity standing wave mode within the cavity.

Wolfinger et al. (2012) considered shallow flow past a rectangular cavity and addressed the flow structure in relation to onset of a gravity standing wave. Emphasis was on the turbulence statistics at mid-depth for the progression of states associated with increasing inflow velocity: pre-lock-on; onset of lock-on; lock-on; and late lock-on. It was found that the largest magnitude Reynolds stress occurred during the locked-on state of the flow oscillation. Not yet addressed are the flow patterns as a function of elevation above the bed, including the interrelationship between topological patterns of streamlines, vorticity, Reynolds stresses, and mass exchange between the cavity and the main flow. The present investigation addresses these unresolved aspects.

3.1.3 Mass Exchange

The mass exchange between the cavity and the mainstream has been addressed using a variety of experimental approaches. Jarrett and Sweeney (1967) used an evaporative surface technique to determine the local mass transfer coefficients of a fully submerged cavity in a non-shallow flow and Valentine and Wood (1979) used dissolved tracer to determine the effects of a sequence of small cavities along the bed (bottom surface) on longitudinal dispersion beneath the free surface. More recently, Uijttewaal et al. (2001) and Kurzke et al. (2002) visualized the flow with colored dye; they used variation with time of patterns of dye

concentration to determine the mass exchange coefficients. The mass exchange coefficient was determined from planar concentration analysis (PCA). Jamieson and Gaskin (2007) used colored dye visualization and particle tracking and observed that three-dimensional flow structures have an important role in the mass exchange process. These studies concluded that the exchange process between the main stream and the cavity is a first-order process, even though the flow patterns show three-dimensional characteristics. A method that does not use marker fluid was advanced by Weitbrecht et al. (2008), who used (free-) surface particle image velocimetry, in order to determine the mass exchange coefficient in terms of the cross-stream velocity fluctuation along the opening of a cavity formed by adjacent groynes. Computations of McCoy et al. (2007) and Constantinescu et al. (2009) have yielded insight into the mass exchange process between the cavities formed by neighboring groynes and the main channel flow. In their simulations, the free surface of the water is treated as rigid, corresponding to the rigid-lid assumption.

3.1.4 Unresolved Issues

Shallow flow past a cavity can give rise to vortex formation in the separated shear layer along the cavity opening. This vortex formation may be highly coherent if coupling occurs between the separated layer and a gravity wave mode within the cavity. Due to the fundamentally different boundary conditions at the bed (bottom surface) and the free-surface above the bed, it is anticipated that the flow structure with and without gravity standing wave coupling will exhibit variations with depth. The nature of, and correlation between, the flow patterns in the bed and free-

surface regions, as well as the regions between them, have not been addressed. Complementary representations of the flow structure, involving streamlines, vorticity contours and contours of constant velocity components can provide a basis for interpretation of the flow physics as a function of elevation above the bed (bottom surface). Use of topological concepts allows identification of critical points of the streamline patterns, in relation to patterns of vorticity and velocity, thereby providing insight into the degree to which the imprint of highly coherent vortex formation above the bed exists adjacent to the bed. These aspects have not yet been pursued.

Significant turbulent stresses, that is, Reynolds normal and shear stresses, are expected to occur in the separated shear layer along the cavity opening. Enhanced turbulent shear stress in the separated shear layer would increase the entrainment from the cavity into the separated shear layer, thereby altering the flow patterns within the cavity. These normal and shear stresses may also have significant magnitudes along the impingement (trailing) wall of the cavity, as well as in the interior of the cavity. All of these features involving turbulent stresses have not been characterized in relation to elevation above the bed, for cases with and without coupling with a gravity wave mode of the cavity. The mass exchange between the cavity and the main stream is a function of the turbulence characteristics of the separated shear layer along the cavity opening. The manner in which the structure of the separated layer varies with elevation above the bed, and

its relation to the effectiveness of the mass exchange between the cavity and the main stream, has not been determined.

3.2 EXPERIMENTAL SYSTEM AND METHODOLOGY

Experiments were performed in a large-scale recirculating, free-surface water channel that has low free stream turbulence intensity (0.2%). The main test section of this channel has an adjustable depth of 610 mm, a length of 4,877 mm and a width of 927 mm. A primary objective of the present study is to determine the structure of a shallow, unsteady shear layer along the mouth of a cavity. Specifically, both non-coupled and fully coupled shear layer oscillations with the gravity wave mode of the cavity are of interest. A test section was designed to control the cavity dimensions, water depth, and flow velocity. Full details of the experimental system are given by Wolfinger et al. (2012). A side view of the experimental system is given in Figure 3.1. Upstream of the test section, the flow passed through a settling chamber with flow conditioning in the form of honeycombs and screens, followed by a contraction. In addition, a contraction is located upstream of the leading edge of the cavity, as indicated in the plan view of Figure 1 of Wolfinger et al. (2012). This contraction reduces the width of the test section from 927 mm to 470 mm. The width and streamwise length of the channel located downstream of the contraction are respectively W_e = 470 mm and L_e = 1384 mm.

The cavity width W, cavity length L and water depth h_w were varied in order to attain non-coupled and fully-coupled states. The cavity section has a length L = 305 mm and a width W = 457 mm. All of the acrylic components have a height h_a = 102 mm. Boundary layer trips of 1.6 mm thickness and a length of 13 mm are located at the marked positions in Figure 3.1 on the top wall of the raised plate and the vertical surface of the inflow channel, at a location immediately downstream of the contraction. By using this arrangement, it was possible to produce rapid onset of a turbulent boundary layer and attainment of a fully turbulent boundary layer at the leading edge of the cavity. The water level h_w could be adjusted to an arbitrary value, as shown in the side view of Figure 3.1. A value of h_w = 38.1 mm was employed in the present experiments; it was associated with the largest amplitude of the resonant-coupled oscillations of the free surface within the cavity. The amplitude of the gravity standing wave was h_d = 3 mm which is shown in the plan view (section A-A) in Figure 3.2. This peak amplitude corresponds to a ratio of wave amplitude h_d to the water depth h_w of h_d / h_w = 0.078.

The eigenfrequencies of the eigenmodes of the gravity standing wave in the cavity is aligned in the streamwise direction is given by Kimura and Hosoda (1997) and Naudascher and Rockwell (1994):

$$f_n = \frac{n\sqrt{gh}}{2L}, \quad n = 1, 2, 3 \ldots \tag{3.1}$$

in which L is the cavity length, h_w is the water depth, g is the gravitational acceleration, and n and f_n are the mode and frequency of the oscillation. The first

mode of the standing wave corresponds to $n = 1$, for which the wavelength of the gravity standing wave is twice the cavity length. This mode is represented by the schematic of Figure 3.2 (section A-A). The predicted frequency according to Equation 3.1 is $f_1 = 1.0$ Hz, which compares with the experimentally determined value of $f_1 = 1.02$ Hz. When the frequency f_n of the gravity standing wave mode within the cavity approaches and matches the most instable frequency f_s of the separated shear layer, a coupled, self-sustained oscillation occurs. Lock-on exists when the frequency of the coupled oscillation remains at $f_s / f_n = 1$ as the reduced velocity U/f_nL is varied. Within this range, the fully-coupled maximum amplitude of oscillation is attained; it is of primary interest herein, and is attained at a value of depth-averaged inflow velocity of $U = 433$ mm/s. The representative non-coupled state involving insignificant amplitude of the coherent oscillation occurs at $U = 236$ mm/s. The velocity variation with depth follows the one-seventh power law, in accord with the fully turbulent nature of the shallow water layer. At each elevation z_L/h_w above the bed (bottom surface), the local velocity U in the main stream was employed for normalization of velocity components, turbulence statistics and vorticity.

To characterize analogous systems involving coupling between a flow instability and a resonator, the reduced velocity $U_r = U/f_nL$ (inverse of Strouhal number) is employed (Naudascher & Rockwell, 1994). The two aforementioned states of the flow occur at $U/f_nL = 0.78$ for the non-coupled state and $U/f_nL = 1.44$ for the coupled state. For shallow flow having a free-surface (air-water interface),

in absence of an adjacent resonator, the Froude number $U/(gh_w)^{1/2}$ is used to define the onset of both gravitational and hydrodynamic instabilities, as described by Ghidaoui and Kolyshkin (1999). The corresponding values of Froude number based on the depth-averaged inflow velocity and water depth are $Fr = U/(gh_w)^{1/2} = 0.39$ for the uncoupled state and $Fr = 0.71$ for the coupled state. In order to investigate the flow structure as a function of depth, elevations above the bed of $z_L/h_w = 0.033$, 0.067, 0.167, 0.333, 0.500, 0.667 and 0.833 were considered. The values of Reynolds number, based on the width W of the inflow channel, for values of $U/f_nL = 0.78$ and 1.44, were respectively $Re_W = 1.1\text{x}10^5$ and $Re_W = 2\text{x}10^5$; based on water depth h_w, $Re_{hw} = 9\text{x}10^3$ and $Re_{hw} = 1.6\ \text{x}10^4$.

The stability parameter S was computed using the standard definition $S = \bar{c_f}\delta\,\overline{U}/2h_w\Delta U$. As mentioned in Section 1.3, velocity field data obtained from digital particle image velocimetry were used to determine the shear layer thickness δ, and $\bar{c_f}$ was determined using the correlation $\frac{1}{\sqrt{\bar{c_f}}} = -4log\left(\frac{1.25}{Re\sqrt{\bar{c_f}}}\right)$, also employed by Chu and Babarutsi (1988). The values of stability parameter S determined herein, $S = 0.002$ for the non-coupled state and $S = 0.003$ for the coupled state, are of the same order as those determined in the investigations of Chu and Babarutsi (1988), and Kolyshkin and Ghidaoui (2002). Kolyshkin and Ghidaoui (2002) addressed both shear and gravitational instabilities in shallow water flows in compound channels. Even though the present configuration is a constant depth channel, it is desirable to consider limiting values for onset of an instability. Bed friction does not stabilize the flow below values of the stability

parameter S_{cr} of the order S_{cr} = 0.01 to 0.1 (Kolyshkin & Ghidaoui, 2002). That is, below these critical values of S_{cr}, instabilities occur due to the destabilizing effect of the velocity difference ΔU across the shear layer; in the present study, the values of the stability parameter are S = 0.002 and S = 0.003. Kolyshkin and Ghidaoui (2002) also provided insight into the effects of channel width on the stability of the shallow flows. Using the terminology herein, the dimensionless channel width is defined as $W_d = W_e / h_w$, where h_w is the water depth and W_e is the width of the channel. In present study, the dimensionless width of the channel is W_d = 12.3. By considering the wavenumber of the instability k = 0.4 and comparing with computations of Kolyshkin and Ghidaoui (2002, Figure 5), the growth rate of the instability does not vary significantly for values of the dimensionless channel width W = 10 to ∞. One can therefore conclude that an increase of channel width in the present experiment would not affect the instability of the flow.

The frequency and amplitude of both shear layer and gravity standing wave oscillations were determined with PCB piezoelectric pressure transducers (model number 106B50). The pressure transducers were located at the impingement corner of the cavity (p_a) and within the cavity (p_b) at a location 229 mm from the impingement corner. Both transducers p_a and p_b are located at an elevation of h_p = 13 mm from the bed (bottom surface). Transducer p_b was employed as a phase reference for phase-averaging of images. A low-pass digital filter was employed during signal processing; it had a cutoff frequency of 5 Hz. The pressure signal is sampled with 20 Hz which was well above the Nyquist frequency. Sampling was

conducted over a time span of 102.4 s, corresponding to a total of 2048 samples. Ten of these time records were acquired for each inflow velocity and then transformed into the frequency domain and averaged.

The flow patterns of the non-coupled and fully-coupled oscillations were characterized with high-image-density particle image velocimetry (PIV). The main components of this system are indicated in Figures 3.1 and 3.2. In order to avoid a large number of spurious vectors and to allow optimal evaluation of the particle image patterns, the time delay between the two pulses of the laser was varied from 2.5 to 3.5 ms depending on the inflow velocity and the depth elevation. The elevation of the laser sheet z_L above the bed (bottom surface), relative to the water depth h_w, had values of z_L/h_w = 0.033, 0.067, 0.167, 0.333, 0.500, 0.667 and 0.833.

For each set of PIV experiments, 200 sets of images were recorded simultaneously with the pressure signal. For each water depth, 15 sets of experiments were conducted, corresponding to 3,000 sets of images were recorded. The time-averaged flow structure and turbulence quantities were evaluated using 3,000 instantaneous velocity fields. Phase averaging of the flow structure was also done for the fully coupled state corresponding to a reduced velocity of U/f_nL = 1.44. As mentioned in Section 2.5, a laser trigger signal was recorded simultaneously with the digitally-filtered pressure signal from the transducer p_b located inside the cavity to define the phase information for each velocity field. Images were recorded at different phases of the gravity wave oscillation and the information from the trigger signal was used to determine the phase of the each

image. The phase window size for this determination was ten degrees, where the complete cycle corresponded to 360 degrees. This method led to a minimum of 60 velocity fields per phase window and, these velocity fields were used to evaluate the phase-averaged flow structure and turbulence specifications.

3.3 IDENTIFICATION OF COUPLING AND LOCK-ON

In contrast to the onset of instabilities in isolated, shallow separated layers such as jets, mixing layers and wakes, the present configuration of shallow flow past a cavity can give rise to coupling between a gravity wave mode of the cavity and the inherent instability of the separated shear layer along the cavity. This coupling can lead to not only resonant response of the system, but also to lock-on of the overall oscillation frequency to the eigenfrequency of the gravity standing wave mode, that is, $f / f_n = 1$. This type of coupling and locked-on response has direct analogies with the cases of airflow past a deep cavity, whereby an acoustic mode of the cavity is excited, and flow past an elastically-mounted cylinder, where a structural mode of the cylinder is excited (Naudascher & Rockwell, 1994). If one denotes the natural frequency of a mode as f_n, then the reduced velocity is typically represented in the form U/f_nL, where U is the inflow velocity and L is the characteristic dimension of the deep cavity or the cylinder ($L = D$). In accord with this terminology, the same form of the reduced velocity will be employed herein.

The pressure response of the cavity was assessed for different flow velocities, in order to determine the level of coupling between the separated shear

layer along the mouth of the cavity and the gravity standing wave within the cavity. Pressure measurements were made at the locations indicated in Figure 3.2. The transducer at the impingement corner (p_a) indicates the combined influence of the unsteady shear layer along the cavity opening and the gravity standing wave, while the transducer inside the cavity (p_b) senses only the contribution from the gravity standing wave within the cavity.

The pressure fluctuation $p_b(t)$ in the cavity and the corresponding spectra are given in the upper part of Figure 3.3, i.e., Figure 3.3a. The difference between the non-coupled case U/f_nL = 0.78 (dashed line) and the coupled case U/f_nL = 1.44 (solid line) is seen clearly. In the coupled case, the signal is well defined and periodic, which is represented by a sharp peak in the spectrum. On the other hand, the spectral peak for the non-coupled case is barely detectable.

In Figure 3.3b (left plot), the magnitudes of the spectral peaks, designated as $S_p(f)_{max}/(1/2\rho U^2)$, are plotted against dimensionless inflow velocity U/f_nL for the pressures p_a and p_b. It is clear that the magnitude of the peak is consistently higher for pressure p_a at the corner of the cavity, due to the impingement of unsteady shear layer (Tang & Rockwell, 1983). The magnitudes $S_p(f)_{max}/(1/2\rho U^2)$ of the spectral peaks of p_a and p_b rapidly increase with increasing U/f_nL and reach a maximum at U/f_nL = 1.44. Then, drastic decreases occur with increasing U/f_nL.

In Figure 3.3b (right plot), both the dimensionless frequency f/f_n and the magnitude of the spectral peak $S_p(f)_{max}/(1/2\rho U^2)$ are plotted against dimensionless

inflow velocity U/f_nL for the pressure fluctuation p_b within the cavity. The symbol f denotes the spectral peak $S_p(f)_{max}/(1/2\rho U^2)$ of the oscillation at a given value of dimensionless inflow velocity U/f_nL. At low inflow velocities, f / f_n increases quasi-linearly with the increasing U/f_nL. Moreover, the magnitude of $S_p(f)_{max}/(1/2\rho U^2)$ is lower at low U/f_nL due to the lack of sufficient coupling with the gravity standing wave mode of the cavity. At U/f_nL = 1.1, onset of lock-on occurs, represented by the line f / f_n = 1 and the magnitude of $S_p(f)_{max}/(1/2\rho U^2)$ starts to increase rapidly. For further details of this coupling phenomenon, the reader is referred to the investigation of Wolfinger et al. (2012).

3.4 QUANTITATIVE FLOW STRUCTURE

3.4.1 Time-Averaged Flow Patterns

Figure 3.4 shows patterns of time-averaged contours of constant velocity magnitude $<V>/U$ and time-averaged streamlines $<\psi>$. The images in the left column (U/f_nL = 0.78) represent the case where a gravity standing wave does not occur within the cavity and the images in the right column (U/f_nL = 1.44) correspond to existence of a gravity standing wave.

Comparison of the contours of constant velocity magnitude $<V>/U$ in the right column with the corresponding contours in the left column shows the effect of coupling between the unstable shear layer along the opening of the cavity and the gravity standing wave mode within the cavity. At both elevations z_L/h_w = 0.067 and 0.667 from the bed (bottom surface), existence of the gravity standing wave is

associated with an increase of the velocity magnitude $<V>/U$ within the cavity. As defined by the color bar at the bottom of the image layout, light blue and light green colors represent larger magnitudes relative to the dark blue color, which corresponds to a very low magnitude of $<V>/U$. On the other hand, the overall form of the streamline patterns $<\psi>$ is relatively unaffected by the onset of the gravity standing wave at both elevations $z_L/h_w = 0.067$ and 0.667.

Figure 3.5 shows patterns of time-averaged streamlines $<\psi>$. Images in the left and right columns represent respectively cases without and with a gravity standing wave within the cavity. The successive rows of images, from top to bottom, correspond to elevations closer to the bed (bottom surface). The first two rows of images correspond to elevations well above the bed, i.e., five-sixths ($z_L/h_w = 0.833$) and two-thirds ($z_L/h_w = 0.667$) of the depth h_w of the shallow water layer. At these elevations, the recirculation pattern within the cavity does not show any unusual features and, furthermore, the separation line from the leading edge of the cavity to the trailing edge is nearly straight, with very little deflection.

At an elevation closer to the bed, corresponding to $z_L/h_w = 0.167$, the separation line from the leading corner of the cavity is deflected inward (downward) in the vicinity of the trailing-corner. Along the trailing (downstream) wall of the cavity, an alleyway of streamlines occurs, corresponding to a layer of downward oriented, jet-like flow. Moreover, along the leading (upstream) wall of the cavity, a small-scale separation bubble forms.

The appearance of three-dimensional vortex systems in the presence of groynes in river flows has been computed by McCoy et al. (2007). They showed that a horseshoe-like vortex can be present at the base of a groyne. In the present experiment, a three-dimensional vortical structure may exist at the base of the trailing corner of the cavity; it could distort the sectional streamline pattern in that region.

Finally, in Figure 3.5, at the two elevations z_L/h_w = 0.067 and 0.033 closest to the bottom surface (bed) of the cavity, the scale of the separation bubble adjacent to the leading (upstream) wall of the cavity is generally larger. Moreover, the streamlines along the opening of the cavity diverge substantially with increasing streamwise distance as they are deflected towards the interior of the cavity. The inward-directed, jet-like flow along the trailing (downstream) wall of the cavity is pronounced. These features can be defined with topological concepts involving critical points of the flow, which are most evident at z_L/h_w = 0.033 (right image, with gravity standing wave). A focus *F* occurs near the leading (upstream) corner of the cavity; it is the center of a swirl pattern of the streamlines. A bifurcation line BL^+ corresponds to very rapid divergence of the streamlines with increasing streamwise distance along the opening of the cavity; this divergence starts near the leading-corner of the cavity where the streamlines are very closely spaced. Another type of bifurcation line BL^- occurs near the trailing (downstream) wall of the cavity. That is, convergence of streamlines occurs along this line. Finally, a saddle point *SP* occurs just upstream of the trailing (downstream) corner

of the cavity; it represents the upstream migration of the wall stagnation point that is evident at larger values of elevation z_L/h_w = 0.833, 0.667 and 0.167 of the laser sheet. Moreover, the bifurcation line BL^- adjacent to the trailing (impingement) wall of the cavity is also present at z_L/h_w = 0.167. These critical points and unusual features are generally present in all of the streamline patterns close to the bed, that is, at 0.067 and 0.033, though certain of them are not detectable at elevations close to the free surface, that is, at z_L/h_w = 0.833 and 0.667. It is hypothesized that these unusual features close to the bottom surface (bed) are due to three-dimensional effects.

It is therefore evident that the region of flow close to the bed (bottom surface) is associated with the onset of a number of critical points, which distinguish the flow patterns from those occurring at higher elevations above the bed. In addition, a generic feature of the flow patterns close to the bed is the inward deflection of the streamlines towards the cavity, more specifically, towards the center of the overall pattern of curved streamlines. This streamline deflection, towards the origin of the radius of curvature, has been observed in quite different applications, for example, along the end wall of a turbomachine (Lakshminarayana, 1996). The concept of streamline deflection is illustrated in the schematic of Figure 3.6. Consider flow along the two streamlines designated as 1 and 2 in Figure 3.6. The flow is assumed to be inviscid, and in the region indicated, equilibrium exists between the centrifugal and pressure forces. The pressure gradients in the normal *n* direction at 1 and 2 are:

$$\left.\frac{\partial p}{\partial n}\right|_1 = \rho\frac{V_1^2}{R_1} \qquad \left.\frac{\partial p}{\partial n}\right|_2 = \rho\frac{V_1^2}{R_2} \tag{3.2}$$

Assuming that the static pressure does not vary across the boundary layer:

$$\left.\frac{\partial p}{\partial n}\right|_1 = \left.\frac{\partial p}{\partial n}\right|_2 \tag{3.3}$$

The flow velocity decreases as the wall is approached, that is, V_2 is less than V_1. To satisfy the foregoing conditions, the radius of curvature must decrease, that is R_2 becomes smaller than R_1. So the streamline near the bed is deflected from *2* to *2′* and a corresponding radial flow occurs in the boundary layer. An equivalent explanation of the streamline deflection towards the origin of the radius of curvature is given by Einstein (1926); he explains the meandering of a river using a tea cup analogy. The centrifugal force, which varies as the square of the velocity, is smaller close to the bottom surface (bed) due to friction effects; this decreased force gives rise to an inward-oriented flow. The foregoing concepts are therefore the basis for the inward deflection of the streamlines in the region close to the bed in Figure 3.5.

Figure 3.7 provides time-averaged contours of constant transverse velocity $\langle v \rangle/U$. As in previous layouts, the left column of images (U/f_nL = 0.78) corresponds to absence of a gravity standing wave and right column (U/f_nL = 1.44) represents the case where the gravity standing wave is present. Rows of images from top to bottom correspond to successive layers closer to the bed (bottom surface). Blue contours of $\langle v \rangle/U$ indicate flow in the outward direction (positive y

direction) away from the cavity and red contours in the inward direction (negative y direction) towards the interior of the cavity.

The first general observation is that the magnitudes of the transverse velocity $<v>/U$ are larger in the right column of images (U/f_nL = 1.44), corresponding to the case with the gravity standing wave. That is, the magnitudes of both the positive (blue) and negative (red) regions are larger than those in the left column of images (U/f_nL = 0.78) where the gravity standing wave does not occur. It is interesting to note that in the region near the bed, corresponding to elevations of z_L/h_w = 0.067 and 0.033, relatively high velocity (dark red color) flow into the cavity occurs along the trailing (impingement) wall. Furthermore, high velocity (darker blue color) flow occurs out of the cavity towards the cavity opening. One can therefore conclude that coupling between the separated shear layer at the mouth of the cavity and the mode of the gravity standing wave within the cavity, which is associated with existence of the gravity standing wave, induces a global influence throughout the interior of the cavity, that is, enhanced recirculation flow, indicated by the higher levels of red and blue contours within the cavity.

In Figure 3.7, within the left column of images (U/f_nL = 0.78) corresponding to the case of no gravity standing wave, specifically the region near the bed, at elevations z_L/h_w = 0.033 and 0.067, the extended blue contours along the upper edge of the cavity indicate significant outward deflection (upward oriented arrow) of the flow in that region. On the other hand, in the corresponding images in the right column, where the gravity standing wave exists, these extended blue

regions are eliminated in favor of pronounced downward flow directed towards the interior of the cavity along the entire length of the cavity opening. A common feature of these regions close to the bed, i.e., at z_L/h_w = 0.067 and 0.033, is a high concentration of outward oriented (blue) flow at the trailing-corner of the cavity. This concentration is associated with the saddle point of the streamline pattern shown in the image at the lower right of Figure 3.5; it occurs in conjunction with a region of localized flow separation at the trailing-corner.

Figure 3.8 gives time-averaged contours of constant vorticity $<\omega>L/U$. At elevations above the bed region, the highest levels of vorticity are attenuated more rapidly along the cavity opening when the gravity standing wave is present (right column) in comparison with absence of the gravity standing wave (left column). This comparison is made for a given green level of vorticity ($<\omega>L/U$ = -6) at the elevation z_L/h_w = 0.667. The length of the line indicated with an arrow is shorter in the right image than in the left image. As will be shown subsequently, this more rapid degradation of high-level vorticity in streamwise direction is associated with occurrence of larger turbulent shear and normal stresses in the separated shear layer along the cavity opening. A further trend is enhanced deflection of a region of vorticity towards the interior of the cavity, which occurs at the trailing (impingement) corner. That is, especially at elevations close to the bed, z_L/h_w = 0.033 and 0.067, the layer of vorticity extending into the cavity has a relatively large width, and the extent of this region is enhanced in presence of the gravity standing wave. Comparison of the images of $<\omega>L/U$ in the right column

with those in the left column shows that this inward deflection of the vorticity layer is compatible with the streamline patterns of Figure 3.5, and the patterns of transverse velocity of Figure 3.7, especially in the vicinity of the trailing corner of the cavity.

Figures 3.9 and 3.10 show contours of constant root-mean-square streamwise u_{rms} and transverse v_{rms} velocity fluctuations. The influence of the coupled oscillation involving a gravity standing wave $U/f_nL = 1.44$ (right column of images) is evident at all values of elevation above the bed, extending from $z_L/h_w = 0.067$ to 0.500. Magnitudes of both u_{rms}/U and v_{rms}/U are substantially higher at all elevations above the bed (bottom surface), and extend over a larger width in presence of the gravity standing wave.

Figure 3.9 shows that large-scale, high-level clusters of u_{rms}/U occur in the immediate vicinity of the trailing-corner of the cavity as the bed is approached ($z_L/h_w = 0.067$ and 0.167). These clusters are associated with the onset of the saddle point in the vicinity of the trailing (impingement) corner, in the streamline patterns of Figure 3.5. The patterns of v_{rms}/U given in Figure 3.10 show high levels of v_{rms}/U at the trailing-corner of the cavity at all elevations. In the region closest to the bed ($z_L/h_w = 0.067$), two peaks of v_{rms}/U are evident, thereby indicating large transverse undulations at the location of the saddle point indicated in Figure 3.5.

Corresponding patterns of Reynolds stress $<u'v'>/U^2$ are given in Figure 3.11. In essence, the Reynolds stress represents the degree of correlation between

the streamwise u' and transverse v' velocity fluctuations. This correlation is clearly high when the gravity standing wave exists, as shown in the top two figures in the right column of images, corresponding to elevations z_L/h_w = 0.500 and 0.333. As the bed region (z_L/h_w = 0.167 and 0.067) is approached, however, the peak value of Reynolds stress is significantly attenuated. Enhanced Reynolds stress increases the entrainment demand of the separated shear layer along the cavity. It is therefore anticipated that the mass exchange between the cavity and the free stream will be higher for the case where the standing wave occurs (right column of images, U/f_nL = 1.44). Note that the magnitude of the Reynolds stress decreases as the bed is approached (z_L/h_w = 0.167 and 0.067). This observation suggests that the mass exchange will decrease as the bed region is approached. Detailed calculations and interpretation of mass exchange as a function of depth are addressed subsequently.

3.4.2 Phase-Averaged Flow Patterns

In order to understand the effect of coupling between the separated shear layer along the mouth of the cavity and the gravity standing wave within the cavity, phase-averaging of the velocity fields (at U/f_nL = 1.44*)* was conducted, using the pressure fluctuation within the cavity as a reference signal. Different interpretations of the flow structure were then constructed using the phase-averaged velocity fields.

Figure 3.12 shows patterns of phase-averaged streamlines $<\psi>_p$ and phase-averaged contours of constant velocity magnitude $<V>_p/U$ for three different

phases (ϕ = 80°, 200°, 320°) of the oscillation cycle. The left column of images represents the region well above the bed (z_L/h_w = 0.667) and the right column of images corresponds to the region near the bed (z_L/h_w = 0.067).

For both the regions well above the bed (z_L/h_w = 0.667) and at the bed (z_L/h_w = 0.067), flapping motion of the shear layer along the cavity mouth is evident. At z_L/h_w = 0.667, the recirculation pattern within the cavity does not show any abnormalities and deflection of the separation line along the cavity opening is apparent. At z_L/h_w = 0.067, the formation of the separation bubble along the leading (upstream) wall of the cavity is clearly evident. Furthermore, the downward directed, jet-like flow patterns along the trailing (impingement) wall of the cavity are related to formation of a saddle point, as designated in Figure 3.5.

The bottom half of Figure 3.12 shows contours of constant velocity magnitude $<V>_p/U$. In accord with the aforementioned patterns of the time-averaged velocity magnitude $<V>/U$ given in Figure 3.4, the magnitudes of $<V>_p/U$ at the trailing (impingement) edge of the cavity are higher in the bed region (z_L/h_w = 0.067, right column of images), relative to the region well above the bed (z_L/h_w = 0.667, left column of images). Furthermore, it is evident that the interface along the cavity opening exhibits undulations at both elevations z_L/h_w = 0.667 and 0.067.

Figure 3.13 shows phase-averaged contours of constant vorticity $<\omega>_pL/U$ and transverse velocity $<v>_p/U$ for three different phases (ϕ = 80°, 200°, 320°) of

the oscillation cycle. The left column of images represents the region well above the bed (z_L/h_w = 0.667) and the right column of images corresponds to the region near the bed (z_L/h_w = 0.067). At both z_L/h_w = 0.667 and 0.067, the patterns of $<\omega>_p L/U$ show the onset and development of a large-scale vortical structure. It moves in the downstream direction with increasing phase angle ϕ. At z_L/h_w = 0.667, the patterns of vorticity are highly ordered and do not show significant irregularities. On the other hand, at z_L/h_w = 0.067, notable distortions or irregularities occur; they are due to the decreased coherence of vortex formation along the bed region. Moreover, the cluster of vorticity that is along the trailing (impingement) wall of the cavity at z_L/h_w = 0.067 persists over all values of phase angle. On the other hand, this cluster of vorticity does not exist along the trailing (impingement) wall of the cavity at z_L/h_w = 0.667. These observations are in accord with the patterns of the time-averaged streamlines of Figure 3.5.

The bottom half of Figure 3.13 shows contours of constant phase-averaged transverse velocity $<v>_p/U$. The red color indicates the direction of transverse velocity oriented in the negative vertical direction, that is, into the cavity, whereas blue color indicates an orientation in the positive vertical direction, that is, out of the cavity. In accord with the aforementioned patterns of the time-averaged vorticity (Figure 3.8) and transverse velocity (Figure 3.7), as well as patterns of phase-averaged vorticity (Figure 3.13), the magnitudes of the inward-directed (red) transverse velocity at the trailing edge and outward (blue) oriented velocity at the leading edge of the cavity are higher in the bed region at z_L/h_w = 0.067 (right

column of images), relative to the region well above the bed z_L/h_w = 0.667 (left column of images).

Consider, in Figure 3.13, the concentrations of $<v>_p/U$ along the opening of the cavity. They are labeled as *a*, *b*, and so on. In the left column of images, corresponding to the elevation z_L/h_w = 0.667 above the bed, the first image at ϕ = 80° shows concentrations *a* and *b*; these concentrations correspond to the vorticity $<\omega>_pL/U$ concentration at ϕ = 80°. At successively larger values of ϕ, these concentrations move downstream and the successor a_2 appears and increases in scale. In the right column of images, corresponding to the region of the bed z_L/h_w = 0.067, the arrangement of the concentrations of $<v>_p/U$ is more complex. A prominent feature is the occurrence of large scale, high magnitude $<v>_p/U$ immediately above the trailing-corner of the cavity, which is due to the predecessor of concentration *b.* It glides above the impingement corner, rather than impinging directly upon it. In addition, a large magnitude of $<v>_p/U$ occurs along the trailing (impingement) wall of the cavity; this region arises from deflection of concentration *a* down along the impingement wall.

Included in Appendix A are additional phase-averaged figures showing the patterns of streamlines $<\psi>_p$, transverse velocity $<v>_p/U$, and vorticity $<\omega>_pL/U$ for nine different phases ϕ of the oscillation cycle at seven different elevations extending from bed to the free surface.

3.4.3 Time-Averaged Exchange Velocity Patterns

A dimensionless exchange coefficient is employed, in accord with Weitbrecht et al. (2008), in order to characterize the mass exchange between the flow within and outside the cavity. Determination of this exchange coefficient requires, first of all, knowledge of the exchange velocity *E*. It is determined using the distribution of transverse velocity along the mouth of the cavity, which extends from the leading to the trailing corner of the cavity. At a given instant of time, fluid may either enter or leave the cavity, depending upon the streamwise distance along the cavity opening. The volume $\forall_{cav}$ enclosed by the cavity boundary and a line between leading (upstream) corner and trailing (downstream) corner of the cavity is given as $\forall_{cav} = LW$. The time needed for complete flushing of the fluid from the cavity is:

$$T_D = \frac{\forall_w}{Q} \tag{3.4}$$

in which $\forall_w$ is the volume of the exchanged water, $Q = EL$ is the mass flux between the cavity and main stream, and *E* is the exchange velocity. During the complete flushing of fluid from the cavity, the volume of exchanged water $\forall_w$ is twice the cavity volume $\forall_{cav}$. That is, during the time interval T_D, a volume of water equal to twice the volume $\forall_{cav}$ is transported across the interface between cavity and main stream. Then Equation 3.4 leads to:

$$T_D = \frac{2\forall_{cav}}{Q} = \frac{2W}{E} \tag{3.5}$$

The instantaneous exchange velocity *E(t)*, spatially averaged over the cavity mouth, is given as:

$$E(t) = \frac{1}{L}\int_0^L |v(t)|dx \tag{3.6}$$

where *v(t)* is the transverse (cross-stream) component of velocity. Time averaged values $\overline{E(t)}$ were obtained by averaging 3000 instantaneous velocity distributions. The mass exchange coefficient *k* was then calculated by normalizing with the main stream velocity *U* and width of the cavity *W* to give:

$$k = \frac{\overline{E(t)}}{2U} \tag{3.7}$$

in which *U* is the velocity of the main stream.

Patterns of time-averaged exchange velocity $\overline{E(t)}$ are given in Figure 3.14. They were obtained by taking time averages over defined successive segments of length $\Delta x/L$ = 0.1 along the opening of the cavity, then connecting the time-averaged values. The left graph shows the case of no gravity standing wave (U/f_nL = 0.78) and the right graph shows the case where the gravity standing wave exists (U/f_nL = 1.44). The coordinate z_L/h_w represents, as in preceding Figures, the elevation above the bed (bottom surface) and the *x/L* axis shows the streamwise

location along the opening of the cavity. The blue point represents the leading edge (x/L = 0) of the cavity and red point shows the trailing edge (x/L = 1) of the cavity.

It is evident that the overall magnitudes of the exchange velocity are higher for the case corresponding to the coupled oscillation associated with the gravity standing wave (U/f_nL = 1.44). From Equation 3.7, one can therefore deduce that the mass exchange coefficient k will be larger in presence of the gravity standing wave. Moreover, for this case, the largest values of the exchange velocity $\overline{E(t)}$ occur at approximately z_L/h_w = 0.500, and the smallest values occur at z_L/h_w = 0.067, i.e., in the bed region. Furthermore, the largest magnitudes occur at a streamwise location of approximately x/L = 0.6.

Comparing with the patterns of time-averaged Reynolds stress $<u'v'>/U^2$ in Figure 3.11, it is clear that regions of large Reynolds stress correspond to the largest values of exchange velocity $\overline{E(t)}$. This correspondence between Reynolds stress $<u'v'>/U^2$ and exchange velocity $\overline{E(t)}$ at z_L/h_w = 0.500 is illustrated in Figure 3.15. The x/L axis is along the opening of the cavity and the y/L axis is in the transverse (cross-stream) direction. The pattern of $<u'v'>/U^2$ is displayed along the bottom surface of this layout and the profile of $\overline{E(t)}$ is represented by the solid line. This line corresponds to the opening of the cavity (y/L = 0) at an elevation of z_L/h_w = 0.500. It is evident that $\overline{E(t)}$ is largest where the $<u'v'>/U^2$ is large. A further point is that $\overline{E(t)}$ increases in the vicinity of the trailing (impingement) corner (x/L = 1.0). This observation agrees with the study of Zhang (1995), which

indicates that the fluid exchange from the cavity to the main flow occurs primarily near the trailing (impingement) corner of the cavity.

The images of Figures 3.4, 3.5, and 3.7 do not provide a direct indication of the influence of potentially significant vertical velocity (v_z) within the cavity. Integration of the transverse velocity v component along the cavity opening was conducted to determine the difference between the mass flux into the cavity and out of the cavity at each of the elevations above the bed. The integration is normalized with cavity length L and free stream velocity U at the corresponding depth z_L/h_w. It was found that the net mass flux $\int vdx/LU$ from the cavity opening at each elevation is not equal to the zero and has values between -0.007 and 0.005. This observation suggests the existence of vertical velocities v_z. On the other hand, the values of the mass exchange $\int|v|dx/LU$ between the cavity and main stream are in the range of 0.065 to 0.083. The ratio of net mass flux $\int vdx/LU$ to the mass exchange $\int|v|dx/LU$ is 0.031, -0.080, 0.088, -0.084, 0.037 and 0.067 at each respective elevation above the bed z_L/h_w = 0.833, 0.667, 0.500, 0.333, 0.167 and 0.067. The presence of vertical velocities is suggested in the study of Jamieson and Gaskin (2007) where dye marker was ejected in the vertical (z-direction).

Profiles of the time-averaged exchange velocity $\overline{E(t)}$ along the mouth of the cavity at different elevations z_L/h_w above the bed are given in the left plot of Figure 16. The value of $\overline{E(t)}$ at each elevation z_L/h_w is obtained by integrating the v along the opening (y = 0) of the cavity. The blue line represents the case where a gravity

standing wave does not occur within the cavity (U/f_nL = 0.78) and red line corresponds to existence of a gravity standing wave (U/f_nL = 1.44). It is evident that magnitudes of $\overline{E(t)}$ along the opening of the cavity are higher for the locked-on case (U/f_nL = 1.44*)* at all elevations z_I/h_w. In accord with aforementioned patterns of $\overline{E(t)}$ (Figure 3.14), values of $\overline{E(t)}$ in Figure 3.16 decreases near the bed and become largest at z_I/h_w = 0.500. The mass exchange coefficient k was calculated from the information in the left plot of Figure 3.16 by using Equation 3.7, and is shown with respect to elevation z_I/h_w in the right plot of Figure 3.16. Mass exchange coefficient values are 40% higher in presence of the gravity standing wave (U/f_nL = 1.44). One can therefore conclude that the mass exchange between the cavity and the main stream increases due to the coupling between the unstable shear layer along the mouth of the cavity and the gravity wave mode within the cavity. The range of the mass exchange coefficient k is from 0.026 to 0.042 for different elevations z_I/h_w. These values compare well with $k \approx 0.03$ obtained by Weitbrecht et al. (2008).

3.5 CONCLUDING REMARKS

The aim of the present investigation is to characterize the flow structure and mass exchange due to shallow flow past a cavity, as a function of elevation above the bed (bottom surface). In addition, the effects of coupling between the unstable shear layer along the opening of the cavity and a gravity wave mode within the cavity are accounted for at successive elevations above the bed. The time- and phase-averaged flow patterns were determined via a technique of high-image-

density particle image velocimetry in conjunction with pressure measurements. This approach revealed the relationship between the depthwise variations of the flow structure of the unsteady shear layer along the opening of the cavity and the recirculating flow within the cavity. The principal findings of this investigation are described in the following.

Effective coupling between the inherent instability of the separated shear layer along the opening of the cavity and the fundamental gravity standing wave mode within the cavity is a global phenomenon that persists for regions close to and well above the bed (bottom surface). Such coupling is associated with large-scale coherent vortical structures in the unstable shear layer and periodic oscillations of the free surface within the cavity. Phase-averaged patterns of vorticity show the timewise development of the undulating vorticity layer along the opening of the cavity in relation to elevation above the bed. Sufficiently far from the bed, the undulating layer evolves into a highly coherent vortex, which eventually impinges upon the corner of the cavity. Close to the bed, these overall patterns of vorticity are maintained and are synchronized with those above the bed, but the degree of coherence of the vortical structure is decreased. In addition, immediately adjacent to the bed, a layer of vorticity is ejected into the cavity along the impingement wall. Time-averaged patterns of vorticity also show this ejected layer and indicate that it becomes more extensive at elevations closer to the bed. Moreover, for all elevations above the bed, the consequence of the organized

undulations of vorticity along the cavity opening is to attenuate the magnitude of time-averaged vorticity in the streamwise direction along the cavity opening.

Corresponding phase-averaged patterns of transverse velocity indicate a region of large magnitude velocity along the impingement wall of the cavity, corresponding to the aforementioned vorticity layer along the impingement wall. Moreover, along the cavity opening, the organized undulations of the separated vorticity layer are associated with corresponding concentrations of transverse velocity that are highly ordered at elevations well above the bed, and take on a more complex, but nevertheless ordered form, at elevations very close to the bed. Time-averaged patterns of transverse velocity indicate that, in presence of the gravity standing wave, and at elevations close to the bed, the flow along the cavity opening is oriented towards the interior of the cavity, over the entire streamwise extent of the cavity opening.

Patterns of both phase-averaged and time-averaged streamlines show common features, when interpreted within a framework of topological concepts using critical points. At locations well above the bed, the number of critical points is minimal, but as the bed region is approached, well defined critical points occur in the form of a focus adjacent to the upstream (leading) wall of the cavity, a negative bifurcation line originating from the leading corner of the cavity, a saddle point immediately upstream of the trailing impingement corner of the cavity and a positive bifurcation line adjacent to the trailing impingement wall of the cavity. Moreover, the streamlines along the cavity opening, at elevations close to the bed,

are deflected in a direction towards the interior of the cavity, and a physical explanation is provided in terms of secondary flow related to streamline curvature. A further, remarkable result is that the form of the time-averaged streamline pattern at a given elevation above the bed is relatively insensitive to the existence or nonexistence of the gravity standing wave within the cavity.

Patterns of normal and shear turbulent Reynolds stresses are substantially enhanced in presence of the gravity standing wave. In the region close to the bed, however, the Reynolds shear stress is attenuated in the separated shear layer along the cavity opening, which is due to decreased correlation between the velocity fluctuation components in the streamwise and transverse directions.

Time-averaged exchange velocity and mass exchange coefficient, determined along the opening of the cavity, indicate substantial (40 percent) enhancement in presence of the gravity standing wave. This observation is in accord with the enhanced Reynolds stresses in the separated shear layer along the opening of the cavity.

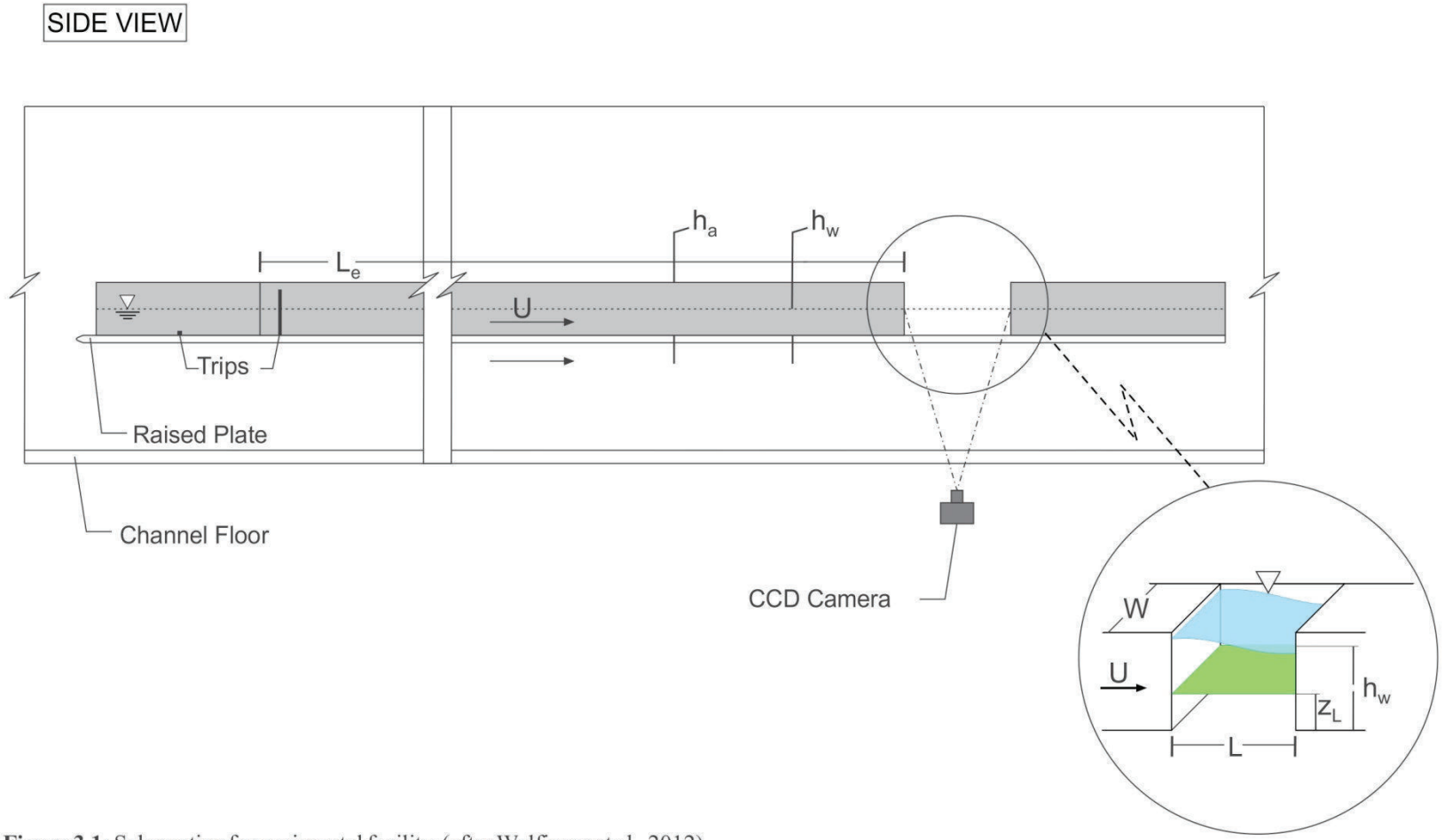

Figure 3.1: Schematic of experimental facility. (after Wolfinger et al., 2012)

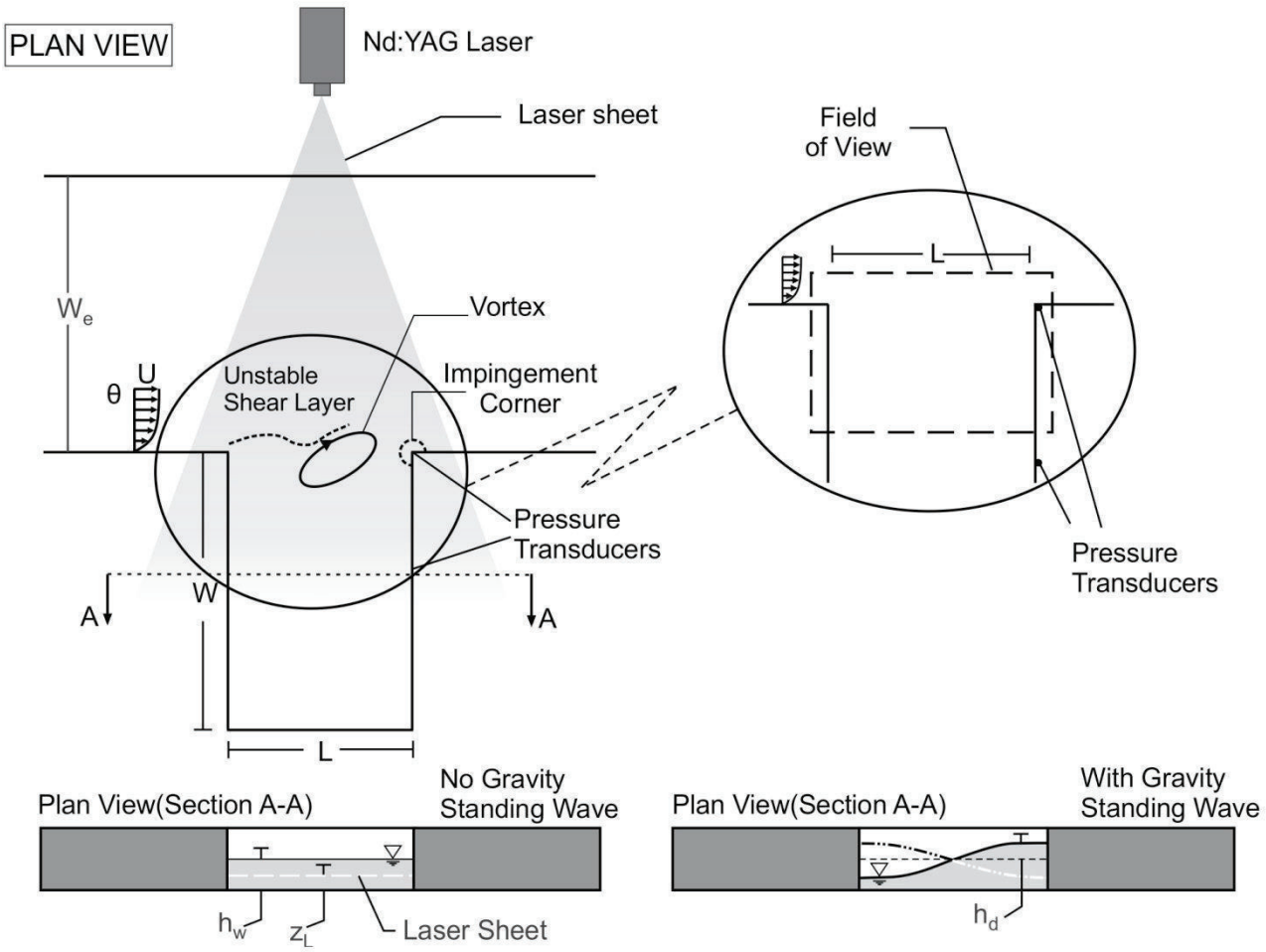

Figure 3.2: Schematic of experimental test section and quantitative imaging system. Also illustrated are unstable shear layer along the opening of the cavity and deformation of free surface due to the gravity standing wave within the cavity.

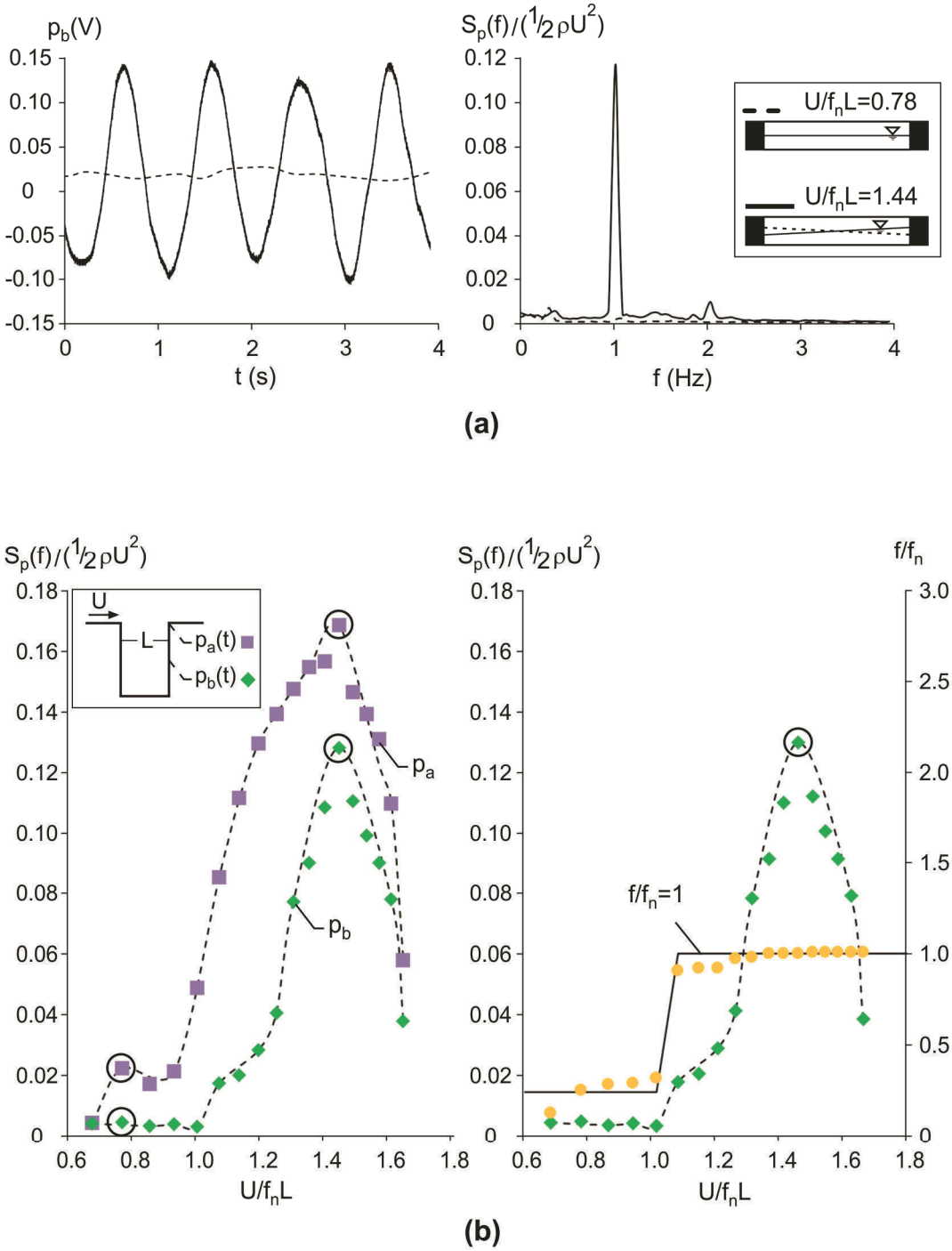

Figure 3.3: (a) Pressure fluctuation at two dimensionless velocities $U/f_nL = 0.78$ (dashed line) and $U/f_nL = 1.44$ (solid line) that represent, respectively, cases without and with a gravity standing wave. **(b)** Corresponding amplitude of spectral peak $S_p(f)/(\frac{1}{2}\rho U^2)$ and frequency f_n of peak response.

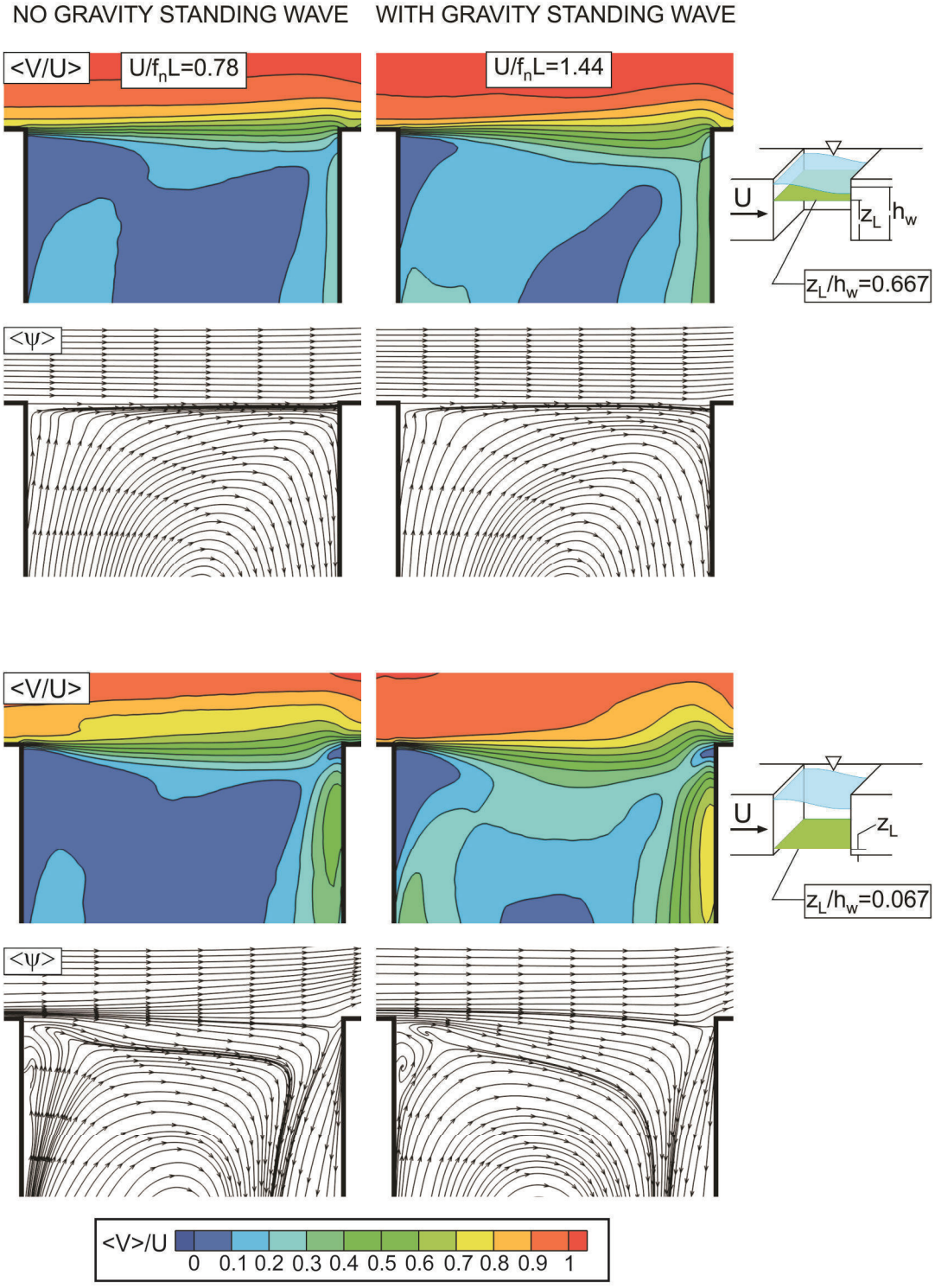

Figure 3.4: Contours of time-averaged velocity magnitude $\langle V \rangle / U$ and patterns of streamlines $\langle \psi \rangle$ at two different elevations: well above the bed ($z_L/h_w = 0.667$); and near the bed ($z_L/h_w = 0.067$). Dimensionless velocities $U/f_nL = 0.78$ (left column) and $U/f_nL = 1.44$ (right column) correspond, respectively, to cases without and with a gravity standing wave.

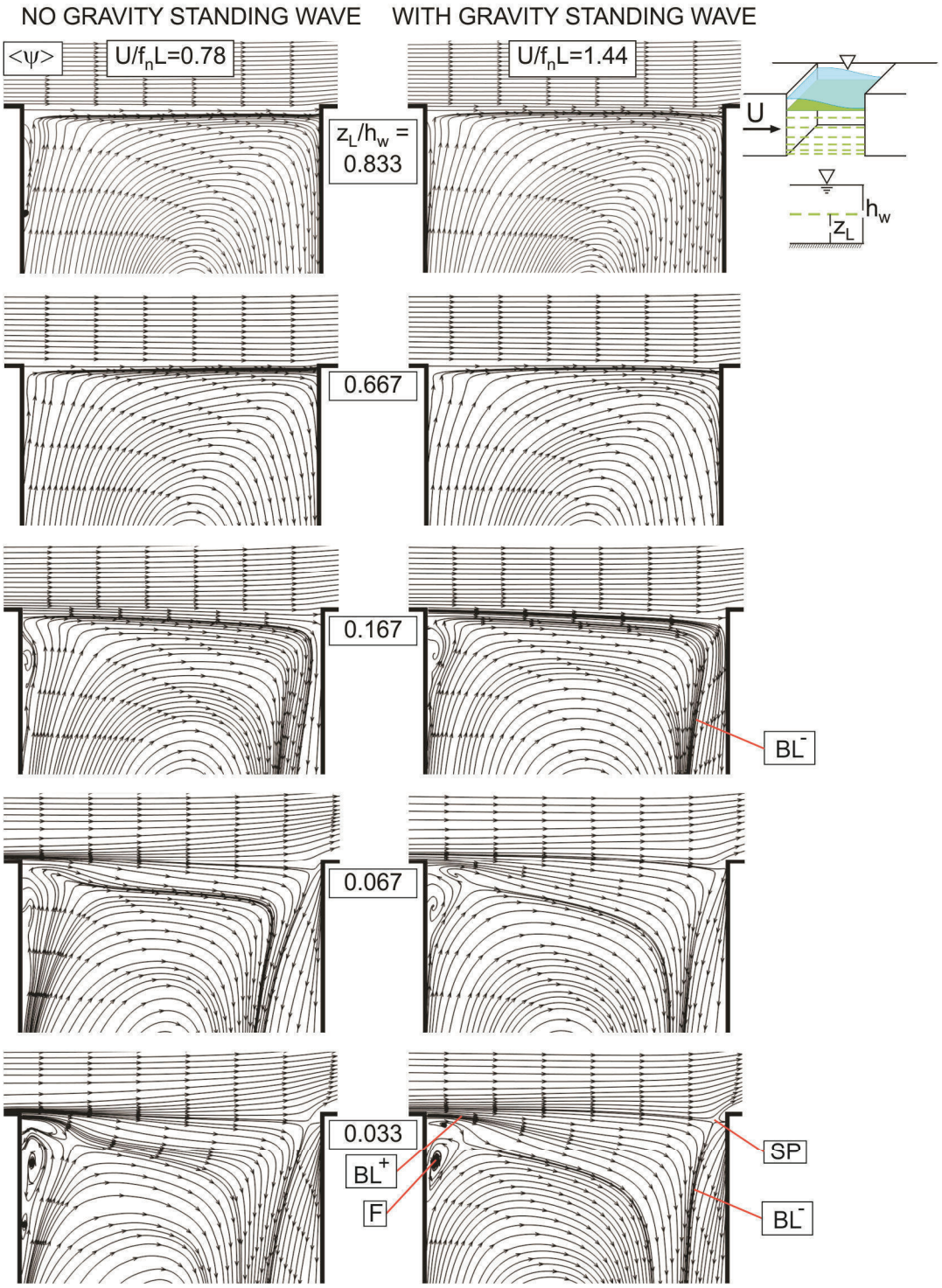

Figure 3.5: Patterns of time-averaged streamlines <ψ> at different elevations above the bed (z_L/h_w = 0.033-0.833). Dimensionless velocities U/f_nL = 0.78 (left column) and U/f_nL = 1.44 (right column) correspond, respectively, to cases without and with a gravity standing wave.

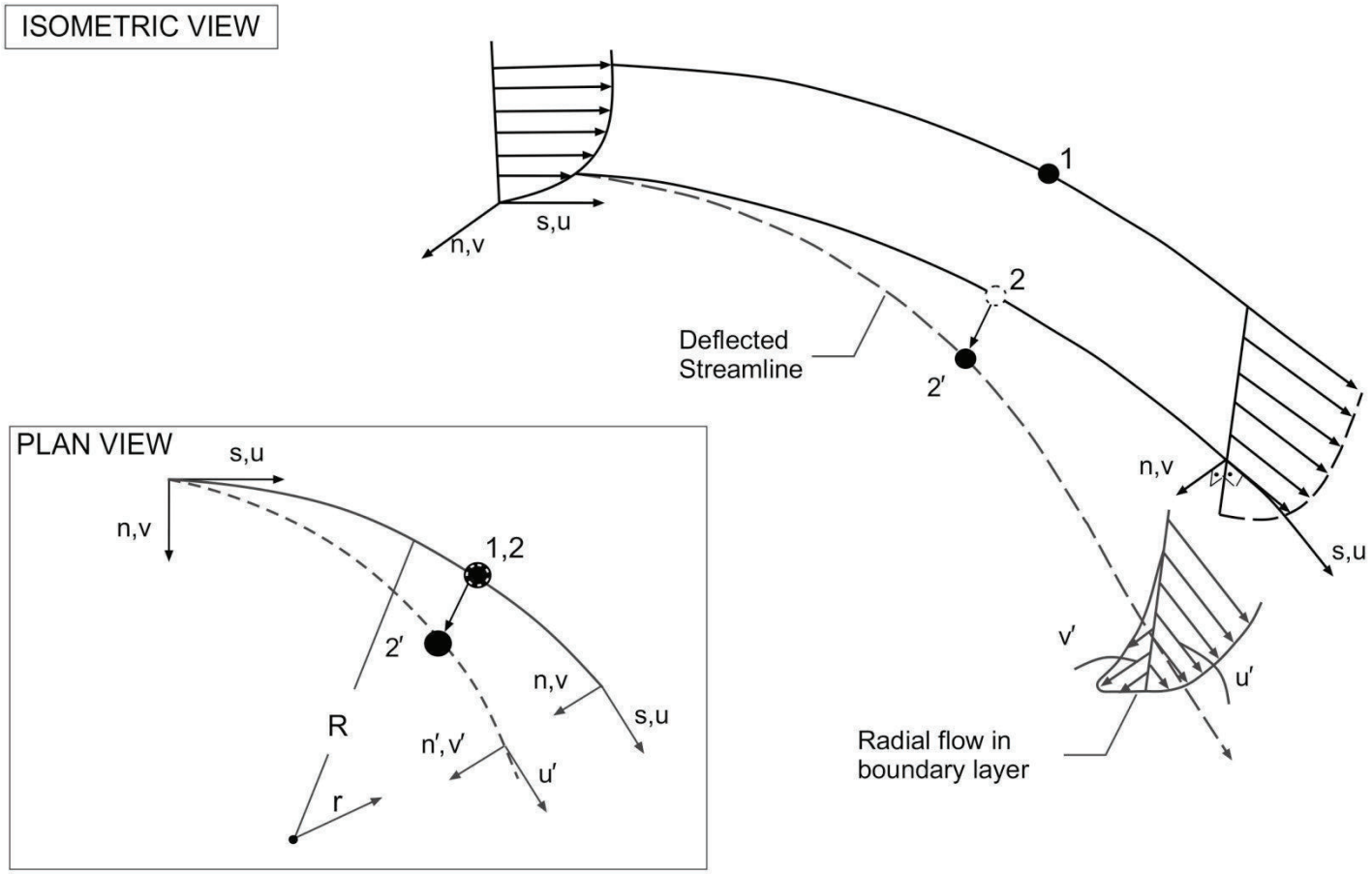

Figure 3.6: Illustration of the concept of radial (secondary) flow due to streamline curvature. Streamline (1) is located at the edge of the boundary layer. Due to the radial pressure gradient, streamline (2) within boundary layer is deflected to position (2′), giving rise to radial flow towards the center of curvature. (after Lakshminarayana, 1996)

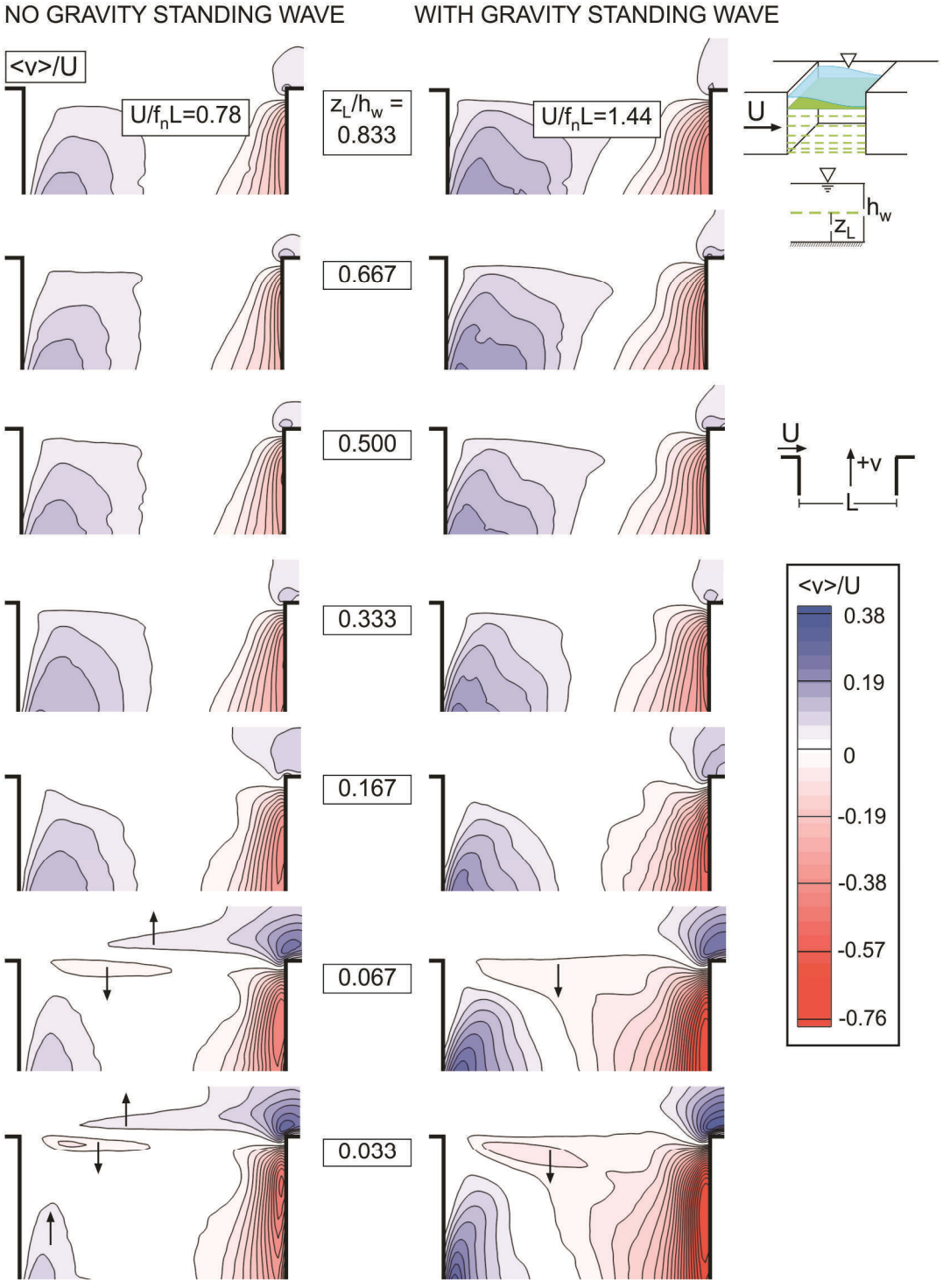

Figure 3.7: Contours of time-averaged transverse velocity $\langle v \rangle / U$ at two different elevations above the bed (z_L/h_w = 0.033-0.833). Dimensionless velocities U/f_nL = 0.78 (left column) and U/f_nL = 1.44 (right column) correspond, respectively, to cases without and with a gravity standing wave. Red contour levels represent flow toward the interior of the cavity and blue contours represent the flow toward to exterior of the cavity.

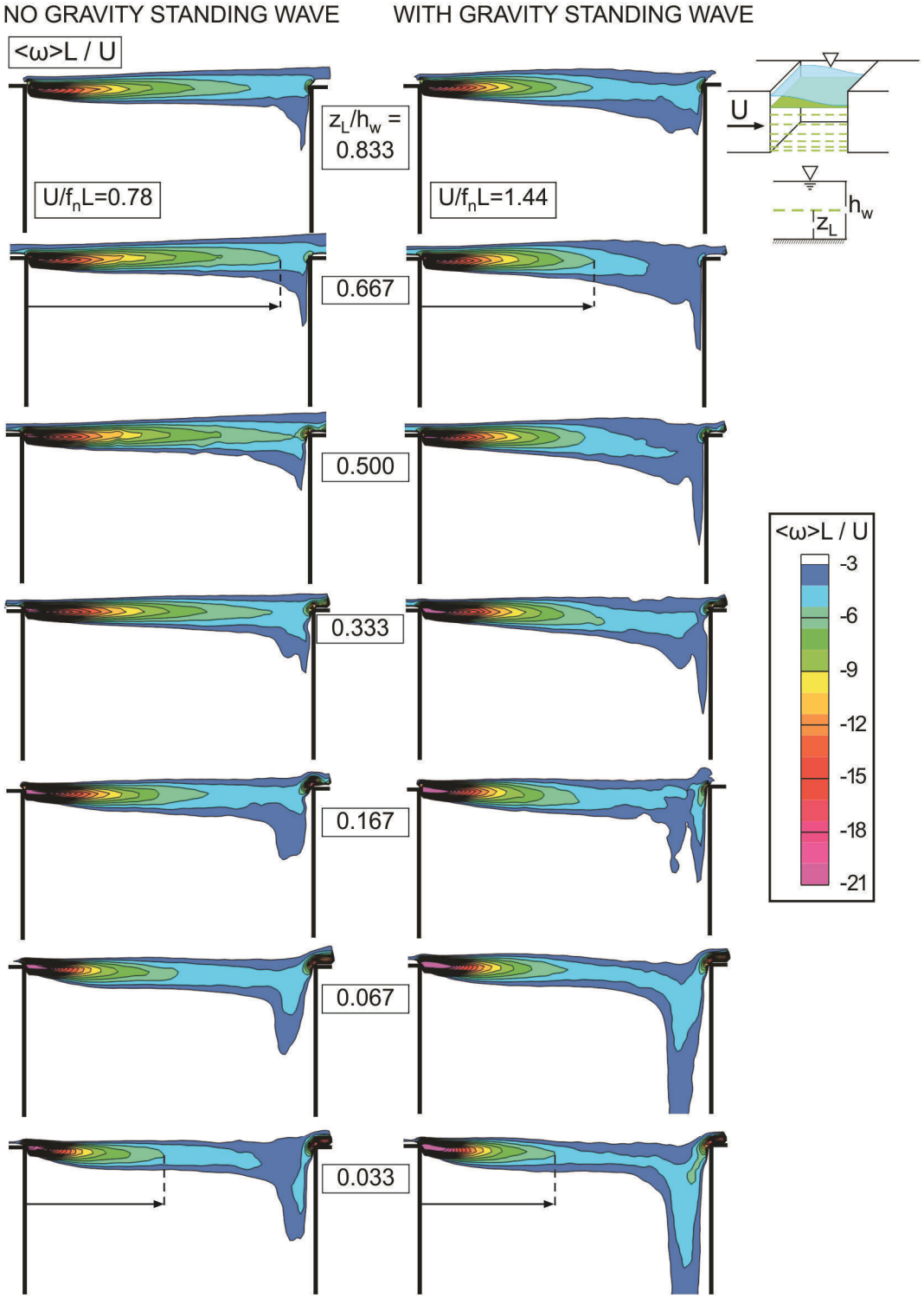

Figure 3.8: Contours of time-averaged transverse velocity $<\omega>L/U$ at two different elevations above the bed (z_L/h_w = 0.033-0.833). Dimensionless velocities U/f_nL = 0.78 (left column) and U/f_nL = 1.44 (right column) correspond, respectively, to cases without and with a gravity standing wave.

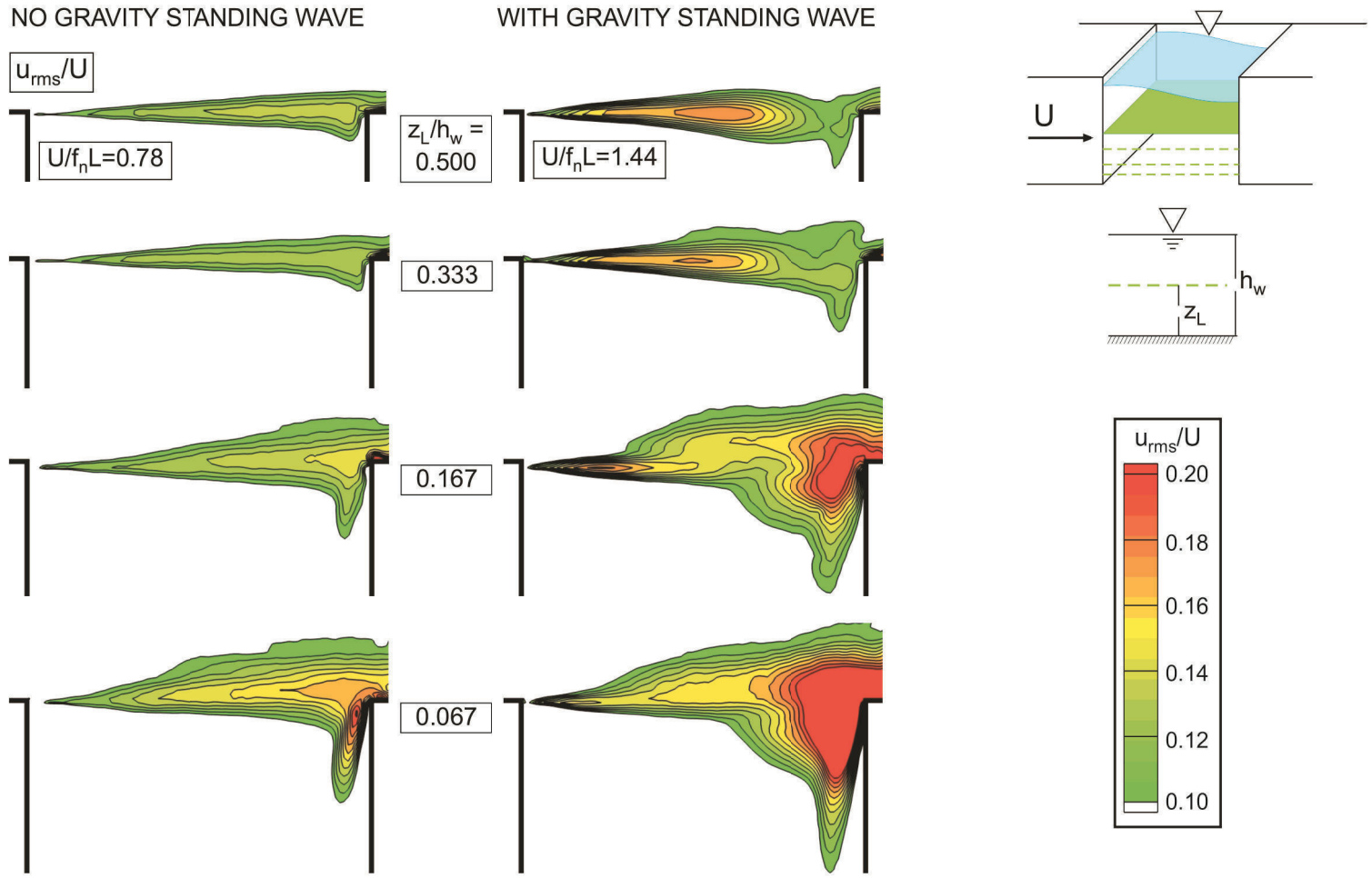

Figure 3.9: Patterns of root-mean-square streamwise velocity fluctuation u_{rms}/U at different elevations z_L/h_w above the bed (bottom surface). Dimensionless velocities $U/f_nL = 0.78$ (left column) and $U/f_nL = 1.44$ (right column) correspond, respectively, to cases without and with a gravity standing wave.

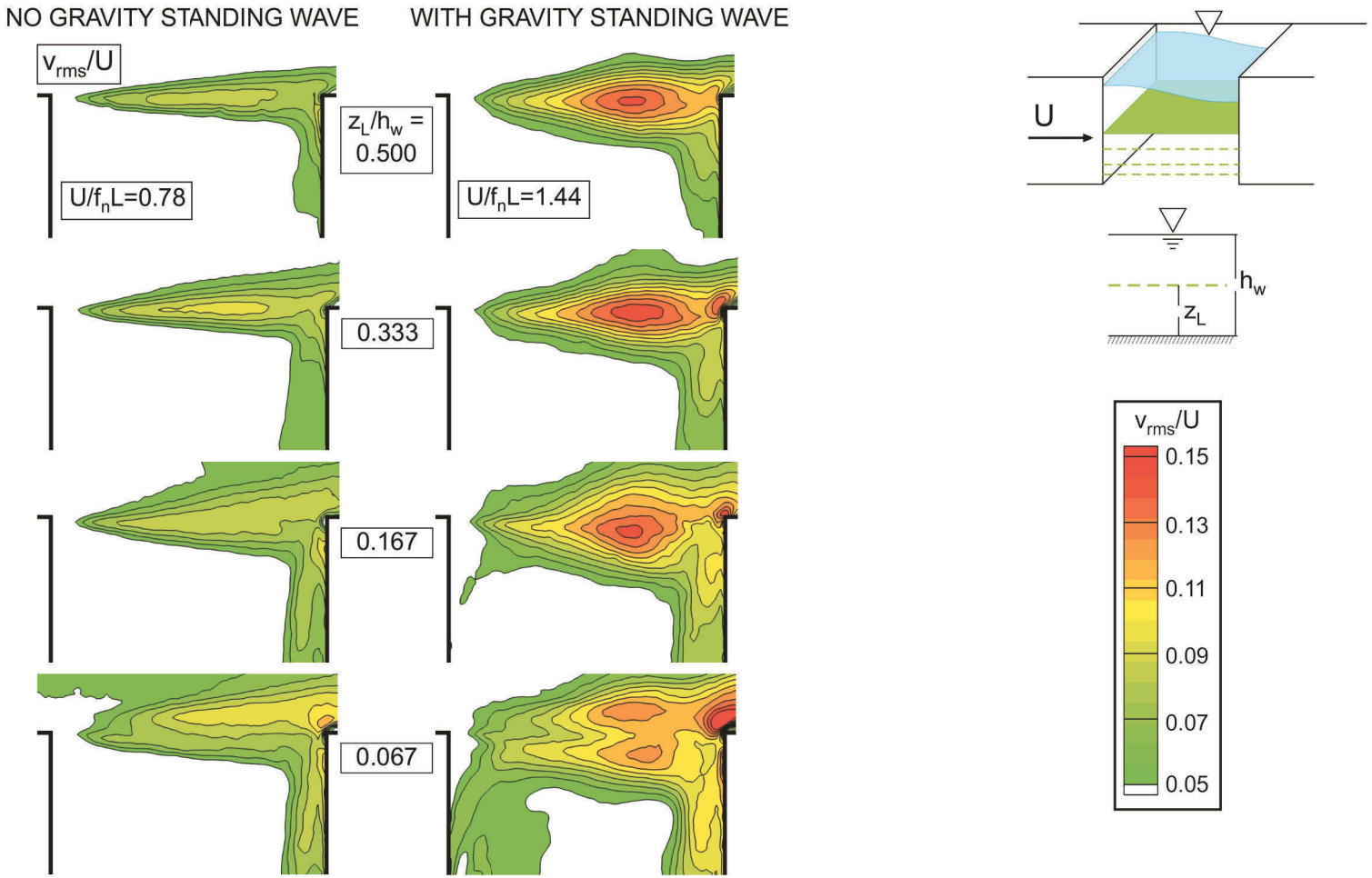

Figure 3.10: Patterns of root-mean-square transverse velocity fluctuation v_{rms}/U at different elevations z_L/h_w above the bed (bottom surface). Dimensionless velocities $U/f_nL = 0.78$ (left column) and $U/f_nL = 1.44$ (right column) correspond, respectively, to cases without and with a gravity standing wave.

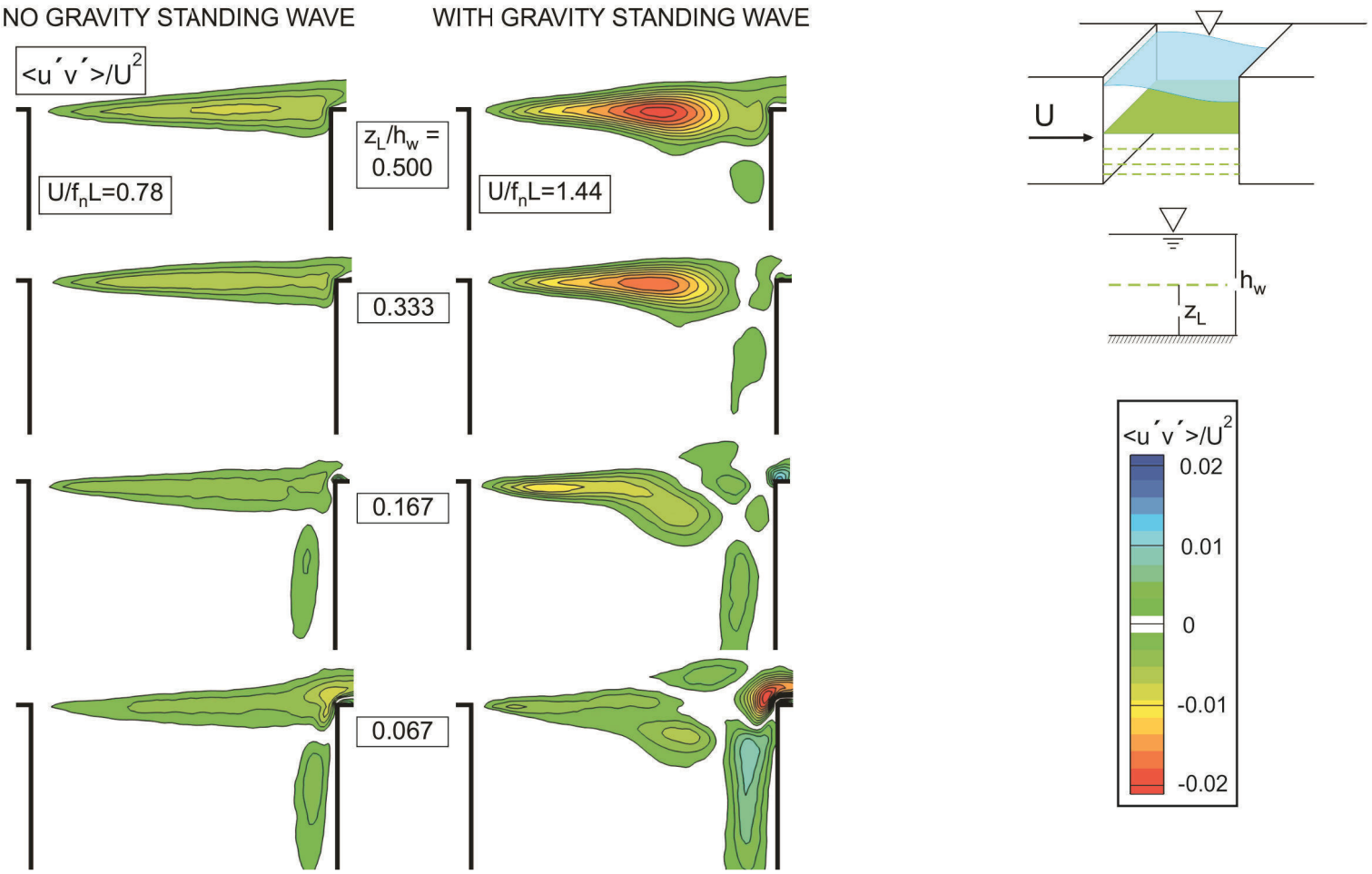

Figure 3.11: Patterns of Reynolds stress $\langle u'v' \rangle / U^2$ at different elevations z_L/h_w above the bed (bottom surface). Dimensionless velocities $U/f_nL = 0.78$ (left column) and $U/f_nL = 1.44$ (right column) correspond, respectively, to cases without and with a gravity standing wave.

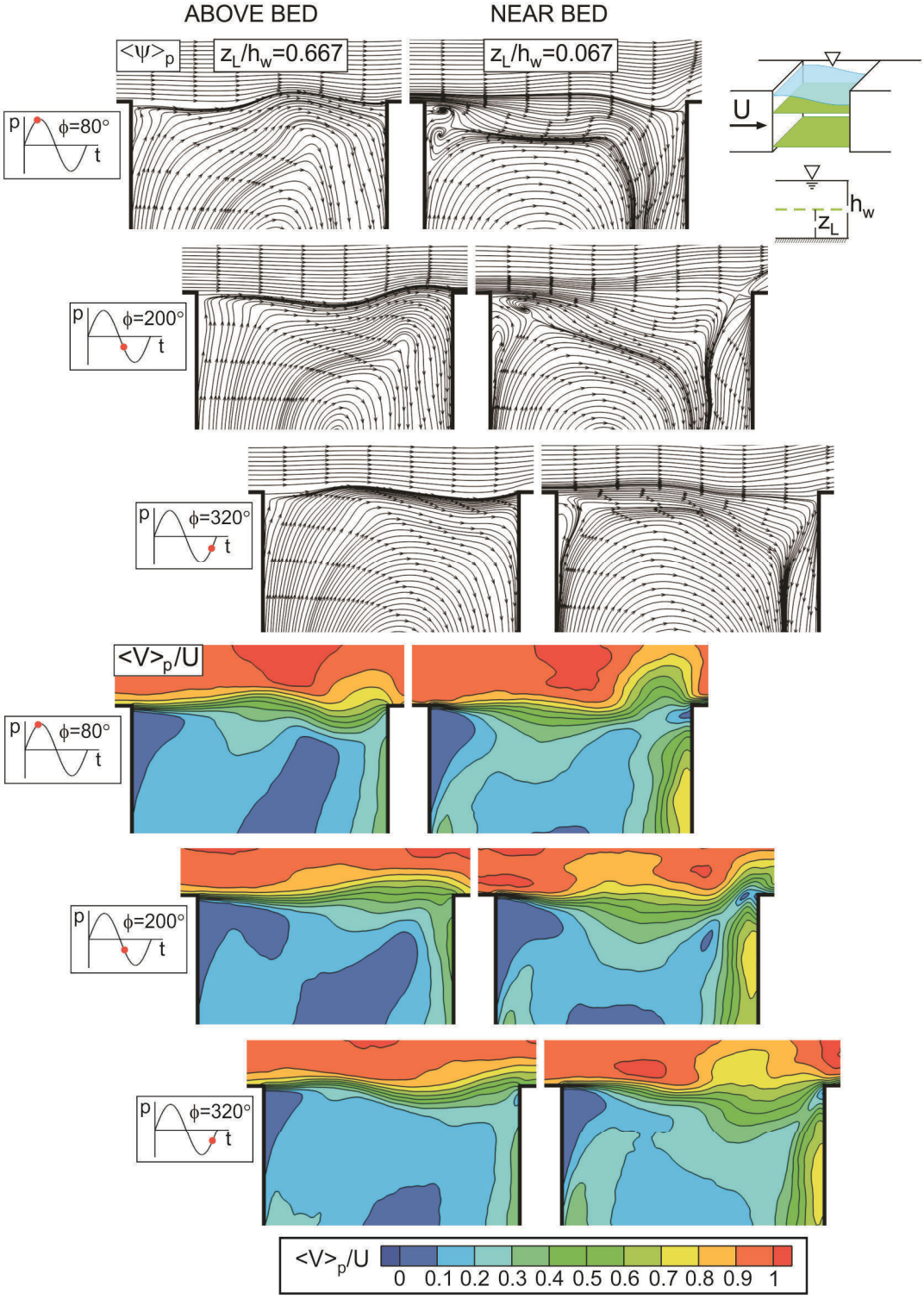

Figure 3.12: Phase-averaged patterns of streamlines $\langle\psi\rangle_p$ and contours of velocity magnitude $\langle V\rangle_p/U$ at two different elevations: well above the bed (z_L/h_w = 0.667); and near the bed (z_L/h_w = 0.067) in presence of a gravity standing wave (U/f_nL = 1.44).

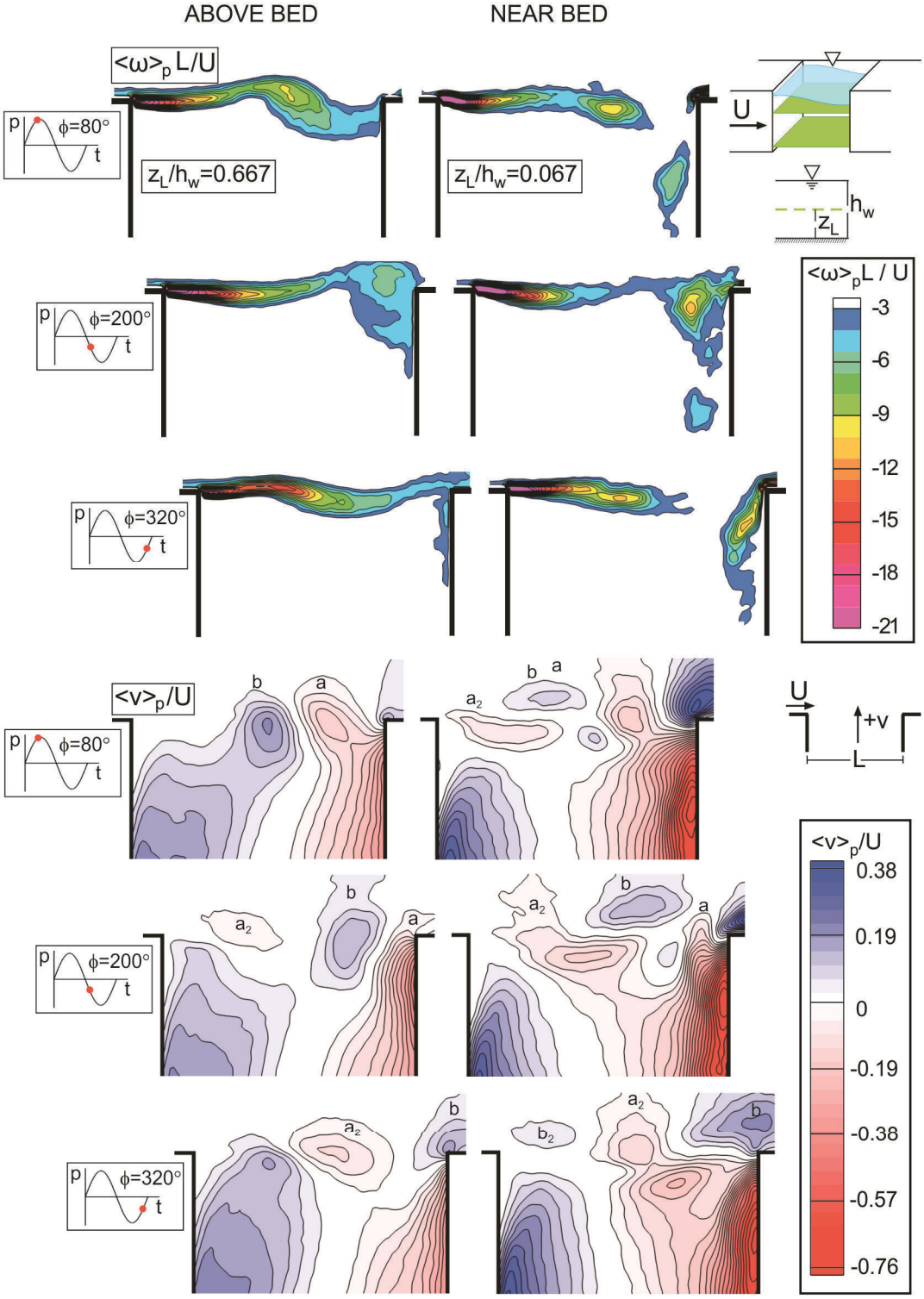

Figure 3.13: Contours of phase-averaged vorticity $\langle\omega\rangle_p L/U$ and transverse velocity $\langle v\rangle_p/U$ at two different elevations: well above the bed ($z_L/h_w = 0.667$); and near the bed ($z_L/h_w = 0.067$) in presence of a gravity standing wave ($U/f_n L = 1.44$) .

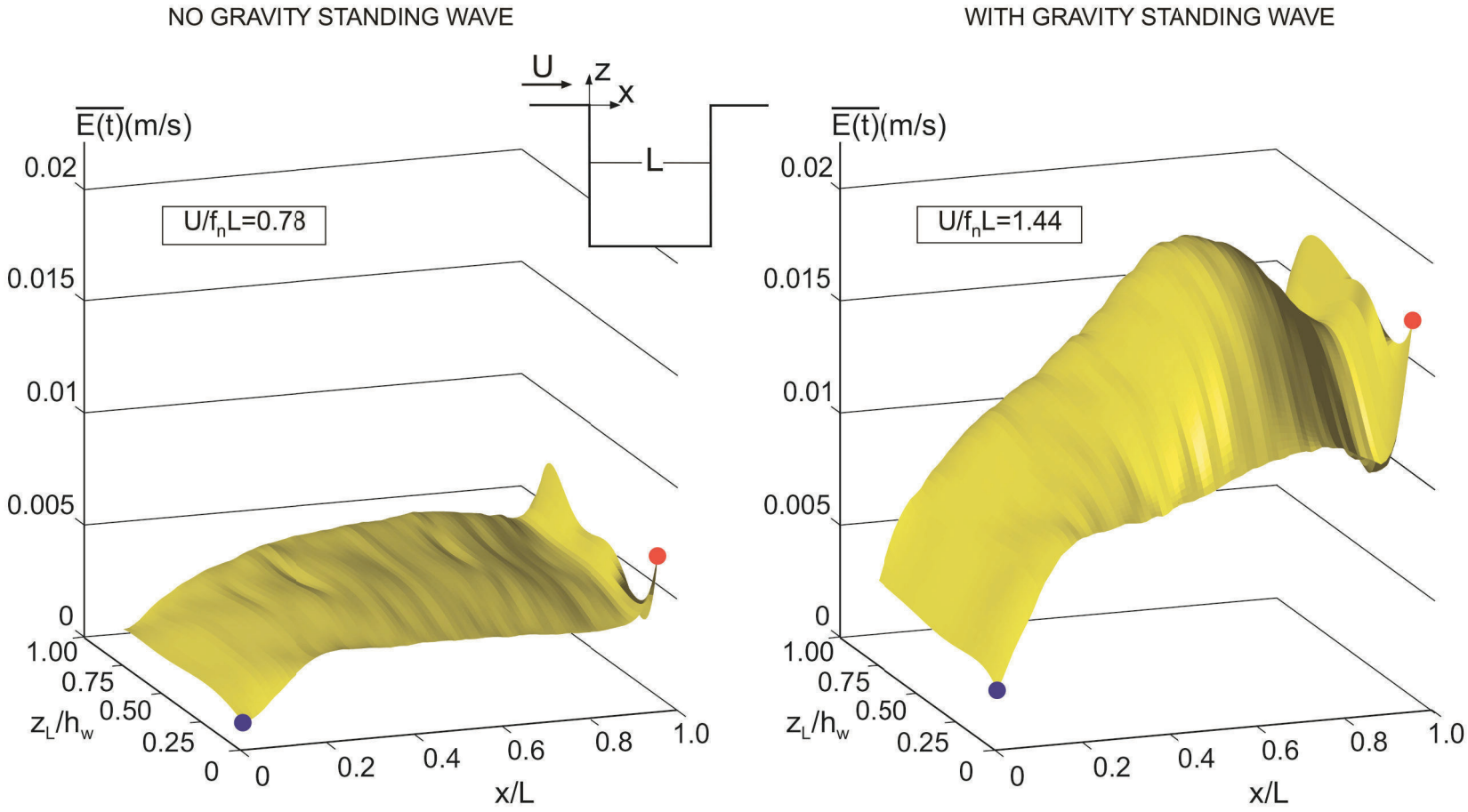

Figure 3.14: Patterns of time-averaged exchange velocity $\overline{E(t)}$ at different elevations z_L/h_w above the bed (bottom surface). Dimensionless velocities $U/f_nL = 0.78$ (left column) and $U/f_nL = 1.44$ (right column) correspond, respectively, to cases without and with a gravity standing wave. Blue point shows the leading edge of the cavity (x/L=0), and red point shows the trailing edge of the cavity (x/L=1).

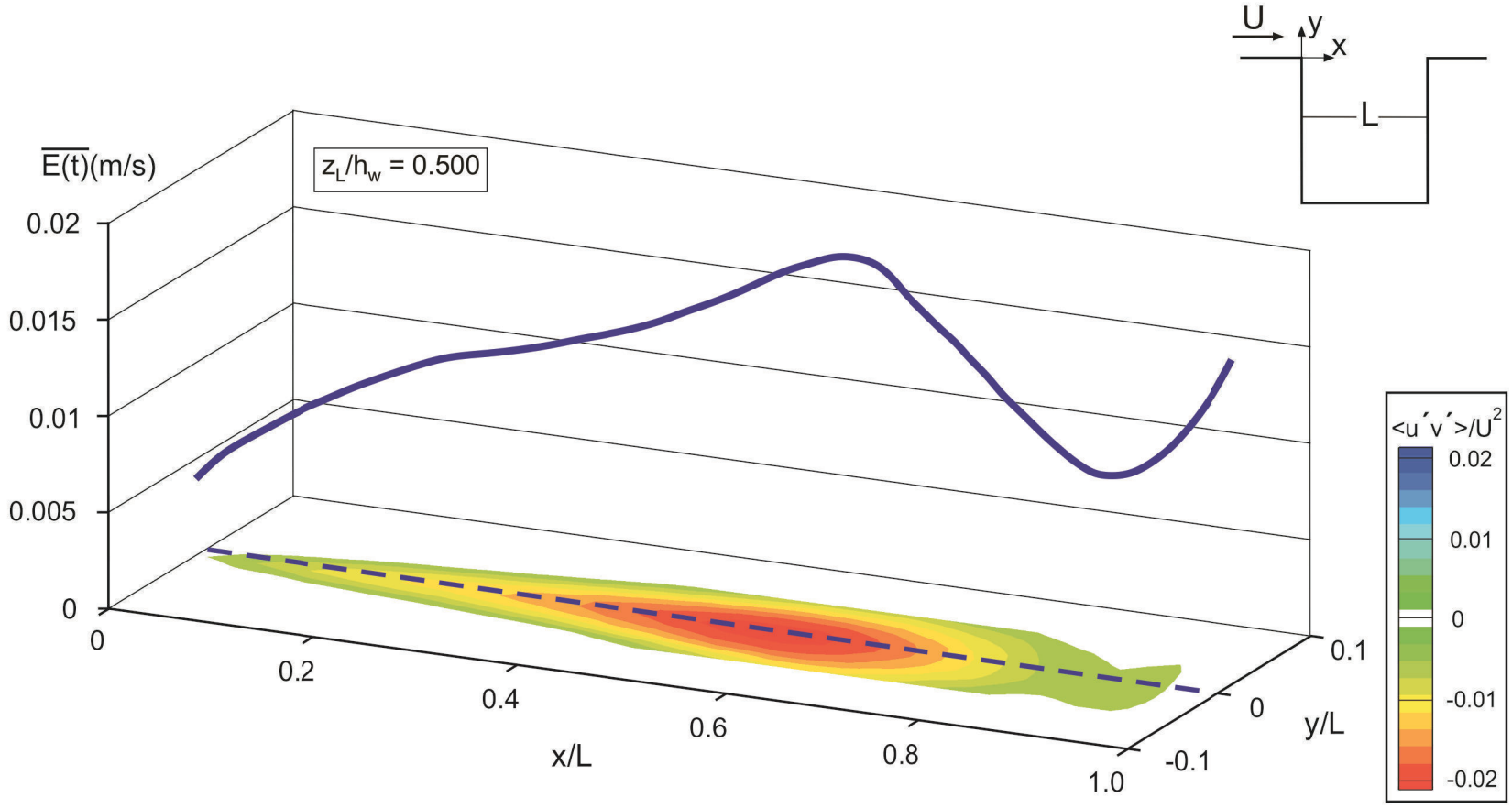

Figure 3.15: Pattern of time-averaged exchange velocity $\overline{E(t)}$ and Reynolds stress $\langle u'v' \rangle / U^2$ at the mouth of the cavity ($y/L = 0$) for the dimensionless velocity $U/f_n L = 1.44$ corresponding to the case with a gravity standing wave.

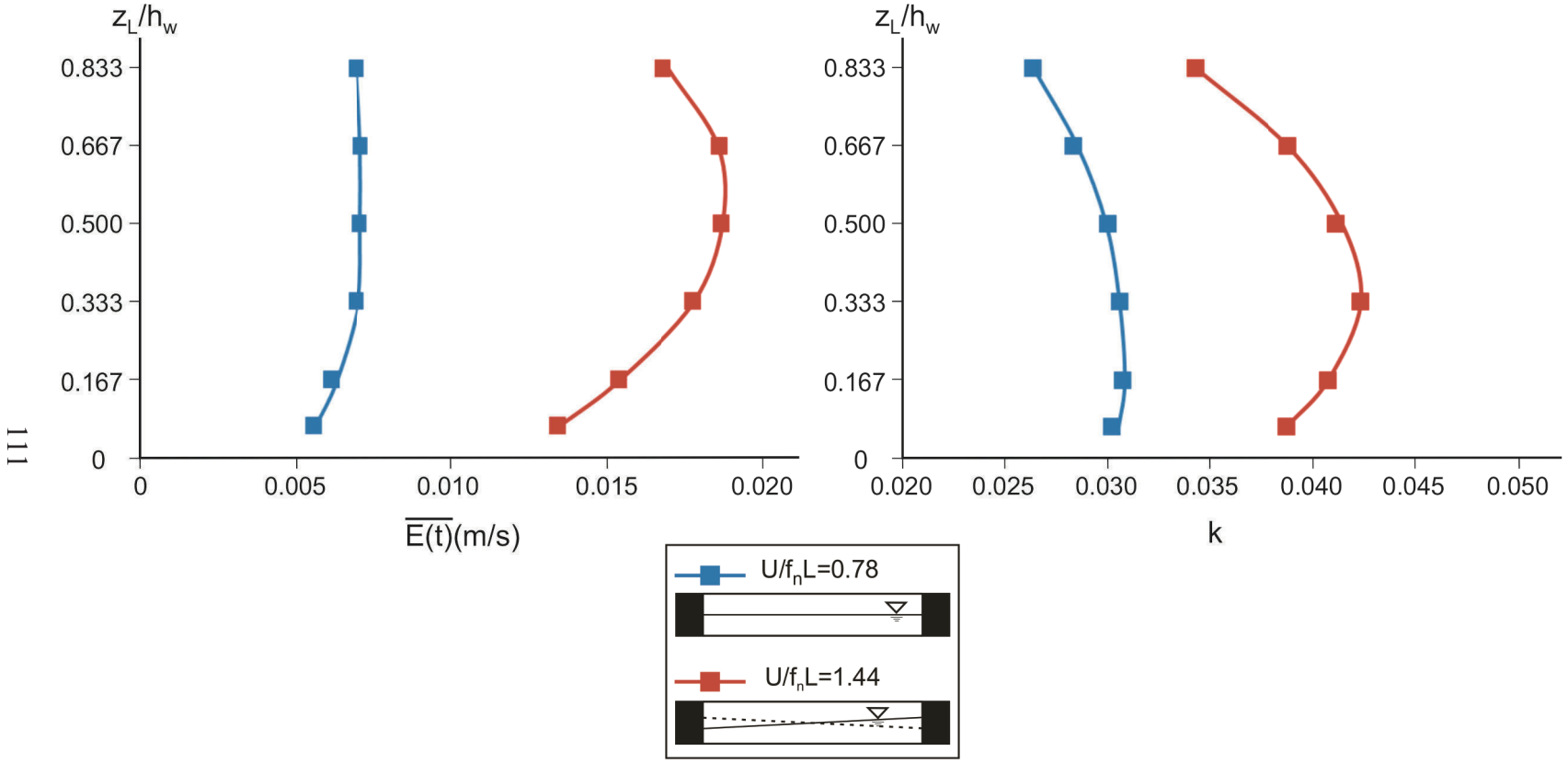

Figure 3.16: Patterns of time-averaged exchange velocity $\overline{E(t)}$ and mass exchange coefficient k at different elevations z_L/h_w above the bed (bottom surface). Dimensionless velocities $U/f_nL = 0.78$ (blue) and $U/f_nL = 1.44$ (red) correspond, respectively, to cases without and with a gravity standing wave coupling.

CHAPTER 4

ATTENUATION OF OSCILLATIONS VIA A BED PERTURBATION

Fully turbulent shallow flow past a cavity can give rise to highly coherent oscillations, which arise from coupling between the inherent instability of the separated shear layer along the cavity opening and a gravity standing wave within the cavity. The objective of the present investigation is to attenuate these oscillations by a single geometric perturbation (cylinder) on the bed (bottom surface), which is located near the leading corner of the cavity. The patterns of the flow structure are characterized as a function of height of the cylinder above the bed by using digital particle image velocimetry. Reduced amplitude of the coupled oscillation can be attained for values of cylinder diameter and height nearly an order of magnitude smaller than the water depth. The reduction of oscillation amplitude is associated with an increased width of the separated shear layer along the opening of the cavity, even at elevations above the bed much larger than the height of the cylinder. Near the bed, a vorticity defect in the separated shear layer and deflection of the layer away from the cavity opening are evident. Attenuation of the oscillation amplitude is associated with: a major decrease in the peak values of the normal and shear Reynolds stresses in the separated shear layer; degradation

of coherent, phase-averaged patterns of vortex formation; and decreased scale of the coherent vortical structures that propagate downstream along the cavity opening. These changes in the stresses and the flow structure are, in turn, directly correlated with lower values of exchange velocity along the opening of the cavity, which is due to the decreased entrainment demand of the separated shear layer. This decrease in magnitude of the exchange velocity in the presence of the cylinder results in a 50% reduction of the value of mass exchange coefficient between the cavity and the mainstream.

4.1 BACKGROUND

Environmental flows such as rivers, lakes and coastal regions are representative examples of shallow flows, which have a free surface and a shear-supporting bottom surface (bed) (Jirka & Uijttewaal, 2004). The dimensions of the flow domain in the horizontal plane greatly exceed the water depth and either the wavelength λ of an instability or the characteristic diameter D of a large-scale vortical structure is much larger than the water depth h_w; that is, $\lambda / h_w >> 1$ and $D/h_w >> 1$. Such flows are typically fully-developed in the region between the bed and the free surface. The turbulence between the free surface and the bottom surface (bed) has a characteristic length scale L_T which is limited by the water depth h_w. Classical examples of shallow separated flows involve shallow wakes, shallow jets, and shallow mixing layers. Mixing layers commonly occur in environmental flows, for example, flow past a series of cavities formed by multiple groyne fields (dead water zones) along a river, a sequence of spur dikes along an

ocean coastline, embayments along tidal flows/rivers, and harbors in coastal regions.

Oscillations due to flow past a cavity occur in a wide variety of practical applications, including environmental flows. Rockwell and Naudascher (1978) divided self-sustaining oscillations of flow along a cavity into three categories: (i) fluid-dynamic involving disturbance amplification in the unstable, separated shear layer in conjunction with a feedback mechanism; (ii) fluid-resonant, associated with coupling between the shear layer instability and a resonant mode of the cavity arising from compressible or gravity wave effects; and (iii) fluid-elastic , due to coupling between the shear layer instability and elastic displacement of a boundary. The present investigation addresses oscillations of the fluid-resonant type in shallow water flows having a free surface. These oscillations arise from coupling between the inherent instability of the unstable shear layer and the gravity standing wave mode of the cavity; large amplitude oscillations of the free surface occur within the cavity.

Attenuation of this class of self-excited oscillation is of primary interest herein. Reduction of the degree of coupling between the gravity standing wave and the inherent instability of the shear layer is pursued through passive modification of the flow structure.

4.1.1 Previous investigations of instability and vortex formation in shallow mixing layers

In recent decades, computations and experiments have provided substantial insight into our understanding of shallow mixing layers. Chu and Babarutsi (1988), Uijttewaal and Booij (2000), and van Prooijen and Uijttewaal (2002) experimentally investigated the instabilities and vortex formation in shallow mixing layers having infinite streamwise extent. Experiments of Chu and Babarutsi (1988) and van Prooijen and Uijttewaal (2002) showed that the lateral spreading of a shallow mixing layer is reduced by the influence of bottom friction. Uijttewaal and Booij (2000) concluded that instabilities in the shallow mixing layer gave rise to the development of large scale turbulent structures, which contribute to the exchange of mass and momentum in the mixing layer. Uijttewaal (2011) conducted experiments to assess different mechanisms that govern the momentum and mass exchange in shallow mixing layers and reported that the properties of these layers were substantially affected by the bottom-induced three-dimensional turbulence. The reader is referred to the computational work of Constantinescu (2013) for comprehensive review on usage of eddy-resolving techniques to investigate the effect of coherent structures, which are forming within the mixing layers, on the mass and momentum exchange processes.

Theoretical analyses and numerical simulations of shallow mixing layers have been undertaken in a range of studies. Chu et al. (1991), Chen and Jirka (1998), and Socolofsky and Jirka (2004) conducted linear stability analyses of

shallow mixing layers. Their interpretation, using the rigid-lid concept, showed that velocity gradients in the horizontal plane promoted the onset of an instability leading to vortex formation, whereas bed friction exerted a damping influence. Ghidaoui and Kolyshkin (1999), Kolyshkin and Ghidaoui (2003), and Nazarovs (2005) assessed the accuracy of the rigid-lid assumption. They concluded that the error in calculating the critical value of shear instabilities substantially increases when the Froude number becomes sufficiently large, that is, $Fr > 1$. It is therefore important to consider gravitational effects as addressed in the study of Kolyshkin and Ghidaoui (2002). Their investigation defined a threshold value of Froude number, above which the flow was unstable with respect to gravitational effects and below which the flow was unstable with respect to shear layer effects, for a defined range of the bed friction number.

Furthermore, numerical and experimental investigations of shallow mixing layers having a finite streamwise length scale, i.e., shallow flow past a cavity configuration, have substantially advanced our understanding of this class of flows. The fully three-dimensional computations of McCoy et al. (2006), Chang et al. (2007), and Constantinescu et al. (2009) characterized the structure of the shear layer along the cavity opening, whereby vertical obstructions (spur dykes or groynes) formed the cavity, and thereby provided a finite length scale. They pointed out the effects of the flow structure at the interface between the cavity and the mainstream on the mass exchange process. Uijttewaal et al. (2001) visualized shallow flow past groyne fields with colored dye, and observed that a decrease in

depth of the shallow flow resulted in an increase in the influence of the bottom friction on the flow patterns; on the other hand, the shallowness of the water layer did not affect the mass exchange parameters between the groyne field and the main stream. More recently, Sanjou and Nezu (2013) conducted an experimental study to examine the changes in the flow structures inside the groyne field by varying the bed slope. They noted that mass exchange velocity between the main stream and the groyne field increased in coincidence with large magnitudes of Reynolds stress in the separated shear layer. Moreover, Brevis et al. (2014) investigated the flow structure in a shallow open-channel flow with a dead zone having two different aspect ratios. Their experimental and computational results show that the flow outside the dead zone was insensitive to the aspect ratio; however, the flow structure within the dead zone showed important differences. The experimental works of Wallast et al. (1999), Weitbrecht and Jirka (2001), Kurzke et al. (2002), and Uijttewaal (2005) qualitatively analyzed the effects of groyne layout on the flow structure and the mass exchange process between the groyne field and the main stream. Uijttewaal (2005) observed a free surface oscillation within the groyne field and this oscillation was related to the strongly varying flow at the groyne tip. In another study by Meile et al. (2011), free surface oscillation within groyne fields, i.e., cavity-like configurations, experimentally studied, and they determined the frequency and amplitude of periodic oscillations of the free surface in the transverse direction within rectangular cavities along both sides of a channel.

Shallow flow systems involving channels, harbors, and embayments, which have a mixing layer of finite streamwise length along their openings, can potentially give rise to one or more modes of gravity standing waves, as indicated by the field measurements of Kimura and Hosoda (1997), Ikeda et al. (1999), and Nezu and Onitsuka (2002). For a cavity configuration with a shallow flow, Wolfinger et al. (2012) visualized the flow structure by considering the onset of a longitudinal gravity standing wave within the cavity. Enhancement of turbulent Reynolds stresses in the separated shear layer was determined at different inflow velocities that corresponded to different stages of coupling between the separated shear layer and the gravity standing wave mode of the cavity. Tuna et al. (2013) related changes of the turbulent statistics to the mass exchange coefficients. In doing so, they considered patterns of the flow structure as a function of elevation above the bottom surface (bed). It was found that onset of a gravity standing wave within the cavity yielded a large increase in the time-averaged entrainment of the mixing layer and the mass exchange coefficient between the cavity and the main stream.

4.1.2 Control of flow-induced oscillations along and within a cavity

Control of flow-induced oscillations has received a great deal of attention. Techniques to control cavity oscillations were classified as active and passive control by Cattafesta et al. (2008). Passive control of cavity oscillations has been successfully implemented via geometric modifications for flows of large spanwise width. Examples include geometric devices that are placed in the boundary layer

near the upstream wall of the cavity, and extend along the entire span, include a fence, a spoiler, or a cylinder. Ukeiley et al. (2004) examined the effect of a leading-edge fence on the cavity oscillations at Mach numbers between M = 0.6 and 1.4, and reported a reduction in the fluctuating pressure loads inside the cavity. Mongeau et al. (1999) and Zhang et al. (1999) conducted experiments with a leading-edge spoiler and a leading-edge ramp respectively. These geometric modifications produced a reduction in the sound pressure level at values of Mach number M = 1.5 and 2.5. Furthermore, Arunajatesan et al. (2002) computationally analyzed the configuration of a cylinder as a passive control device; it was located at the leading wall of a cavity. They demonstrated that, at subsonic conditions, control is partially achieved by deflection of the shear layer away from the cavity opening. Panickar and Raman (2008) and Sarpotdar et al. (2009) investigated the effect of a rod (cylinder) that extended across the span of the leading edge of the cavity and resulted in modification of the stability characteristics of the shear layer at M = 0.6. They concluded that different gap values had different physical mechanisms for suppression of the oscillations. Martinez and Onorato (2009) attained suppression of the self-sustained oscillations for low-speed experiments in water with a cylindrical rod positioned just upstream of the cavity; von Karman vortex shedding occurred from the rod. They concluded that the suppression is attained by alteration of the instability characteristics of the shear layer. Dudley and Ukeiley (2011) conducted numerical simulations to investigate the suppression of oscillations for a supersonic cavity flow in presence of a rod near the leading edge

of the cavity, and they observed deflection of the shear layer near the leading edge of the cavity and decreased organization of the flow structure along the cavity opening. The suppression mechanisms for this type of attenuation are summarized in the study of Martinez et al. (2012) as: upward deflection of the shear layer, alteration of stability characteristics of the shear layer, and reorganization of the vorticity in the shear layer.

4.1.3 Unresolved issues

From previous investigations, it is known that shallow flow past a cavity is highly prone to coupled oscillations of the separated shear layer along the cavity opening and a gravity standing wave within the cavity. These coupled oscillations can lead to large-scale, highly coherent vortex patterns in the shear layer, which, in turn, can radically alter the mass exchange process across the unsteady shear layer. Passive control techniques for this class of shallow flows have received very little attention; the manner in which such techniques alter the physics of vortex formation and mass exchange has remained unexplored. The foregoing investigations, which employ a cylinder extending across the entire span of the leading (upstream) corner of the cavity, have provided insightful contributions. They do not, however, include the configuration where the cylinder extends over only a fraction of the span of the cavity.

For the class of flows of interest herein, namely a shallow flow involving a free surface and a solid bottom surface (bed), the aim is to minimize the scale of the

control cylinder by minimizing its height above the bed, i.e., its spanwise extent. The effectiveness of this control concept will be assessed in terms of the degree of attenuation of the coupled oscillation involving the inherently unstable shear layer along the cavity and the gravity standing wave mode within the cavity. It is anticipated that this reduction of the oscillation amplitude will be associated with attenuated turbulent Reynolds stresses in the separated shear layer along the cavity opening, thereby reducing the entrainment of the fluid from the cavity into the separated shear layer and, in turn, altering the flow patterns within the cavity. All of these features have not been characterized for the case where the height of the cylinder is much smaller than the depth of the shallow flow.

It is also assumed that the flow structure will exhibit depthwise variations with depth due to the following effects. First of all, the boundary conditions at the bottom surface (bed) and at the free surface above the bed are fundamentally different. Second, the height of the cylinder that extends vertically above the bed is much smaller than the water depth. The present investigation employs a technique of quantitative imaging to determine the depthwise variations of the flow structure. This technique leads to global representations of patterns of velocity components, vorticity, turbulence statistics, and streamline patterns in relation to the possible attenuation of oscillations due to coupling between the separated shear layer and a gravity standing wave mode within the cavity.

4.2 EXPERIMENTAL SYSTEM AND TECHNIQUES

A free surface water channel was employed for the present experiments. It had an overall test section length of 4,877 mm, a width of 927 mm, and an adjustable depth of 610 mm. The upstream flow conditioning was accomplished by use of a honeycomb-screen arrangement involving a sequence of five screens, in order to maintain the turbulence intensity in the main stream at a relatively low value of 0.1%.

Detailed schematics of the experimental system are given in Figures 4.1 and 4.2. In Figure 4.1, two perspectives of the experimental facility are indicated. The streamwise length L_i of the shallow water layer, i.e., the distance between the leading (upstream) corner of the cavity to the leading edge of the acrylic plate, is L_i = 1,907.5 mm. Thus, the ratio of the inflow length L_i to water depth h_w is L_i/h_w = 50.1, which corresponds to the criterion of L_i/h_w = 50 of Uijttewaal et al. (2001) for attainment of fully developed turbulent flow in the shallow layer. In order to obtain a fully-coupled state of the oscillation, the cavity width W, the cavity length L and the water depth h_w were varied during diagnostic experiments. To determine the conditions for optimal attenuation, the cylinder diameter d, the gap ε between the cylinder and the upstream wall, and the height of the cylinder h_c were also varied.

During the initial unsteady pressure measurements, the depth-averaged inflow velocity U was varied between U = 243 and 470 mm/s. The flow structure

was determined via particle image velocimetry at a value of depth-averaged inflow velocity U_r = 433 mm/s, which corresponded to a fully-coupled (maximum amplitude) state of the gravity standing wave within the cavity. The aim of this study is to assess the effects of a cylinder, which is located adjacent to the leading edge of the cavity, on the structure of the unsteady shear layer along the opening of the cavity. This flow structure will be related to the degree of coupling between the inherent instability of the separated shear layer and a gravity standing wave of the cavity. To achieve these objectives, a test-section insert was designed; it allowed the control of the water depth, the cavity dimensions, and the flow velocity.

The focus of the present investigation is on hydrodynamic instabilities of the shallow flow; it is therefore essential to ensure that the parameter range of the experiments excludes gravitational instabilities. Ghidaoui and Kolyshkin (1999) identified the onset of both hydrodynamic and gravitational instabilities by using the Froude number $U/(gh_w)^{1/2}$ for a shallow water layer having a (shear-free) free surface. The corresponding value of Froude number based on the depth-averaged inflow velocity U_r = 433 mm/s and the water depth h_w = 38.1 mm was $Fr = U_r/(gh_w)^{1/2}$ = 0.71 in the present configuration. As was pointed out in in Section 1.3, this value of the Froude number (Fr = 0.71) is in the subcritical range ($Fr_{cr} < 1$). Therefore, the present experiments do not involve gravitational instabilities. The value of Reynolds number, based on the width W of the inflow channel and the water depth h_w were correspondingly $Re_W = 2\text{x}10^5$ and $Re_{hw} = 1.6\text{x}10^4$.

For all experiments herein, as defined in Figure 4.1, the cavity had a length of L = 305 mm, a width of W = 457 mm. The water level was adjusted to a value of h_w = 38.1 mm. The diameter of the cylinder located at the leading edge of the cavity was d = 6.35 mm, and the gap between the cylinder and upstream corner of the cavity was ε = 6.35 mm. Two different cylinders were placed at the leading edge of the cavity; they had heights of h_c = 3.175 mm and 6.35 mm. The case where the cylinder was not present is designated as h_c = 0 mm. The corresponding dimensionless heights of the cylinder are: h_c/h_w = 0, h_c/h_w = 0.083 and h_c/h_w = 0.167. The maximum amplitude of the spectral peak of the pressure fluctuation, i.e. the fully-coupled state, occurred at h_c/h_w = 0; this state corresponds to the maximum amplitude of the gravity standing wave, which was h_d/h_w = 0.08, where h_d is the amplitude of the gravity standing wave. In this case, the wavelength λ of the gravity standing wave was twice the cavity length L, which is represented in the schematic of Figure 4.2 (section A-A).

The stability of shallow mixing layers is represented by the dimensionless stability parameter S. Chu and Babarutsi (1988) experimentally investigated the evolution of a shallow mixing layer in an open channel flow. As mentioned previously in Section 4.1, the stability parameter S was computed using the definition $S = \overline{c_f}\,\delta\,\overline{U}/2h_w\Delta U$, where $\overline{c_f}$ is the bed friction coefficient, δ is the width of the transverse shear flow, $\overline{U}$ denotes the average velocity across the shear layer, ΔU is the corresponding velocity difference across the shear layer, and h_w is the water depth. The values of the stability parameter S determined herein are:

S = 0.003 for the fully coupled state of the oscillation in absence of the cylinder, i.e., h_c/h_w = 0; and S = 0.008 and 0.012 for the partially attenuated states of the oscillation in presence of the cylinder having heights h_c/h_w = 0.083 and 0.167. These values of S are of the same order as those determined by Chu and Babarutsi (1988). Kolyshkin and Ghidaoui (2002) addressed both shear and gravitational instabilities in shallow water flows in compound channels. It is insightful to consider critical values for the onset of an instability that are given therein. The bed friction does not stabilize the flow below values of the stability parameter S_{cr} of the order S_{cr} = 0.01 to 0.1 (Kolyshkin & Ghidaoui, 2002). That is, below these critical values of S_{cr}, instabilities occur due to the destabilizing effect of the velocity difference ΔU across the shear layer. In the present experiments, the values of the stability parameter are S = 0 .003 (h_c/h_w = 0) and S = 0.008 (h_c/h_w = 0.083) which are below the critical values of the stability parameter S. However, the value of the stability parameter S = 0.012 at h_c/h_w = 0.167 is in the critical range (S_{cr} = 0.01 to 0.1). Therefore, it is possible to hypothesize that the onset and development of the instability of the shallow mixing layer will be affected, and thereby the degree of coupling with the gravity mode of the cavity; in turn, the amplitude of the free surface oscillations may be attenuated or eliminated.

A PCB piezoelectric pressure transducer (model number 106B50) was employed for unsteady pressure measurements. The unsteady pressure at the trailing edge of the cavity served as a phase reference, and it led to determination of the frequency and amplitude of gravity standing wave oscillations within the

cavity. The plan view of Figure 4.2 shows the location of the pressure transducer, designated as *p;* it was located within the cavity at a horizontal distance of 229 mm from the trailing (impingement) corner, and at an elevation of h_p = 13 mm from the bed (bottom surface). For the acquisition of pressure data, the sampling rate was set to 20 samples per second, corresponding to a Nyquist frequency of 10 Hz, which was well above the maximum frequency of interest in the present study. Sampling was conducted over a time span of 102.4 s, corresponding to a total of 2,048 samples. Ten of these time records were acquired for each inflow velocity. A low-pass digital filter with a 5 Hz cutoff frequency was employed during signal processing.

Quantitative, instantaneous flow patterns of both the fully-coupled and reduced amplitude oscillations were characterized with high-image-density digital particle image velocimetry (DPIV). During the PIV experiments, the laser sheet was oriented in a horizontal plane, as shown in Figures 4.1 and 4.2. In order to investigate the flow structure as a function of depth, the elevation of the laser sheet z_L above the bed (bottom surface) relative to the water depth h_w was adjusted to the following values: z_L/h_w = 0.067, 0.167, 0.333, and 0.667. The dimensionless inflow velocity was maintained at U/U_r = 1. Normalization of the velocity components, vorticity, and turbulence statistics employed the depth-averaged inflow velocity at the fully coupled state U_r = 433m/s. The camera was placed below the water channel, and its direction of view was orthogonal to the horizontal plane, as shown in the side view of Figure 4.1. The aforementioned double-pulsed laser and the

camera were triggered by a synchronizer. The camera operated at a maximum of 30 frames per second, which gave 15 sets of image pairs per second. This technique resulted in 7,227 vectors with an effective grid size of 3.7 mm. An estimation of uncertainty of the velocity measurement was calculated by using the scheme given by Adrian and Westerweel (2010). The uncertainties of the measurements of streamwise and transverse velocity were 1.9% of the depth averaged free stream velocity.

For each set of PIV experiments, 200 sets of images were recorded simultaneously with the pressure signal. At each elevation z_L/h_w, 15 sets of experiments were conducted, and 3,000 sets of images were recorded. The time-averaged flow structure was evaluated by averaging 3,000 instantaneous velocity fields. As mentioned in Section 2.5, a phase-referencing technique was used to acquire the phase-averaged flow structure at each value of z_L/h_w. The phase-referencing technique employs the unsteady pressure in the cavity and the Q-Switch (synch-out) signal of the laser. The width of the phase window size for determination of the phase of each image was 10 degrees, where the complete cycle corresponded to 360 degrees. This method led to a minimum of 60 velocity fields per phase and these velocity fields were selected from the pool of 3,000 randomly-acquired velocity fields.

4.3 IDENTIFICATION OF COUPLING AND DEGREE OF ATTENUATION

Shallow, fully-developed turbulent flow past a cavity can give rise to excitation of an eigenmode of a gravity standing wave within the cavity, due to coupling with an inherent instability of the separated shear layer along the cavity opening. That is, when the most unstable frequency f_s of the separated shear layer matches the frequency f_n of the gravity standing wave mode within the cavity, a coupled, self-sustained oscillation occurs. Lock-on of the overall oscillation frequency f_s to the eigenfrequency f_n of the gravity standing wave mode of the adjacent cavity over a range of flow velocity U can be attained due to this coupling. The maximum oscillation amplitude due to the fully-coupled, locked-on state corresponds herein to a value of depth averaged free stream velocity U_r = 433 mm/s. For further details of this coupling phenomenon, the reader is referred to the experimental study of Tuna et al. (2013).

The unsteady pressure fluctuation within the cavity was measured at the locations specified in the foregoing for different inflow velocities U/U_r, in order to determine: (i) the degree of coupling between the separated shear layer along the mouth of the cavity and the gravity standing wave within the cavity in absence of cylinder (h_c/h_w = 0); and (ii) the degree of attenuation of the oscillation in presence of the cylinder (h_c/h_w = 0.083 and 0.167) at the leading corner of the cavity.

In Figure 4.3, the magnitude of the spectral peak of the pressure fluctuation within the cavity at each inflow velocity, designated as $S_p(f)_{max}/(1/2\rho U^2)$, is plotted

against the dimensionless inflow velocity U/U_r for cases with and without the cylinder located at the leading corner of the cavity. The fully-coupled case $h_c/h_w = 0$ is indicated with the square symbol, while reduced oscillation cases $h_c/h_w = 0.083$ and 0.167 are illustrated respectively with diamond and triangular symbols. The maximum amplitude oscillation is reached at the value of dimensionless velocity $U/U_r = 1$ for all cases, and the representative spectra $S_p(f)_{max}/(1/2\rho U^2)$ of each case at $U/U_r = 1$ are given in the small plots in Figure 4.3. There is a sharp peak in the spectrum of each case at the oscillation frequency of $f_n = 1.02$ Hz; however, the magnitude of the spectral peak is larger at $h_c/h_w = 0$ compared to the cases with the control cylinder. Similarly, it is clear that the magnitudes of the spectral peaks over the entire range of U/U_r are consistently higher in absence of the cylinder $h_c/h_w = 0$ (square symbols), thereby suggesting enhanced coupling of the instability of the shear layer with the gravity standing wave mode of the cavity. Over this range, a substantial decrease of amplitude of the spectral peak occurs in presence of the cylinder ($h_c/h_w = 0.083$ and 0.167). This observation indicates that deployment of the cylinder at the leading edge of the cavity leads to substantial reductions of the degree of coupling of the oscillation. The extent of attenuation, however, is dependent on the height of the cylinder at the leading corner of the cavity. The magnitudes of the spectral peak $S_p(f)_{max}/(1/2\rho U^2)$ for $h_c/h_w = 0.083$ and 0.167 are respectively 53% and 30% of the maximum spectral peak of $S_p(f)_{max}/(1/2\rho U^2)$ for $h_c/h_w = 0$.

4.4 QUANTITATIVE IMAGING OF FLOW STRUCTURE

Quantitative imaging of the flow structure was employed to provide a physical basis for interpretation of the effect of the control cylinder on the coupled oscillation. Time-averaged patterns of mean and fluctuating velocity components, vorticity, and streamline topology were evaluated from randomly acquired velocity fields. The time-averaged entrainment velocity and mass exchange coefficient were also calculated. In addition, by employing the pressure at the trailing edge of the cavity as a phase reference, it was also possible to average images at a defined phase of the cycle of the coupled oscillation, thereby giving phase-averaged patterns of velocity, vorticity, and streamline topology.

4.4.1 Time-Averaged Flow Patterns

Contours of time-averaged patterns of streamwise velocity $<u>/U_r$ are shown in Figure 4.4. Comparison of the contours of $<u>/U_r$ in the left column ($h_c/h_w = 0$) with the corresponding contours in the middle ($h_c/h_w = 0.083$) and right ($h_c/h_w = 0.167$) columns shows the effect of the cylinder at the leading corner of the cavity on the coupled oscillation. At all elevations above the bed extending from $z_L/h_w = 0.067$ to $z_L/h_w = 0.667$, presence of the cylinder at the leading corner of the cavity is associated with a decrease of the streamwise velocity magnitude $<u>/U_r$ within the cavity. This aspect is especially pronounced in the last row of images, i.e., at an elevation of the laser sheet $z_L/h_w = 0.067$ close to the bed. As defined by the color bar at the bottom of the image layout, the light green color represents a

larger magnitude of $<u>/U_r$ relative to the light blue color. This low magnitude streamwise velocity within the cavity corresponds to a relatively weakened recirculation flow in the presence of the cylinder (h_c/h_w = 0.067 and 0.167).

Figure 4.5 shows contour levels of time-averaged streamwise velocity $<u>/U_r$, which emphasize the effect of the cylinder. The left column of images corresponds to the case without the cylinder (h_c/h_w = 0). At all elevations z_L/h_w, the defined cluster of $<u>/U_r$ remains relatively thin and concentrated. Moreover, the predominance of dark blue color indicates lower magnitudes of velocity $<u>/U_r$; higher velocity, corresponding to the red color is evident at the elevation closest to the bed z_L/h_w = 0.067. The middle column of images corresponds to the cylinder of smaller height (h_c/h_w = 0.083). Close to the bed (z_L/h_w = 0.067), the laser sheet intersects the cylinder, represented by the filled circular symbol. At larger elevations z_L/h_w above the bed, the circular symbol is open, indicating that the plane of observation is at an elevation larger than the height h_c of the cylinder. Remarkable is the influence of the cylinder at larger elevations above the bed, extending as high as z_L/h_w = 0.667, which is nearly a factor of ten larger than the height of the cylinder. It appears that the influence of three-dimensional wake from the cylinder rapidly penetrates to higher elevations above the bed. The consequence is a substantial widening of the cluster of $<u>/U_r$ at z_L/h_w = 0.667, especially over the region approaching the impingement corner of the cavity; significant widening of the contour pattern of $<u>/U_r$ also occurs immediately downstream of the cylinder. In these regions of widening of the cluster of $<u>/U_r$, larger values of

velocity are induced, as indicated by the predominantly red and green colors. Such widening apparently arises from flow past the cylinder and through the gap between the cylinder and the surface of the leading-corner of the cavity. Finally, the right column of images represents the cylinder height $h_c/h_w = 0.167$. In this case, the widened cluster extends continuously from the cylinder to the impingement corner of the cavity, except at the largest elevation $z_L/h_w = 0.667$.

The stability parameter S is a function of the entire width of the shear layer δ, which also undergoes a large increase of width (not shown herein), in accord with the width increase in presence of the cylinder indicated in Figure 4.5. This increase of the value of δ results in a larger value of the stability parameter S. For purposes of reference, the values of the stability parameter S are $S = 0.003$, 0.008, and 0.012 respectively for the first, second and third columns of images; as indicated in the Section 4.2, these values correspond to an increasingly stable shear layer, which is consistent with decreased amplitude of the coupled oscillation.

Figure 4.6 shows time-averaged streamline $<\psi>$ patterns. Each pattern involves a recirculation zone, an inward-oriented flow in the vicinity of the impingement corner of the cavity, and an outward-oriented flow along and above the opening of the cavity. The first row of images corresponds to an elevation well above the bed, i.e., $z_L/h_w = 0.667$, which corresponds to two-thirds the depth h_w of the shallow water layer. At this elevation, the recirculation pattern within the cavity does not show distinctively different features for all values of h_c/h_w; moreover, a stagnation streamline originates from the leading corner of the cavity and impinges

upon the trailing corner for all cases. On the other hand, at an elevation closer to the bed, corresponding to $z_L/h_w = 0.333$, the separation line from the leading corner of the cavity is substantially deflected inward in the vicinity of the trailing corner at $h_c/h_w = 0$, while the separation line is nearly undeflected in presence of the cylinder, i.e., at $h_c/h_w = 0.083$ and 0.167.

At the two elevations $z_L/h_w = 0.167$ and 0.067 closest to the bottom surface (bed) of the shallow water layer, a focus F occurs near the leading (upstream) corner of the cavity; it is the center of a swirl pattern of streamlines, that form a separation bubble. The scale of the separation bubble along the leading (upstream) wall of the cavity gradually increases with decreasing elevation for all cases, and the extent of the separation bubble becomes larger with increasing dimensionless height h_c/h_w of the cylinder. At the elevation closest to the bed $z_L/h_w = 0.067$, a positive bifurcation line BL^+, originates from the upstream corner of the cavity. These streamlines diverge substantially with increasing streamwise distance; furthermore, they are deflected away from the cavity. The degree of deflection of these streamlines increases with the height of the perturbation (cylinder), i.e., the largest streamline deflection occurs at $h_c/h_w = 0.167$. Lastly, the streamline near the downstream (trailing) edge of the cavity, designated as BL^-, corresponds to merging together of streamlines from the leading and trailing corners of the cavity; these streamlines correspond to negative bifurcation lines BL^-.

Figure 4.7 provides time-averaged contours of constant transverse velocity $\langle v \rangle/U_r$. As in previous layouts, the left column of images ($h_c/h_w = 0$) corresponds

to the maximum-amplitude of the gravity standing wave, and the middle and right columns (h_c/h_w = 0.083 and 0.167) represent the cases where these oscillations are attenuated. Rows of images from top to bottom correspond to successive layers closer to the bed (bottom surface). Blue contours indicate outward-oriented transverse flow, i.e., flow away from the interior of the cavity, and red contours indicate inward-oriented flow, that is, towards or into the cavity.

In Figure 4.7, in the left column of images (h_c/h_w = 0), large magnitude, outward-oriented (dark blue) flow moves towards the mouth of the cavity and inward-oriented (dark red) flow occurs into the cavity; these images correspond to the fully-coupled (locked-in) oscillation. The peak magnitude of both the inward-oriented and outward-oriented flow decreases in presence of the cylinder (h_c/h_w = 0.083 and 0.167), as indicated in the images in the middle and right columns. One can therefore conclude that the presence of a cylinder (h_c/h_w = 0.083 and 0.167) at the leading edge of the cavity results in a substantial decrease in the strength of the recirculation flow within the cavity. A further, common feature of all cases is the existence of a localized region of outward-oriented (blue) flow at the downstream (impingement) corner of the cavity. The peak magnitude of this localized region decreases in presence of the cylinder (h_c/h_w = 0.083 and 0.167) at the leading edge of the cavity; simultaneously, its scale increases. Consideration of this localized blue region in conjunction with the red region, located along the downstream (impingement) surface edge of the cavity, suggests the existence of a

stagnation point in the vicinity of the impingement corner, as indicated by the streamline patterns of Figure 4.6.

Furthermore, a distinctive feature of the images of Figure 4.7, in presence of the cylinder (h_c/h_w = 0.083 and 0.167), is a region of outward (blue color) transverse velocity located downstream of the cylinder. This outward transverse velocity exists at elevations z_L/h_w = 0.067 and 0.167. It is associated with deflection of streamlines in the outward direction away from the cavity, as shown in Figure 4.6. Moreover, it is coincident with the positive bifurcation line BL^+ within the pattern of streamlines given in Figure 4.6.

Contours of time-averaged patterns of vorticity $<\omega>L/U_r$ are shown in Figure 4.8. The high level (green color) vorticity $<\omega>L/U_r$ is rapidly attenuated in the streamwise direction in absence of the attenuation cylinder (h_c/h_w = 0), and in presence of the cylinder (h_c/h_w = 0.083 and 0.167), this region progressively extends downstream and eventually intersects the impingement corner. To clarify this point, a comparison between two limiting cases (h_c/h_w = 0 and 0.167) is made with the green level of vorticity ($<\omega>L/U_r$ = -6) at the elevations z_L/h_w = 0.667 and 0.067. The length of the line l_ω is shorter in the image in the left column (h_c/h_w = 0) than the one in the right column (h_c/h_w = 0.167). This streamwise degradation of high level vorticity is related to the large-amplitude transverse undulations of the vorticity layer. Furthermore, the width of the vorticity layer is relatively large in the absence of the attenuation cylinder (h_c/h_w = 0), especially at an elevation well

above the bed, $z_L/h_w = 0.667$. Finally, the width of the vorticity layer that protrudes into the cavity (blue contour) is substantially larger at $h_c/h_w = 0$ relative to the cases $h_c/h_w = 0.083$ and 0.167.

A further feature of the images of vorticity contours given in Figure 4.8 is a distinct, narrow band of vorticity in presence of the cylinder ($h_c/h_w = 0.083$ and 0.167); it extends from the cylinder to the downstream corner of the cavity. The scale of this separate band of vorticity decreases with increasing elevation above the bed, and is not detectable well above the bed ($z_L/h_w = 0.667$). This vorticity band occurs in conjunction with the region of transverse velocity oriented away from the cavity, which is indicated in Figure 4.7, and the deflection of streamlines away from the cavity opening, shown in Figure 4.6.

Figure 4.9 shows the effects of the control cylinder on the patterns of root-mean-square transverse velocity fluctuation v_{rms}/U_r. The common feature of all these images is, first of all, a substantial attenuation of the peak magnitude in the presence of the cylinder at all elevations above the bed, even for the smallest cylinder $h_c/h_w = 0.083$. Furthermore, in presence of the control cylinder, the highest level of v_{rms}/U_r tends to occur at, and immediately upstream of, the trailing (impingement) corner of the cavity. These higher-level regions are associated with the onset of the saddle point in the vicinity of the trailing corner in the streamline patterns of Figure 4.6.

Patterns of Reynolds stress $<u'v'>/U_r^2$, that is the degree of correlation between the streamwise u' and transverse v' velocity fluctuations, are shown in Figure 4.10. The peak values of $<u'v'>/U_r^2$ in absence of the cylinder $h_c/h_w = 0$, shown in the left column of images, are significantly attenuated in the presence of the cylinder (h_c/h_w = 0.083 and 0.167), as evident in the middle and right columns of the images. The magnitude of the Reynolds stress in the separated shear layer along the cavity opening is directly related to the entrainment demand of the separated layer and thereby is expected to influence the mass exchange process between the cavity and main stream; this aspect will be addressed subsequently.

4.4.2 Phase-Averaged Flow Patterns

Phase-averaged streamline $<\psi>_p$ patterns are given in Figure 4.11 for two different phases (ϕ = 90° and 270°) of the oscillation cycle. As in previous layouts, the left column of images ($h_c/h_w = 0$) corresponds to the fully coupled oscillation without the control cylinder, and the middle and right columns (h_c/h_w = 0.083 and 0.167) represent cases where the oscillations is attenuated to varying degrees by the control cylinder. The top two rows of images represent the region well above the bed (z_L/h_w = 0.667), and the bottom two rows correspond to the region at the bed (z_L/h_w = 0.067).

In the left column of images ($h_c/h_w = 0$), the separation streamline originating from the leading edge of the cavity undergoes relatively large amplitude undulations; in presence of the control cylinder, represented by the images in the

second and third columns (h_c/h_w = 0.083 and 0.167), the amplitude of this undulation is substantially attenuated. The patterns of recirculating streamlines within the cavity, at z_L/h_w = 0.667, do not show any unusual features. At the bed (z_L/h_w = 0.067), however notable distortions occur. Deflection of the streamlines away from the cavity in the presence of the cylinder (bed perturbation) occurs. The deflection of shear layer was also indicated in the computational study of Arunajatesan et al. (2002). In addition, a downward directed jet-like flow occurs adjacent to the trailing (impingement) corner of the cavity. These features are defined with topological concepts in the time-averaged streamline $<\psi>$ patterns in Figure 4.6.

Figure 4.12 shows patterns of phase-averaged streamlines $<\psi>_p$ in a reference frame corresponding to one-half of the free stream velocity U_r, and at two different phases (ϕ = 90° and 270°) of the oscillation cycle. In all images at z_L/h_w = 0.667 in Figure 4.12, a concentrated, ordered pattern of spiraling streamlines forms in the shear layer along the cavity opening. The scale of these concentrated patterns is relatively large in absence of the control cylinder (h_c/h_w = 0) compared to cases with the control cylinder (h_c/h_w = 0.083 and 0.167) at both elevations above the bed. In absence of the control cylinder (h_c/h_w = 0), represented by the left column of images, the streamline patterns are clearly correlated with the patterns of phase-averaged transverse velocity $<v>_p/U_r$ of Figure 4.13 and phase-averaged contours of constant vorticity $<\omega>_pL/U_r$ of Figure 4.14. At an elevation z_L/h_w = 0.067 close to the bed, however, the patterns of

swirling streamlines are more complex, and the comparisons indicated in the foregoing are not attainable.

Figure 4.13 shows corresponding contours of constant phase-averaged transverse velocity $\langle v \rangle_p / U_r$. As in the previous layout of time-averaged transverse velocity of Figure 4.7, red contours of $\langle v \rangle_p / U_r$ indicate flow in the inward direction (negative y direction) towards the interior of the cavity, and blue contours of $\langle v \rangle_p / U_r$ indicate the flow in the outward direction (positive y direction) away from the cavity. The top two rows of images represent the region well above the bed (z_L/h_w = 0.667), and the bottom two rows of images correspond to the region close to the bed (z_L/h_w = 0.067) for two different phases (ϕ = 90° and 270°) of the oscillation cycle.

First of all, for cases with and without the control cylinder (h_c/h_w = 0, 0.083, and 0.167), the magnitudes of the outward (blue) oriented transverse velocity along the face of the leading (upstream) edge and inward-directed (red) transverse velocity along the face of the trailing edge are higher close to the bed at z_L/h_w = 0.067, relative to the region well above the bed at z_L/h_w = 0.667. A similar trend was observed for the aforementioned patterns of the time-averaged transverse velocity $\langle v \rangle / U_r$ (Figure 4.7) and vorticity $\langle \omega \rangle L/U_r$ (Figure 4.8). Furthermore, at z_L/h_w = 0.067, in the left column of images (h_c/h_w = 0), red and blue clusters of transverse velocity propagate downstream along the cavity opening. These downstream-propagating clusters are barely detectable in the middle and right

columns of images (h_c/h_w = 0.083 and 0.167). This phenomenon can be related to the loss in the coherence of the large-scale vortex formation in the shear layer along the cavity opening due to the effect of the bed perturbation (cylinder).

A further observation in Figure 4.13 is that, at z_L/h_w = 0.067, high levels of outward-oriented (blue) clusters of phase-averaged transverse velocity $<v>_p/U_r$ are located downstream of the cylinder as indicated in the middle and right columns of images (h_c/h_w = 0.083 and 0.167). This observation is in accord with the images in the middle and right columns of the time-averaged transverse velocity $<v>/U_r$ in Figure 4.7. Within the cavity, it is evident that the magnitudes of both the inward-oriented (red) and outward-oriented (blue) transverse velocity $<v>_p/U_r$ within the cavity are reduced in presence of the cylinder (h_c/h_w = 0.083 and 0.167).

Figure 4.14 shows phase-averaged contours of constant vorticity $<\omega>_pL/U_r$ for two different phases (ϕ = 90° and 270°) of the oscillation cycle. The top two rows of images represent the region well above the bed (z_L/h_w = 0.667), and the bottom two rows of images represent the region at the bed (z_L/h_w = 0.067). By comparison of images in a given row of this layout, it is possible to determine the consequences of the control cylinder on the structure of the shear layer.

Onset and development of a large-scale vortical structure is present in the left column of images (h_c/h_w = 0) at both elevations z_L/h_w = 0.067 and 0.667; it forms at the leading edge of the cavity and moves in the downstream direction with the increasing phase angle ϕ. On the other hand, formation of a large cluster of

vorticity does not occur in the middle and right columns of images (h_c/h_w = 0.083 and 0.167). It should also be noted that for the case of the maximum-amplitude oscillation (h_c/h_w = 0), represented in the left (first) column of images, large-amplitude transverse excursions of the vorticity layer occur over an oscillation cycle; and, for the reduced-amplitude oscillations (h_c/h_w = 0.083 and 0.167), represented in the middle and right columns of images, the vorticity layer shows small amplitude transverse undulations about a nominal state.

Furthermore, at z_L/h_w = 0.067 in Figure 4.14, the scale of the cluster of vorticity that is deflected into the cavity at the trailing edge is relatively larger in magnitude (green contour level) in the absence of the control cylinder (h_c/h_w = 0) compared to cases with the control cylinder (h_c/h_w = 0.083 and 0.167). A further point is that a distinct narrow band of vorticity is detectable in the phase-averaged patterns of vorticity $<\omega>_p L/U_r$ similar to the time-averaged patterns of Figure 4.8. The transverse extent of this band of vorticity layer at h_c/h_w = 0.167 is relatively large compared to h_c/h_w = 0.083; this band of vorticity is not detectable in absence of the cylinder (h_c/h_w = 0), indicated in the left column of images.

Appendix B contains corresponding phase-averaged figures showing the patterns of streamlines $<\psi>_p$, streamwise velocity $<u>_p/U$ transverse velocity $<v>_p/U$, and vorticity $<\omega>_p L/U$ for four different phases ϕ of the oscillation cycle at all elevations mentioned in Section 4.2.

4.4.3 Time-Averaged Mass Exchange Patterns

A major issue is the degree to which the mass exchange between the mainstream and the cavity is influenced by the alterations of the flow structure described in the foregoing. The effects of the control cylinder on the mass exchange process and the patterns of time-averaged exchange velocity $\overline{E(t)}$ are addressed in Figures 4.15 and 4.16.

The instantaneous exchange velocity *E(t)*, spatially averaged along the cavity opening, is given as:

$$E(t) = \frac{1}{L}\int_0^L |v(t)|dx \tag{4.1}$$

where *v(t)* is the transverse (cross-stream) component of velocity. A total of 3,000 randomly-acquired instantaneous velocity vector fields were averaged to calculate the time averaged values of $\overline{E(t)}$. A dimensionless mass exchange coefficient *k* was then calculated according to (Tuna et al., 2013):

$$k = \frac{\overline{E(t)}}{2U_r} \tag{4.2}$$

in which U_r is the depth-averaged free stream velocity. Details of formulation of the exchange velocity and mass exchange coefficient are given in Section 3.4.3.

Figure 4.15 shows surfaces of time-averaged exchange velocity $\overline{E(t)}$. In accord with previous layouts of images of the flow structure, the left column

(h_c/h_w = 0) corresponds to the maximum-amplitude oscillation case, and the middle and right columns (h_c/h_w = 0.083 and 0.167) represent the cases of the reduced-amplitude oscillation. The coordinate z_L/h_w indicates the elevation above the bed (bottom surface) and the x/L axis shows the streamwise location along the mouth of the cavity. The blue point designates the leading edge (x/L = 0) of the cavity, and the red point defines the trailing edge (x/L = 1).

The most striking result of the comparison of these plots is that the overall magnitude of the time-averaged exchange velocity $\overline{E(t)}$ is higher in the absence of the control cylinder, i.e., in the left plot (h_c/h_w = 0) in Figure 4.15. The magnitude of $\overline{E(t)}$ decreases as the dimensionless height h_c/h_w of the cylinder increases, corresponding to the middle and right plots. This decreased magnitude of the time-averaged exchange velocity $\overline{E(t)}$ stems from the attenuated Reynolds stress $<u'v'>/U_r^2$ patterns, which were described in Figure 4.10. That is, an attenuated magnitude of Reynolds stress, due to presence of the control cylinder (h_c/h_w = 0.083 and 0.167), is related to a decrease in value of time-averaged exchange velocity $\overline{E(t)}$. On the other hand, regions of large Reynolds stress $<u'v'>/U_r^2$ correspond to the largest value of $\overline{E(t)}$, as clearly seen at the streamwise location of x/L = 0.6 at z_L/h_w = 0.500 in the left plot (h_c/h_w = 0) of Figure 4.15. These results indicate that the amount of fluid that is exchanged between the cavity and main stream will be much smaller in the presence of the control cylinder.

The dimensionless mass exchange coefficient k was calculated from Equation 4.2 using the time-averaged exchange velocity distributions $\overline{E(t)}$ given in Figure 4.15. The values of k are shown in Figure 4.16 with respect to elevation above the bed, designated as z_L/h_w. The red line represents the maximum-amplitude oscillation ($h_c/h_w = 0$), while the blue and green lines correspondingly represent the reduced-amplitude oscillation cases ($h_c/h_w = 0.083$ and 0.167). Values of k are 60%-90% higher in the absence of the cylinder ($h_c/h_w = 0$). Maximum values of mass exchange coefficient are $k = 0.4$ for $h_c/h_w = 0$, $k = 0.25$ for $h_c/h_w = 0.083$, and $k = 0.2$ for $h_c/h_w = 0.167$.

4.5 CONCLUSIONS

Shallow flow past a cavity can give rise to large amplitude oscillations, which arise from coupling between the separated shear layer along the opening of the cavity and the gravity standing wave mode of the cavity. In this investigation, emphasis is on control of the self-excited oscillations via a small diameter cylinder, which has a height much smaller than the water depth. Techniques of high-image-density particle image velocimetry and unsteady pressure measurements are combined to characterize the structure of shallow flow past and within the cavity. The structure of the unsteady shear layer along the opening of the cavity, the gravity standing wave within the cavity, and the mass exchange process between the cavity and the main stream are addressed as a function of elevation above the bed.

Although the diameter and height of the cylinder are nearly an order of magnitude smaller than the depth of the shallow layer, its presence exerts an influence at elevations well above the height of the cylinder. In essence, this influence is associated with an increase of width of the shear layer along the opening of the cavity, which, in turn, promotes a more stable separated shear layer, in accord with stability theory for a shallow flow.

Patterns of time-averaged streamwise velocity, transverse velocity, streamline patterns, vorticity, root-mean-square of transverse velocity fluctuation, and Reynolds stress define the physics of attenuation of the oscillation via a small control cylinder. Outward (away from the cavity) deflection of the streamlines occurs near the bed. Substantial attenuation of the peak amplitudes of the contours of vorticity, root-mean-square of the transverse velocity, and the Reynolds stress occurs in the separated shear layer along the cavity opening; reduction of peak amplitudes of these quantities can be as high as 35% to 70%. Moreover, reduction of peak values of the streamwise and transverse velocity components occurs within the cavity. This reduction corresponds to a decrease in the strength of the recirculation flow within the cavity.

Finally, the value of the mass exchange coefficient, which is evaluated using the time-averaged exchange velocity along the opening of the cavity, shows a steep decrease (37% to 50%) in presence of the control cylinder. This decrease in the mass exchange coefficient is correlated with attenuation of patterns of Reynolds stress along the cavity opening in presence of the control cylinder.

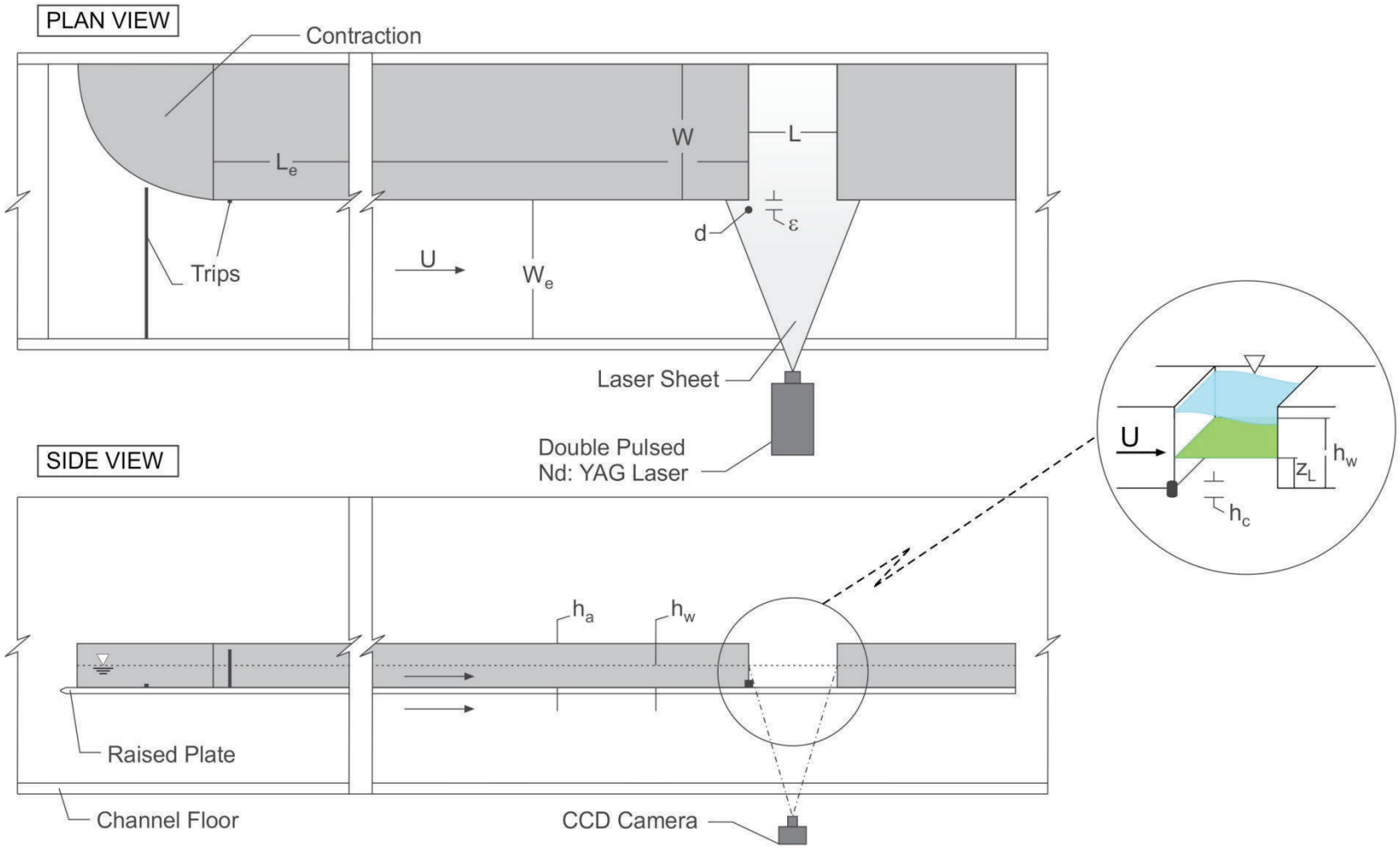

Figure 4.1: Schematic of experimental facility. (after Tuna et al., 2013)

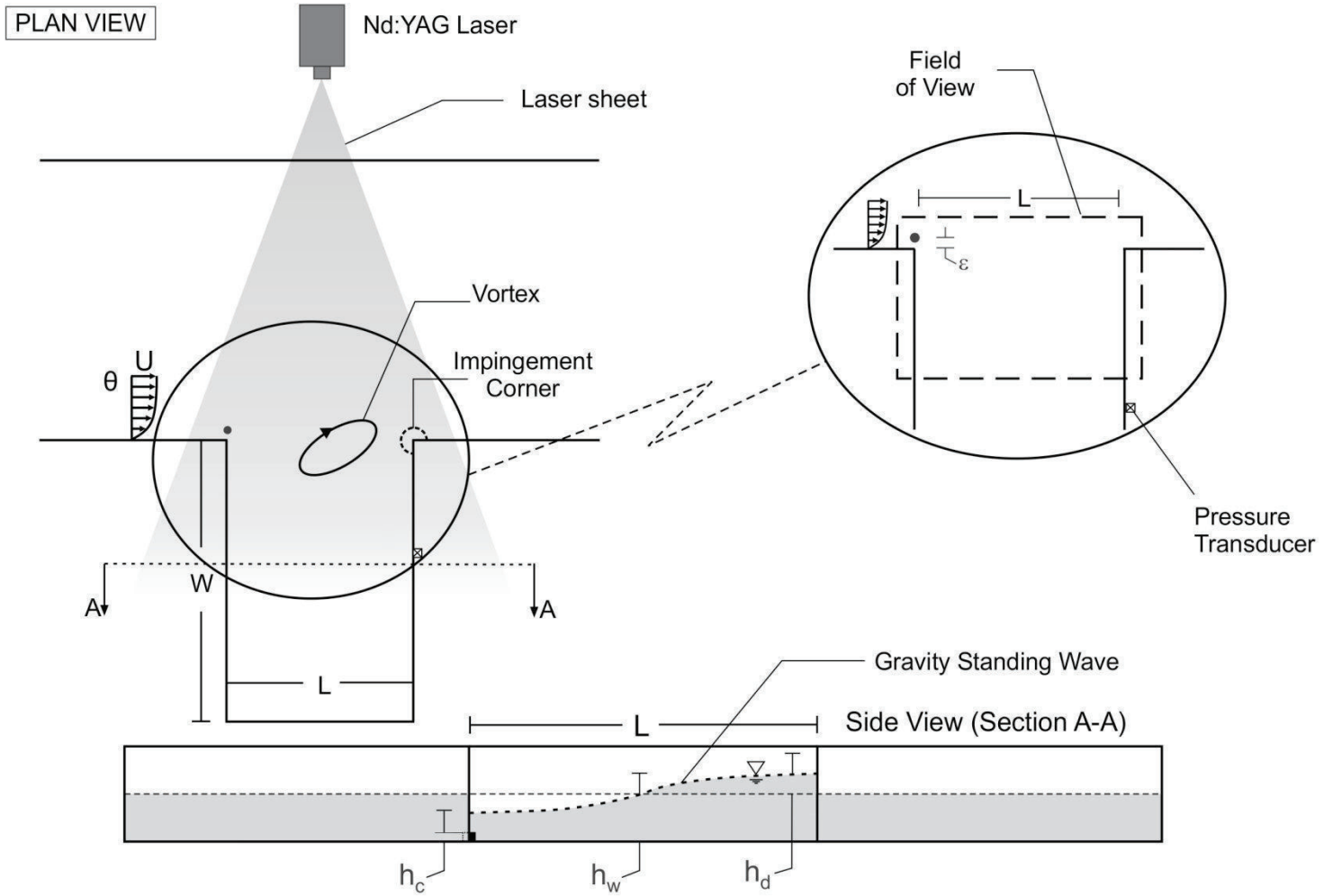

Figure 4.2: Schematics of experimental test section and quantitative imaging system. Also illustrated are representations of unstable shear layer along opening of the cavity and deformation of free- surface due to gravity standing wave within the cavity.(not to scale)

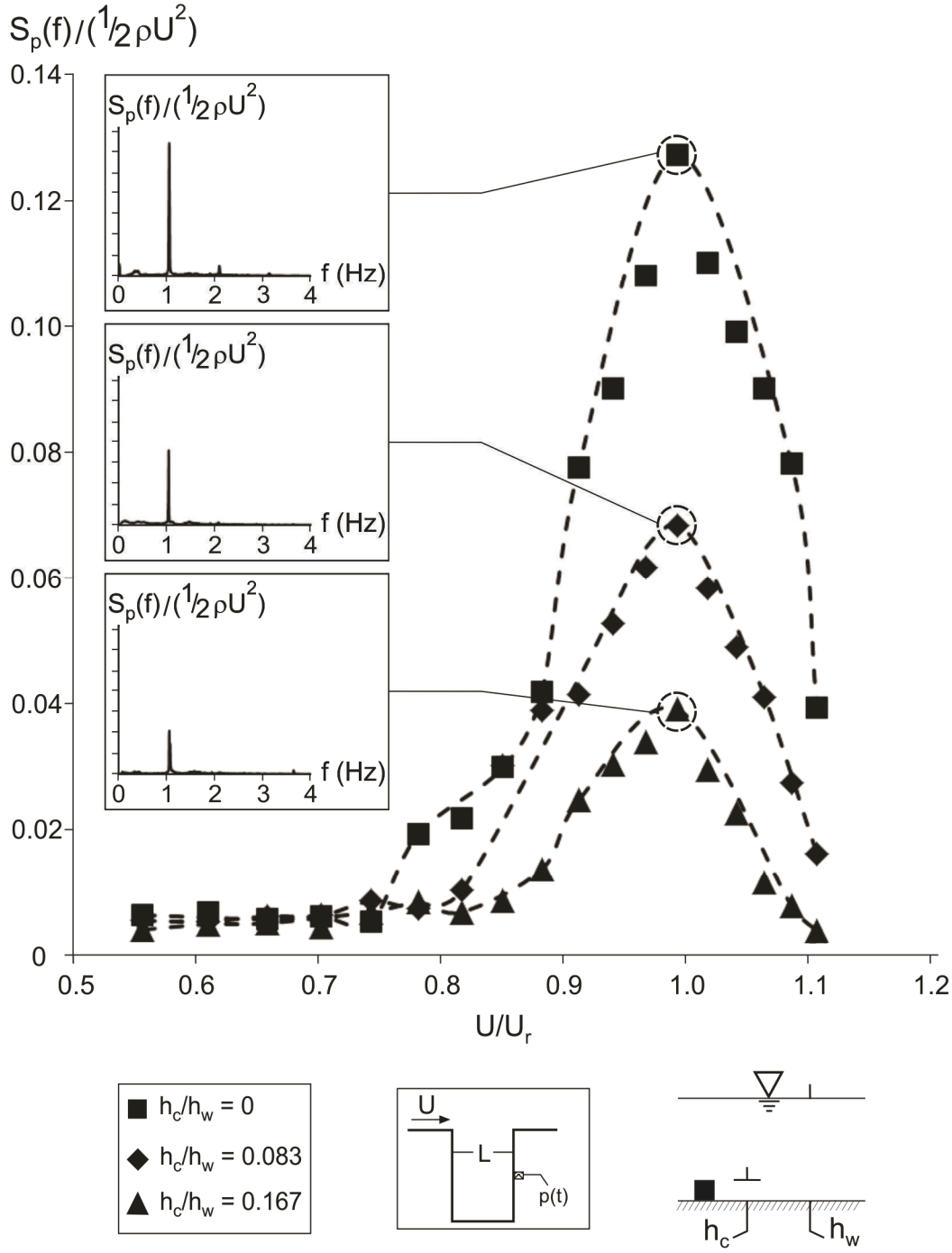

Figure 4.3: Amplitude of spectral peak $S_p(f)/(^1/_2\rho U^2)$ of pressure fluctuation as a function of dimensionless inflow velocity U/f_nL for cases with and without the cylinder. Case h_c/h_w = 0 corresponds to non-attenuated oscillation in absence of the cylinder; h_c/h_w = 0.083 and 0.167 correspond to attenuated cases in presence of the cylinder.

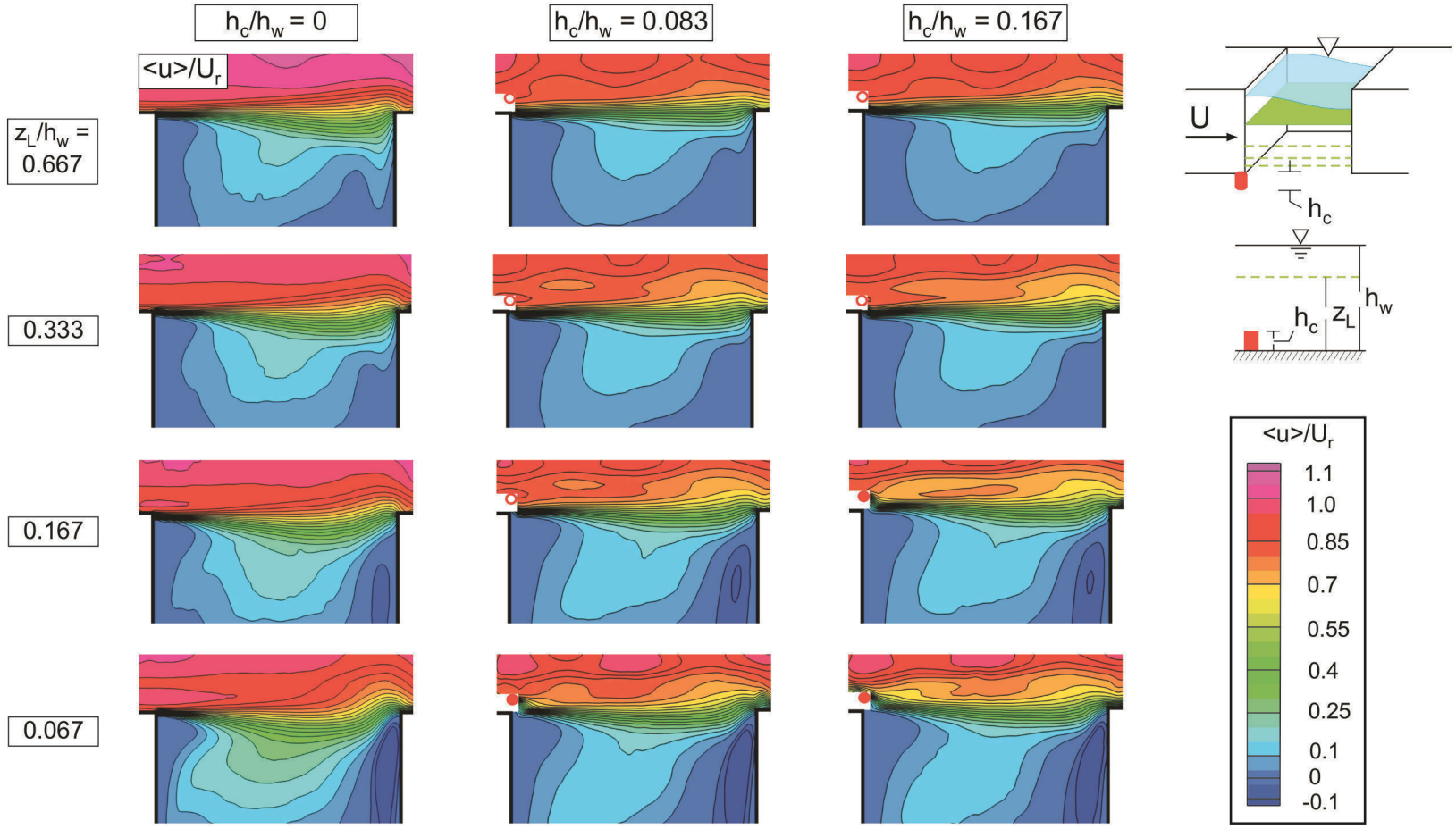

Figure 4.4: Contours of time-averaged streamwise velocity magnitude $<u>/U_r$ at different elevations z_L/h_w above the bed for cases with and without the cylinder. Case $h_c/h_w = 0$ corresponds to the non-attenuated oscillation in absence of the cylinder; $h_c/h_w = 0.083$ and 0.167 correspond to attenuated cases in presence of the cylinder.

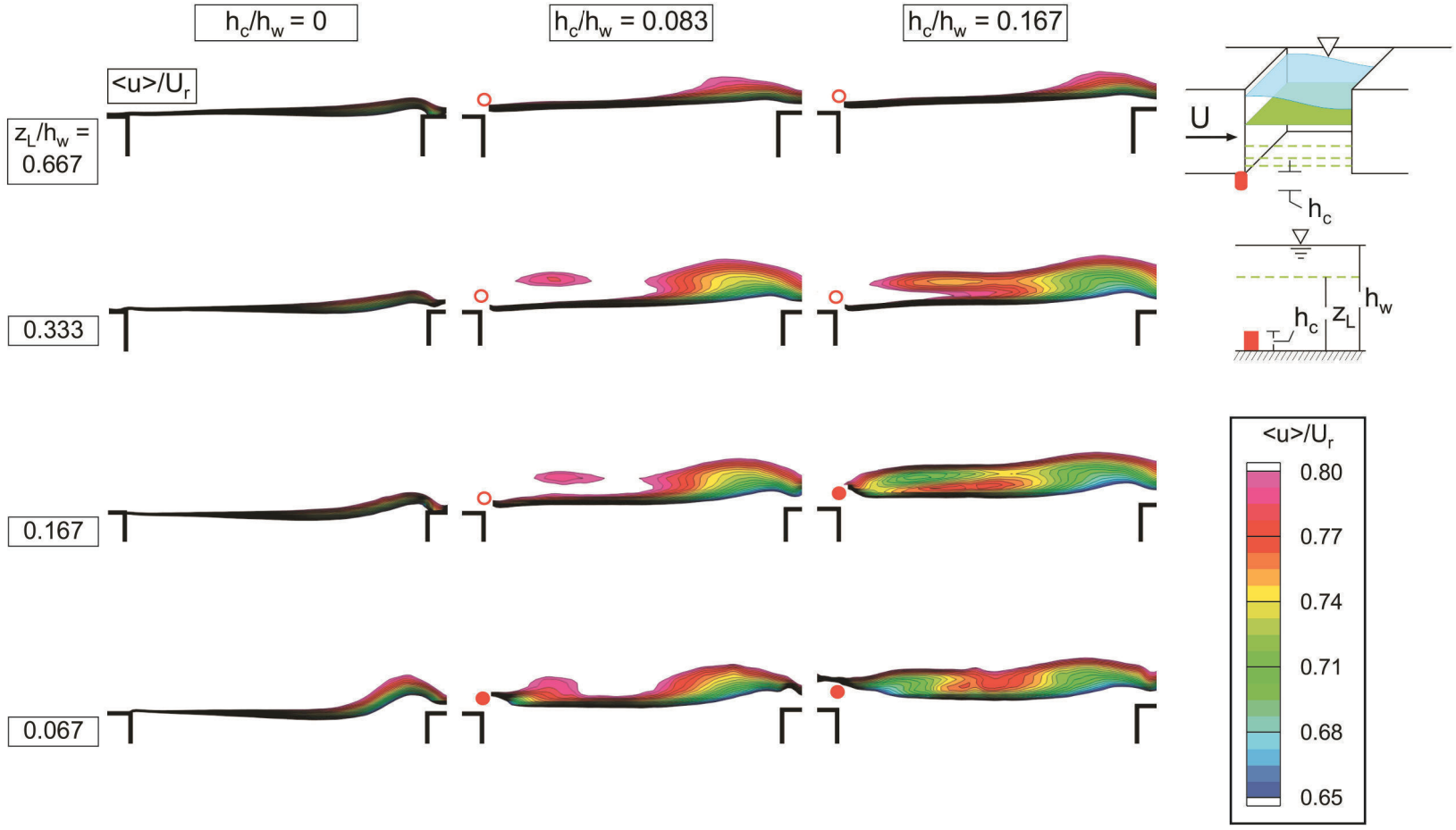

Figure 4.5: Contours of time-averaged streamwise velocity magnitude $<u>/U_r$ at different elevations z_L/h_w above the bed for cases with and without the cylinder. Case $h_c/h_w = 0$ corresponds to the non-attenuated oscillation in absence of the cylinder; $h_c/h_w = 0.083$ and 0.167 correspond to attenuated cases in presence of the cylinder.

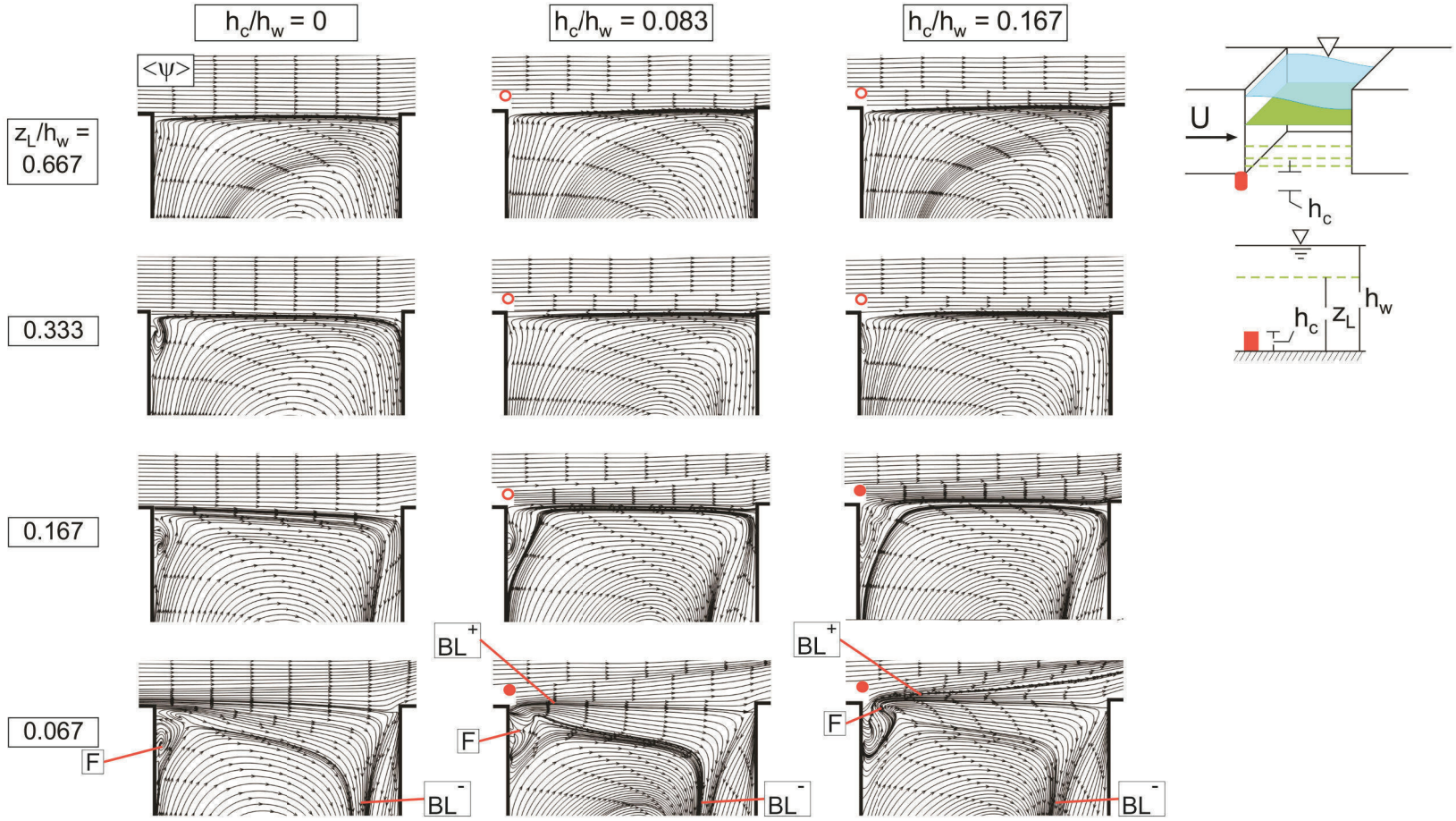

Figure 4.6: Patterns of time-averaged streamlines velocity magnitude <ψ> at different elevations z_L/h_w above the bed for cases with and without the cylinder. Case $h_c/h_w = 0$ corresponds to the non-attenuated oscillation in absence of the cylinder; $h_c/h_w = 0.083$ and 0.167 correspond to attenuated cases in presence of the cylinder.

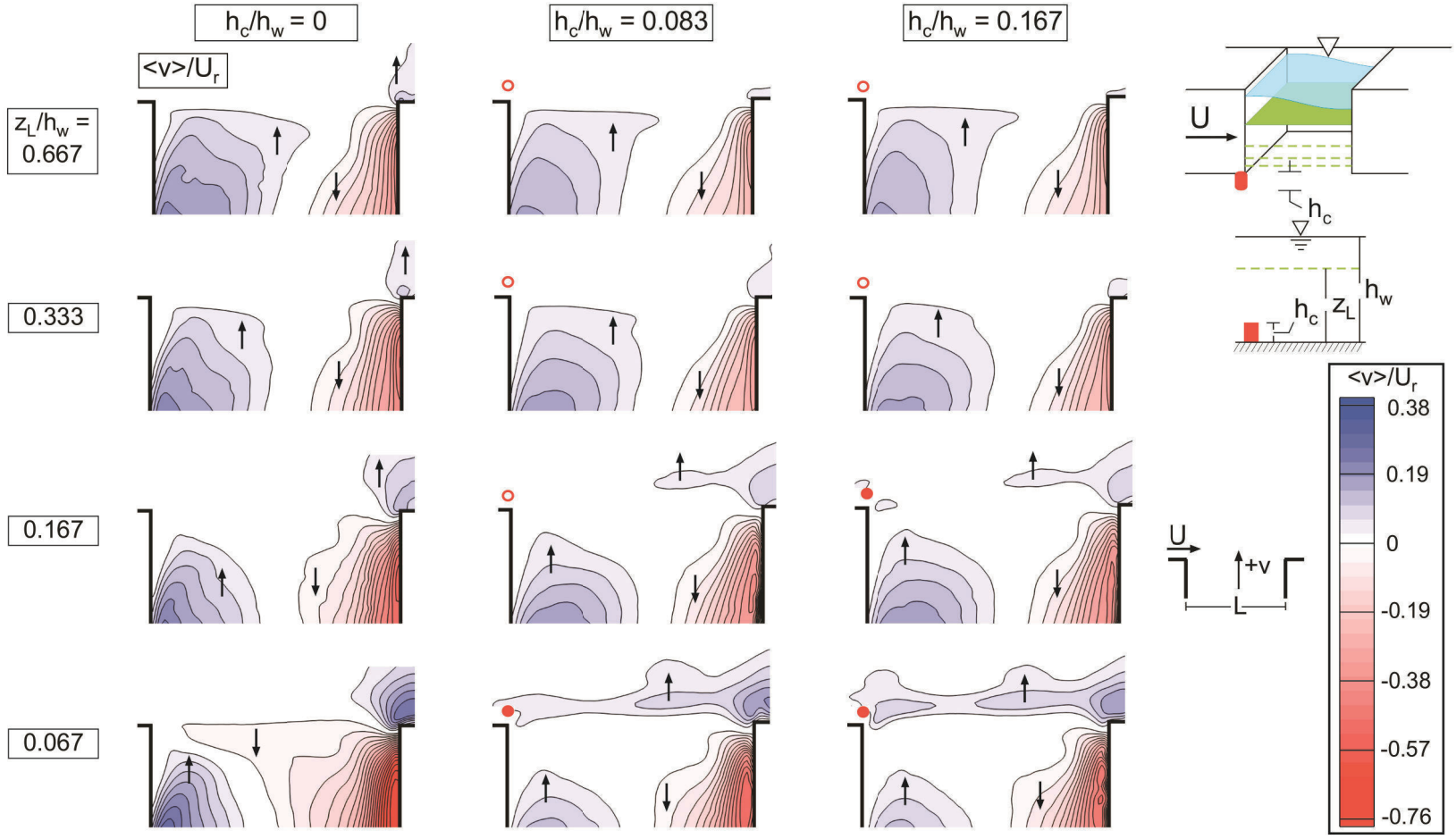

Figure 4.7: Contours of time-averaged transverse velocity $<v>/U_r$ at different elevations z_L/h_w above the bed for cases with and without the cylinder. Case $h_c/h_w = 0$ corresponds to the non-attenuated oscillation in absence of the cylinder; $h_c/h_w = 0.083$ and 0.167 correspond to attenuated cases in presence of the cylinder. Red contour levels represent flow towards the interior of the cavity, and blue contours represent the flow towards the exterior of the cavity.

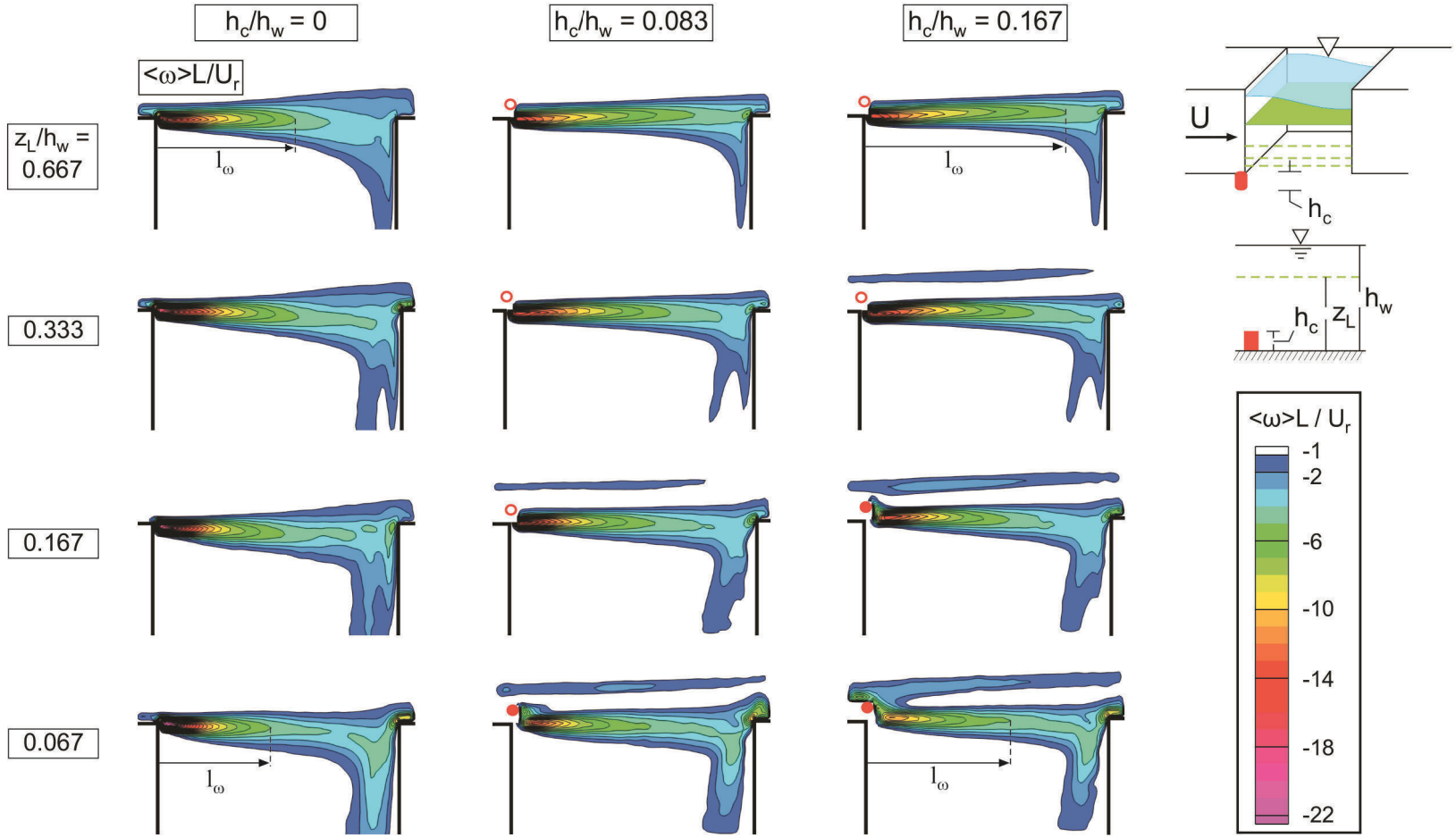

Figure 4.8: Contours of time-averaged vorticity $<\omega>L/U_r$ at different elevations z_L/h_w above the bed for cases with and without the cylinder. Case $h_c/h_w = 0$ corresponds to the non-attenuated oscillation in absence of the cylinder; $h_c/h_w = 0.083$ and 0.167 correspond to attenuated cases in presence of the cylinder.

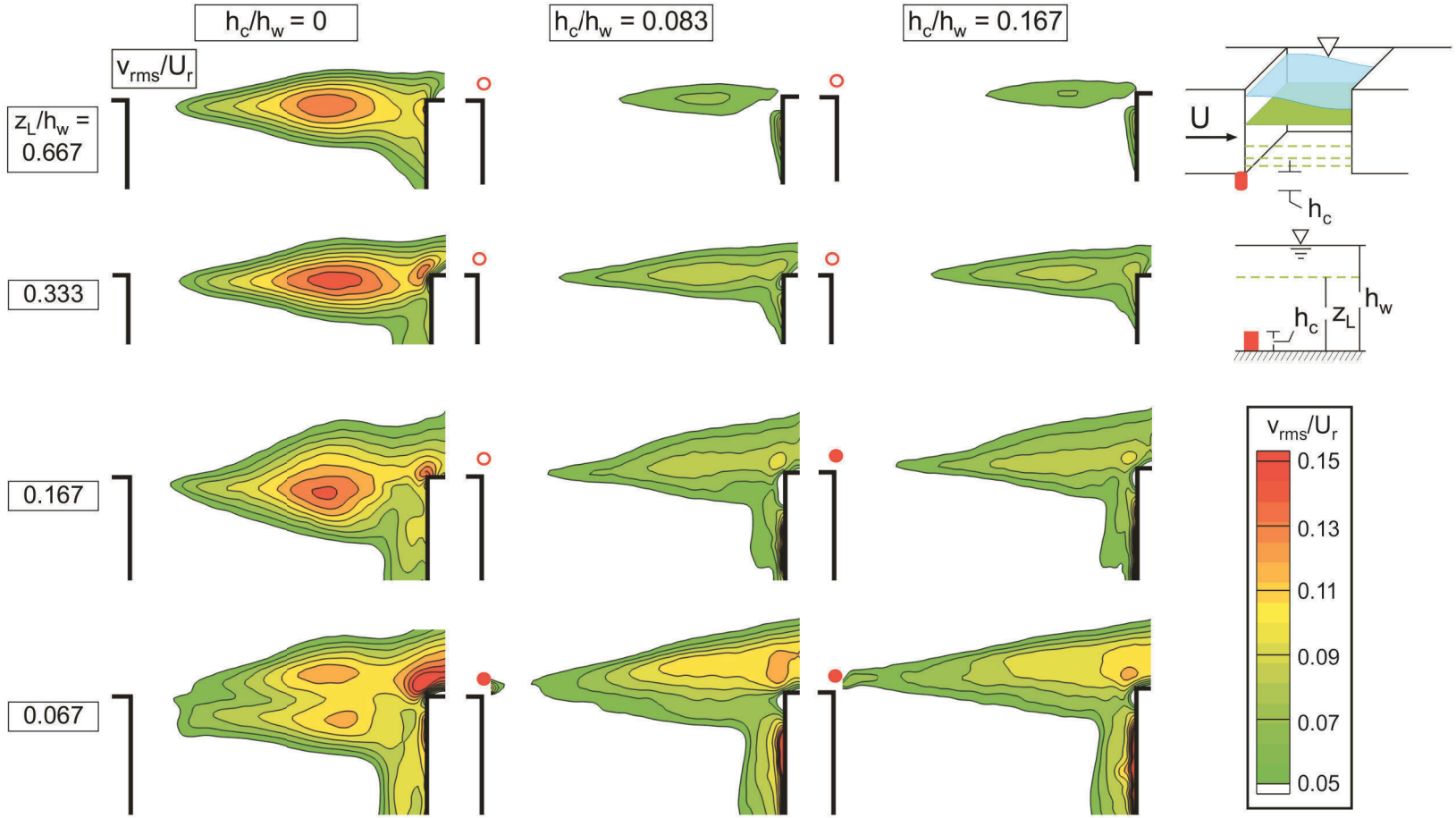

Figure 4.9: Patterns of root-mean-square transverse velocity fluctuation v_{rms}/U_r at different elevations z_L/h_w above the bed for cases with and without the cylinder. Case $h_c/h_w = 0$ corresponds to the non-attenuated oscillation in absence of the cylinder; $h_c/h_w = 0.083$ and 0.167 correspond to attenuated cases in presence of the cylinder.

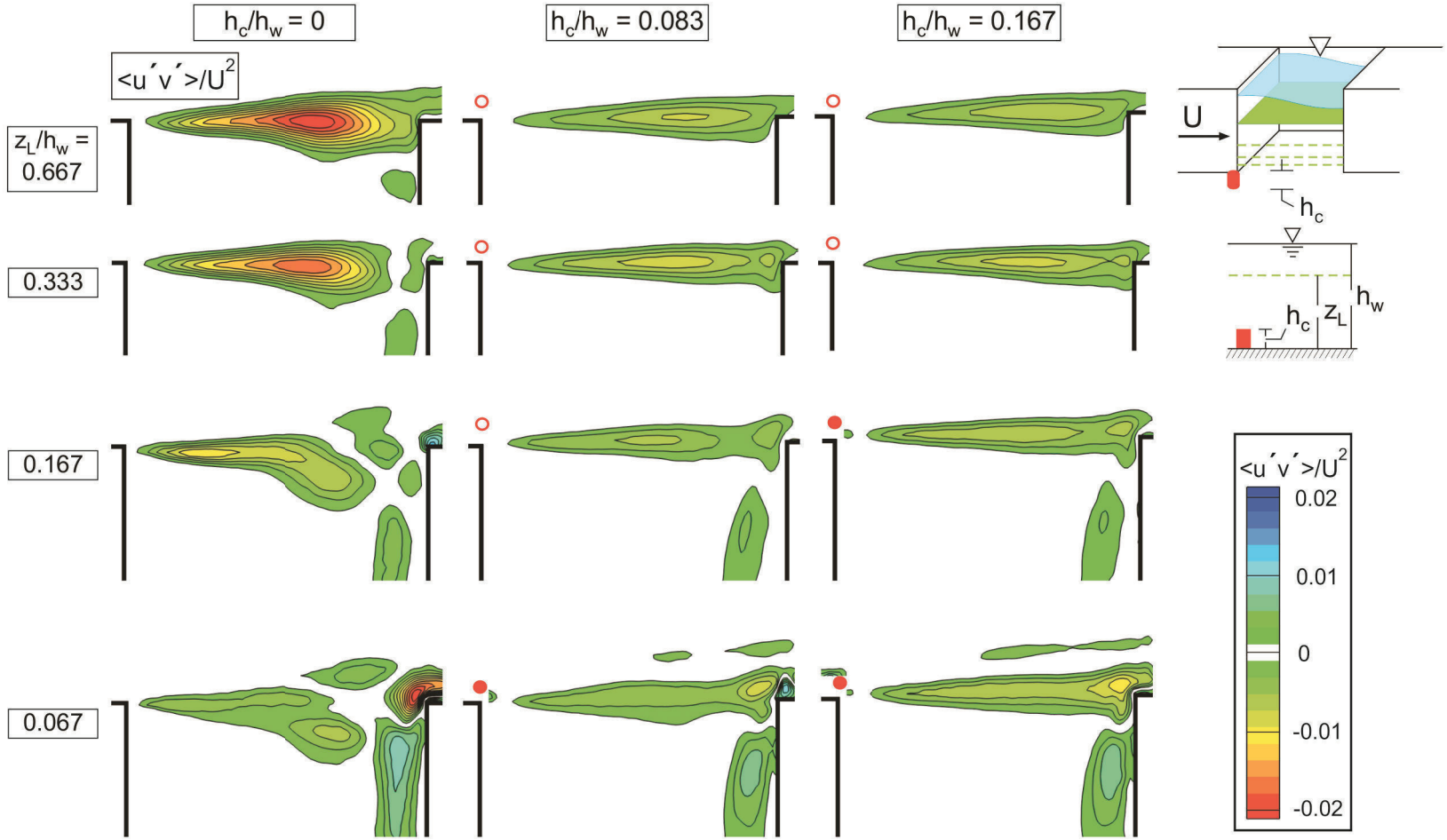

Figure 4.10: Patterns of Reynolds stress $<u'v'>/U_r^2$ at different elevations z_L/h_w above the bed for cases with and without the cylinder. Case $h_c/h_w = 0$ corresponds to the non-attenuated oscillation in absence of the cylinder; $h_c/h_w = 0.083$ and 0.167 correspond to attenuated cases in presence of the cylinder.

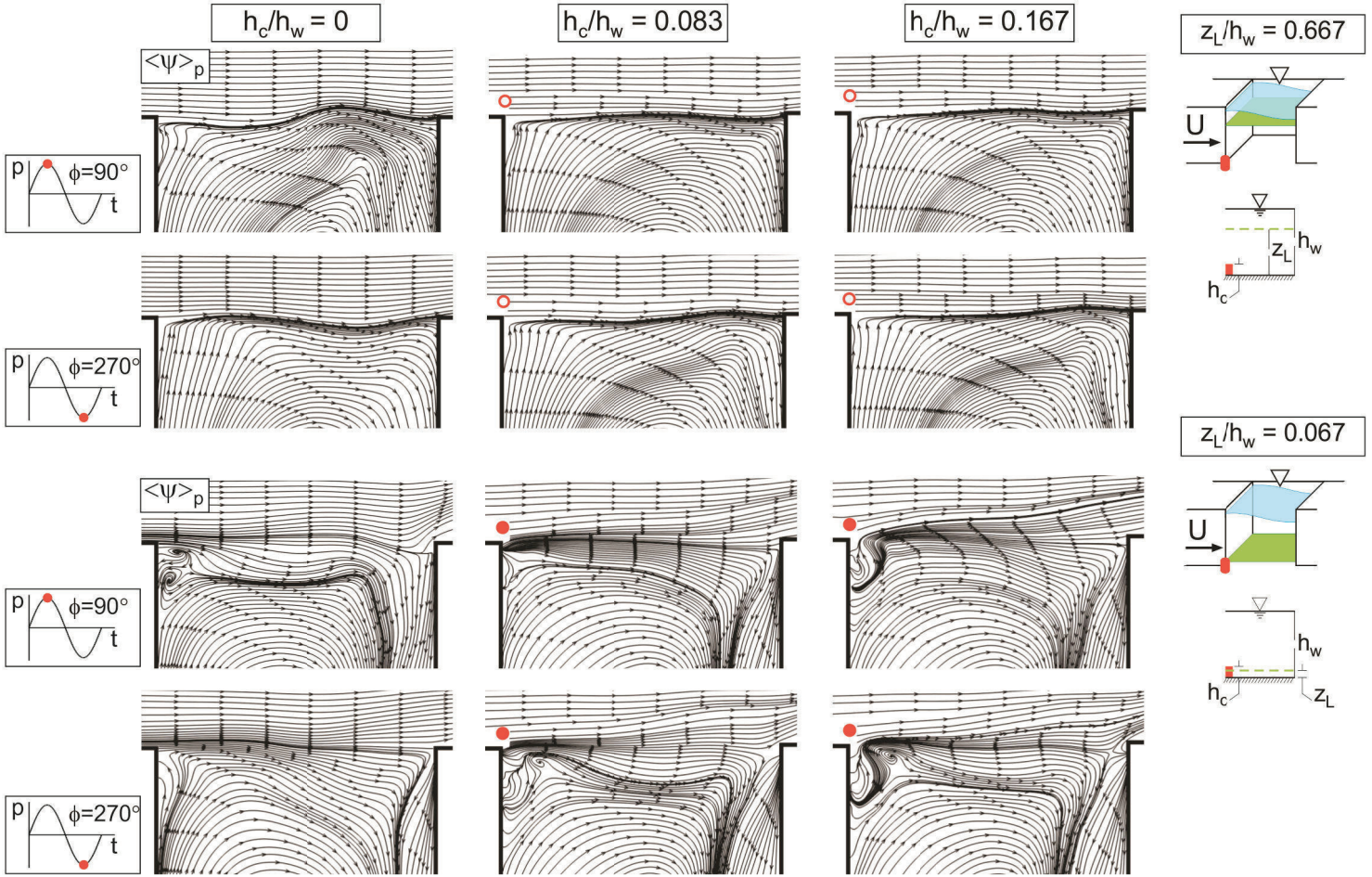

Figure 4.11: Patterns of phase-averaged streamlines $<\psi>_p$ at two different elevations: well above the bed ($z_L/h_w = 0.667$) and near the bed ($z_L/h_w = 0.067$) for two different phases $\phi = 90°$ and $270°$ of the oscillation cycle. Case $h_c/h_w = 0$ corresponds to the non-attenuated oscillation in absence of the cylinder; h_c/h_w=0.083 and 0.167 correspond to attenuated cases in presence of the cylinder.

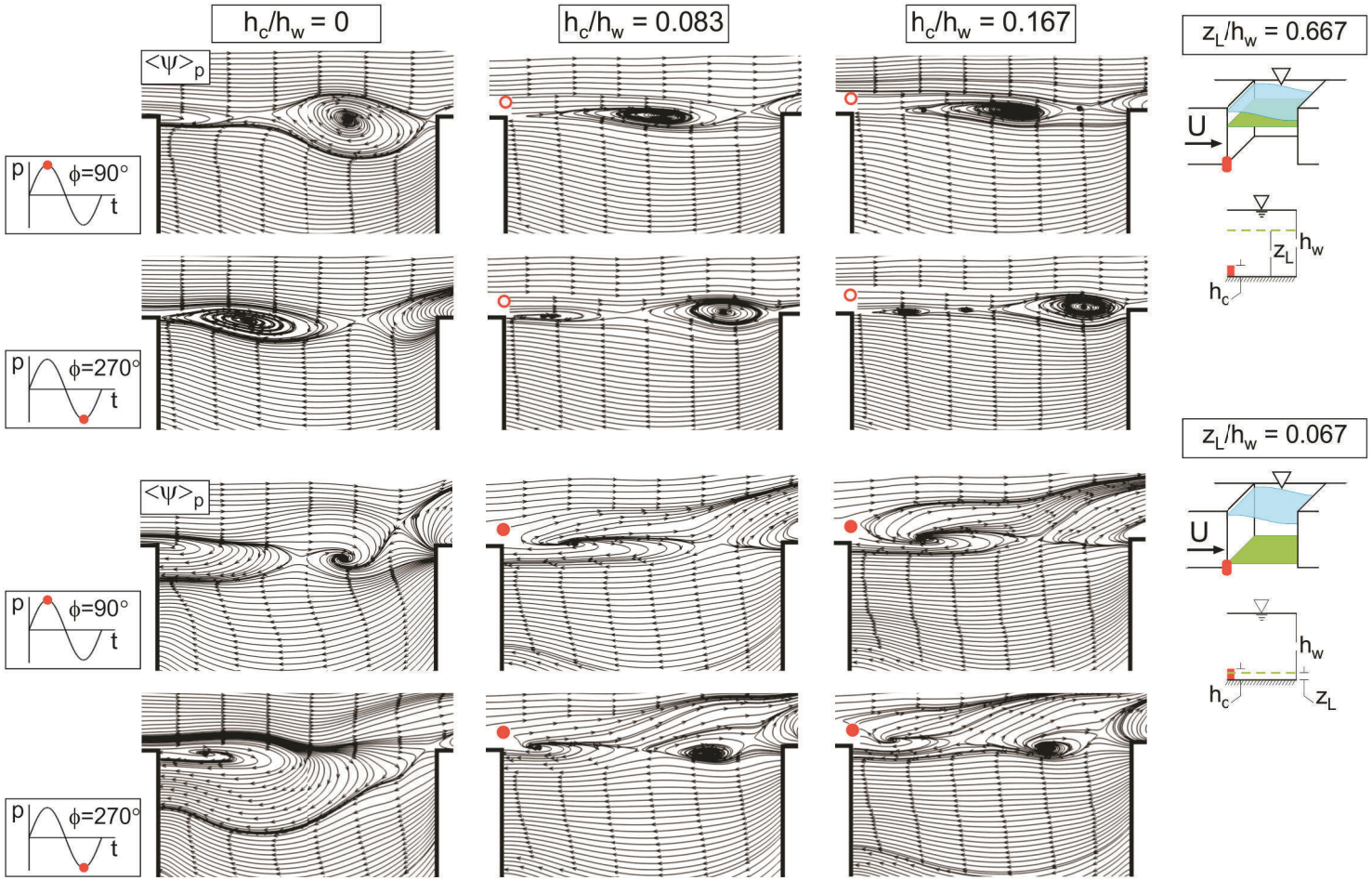

Figure 4.12: Patterns of phase-averaged streamlines $\langle\psi\rangle_p$ in a reference frame moving at $0.5U_r$ where U_r is the free stream velocity at two different elevations: well above the bed ($z_L/h_w = 0.667$) and near the bed ($z_L/h_w = 0.067$) for two different phases $\phi = 90°$ and $270°$ of the oscillation cycle. Case $h_c/h_w = 0$ corresponds to the non-attenuated oscillation in absence of the cylinder; $h_c/h_w = 0.083$ and 0.167 correspond to attenuated cases in presence of the cylinder.

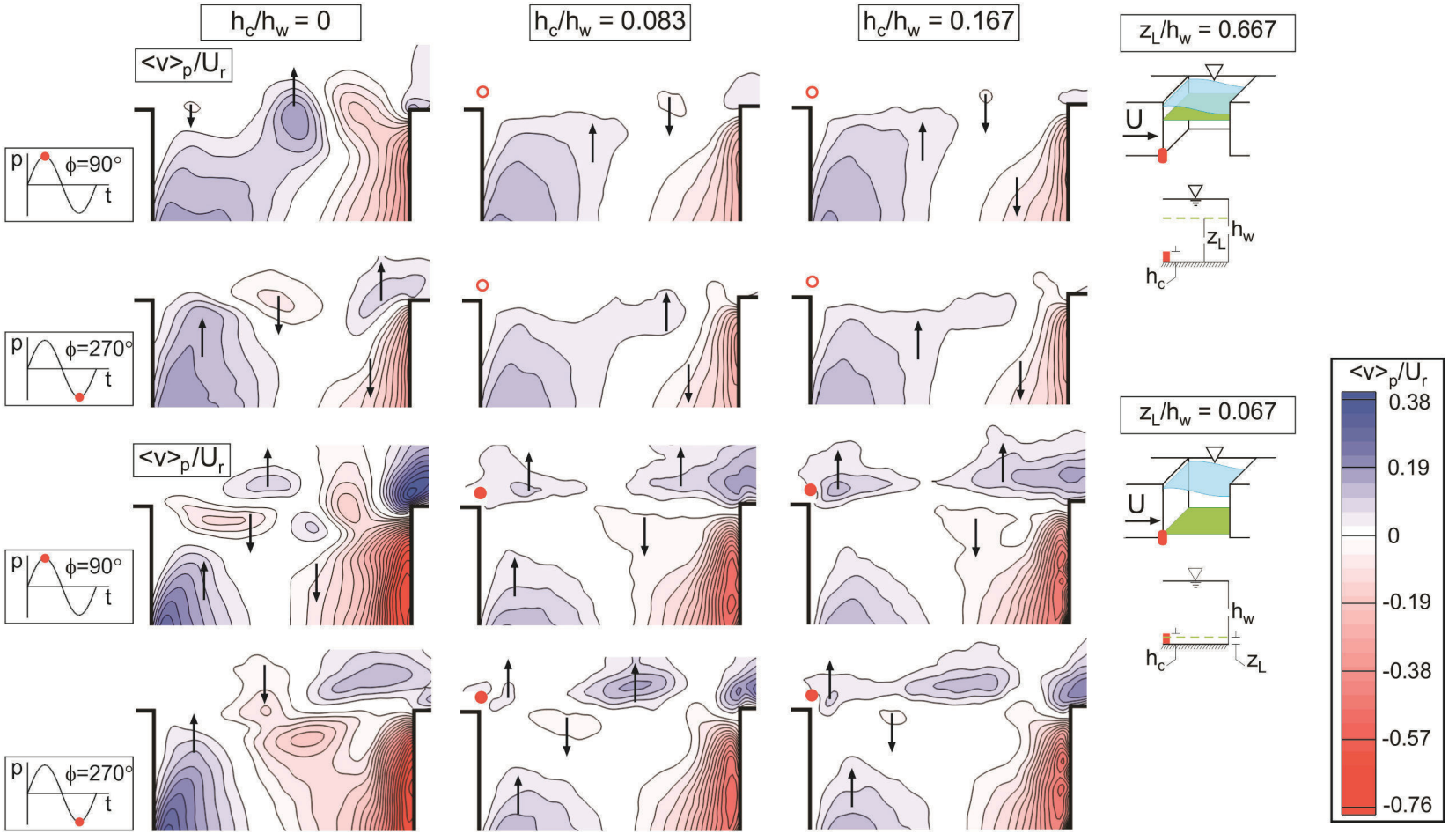

Figure 4.13: Patterns of phase-averaged transverse velocity $\langle v \rangle_p / U_r$ at two different elevations: well above the bed ($z_L/h_w = 0.667$) and near the bed ($z_L/h_w = 0.067$) for two different phases $\phi = 90°$ and $270°$ of the oscillation cycle. Case $h_c/h_w = 0$ corresponds to the non-attenuated oscillation in absence of the cylinder; $h_c/h_w = 0.083$ and 0.167 correspond to attenuated cases in presence of the cylinder.

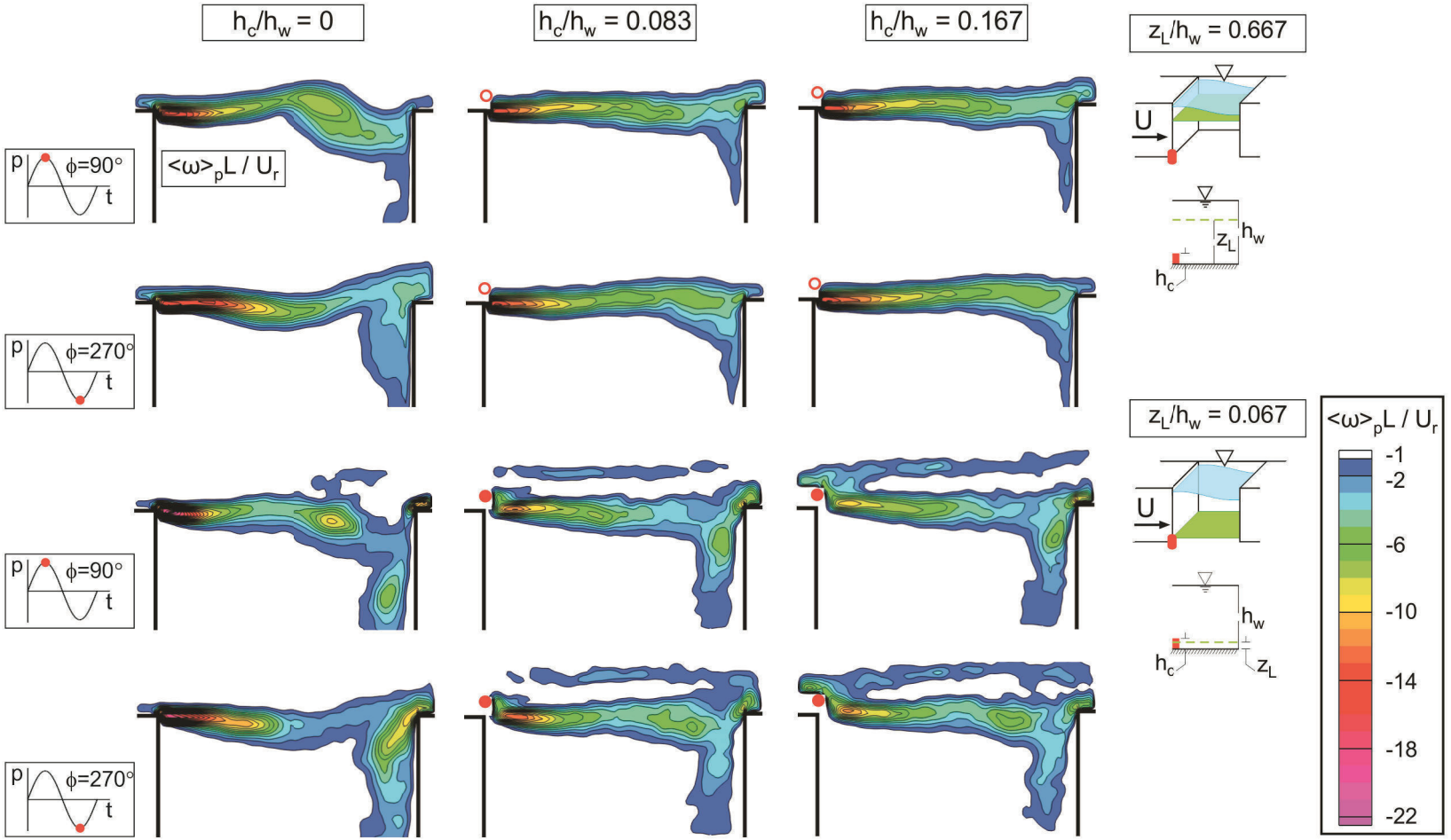

Figure 4.14: Patterns of phase-averaged vorticity $<\omega>_p L/U_r$ at two different elevations: well above the bed (z_L/h_w = 0.667) and near the bed (z_L/h_w = 0.067) for two different phases $\phi = 90°$ and 270° of the oscillation cycle. Case $h_c/h_w = 0$ corresponds to the non-attenuated oscillation in absence of the cylinder; h_c/h_w = 0.083 and 0.167 correspond to attenuated cases in presence of the cylinder.

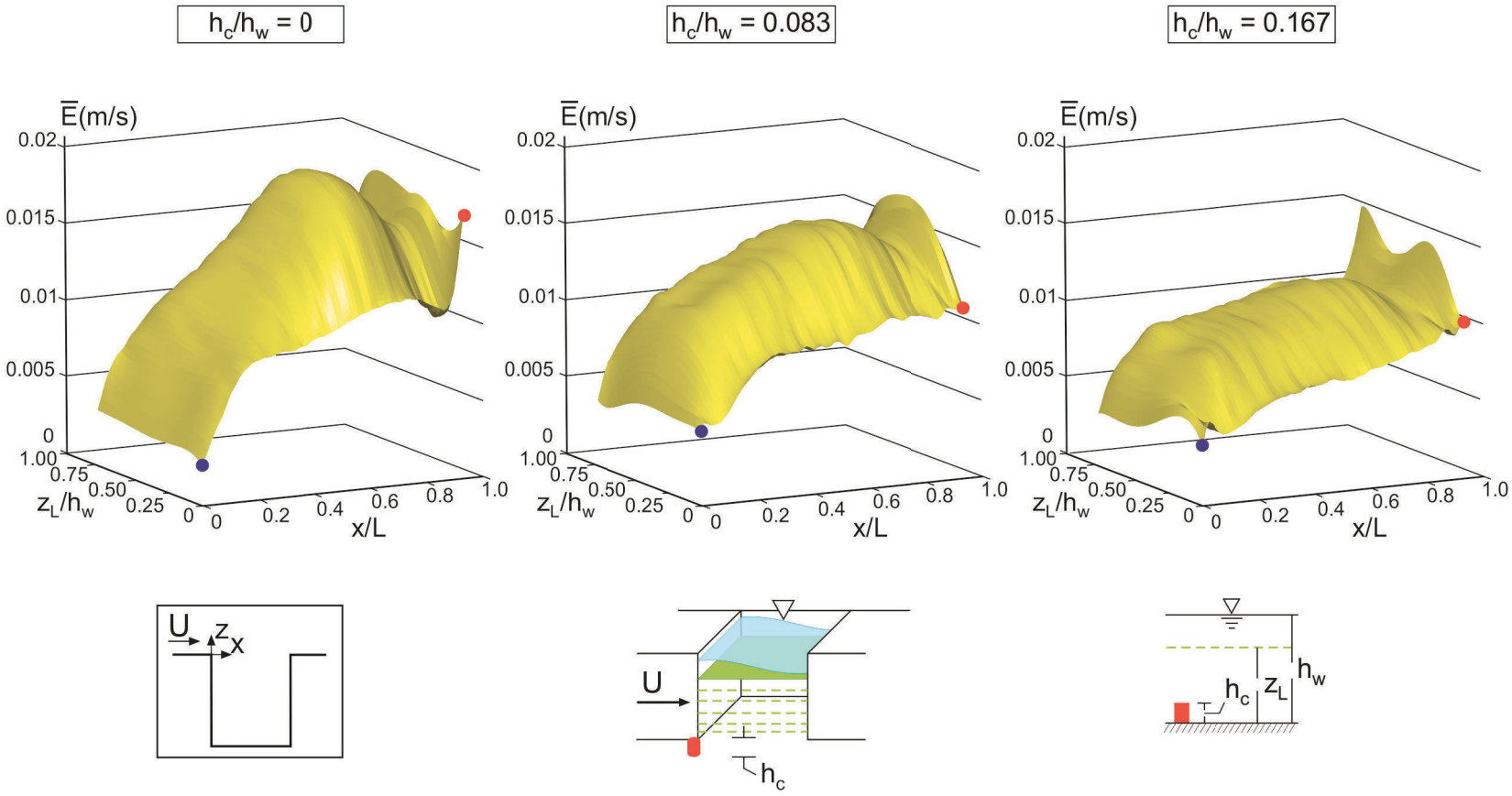

Figure 4.15: Patterns of time-averaged exchange velocity $\overline{E(t)}$ at different elevations z_L/h_w above the bed (bottom surface) for cases with and without the cylinder. Case $h_c/h_w = 0$ corresponds to the non-attenuated oscillation in absence of the cylinder; $h_c/h_w = 0.083$ and 0.167 correspond to attenuated cases in presence of the cylinder. Blue point shows the leading edge of the cavity (x/L=0), and red point shows the trailing edge of the cavity (x/L=1).

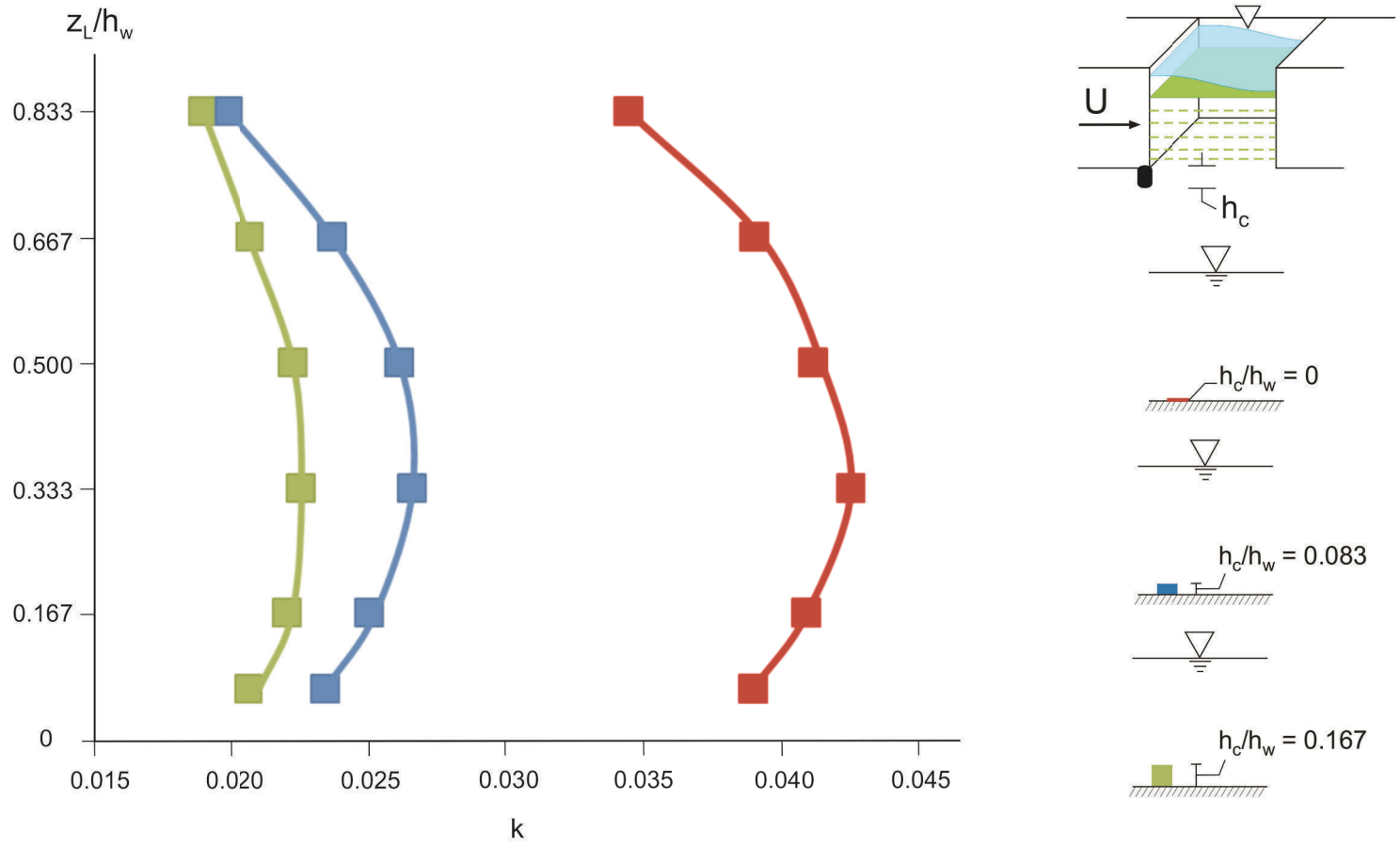

Figure 4.16: Patterns of time-averaged mass exchange coefficient k at different elevations z_L/h_w above the bed (bottom surface) for cases with and without the cylinder. Case $h_c/h_w = 0$ (red) corresponds to the non-attenuated oscillation in absence of the cylinder; $h_c/h_w = 0.083$ (blue) and 0.167 (green) correspond to attenuated cases in presence of the cylinder.

CHAPTER 5

SELF-SUSTAINED OSCILLATIONS OF SHALLOW FLOW PAST SEQUENTIAL CAVITIES

In this chapter, shallow flow past successive cavities is characterized via a technique of high-image-density particle image velocimetry. Highly coherent, self-sustained oscillations arise due to coupling between: the inherent instability of the separated shear layer along the opening of each sequential cavity; and a gravity standing wave mode within each cavity. The globally coupled nature of the flow structure is evident in dominance of the same spectral component in the undulating vorticity layers along each of the successive cavities and the wall pressure fluctuations within the cavities. Unlike coupled phenomena associated with flow past single cavity, optimal coupling for successive cavities requires a defined phase shift between the gravity standing wave patterns in adjacent cavities and, furthermore, an overall phase shift of the undulating shear layer along the cavity openings. The magnitudes of these phase shifts depend on the mode of the gravity standing wave in each cavity, i.e., longitudinal or transverse mode, which is respectively aligned with or normal to the main stream. Such phase shifts result in corresponding displacements of patterns of phase-referenced vorticity

concentrations along the cavity openings and change in timing of impingement of these concentrations upon the downstream corners of successive cavities. All of the foregoing aspects are related to the unsteady recirculation flow within the cavity, the time-dependent streamline topology, and concentrations of Reynolds stress along the cavity opening.

5.1 LITERATURE REVIEW

Turbulent shallow flows in estuaries, lakes, coastal areas of seas/oceans, and rivers can exhibit instabilities in the horizontal plane. Such instabilities have length scales that are much larger than the water depth. A feature of shallow flows is the presence of a shear-supporting bottom surface (bed) and a free surface. Both boundaries suppress vertical motions and restrict the length scale L_T of the three-dimensional turbulence, which is of the order or less than the water depth h_w, i.e., $L_T \leq h_w$. On the other hand, as described by Jirka and Uijttewaal (2004), the characteristic diameter D of two-dimensional turbulent vortical structures in the horizontal plane is much larger than the water depth, that is, $D >> h_w$. Uijttewaal and Tukker (1998) concluded that the turbulence in shallow flows can be considered as quasi two-dimensional.

In recent decades, a number of researchers have addressed the flow patterns in rivers in presence of groyne fields, dead-zones, or embayments, which have important consequences for sediment transport, dispersion of pollutants, erosion, and maintenance of aquatic life. Shallow river flow past two consecutive groynes

that form a cavity is a representative example of a shallow mixing layer having a finite streamwise extent. In the field, a succession of groynes typically occurs, thereby forming a succession of cavities. The primary aim of this investigation is to determine the flow physics and exchange processes for successive cavities.

5.1.1 Instability of a shallow mixing layer

Laboratory investigations, as well as numerical simulations and analyses, have resulted in substantial advances in our understanding of shallow mixing layers. Jirka (2001) defined various generation mechanisms for two-dimensional turbulent coherent structures in shallow flows, which have an important role in the mass and momentum exchange processes between the main river flow and the groyne field. Uijttewaal (2011) assessed several mechanisms that govern the exchange of mass and momentum in shallow mixing layers. According to the experiments of Bian et al. (2011), large-scale vortices form from roll-up of the separated turbulent layer, and these vortices interact with the recirculating flow within the cavity. Different approaches to modelling the growth of shallow mixing layers were developed by Babarutsi and Chu (1993, 1998), Booij and Tukker (2001), van Prooijen and Uijttewaal (2002), and Biron et al. (2004). Tukker and Booij (1996), Uijttewaal and Booij (2000), and Uijttewaal et al. (2001) analyzed the effect of water depth on shallow mixing layers; it influenced the development of large-scale coherent structures. An established feature of all these models and analyses is reduction of the rate of growth of a mixing layer by bottom friction.

Alavian and Chu (1985) addressed the stability of turbulent exchange flow in a shallow compound channel and numerically determined neutral stability curves. Chu and Babarutsi (1988) experimentally studied the effect of bed friction on a shallow mixing layer. In addition, they carried out a corresponding instability analysis. As mentioned previously in Section 1.3, a bed-friction number, i.e., stability parameter S was defined as $S = \overline{c_f}\,\delta\,\overline{U}/2h_w\Delta U$, where $\overline{c_f}$ is the bed friction coefficient, δ is the width of the transverse shear flow, $\overline{U}$ denotes the average velocity across the shear layer, ΔU is the corresponding velocity difference across the layer, and h_w is the water depth. They found the critical value to be S_{cr} = 0.09; below this threshold, bed friction could not stabilize the flow. Babarutsi et al. (1989) and Babarutsi and Chu (1991b) experimentally characterized mixing in shallow recirculating flows, and showed a reduction in transverse mixing due to bed friction. Chu et al. (1991) investigated channel flow with floodplains which created a shallow mixing layer due to the different values of bottom friction in the transverse direction; for this configuration, the critical value was S_{cr} = 0.12.

Socolofsky and Jirka (2004) employed the rigid-lid assumption in their linear stability analysis to determine critical values of the bed-friction parameter. They found that the onset of instability was enhanced due to the large velocity gradient across the mixing layer, and these instabilities resulted in large-scale coherent structures, which had a remarkable role in the exchange processes. The accuracy of the rigid-lid assumption for stability analyses of shallow flows was analyzed by Kolyshkin and Ghidaoui (2003) and Nazarovs (2005). The error in

using the rigid-lid assumption was small for small values of Froude number Fr, and it became larger when $Fr > 1$. Kolyshkin and Ghidaoui (2002) carried out an assessment of the effect of Froude number on the stability of shallow mixing layers in compound and composite channels. They reported that one can employ the rigid-lid assumption within 10% error in the regime $0 < Fr < 0.7$ when determining the critical values of the stability parameter S, i.e., the bed-friction number.

5.1.2 Shallow flow past a single cavity

In recent years, a number of researchers, such as Engelhardt et al. (2004), Ribi et al. (2010), and Fujihara et al. (2011), have analyzed the ecological value of irrigation channels and rivers with groyne fields or embayments. Experimental and numerical studies have been conducted to reveal the flow physics within these configurations. Weitbrecht and Jirka (2001) and Kurzke et al. (2002) experimentally investigated the effects of a groyne field on the flow patterns in rivers and the associated exchange processes. According to their results, large-scale coherent structures played important roles in the momentum and mass exchange processes. This phenomenon was also indicated in the numerical study of McCoy et al. (2007). Mizumura and Yamasaka (2002) and Riviere et al. (2010) studied the recirculation flow patterns in a groyne field, and showed that the depth of the shallow water layer, main stream velocity, and the aspect ratio of the groyne field affected the flow patterns. Uijttewaal (2005) and Kang et al. (2012) revealed the effects of geometry of the groyne field on the flow patterns and exchange processes. More recently, Sanjou and Nezu (2013) conducted an experimental

study to examine the change in the flow structure inside the groyne field by varying the bed slope. In their experiments, the turbulence characteristics of the shear layer at the interface between the groyne field and the main stream, as well as the recirculating flow pattern inside the groyne field, showed different features at different values of bed slope. They further noted that the mass exchange velocity between the main stream and the groyne field increased in accord with large magnitudes of Reynolds stress in the separated shear layer.

The enhancement of turbulent Reynolds stresses in the shear layer was related to the onset of a longitudinal gravity standing wave within the cavity in the studies of Wolfinger et al. (2012) and Tuna et al. (2013). Field experiments of Kimura and Hosoda (1997), Ikeda et al. (1999), Nezu and Onitsuka (2002), Ohmoto et al. (2005), and Kadotani et al. (2008) showed water-surface oscillation inside a cavity-like geometry, i.e., a groyne field, dead-zone, or embayment. Such fluctuations may have been due to coupling between the inherent instability of the separated shear layer along the cavity opening and the gravity standing wave mode within the cavity, but this concept was not addressed.

5.1.3 Shallow flow past a series of cavities

The foregoing investigations of flow past a single groyne field, an embayment, or a cavity have provided valuable insight into the flow structure and associated exchange processes. A number of investigations have revealed the flow patterns past a series of groynes. Sukhodolov et al. (2002, 2004) conducted field

work on the Elbe River in Germany in order to establish the velocity and the turbulence patterns inside the groyne fields. They reported that the patterns of recirculation flow did not significantly change with the downstream location. A computational study by Ercan and Younis (2009) on the Sacramento River, which simulated bank erosion in the presence of a series of cavities, showed important effects of the flow patterns.

In addition to field work, laboratory investigations and analyses have been carried out both numerically and experimentally. Wallast et al. (1999) and Uijttewaal et al. (2001) visualized the flow past a series of groyne fields and used dye to give insight into the mass exchange process. Both studies indicated that the structure of the shear layer between the groyne fields and the main stream varied with downstream position, but their interpretations of the mass exchange process were different. Wallast et al. (1999) observed a decrease in the mass exchange coefficient with downstream location within the multiple groyne fields, while Uijttewaal et al. (2001) noted that each groyne field showed essentially similar mass exchange characteristics regardless of the downstream position. Furthermore, Muto et al. (2000) conducted an experimental study with three successive square embayments, and their results demonstrated differences in strength of the recirculating flow inside each groyne field. Ohmoto et al. (2009) examined the effects of angle of the groynes on the flow structure in the presence of two successive groyne fields; oscillation of the free surface inside the groyne field was detected. Moreover, Yaeger and Duan (2010) quantitatively analyzed the effects of

orientation of dikes for a series of three dikes, i.e., two successive cavities, by using a micro acoustic Doppler velocimetry technique. A larger magnitude of Reynolds stress along the cavity opening was attained in the presence of angled dikes. More recently, the flow in the vicinity of the groynes was investigated by Yossef and de Vriend (2011) in order to assess sediment transport between the main stream and consecutive groyne fields. They concluded that the sediment transport process was dependent on large-scale coherent structures, and the structure of the mixing layer along the opening of the groyne field changed with the downstream location. In the computational studies of McCoy et al. (2008) and Constantinescu et al. (2009), the mass exchange process and the flow characteristics along a series of groyne fields were analyzed. Both studies used the rigid-lid assumption, where the free surface of the water was modeled as a rigid, horizontal boundary with slip. Constantinescu et al. (2009) found that the value of the mass exchange coefficient decreased with downstream location within the groyne field; this phenomenon was previously observed by Wallast et al. (1999). McCoy et al. (2008) indicate that a jet-like flow, parallel to the downstream groyne of each groyne field, was responsible for the momentum and the mass exchange processes between the main stream and the groyne fields.

5.1.4 Unresolved Issues

The foregoing investigations have yielded substantial advances in our understanding of shallow flow past sequential cavities. A major unresolved issue is, however, the effect of gravity standing waves within the cavities, their coupling

with vortex initiation and development along the openings of the cavities, and the manner in which this coupling influences the time-dependent and time-averaged flow patterns. More specifically, the orientation of, and phase shift between, gravity standing waves in successive cavities, as well as the phase variations in the separated shear layer along the openings of these cavities, are expected to exert a major influence. In turn, these effects will influence the mass exchange between the cavities and the mainstream. The present investigation addresses these characteristics using a technique of high-image-density particle image velocimetry combined with unsteady pressure measurements, in order to provide global representations of velocity, vorticity, and turbulence statistics.

5.2. EXPERIMENTAL SYSTEM AND TECHNIQUES

Experiments were conducted in a recirculating free-surface water channel. Upstream of the test section, the flow passes through a flow conditioning unit, which includes honeycombs and screens to yield a turbulence intensity of 0.2%. The main test section has a length of 4,877 mm, a width of 927 mm, and an adjustable depth of 610 mm. The goal of this investigation was to determine the flow structure along and within two successive cavities. A test-section insert was designed and constructed in order to allow the control of the water depth, the dimensions of cavities, and the flow velocity. Detailed schematics of the experimental system are given in Figure 5.1, which indicates two perspectives of the experimental facility.

For all experiments described herein, each cavity had a length of L = 152 mm and a width of W = 228 mm. The nominal water level was adjusted to a value of h_w = 38 mm, and the width of the channel was W_e = 470 mm as shown in Figure 5.1. The streamwise length of the shallow water layer, i.e., the distance from the leading edge of the horizontal raised (plexiglass) plate to the leading (upstream) corner of the cavity was L_i = 1,908 mm. Thus, the ratio of the inflow length L_i to water depth h_w was L_i/h_w = 50.1, which corresponds to the criterion of Uijttewaal et al. (2001) for a fully developed turbulent flow. Full details of the experimental system are given in the work of Tuna et al. (2013), which focused on shallow flow past a single cavity.

The onset of hydrodynamic and gravitational instabilities in free-surface (shear free) shallow water flows was identified by Ghidaoui and Kolyshkin (1999), and their criterion for these instabilities is determined by Froude number $U/(gh_w)^{1/2}$. The flow is free of gravitational instabilities below the critical Froude number, i.e., $Fr < 1$. In the present configuration, the corresponding values of Froude number based on the water depth h_w = 38 mm and the depth-averaged inflow velocities U = 273 mm/s and 475 mm/s corresponding to resonant response were respectively Fr = 0.45 to Fr = 0.71. These values of Froude number are therefore in the subcritical range and gravitational instabilities do not have a significant role. Furthermore, values of Reynolds number Re based on the width W of the inflow channel were Re_W = 1.28 x 10^5 and 2.03 x 10^5; based on the water depth h_w, Re_{hw} = 1.04 x 10^4 and Re_{hw} = 1.64 x 10^4.

Chu and Babarutsi (1988) experimentally investigated the transverse development of the shallow mixing layer in an open channel flow, and determined the stability of shallow mixing layers in terms of a dimensionless stability parameter *S*. As mentioned previously, it is defined as $S = \overline{c_f}\,\delta\,\overline{U}/2h_w\Delta U$. The bed friction coefficient $\overline{c_f}$ was calculated with their correlation $\frac{1}{\sqrt{\overline{c_f}}} = -4log\left(\frac{1.25}{Re\sqrt{\overline{c_f}}}\right)$, and the shear layer thickness δ was determined via the velocity field data from particle image velocimetry (PIV). The values of the stability parameter *S* determined herein are S = 0.007 for the transverse mode of the gravity standing wave and S = 0.004 for the longitudinal mode (streamwise-oriented) of the gravity standing wave; they are of the same order as those determined in the experiments of Chu and Babarutsi (1988). Furthermore, these values of *S* are below the critical stability parameter range S_{cr} = 0.01 to 0.1 determined by Kolyshkin and Ghidaoui (2002). They concluded that bed friction does not stabilize the flow below these critical values S_{cr}, and instabilities occur due to the destabilizing effect of the velocity difference ΔU across the shear layer.

The resonant frequency of the experimentally-observed gravity standing wave in each of the cavities shown in Figure 5.1 is calculated as follows. The eigenfrequency f_n of the fundamental eigenmode for a one-dimensional gravity standing wave pattern oriented in the transverse direction, corresponding to open and closed end conditions, is given by Naudascher and Rockwell (1994):

$$f_n = \frac{\sqrt{g h_w}}{4W} \tag{5.1}$$

in which W is the cavity width, h_w is the water depth, g is the gravitational acceleration, and f_n is the frequency of the oscillation. The predicted frequency of this mode is calculated by using Equation 5.1 as f_n = 0.66 Hz; it compares well with the experimentally determined value of f_n = 0.63 Hz. On the other hand, the eigenfrequency of the fundamental eigenmode for a one-dimensional gravity standing wave oriented in the longitudinal direction, corresponding to a closed-closed end conditions is:

$$f_n = \frac{\sqrt{g h_w}}{2L} \tag{5.2}$$

in which L is the cavity length. The theoretically calculated value using Equation 5.2 is f_n = 2.00 Hz, which compares well with the experimental frequency of f_n = 1.96 Hz. These self-excited transverse and longitudinal modes of the gravity standing waves within each of the cavities corresponded to amplitudes h_d of the free-surface deflection that were an order of magnitude smaller than the nominal water depth h_w, i.e., h_d / h_w = 0.094 and h_d / h_w = 0.049.

A technique of high-image-density particle image velocimetry (PIV) led to quantitative determination of the flow patterns along and within the cavities. The major components of this system are indicated in Figure 5.1. The laser sheet of 1 mm thickness was positioned at mid-depth, that is, midway between the nominal elevation h_w of the free-surface and the bed (z_L/h_w = 0.500). Also, the regions close

to the bed (z_L/h_w = 0.067) and near the free-surface (z_L/h_w = 0.833) are investigated. Complete set of images associated with the phase-averaged flow patterns at these elevations z_L/h_w = 0.067 and 0.833 are given in Appendix C. This laser sheet was generated by a dual pulsed Nd: Yag laser system having a maximum output of 90 mJ/pulse. A digital charge-coupled device (CCD) sensor camera with an array of 1,600 pixels x 1,192 pixels was placed below the water channel orthogonal to the horizontal plane of the laser sheet, as shown in the side view of Figure 5.1. The aforementioned double-pulsed laser and camera were triggered by a synchronizer. The framing rate of the camera was 30 frames per second, which gave 15 sets of image pairs per second. The patterns of particle images were processed using a frame-to-frame cross-correlation technique, and an overlap of 50% was used in accord with the Nyquist criterion. This technique resulted in 7,227 vectors with an effective grid size of 3.7 mm. The estimated uncertainties of the streamwise and transverse velocity measurements, which were calculated using the scheme of Adrian and Westerweel (2010), were 2% of the depth-averaged free stream velocity U.

PCB piezoelectric pressure transducers (model number 106B50) were employed for unsteady pressure measurements at five different locations. The pressure transducer p_5 is located at the impingement corner of the trailing (downstream) cavity at an elevation of h_p = 13 mm, as indicated in Figure 5.1, in order to determine the frequency and amplitude of the shear layer oscillations. The pressure transducers $p_{1\text{-}4}$ were located at the back side of the cavity at a location 5

mm from the edges at an elevation of h_p = 13 mm from the bed (bottom surface). They were used to determine the phase shift between the oscillations in adjacent cavities. The unsteady pressure p_4 at the back wall of the cavity, as indicated in the plan view in Figure 5.1, served as a reference signal in the phase-referencing process. These transducers have a nominal sensitivity of 72.5 mV/kPa. To adjust the gain of the transducer, the pressure transducers were connected to a PCB Piezotronics Sensor Signal conditioner (model number 481A), which also employed a low-pass analog filter at a cutoff frequency of 10 Hz. The conditioned analog pressure signals were converted to digital format by a PCI-MIO-16E-4 multi-channel data acquisition board from National Instruments. For the pressure analyses, the sampling rate was set to 20 samples per second, corresponding to a Nyquist frequency of 10 Hz, which was well above the typical maximum frequency of interest in the present study. Sampling was conducted over a time span of 102.4 s, corresponding to a total of 2,048 samples. Ten of these time records were acquired for each inflow velocity. Furthermore, in order to allow phase referencing during the PIV experiments, a sampling rate of 20 kS/s was selected.

As described in Section 2.5, the unsteady pressure p_4 in the cavity and the Q-Switch synch out signal of the laser were used to determine the phase of the flow structure in the oscillation cycle. The size of the phase window at a nominal value of phase was 10 degrees, where the complete oscillation cycle corresponded to 360 degrees. For each set of PIV experiments, 200 sets of images were recorded simultaneously with the pressure signal. A total of 15 sets of experiments were

conducted, and 3,000 sets of images were recorded. The time-averaged flow structure was evaluated by averaging 3,000 instantaneous velocity fields. The phase-referencing technique involved a minimum of 60 velocity fields per phase, which were used to determine the phase-averaged velocity, vorticity, and streamline topology.

5.3 STATES OF RESONANT RESPONSE: SPECTRA AND TURBULENCE STATISTICS

Figure 5.2 shows the amplitude response characteristics of the sequential cavities. This response is represented in Figure 5.2a by the dimensionless amplitude of the spectral peak of the unsteady pressure p, i.e., $S_p(f)_{max}/(1/2\rho U^2)$ as a function of U. As shown in the schematic of Figure 5.2a, the pressure $p_5(t)$ measured at the impingement corner of the trailing cavity is represented by the triangular symbol, and the pressure at the end of the trailing cavity $p_4(t)$ is designated by the square symbol. The peaks in the plots of Figure 5.2a are due to the successive onset of transverse and longitudinal modes of the gravity standing wave; coupling in these modes corresponds to the sharp spectral peaks in the spectra $S_p(f)$. It is evident that the transverse mode is associated with the largest magnitude of $S_p(f)_{max}/(1/2\rho U^2)$.

Figure 5.2b (left plot) shows the magnitude of the spectral peak $S_p(f)_{max}/(1/2\rho U^2)$ as a function of reduced velocity U/f_nL for the transverse-oriented gravity standing wave. The maximum spectral peak is attained at a value of $U/f_nL = 2.9$. It is apparent that the magnitude of the peak is consistently higher for

pressure p_4 at the end of the cavity; in this transverse mode, the standing gravity wave has its maximum amplitude at the closed end of the cavity, and its minimal amplitude at the open end. There is, however, an additional contribution at the open end, arising from unsteady impingement of the unstable, separated shear layer upon the trailing corner of cavity.

Figure 5.2b (right plot) gives the magnitude of the spectral peak $S_p(f)_{max}/(1/2\rho U^2)$ versus U/f_nL in presence of the longitudinal (streamwise-oriented) gravity standing wave. The maximum magnitude of the spectral peak occurs at the dimensionless flow velocity U/f_nL = 1.6. At all values of U/f_nL, the magnitudes of the spectral peaks $S_p(f)_{max}/(1/2\rho U^2)$ are consistently larger for the pressure p_5 at the impingement corner of the trailing cavity, relative to the value p_4 at the end of the cavity. For this longitudinal (streamwise-oriented) mode of the gravity standing wave, the maximum amplitudes occur along the faces of the corners and the faces of the partition wall located between the two cavities. This contribution from the standing wave, along with the contribution from the impingement of the unstable, separated shear layer upon the trailing corner, yields larger overall unsteady pressure amplitude, relative to p_4 at the end of the cavity.

Figure 5.3 shows spectra of the pressure fluctuation at the end of each cavity for the transverse and longitudinal modes of the gravity standing wave, corresponding respectively to values of reduced velocity U/f_nL = 2.9 and 1.6. The plot on the left shows the spectral response of the fluctuating pressure p_2 in the leading cavity, and the one on the right corresponds to the fluctuating pressure p_4 in

the trailing cavity. It is apparent from the graphs that the frequencies of the transverse (f_n = 0.63 Hz) and longitudinal (f_n = 1.96 Hz) modes of the gravity standing wave are the same in the leading and trailing cavities, i.e., the frequency of the coupled oscillations is the same regardless of which cavity is considered. However, the amplitudes of the coupled oscillations are detectably different in the leading and trailing cavities. The magnitude of the spectral peak $S_p(f)_{max}/(1/2\rho U^2)$ for the transverse mode is 15% larger in the trailing (downstream) cavity, and for the longitudinal mode, it is 7% larger in the trailing cavity.

Figures 5.2 and 5.3, described in the foregoing, show two resonant states arising from coupling between the unsteady shear layer along the cavity and a gravity standing wave mode within the cavity; one state involves the transverse mode and the other involves the longitudinal (streamwise-oriented) mode of the gravity standing wave. In these resonant states, the spectra S_v/U of the transverse v component of the velocity fluctuation in the unsteady separated shear layer along the opening (y = 0) of each cavity have the forms indicated in Figure 5.4. Irrespective of whether the transverse or longitudinal mode is considered, and for both the leading and trailing cavities, sharply-defined spectral peaks are evident. However, the maximum value of the spectral peak S_v/U is significantly larger for the transverse mode of the gravity standing wave. For both the transverse and longitudinal modes, however, the spectral peaks have significant amplitudes and are at the same frequency for both of the cavities, thereby indicating that the oscillation of the two cavity system is a globally coupled phenomenon.

Figure 5.5 shows an overview of the patterns of: root-mean-square of the streamwise (longitudinal) velocity fluctuation u_{rms}/U (top row) and transverse (vertical) velocity fluctuation v_{rms}/U (middle row); in addition, patterns of Reynolds shear stress $<u'v'>/U^2$ (bottom row) are given. For the case of the transverse-oriented gravity standing wave, represented by the images in the left column of Figure 5.5, it is evident that the spatial extent and the peak magnitude of each of the aforementioned turbulence quantities are larger for the trailing cavity of the two cavity system. To be sure, substantial amplitudes occur along the leading cavity. A further distinction is that the regions of highest (dark red) magnitude tend to occur in the upstream region of the separated shear layer of the trailing cavity. Regarding the longitudinal (streamwise-oriented) gravity standing wave, the corresponding images in the right column of Figure 5.5 indicate significantly lower amplitudes along the shear layers of both the leading and trailing cavities. The associated fluctuations for both the transverse and longitudinal cases of Figure 5.5 show well defined concentrations, which are different in magnitude, as evidenced by the velocity spectra of Figure 5.4.

5.4 TIME-AVERAGED FLOW STRUCTURE

Figure 5.6 provides time-averaged representations of the flow structure. In Figure 5.6a, contours of time-averaged vorticity $<\omega>L/U$ indicate a wide extent of $<\omega>L/U$, which is consistent with the large magnitudes of the turbulence quantities u_{rms}/U, v_{rms}/U, and $<u'v'>/U^2$ in presence of the transverse mode of the gravity

standing wave given in Figure 5.5. Moreover, when the longitudinal (streamwise-oriented) gravity standing wave exists, as shown in Figure 5.6b, the width of the vorticity layer $<\omega>L/U$ is substantially diminished. The rate of attenuation of high levels of $<\omega>L/U$ in the streamwise direction is also of interest. For the longitudinal mode of the standing wave, the (yellow) region that indicates a high level of vorticity $<\omega>L/U$ extends well downstream towards the impingement region of each cavity. On the other hand, for the transverse mode of the gravity standing wave, the high levels (yellow colors) of $<\omega>L/U$ are rapidly attenuated in the streamwise direction. It is therefore evident that the magnitudes of the aforementioned turbulent stresses in the separated shear layer along the cavity opening are directly correlated to both the rate of degradation of peak vorticity and increase of width of the time-averaged vorticity layer.

Figures 5.6c and 5.6d show contours of constant time-averaged transverse velocity $<v>/U$. Blue contours indicate outward-oriented transverse flow, i.e., flow towards the opening of the cavity, and red contours indicate inward-oriented flow, that is, into the cavity. Larger magnitude, outward-oriented (dark blue) flow and inward-oriented (dark red) flow occurs for the transverse mode (Figure 5.6c), relative to the longitudinal mode (Figure 5.6d), and thereby signifying enhanced recirculation flow within the cavity for the transverse mode. A further, common feature of both cases is the existence of a localized region of outward-oriented flow at the upstream corner of the splitter plate, i.e., impingement corner of the leading cavity. However, the scale of this localized region decreases in presence of the

longitudinal gravity standing wave. Consideration of this localized blue cluster in conjunction with the red contours along the upstream edge of the splitter plate (trailing edge of the leading cavity) suggests a stagnation point near the upstream corner of the splitter plate, i.e., the impingement corner of the leading cavity.

Figures 5.6e and 5.6f show patterns of time-averaged streamlines $<\psi>$. Both of these patterns show existence of a stagnation streamline, which emanates from the upstream corners of the leading and trailing cavities and impinges on the respective downstream corners. Remarkably, the general form of the streamline patterns is very similar for the cases of transverse and longitudinal modes of the gravity standing waves within the cavities and, furthermore, for both the leading- and trailing-cavities in a given mode. Immediately exterior to the region surrounding the foci (centers) of the streamline patterns, the streamline pattern spirals outward in all cases.

5.5 PHASE-AVERAGED FLOW STRUCTURE

An understanding of the origin of the strongly-coupled resonant states described in the foregoing requires consideration of the time sequence of patterns of the flow structure along and within the cavity, with particular attention to: (i) a favorable phase shift between the standing waves that occur in the leading and trailing cavities of the two cavity system; and (ii) an overall phase shift of the transverse undulations of the separated shear layer along the opening of each cavity as well as along the entire extent of the system of successive cavities. In the

following, the phase shift between the gravity standing waves in adjacent cavities is first addressed, followed by the phase shift along the separated shear layer.

Highly coherent oscillations of the nominally turbulent shallow flow past the sequence of cavities are attainable through coupling with gravity standing wave modes within the cavities. The gravity standing wave mode that exists within a given cavity, and its phase relationship to the mode in the adjacent cavity, are central to determining if a self-excited coherent oscillation occurs. Figure 5.7 shows the admissible modes and phase relationships of the gravity standing wave systems, which were determined during self-sustained oscillations from multiple pressure measurements on the walls of the cavities, at the locations (p_1, p_2, p_3, p_4) indicated in Figure 5.1. The elevation of the free surface above the bed (bottom surface), that is, the water depth, is designated by shades of red and blue, where red indicates a water depth larger than the nominal water depth h_w, and blue corresponds to a depth smaller than the nominal value h_w. The vertical displacement h_d corresponds to the amplitude of the free surface oscillation within the cavity, and the extreme amplitudes are designated as $h_w \pm h_d$. For both sets of schematics shown in Figure 5.7, the instantaneous elevation of the free surface is shown at a defined time t and a later time $t + T_w/2$, in which T_w is the period of oscillation of the gravity standing wave. The plots of h_w versus t in Figure 5.7 illustrate the time history of free surface elevation over two oscillation periods, i.e., $2T_w$. In these plots, the solid and dashed lines correspond respectively to the time-dependent elevations of the free-surface in the leading and trailing cavities.

The top row of schematics of Figure 5.7 shows the existence of a transverse gravity standing wave in each cavity; these gravity standing waves are shifted by a phase angle of π (180°). At the instants of time t and $t + T_w/2$, the gravity standing wave in the trailing cavity is shifted by π with respect to the gravity standing wave in the leading cavity. This phase difference of π is, of course, maintained for all values of t as shown in the graph. For the images shown in the top row of Figure 5.7, the (red) free surface elevation in the leading cavity at time t is larger than the nominal elevation h_w of the free surface, while at time $t + T_w/2$ the (blue) free surface elevation in the leading cavity is smaller than the nominal elevation of h_w.

The bottom row of schematics represents the gravity standing waves in the longitudinal (streamwise-oriented) mode in both sequential cavities; they are shifted with respect to each other by $\pi/2$, that is, the phase angle between them is 90°. At time t, in the region along the left boundary of the leading cavity, the elevation (blue) of the free-surface is smaller than the nominal elevation h_w. At time $t + T_w/2$, this same region of the free surface has an elevation (red) greater than the nominal depth h_w. At both instants of time, the elevation of the free surface in the trailing cavity is approximately at the nominal elevation h_w, which shows the $\pi/2$ phase shift of the gravity standing wave between two cavities.

The foregoing patterns of phase shifted gravity standing waves in successive cavities coexist with the separated vorticity layers along the openings of the cavities. Figures 5.8a and 5.8b show patterns of phase-averaged vorticity

$<\omega>_p L/U$ for the transverse and longitudinal modes of the gravity standing waves. By comparison of images at a given phase, it is possible to determine common features of the vortical structures in the separated shear layers. Clusters of phase-averaged vorticity are labeled as *A*, *B*, *C*, and *D*. In Figure 5.8a, at $\phi = 0°$, the clusters of $<\omega>_p L/U$ in the leading and trailing cavities are labeled as *A* and *B*. Similar clusters of vorticity can be identified at $\phi = 180°$; however, at this value of ϕ, cluster *B* is in the leading cavity and cluster *A* is in the trailing cavity as a result of π phase shift between the gravity standing waves in the leading and trailing cavities. A similar comparison can be done at the oscillation phases of $\phi = 90°$ and 270°; where clusters of phase-averaged vorticity are labeled as *C* and *D*. On the other hand, in Figure 5.8b, like clusters of vorticity occur at different phases. At $\phi = 180°$, the vorticity cluster along the leading cavity is labeled as *C*. A similar cluster *C* is evident along the trailing cavity at $\phi = 270°$, due, of course, to the $\pi/2$ phase shift between leading and trailing cavities. This phase shift can also be seen by comparing clusters of vorticity *A*, *B*, and *D* at different phase angles ϕ of the oscillation.

Furthermore, it is possible to determine the consequence of different orientations of the gravity standing wave on the patterns of Reynolds stress correlation $<u'v'>/U^2$ in Figure 5.5 by cross comparison of the patterns of phase-averaged vorticity in Figures 5.8a and 5.8b. For the transverse mode of the gravity standing wave in Figure 5.8a, large-amplitude transverse excursions of the vorticity

layer occur over an oscillation cycle. On the other hand, in Figure 5.8b for the longitudinal standing wave, the vorticity layer shows smaller amplitude transverse excursions about a nominal state. These observations are consistent with the patterns of Reynolds stress correlation $\langle u'v' \rangle / U^2$ given in Figure 5.5.

Another crucial element of the resonant, self-sustained oscillations described in the foregoing is the transverse undulation of the separated vorticity layer along the opening of the cavity, represented by the transverse velocity component v(t). Its streamwise phase variation $\Phi_v(x)$ is central to determination of the phase speed and wavelength. Figure 5.9 shows the streamwise phase variation $[\Phi_v-(\Phi_v)_0]/\pi$, in which $(\Phi_v)_0$ is the phase angle at the separation corner. Two paths were employed for evaluation of $[\Phi_v-(\Phi_v)_0]/\pi$: along a horizontal line at an elevation of y/L = 0.08 (circular symbols) above the leading corner of the sequential cavity configuration; and along a line at the edge of the time-averaged velocity distribution where $\langle u \rangle / U$ = 0.9 (square symbols). Also shown is a representative image of contours of constant vorticity at a selected instant during the oscillation cycle. For the case of the gravity standing wave oriented in the transverse direction, represented by the top plot, the value of $[\Phi_v-(\Phi_v)_0]/\pi$ increases with streamwise distance $x/2L$. Particularly remarkable is that the overall phase difference is $[\Phi_v-(\Phi_v)_0]/\pi \cong 2$ from the separation corner of the leading cavity at $x/2L$= 0 to the impingement corner of the trailing cavity at $x/2L$= 1. Deviations from an exact value of $[\Phi_v-(\Phi_v)_0]/\pi$ = 2 are due to the end condition at impingement, that is, distortion of the vorticity layer as it approaches the

impingement corner. Furthermore, the overall form of the pattern of vorticity, which extends over the leading and trailing cavities, mimics very closely formation of a single vortex. For the case of incompressible flow past a single cavity in absence of free-surface and gravity standing wave effects, it is known that formation of a single vortex along the cavity opening is associated with an overall phase difference along the separated vorticity layer of 2π (Knisely and Rockwell, 1982). In other words, due to the phase difference of π between the transverse gravity standing waves in the leading and trailing cavities of the transverse mode of Figure 5.9, and an overall phase difference of 2π of the undulating shear layer, it is possible to attain a vorticity layer resembling a single large-scale vortex, at least during a portion of the oscillation cycle, thereby mimicking the classical oscillation past a single cavity.

On the other hand, for the case of the longitudinal mode given in Figure 5.9, the overall phase difference is $[\Phi_v-(\Phi_v)_0]/\pi \cong 4$ from the separation corner of the leading cavity at $x/2L = 0$ to the impingement corner of the trailing cavity at $x/2L = 1$, with approximately 2π phase difference along the leading cavity and 2π phase difference along the trailing cavity. Such a phase difference of 2π along each of the cavities allows the oscillation along each cavity to be self-sustained. The corresponding vorticity image indicates an organized, undulating disturbance along each cavity. The structure of the vorticity layer is representative of a low amplitude undulating disturbance that apparently is reinforced through the

condition of a 2π phase shift between perturbations at the leading-edge of the leading cavity and the tip of the partition between the two cavities.

Physical interpretation of the overall phase difference of $2n\pi$, $n = 1, 2, ...$, in the streamwise direction in the undulating vorticity layer, described in the foregoing has been addressed for the case of a single cavity configuration, in absence of a free-surface, by Knisely and Rockwell (1982), Rockwell and Naudascher (1979), and Rockwell (1983). Upstream influence arising from impingement of the undulating vorticity layer upon the trailing (downstream) corner of the cavity induces vorticity fluctuations in the highly receptive region of shear layer separation at the leading (upstream) corner of the cavity. When the overall phase difference of the downstream traveling wave associated with the undulating vorticity layer has a value of $2n\pi$, $n = 1, 2, ...$, this effect of the upstream influence is reinforced to provide a self-sustaining feedback loop, and therefore a highly coherent oscillation. This same concept can be applied to the present case of sequential cavities, for both the foregoing cases of the transverse and longitudinal gravity standing waves.

Complementary insight into the cavity oscillations is provided in Figure 5.10; it shows the contours of constant phase-averaged transverse velocity $<v>_p/U$ over an oscillation cycle. The color red indicates a direction of transverse velocity oriented in the negative vertical direction, that is, into the cavity, whereas color blue indicates an orientation in the opposite direction. These patterns provide a

basis for interpretation of the flow structure associated with both the vorticity and non-vorticity bearing regions of the flow.

Consider first the transverse mode, i.e., the left column of images. In the first two rows of images of Figure 5.10, that is $\phi = 0°$ and 90°, outward oriented (blue contours) flow dominates along the mouth of the trailing cavity, and inward oriented (red contours) flow is prevalent along the mouth of the leading cavity. Due to the π phase shift between the leading and trailing cavities, these patterns are switched at larger values of phase angle ϕ of the oscillation. That is, if the patterns at $\phi = 90°$ and 270° are compared, the patterns of $\langle v \rangle_p / U$ are switched between the leading and trailing cavities. For example, the red and blue contour patterns appearing in the leading cavity at $\phi = 90°$ are located in the trailing cavity at $\phi = 270°$. Likewise, the contour patterns appearing in the trailing cavity at $\phi = 90°$ are approximately replicated in the leading cavity at $\phi = 270°$. The contributions to the patterns of $\langle v \rangle_p / U$ are from the motion of the inviscid gravity standing wave, vorticity bearing fluid in the large-scale recirculation zone within the cavity, as well as vorticity bearing fluid in the separated shear layer along the opening of the cavity. Despite these different contributions, the phase shift of π between the gravity standing waves in the leading and trailing cavities is maintained in the patterns of $\langle v \rangle_p / U$.

The longitudinal mode of the gravity standing wave is represented in the right column of Figure 5.10. The patterns of the gravity standing wave given in

Figure 5.7 indicate a phase shift of $\pi/2$ between the leading and trailing cavity, in absence of the vorticity field associated with the recirculation within the cavity and the separated layers along the cavity openings. This phase shift is reflected in the patterns of Figure 5.10. For example, the patterns of transverse velocity $<v>_p/U$ in the leading cavity at $\phi = 90°$, are very similar to those in and along the trailing cavity at $\phi = 180°$.

For both the transverse and longitudinal modes of the gravity standing wave, represented by the patterns in the left and right columns of Figure 5.10, well-defined red and blue concentrations exist along the cavity opening. Generally speaking, there is a correlation between the center of the vorticity concentrations given in Figures 5.8a and 5.8b and the location midway between the centers of a given pair of concentrations of $<v>_p/U$ in Figure 5.10. Moreover, these pairs of $<v>_p/U$ concentrations propagate downstream along the opening of a given cavity. In turn, this propagation (or phase) speed c_v/U is related to the streamwise variations of phase $[\Phi_v - (\Phi_v)_0]/\pi$ along the cavity opening, given in Figure 5.9. That is, $c_v/U = 2\pi f/(\partial\Phi/\partial x)U$. It is evident from the plots of $[\Phi_v-(\Phi_v)_0]/\pi$ given in Figure 5.9 that the variation of $[\Phi_v-(\Phi_v)_0]/\pi$ with $x/2L$ is nonlinear in the region immediately downstream of the separation corner of the leading cavity, that is, the slope of this curve is small, and thereby the phase speed will be correspondingly small. The averaged phase speed was calculated over the openings of the leading and trailing cavities, that is, extending from $x/2L = 0$ to 1. The values are

c_V/U = 0.70 and 0.63 respectively for the transverse and longitudinal wave systems within the cavities. In addition, it is possible to deduce the averaged wavelength λ/L along the leading and trailing cavities according to the relationship c_V/f. For the transverse and longitudinal modes of gravity standing wave, these values are respectively λ/L = 2 and 1, thereby reinforcing the observations in the foregoing that the transverse mode of the gravity standing wave is associated with approximately one wavelength extending over the openings of the leading and trailing cavities, and thereby the tendency to form a single large-scale vortex. On the other hand, for the case of the longitudinal modes within the leading and trailing cavities, one wavelength exists along each of the cavity.

Phase-averaged streamline $<\psi>_p$ patterns are given in Figure 5.11. It is evident that the magnitude of the undulation of the interface between the mainstream and the cavity is larger in presence of the transverse gravity standing waves, shown in the left column of images, relative to the longitudinal mode of the gravity standing waves, represented in the right column of images. Furthermore, for the transverse mode, the π phase shift between the oscillations of adjacent cavities is apparent. For example, at ϕ = 90° (second row), in the trailing cavity, the streamline patterns at the interface with the mainstream and in the recirculation zone exhibit similarity with the patterns in the leading cavity at ϕ = 270° (fourth row) due to the π phase shift between the transverse gravity standing waves in these cavities. Likewise, for the longitudinal gravity standing wave system (right column

of images), the deformation of the streamlines at the interface of the leading cavity at $\phi = 90°$ is similar to that along the downstream cavity at $\phi = 180°$. Moreover, the overall streamline pattern and the location of the focus (center) of the pattern is very similar for these two cases. These observations are indicators of the $\pi/2$ phase shift between leading and trailing cavities, which are directly linked to the phase shift between the longitudinal gravity standing waves within these cavities.

The streamline $<\psi>_p$ patterns of Figure 5.11 reveal an additional feature involving the interaction of the flow fields between the leading and trailing cavities. Consider the pattern at $\phi = 270°$ for the transverse standing wave (left column). It is possible to identify streamlines, emanating from the interior of the leading cavity, and over the partition between the leading and trailing cavity. Then, these streamlines are deflected into the interior of the trailing cavity, more specifically, along its impingement wall. Thus, the large amplitude oscillations in the transverse mode, involve mass exchange between the leading and trailing cavities during part of the oscillation cycle. At later times, corresponding to values of phase angle ϕ = 0°, 90°, and 180°, the leading cavity shows a stagnation point in the impingement region. With increasing values of ϕ, the stagnation point migrates upward until, at ϕ = 270°, a gap is created, which allows flow to pass into the trailing cavity. This mass exchange is therefore limited to a relatively small window of ϕ during the oscillation cycle. On the other hand, for the longitudinal gravity standing wave mode, represented in the right column of Figure 5.11, the

patterns of $<\psi>_p$ indicate that the stagnation point at impingement in the leading cavity remains at the corner of the impingement surface.

Corresponding patterns of phase-averaged streamlines $<\psi>_p$ in a reference frame that is moving one-half of the free stream velocity U provides a representation of the downstream propagation of the vortical structures at four different phases of oscillation cycle in Figure 5.12. It is evident that the spatial extent of the vortical structures is considerably larger in presence of the transverse-oriented gravity standing wave relative to the longitudinal mode of the gravity standing wave. The phase shift between upstream and downstream cavities can also be identified in these plots. For example, at transverse mode (left column) at $\phi = 0°$ (first row), in the trailing cavity, a large-scale recirculation zone is located in the middle of the interface of the cavity exhibit similarity with the patterns in the leading cavity at $\phi = 180°$. In the same manner, for the longitudinal mode (right column) at $\phi = 0°$ (first row), in the leading cavity, a recirculation zone is attached to the separation corner, and this attached recirculating zone is observed at the trailing cavity at $\phi = 90°$ (second row). These observations, in turn, show π and $\pi/2$ phase shifts correspondingly for the transverse and longitudinal gravity wave systems.

Figure 5.14 shows the contours of constant phase-averaged velocity magnitude $<V>_p/U$ at four different phases ϕ of the oscillation cycle of the transverse and longitudinal modes of the gravity standing wave. At transverse

mode, which is given in the right column of images, it is evident that, large amplitude undulations of the interface along the cavity openings occur. The magnitude of these undulations is remarkably attenuated at longitudinal mode in the right column of images. In fact, examination of $<V>_p/U$ with corresponding Reynolds stress patterns in the last row of Figure 5.5, the separated shear layer is deflected further into the cavity at the downstream cavity at transverse mode, in accord with the increasing magnitude of Reynolds stress correlation $<u'v'>/U^2$. Furthermore, the overall magnitude of $<V>_p/U$ inside the cavities is relatively larger at transverse mode compare to the longitudinal mode, and this trend is similar to that shown in the time-averaged transverse velocity $<v>/U$ patterns in Figure 5.6 (c, d).

5.6 TIME-AVERAGED PATTERNS OF MASS EXCHANGE

All of the foregoing patterns of the flow structure have important consequences for the patterns of mass exchange between the mainstream and the cavity. A dimensionless mass exchange coefficient k can be calculated along the cavity openings; it reveals the effects of orientation of the gravity standing wave on the mass exchange process. The dimensionless mass exchange coefficient is evaluated as:

$$k = \frac{\overline{E(t)}}{2U} \tag{5.3}$$

in which $\overline{E(t)}$ is the time-averaged exchange velocity and U is the free stream velocity.

A total of 3,000 randomly-acquired instantaneous velocity vector fields were averaged to calculate time averaged values of $\overline{E(t)}$, which is given as:

$$E(t) = \frac{1}{L}\int_0^L |v(t)|dx \tag{5.4}$$

where $v(t)$ is the instantaneous cross-stream (transverse) velocity along the cavity opening and L is the length of the cavity. Details of formulation of the exchange velocity and mass exchange coefficient are given by Tuna et al. (2013).

Figure 5.14 shows the time-averaged exchange velocity $\overline{E(t)}$ distribution along the cavity openings together with the patterns of Reynolds stress correlation $<u'v'>/U^2$. The plot at the top represents the transverse mode (Uf_n/L = 2.9) of the gravity standing wave, and the one at the bottom provides the longitudinal mode (Uf_n/L = 1.6). It is clear that the overall magnitude of $\overline{E(t)}$ along the cavity opening is significantly larger in presence of the transverse mode of the gravity standing wave. Furthermore, a comparison of the $\overline{E(t)}$ trends between the leading (upstream) and the trailing (downstream) cavities reveals the relation between the Reynolds stress patterns and mass exchange. Reynolds stress $<u'v'>/U^2$ is an indicator of the increased coupling and thereby the amplitude of the gravity standing wave oscillation. Enhanced $<u'v'>/U^2$ increases the entrainment demand of the separated shear layer along the opening of the cavity, and affects the mass

exchange process between the cavity and the main stream. It is therefore possible to anticipate that mass exchange will be higher as the values of Reynolds stress increases. For the transverse mode, the peak magnitude of $\overline{E(t)}$ along the trailing (downstream) cavity is relatively larger than along the leading (upstream) cavity, due to the larger magnitude of the Reynolds stress concentration. The same general observation holds for the longitudinal mode of the gravity standing wave, though the peak value of $\overline{E(t)}$ is only marginally larger for the trailing cavity, relative to the leading cavity.

Further insight into the distinction between cases of longitudinal and transverse modes of the gravity standing wave is provided in Figure 5.15. The plot at the top shows the time-averaged exchange velocity distributions that are given in Figure 5.14, and the table at the bottom gives details about the dimensionless mass exchange coefficient k at both modes of the oscillation. As stated previously, the value of exchange velocity $\overline{E(t)}$ is larger along both cavities for the transverse mode (Uf_n/L = 2.9). Thus, one can anticipate an increase of the dimensionless mass exchange coefficient for the transverse mode of the gravity standing wave. The values of mass exchange coefficient $k = \overline{E(t)}/2U$ are respectively, in presence of longitudinal and transverse modes of the gravity standing wave, k = 0.032 and 0.048 for the leading cavity, and k = 0.035 and 0.061 for the trailing cavity. The presence of the transverse gravity standing wave therefore results in an increase of the mass exchange coefficient k in the range of 50% to 74%, relative to the longitudinal gravity standing wave.

5.7 CONCLUSIONS

Flow past a single cavity is well known to give rise to pronounced self-excited oscillations, due to resonant coupling between the unstable shear layer along the cavity opening and a standing wave mode within the cavity. In contrast, occurrence of such oscillations due to flow past successive cavities has remained unclarified. The present investigation indicates that highly coherent oscillations of the flow structure can indeed be generated, even from a nominally turbulent state. The physics has been pursued with a technique of high-image-density particle image velocimetry in conjunction with unsteady pressure measurements.

Onset of these highly coherent oscillations involves occurrence of a resonant peak of the unsteady pressure amplitude within the cavity when the reduced velocity is varied. This resonant state occurs simultaneously in each of the successive cavities, thereby indicating a globally coupled resonant response.

The criteria for attainment of this resonant state, that is the occurrence of self-sustained oscillations, are twofold. First of all, a defined phase shift between the standing wave oscillations within successive cavities must be satisfied. This phase shift can take on values of either $\pi/2$ or π, depending on the orientation of the standing wave mode, that is, transverse or longitudinal. Secondly, an overall phase shift criteria must be satisfied in the separated shear layer along the openings of the cavities; in other words, the transverse undulations of the separated layer exhibit a phase difference of either π or 2π between the separation corner and the

impingement corner of a given cavity, depending upon the orientation of the gravity standing wave in each cavity, i.e., transverse or longitudinal. Taken together, these two types of phase shifts allow maintenance of the self-sustained oscillation.

The time- and phase-averaged representations of the flow structure along and within the successive cavities are interpreted in terms of vorticity, velocity, and streamline topology. The timing of vortex formation and impingement along the successive cavities are characterized in terms of patterns of phase-referenced vorticity, which shows analogous, but phase shifted, clusters of vorticity along successive cavities. These patterns of time-dependent vorticity are compatible with regions of outflow and inflow that extend continuously from deep within the cavity across the separated shear layer. That is, compatibility exists between the dynamics of the recirculation zone within the cavity and the separated shear layer along the cavity opening. Patterns of streamline topology indicate that, if the oscillation amplitude is sufficiently large, mass transfer occurs between successive cavities during a portion of the oscillation cycle; such transfer is, however, not a necessary condition for the occurrence of a locked-on state of the system of successive cavities.

A consequence of these locked-on states of the highly coherent oscillations of the flow in successive cavities is generation of concentrated regions of Reynolds stress, which, in turn, are related to the magnitudes of the mass exchange between the cavity and the mainstream. The magnitudes of both the Reynolds stress and the

mass exchange are a strong function of the orientation of the gravity standing wave, i.e., transverse versus longitudinal, in successive cavities.

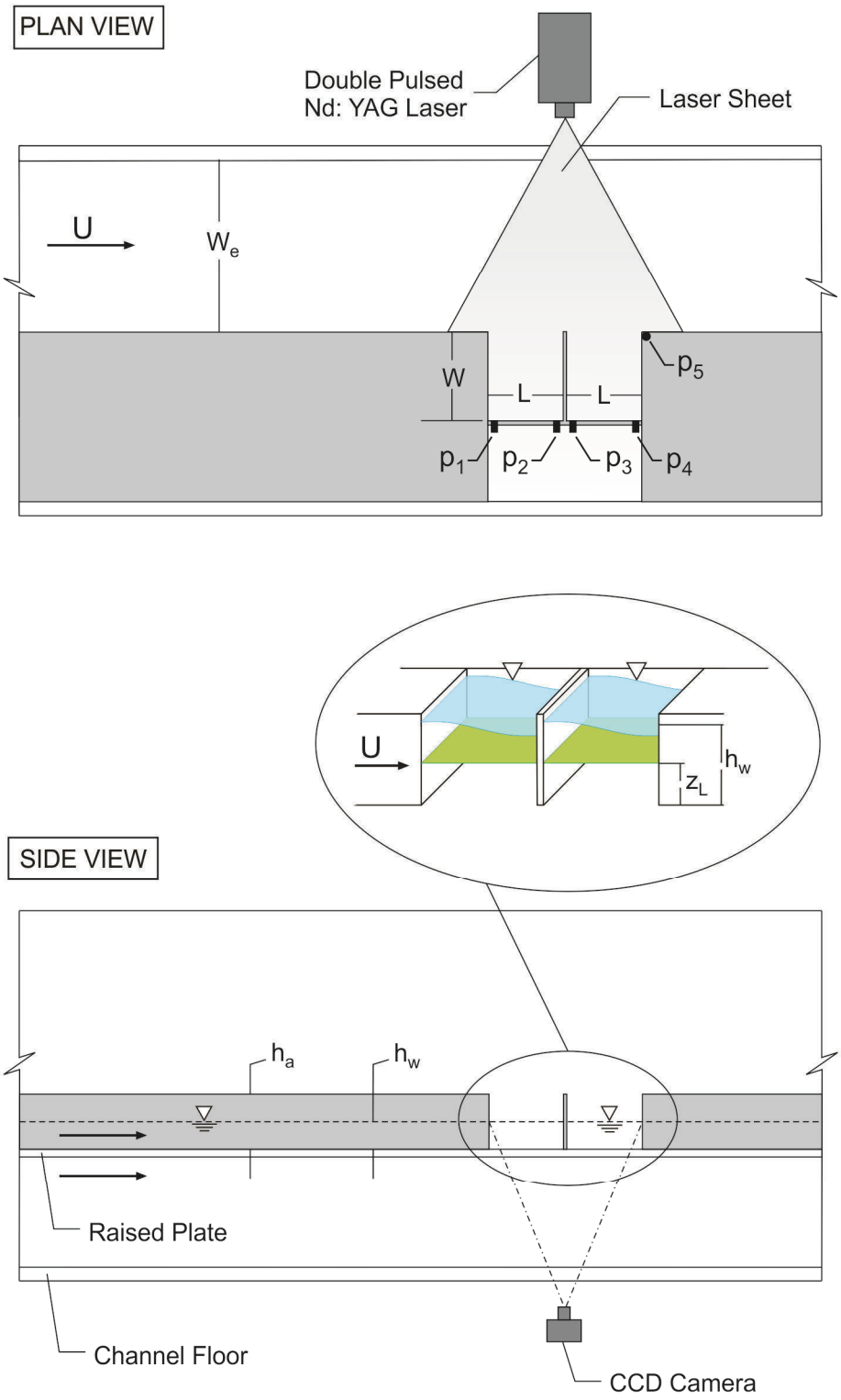

Figure 5.1: Schematic of experimental setup.

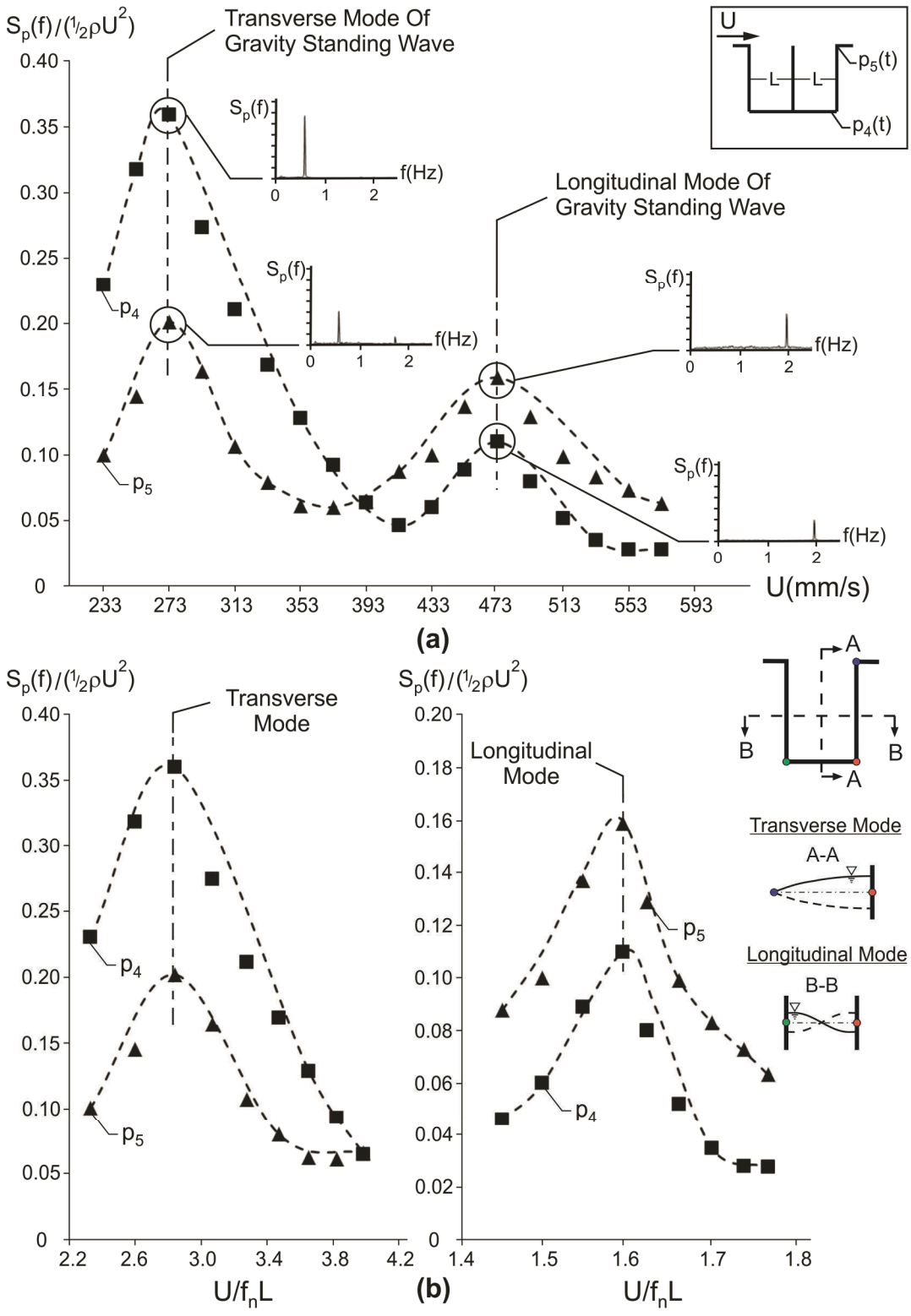

Figure 5.2: Amplitude of spectral peak $S_p(f)/(\frac{1}{2}\rho U^2)$ as a function of: **(a)** free stream velocity U; and **(b)** reduced inflow velocity U/f_nL.

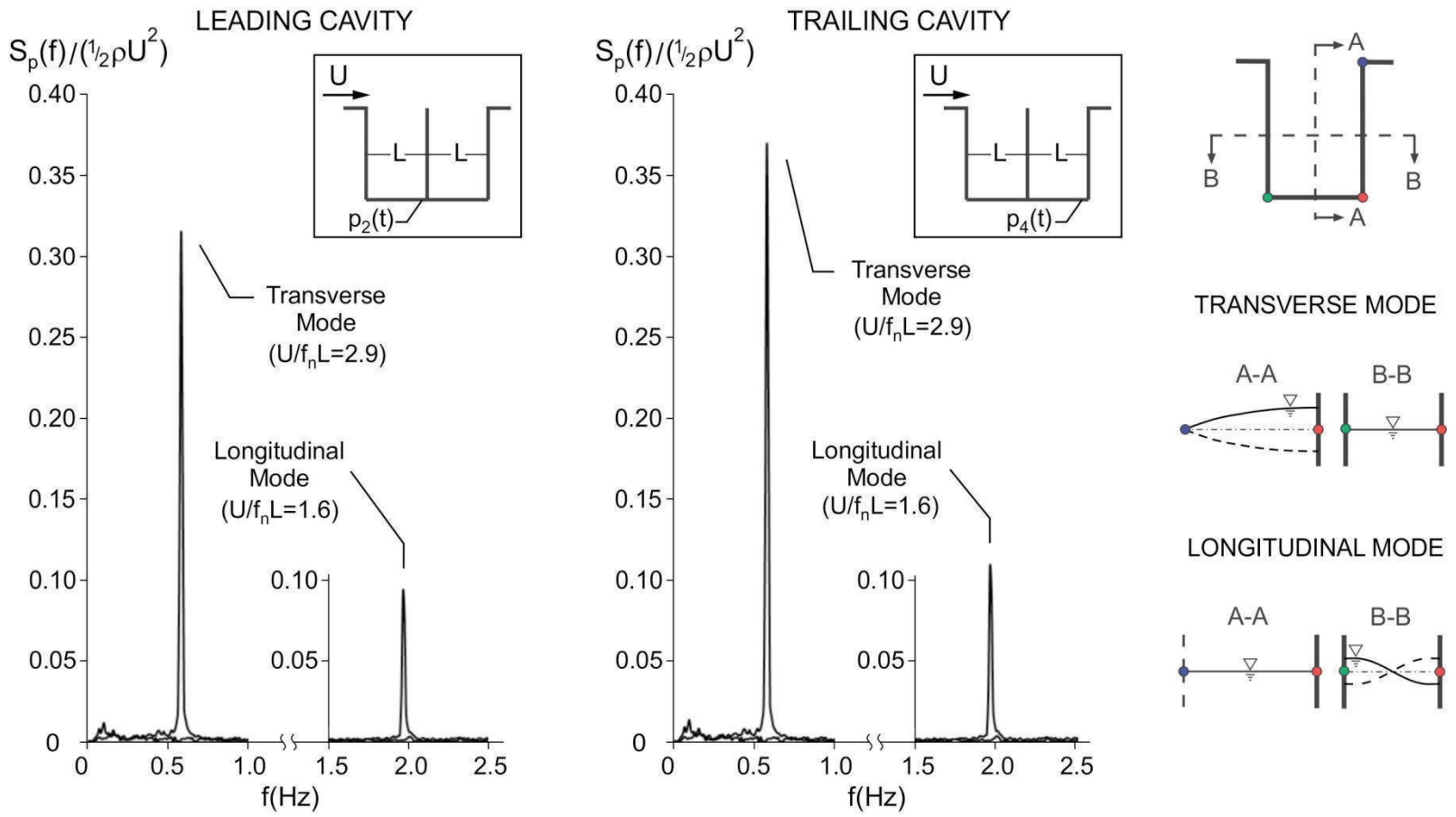

Figure 5.3: Amplitude of spectral peak $S_p(f)/(½\rho U^2)$ of pressure fluctuation in leading and trailing cavities for transverse and longitudinal modes of gravity standing waves within cavities.

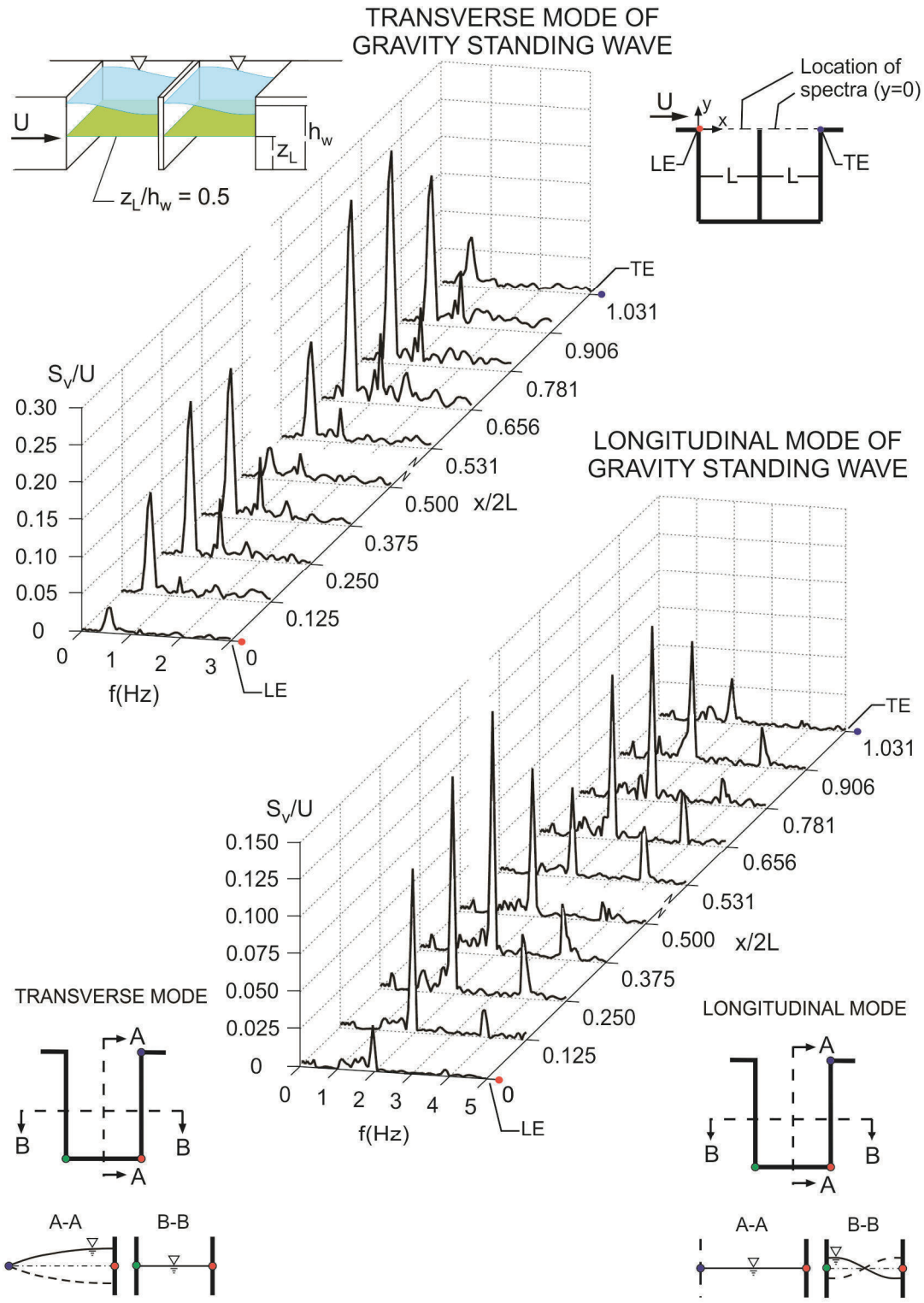

Figure 5.4: Spectra S_v/U of cross-stream velocity fluctuation in shear layer along openings of cavities (y = 0), for transverse (top) and longitudinal (bottom) modes of gravity standing waves within cavities.

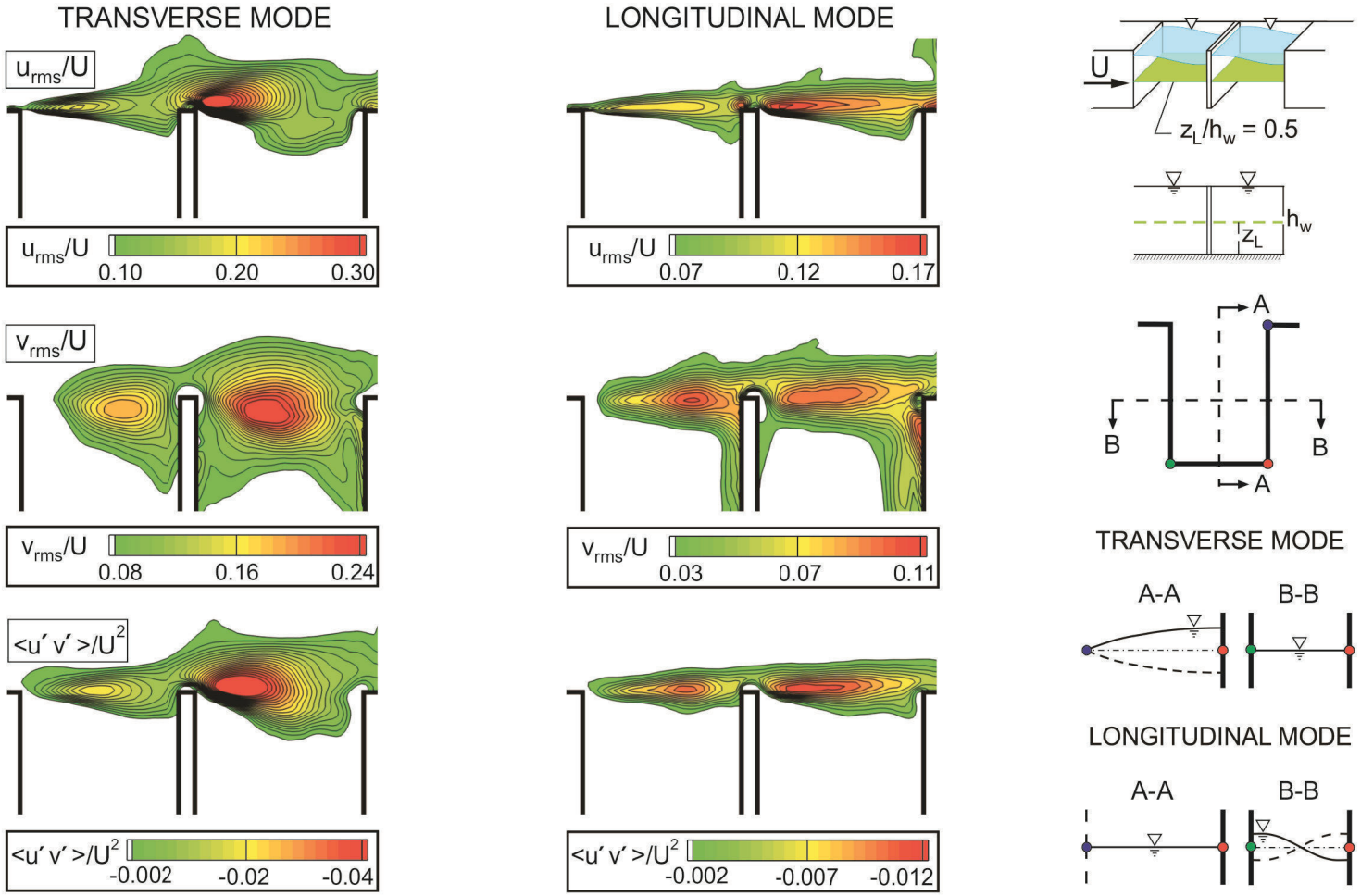

Figure 5.5: Patterns of root-mean-square streamwise (u_{rms}/U) and transverse (v_{rms}/U) velocity fluctuations; in addition Reynolds stress ($<u' v'>/U^2$), for transverse and longitudinal modes of gravity standing waves within cavities, are represented respectively by images in left and right columns.

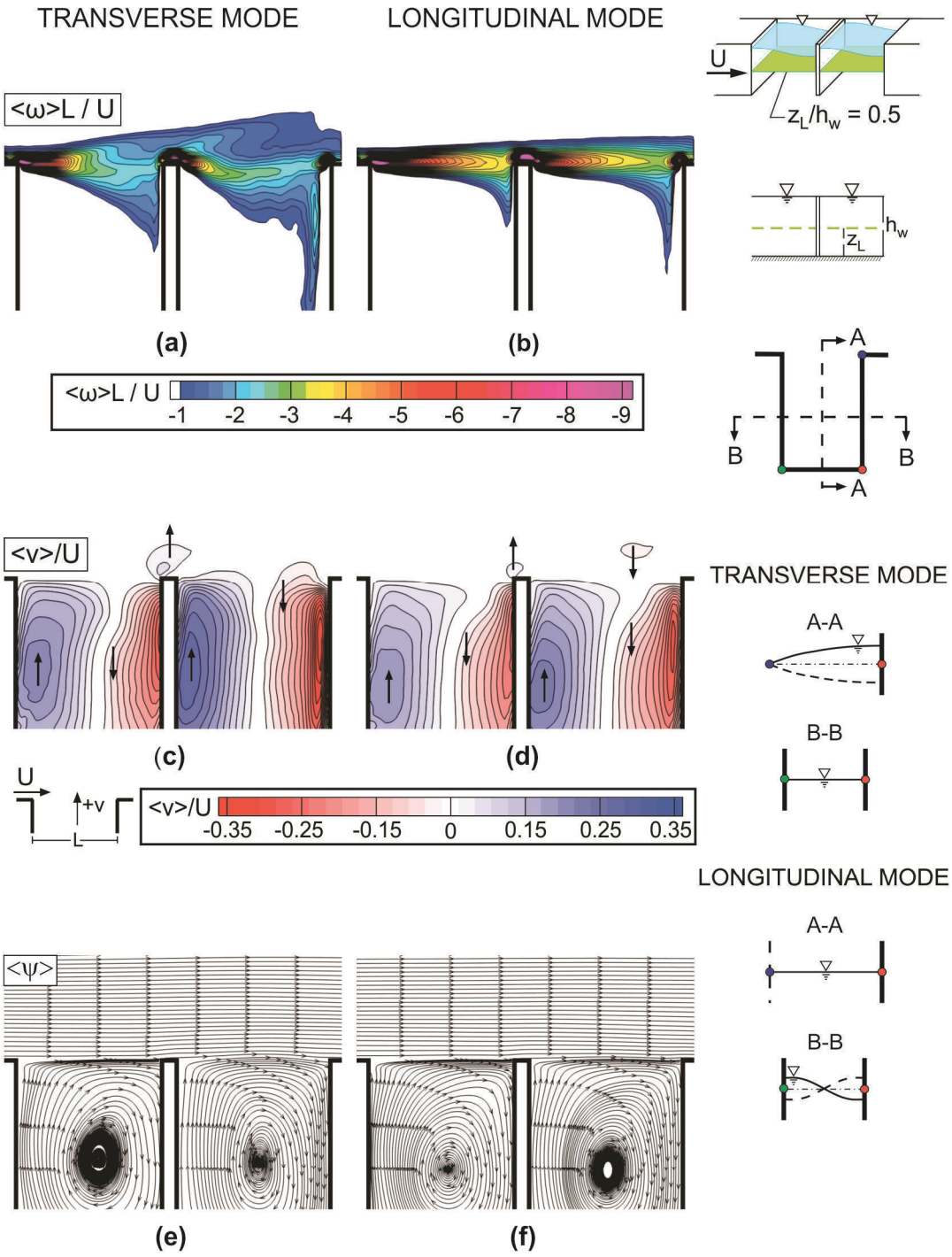

Figure 5.6: (**a, b**) Contours of time-averaged vorticity $\langle\omega\rangle L/U$; (**c, d**) transverse velocity $\langle v\rangle/U$; and (**e, f**) streamlines $\langle\psi\rangle$, for transverse and longitudinal modes of gravity standing waves within cavities, are represented respectively by images in left and right columns.

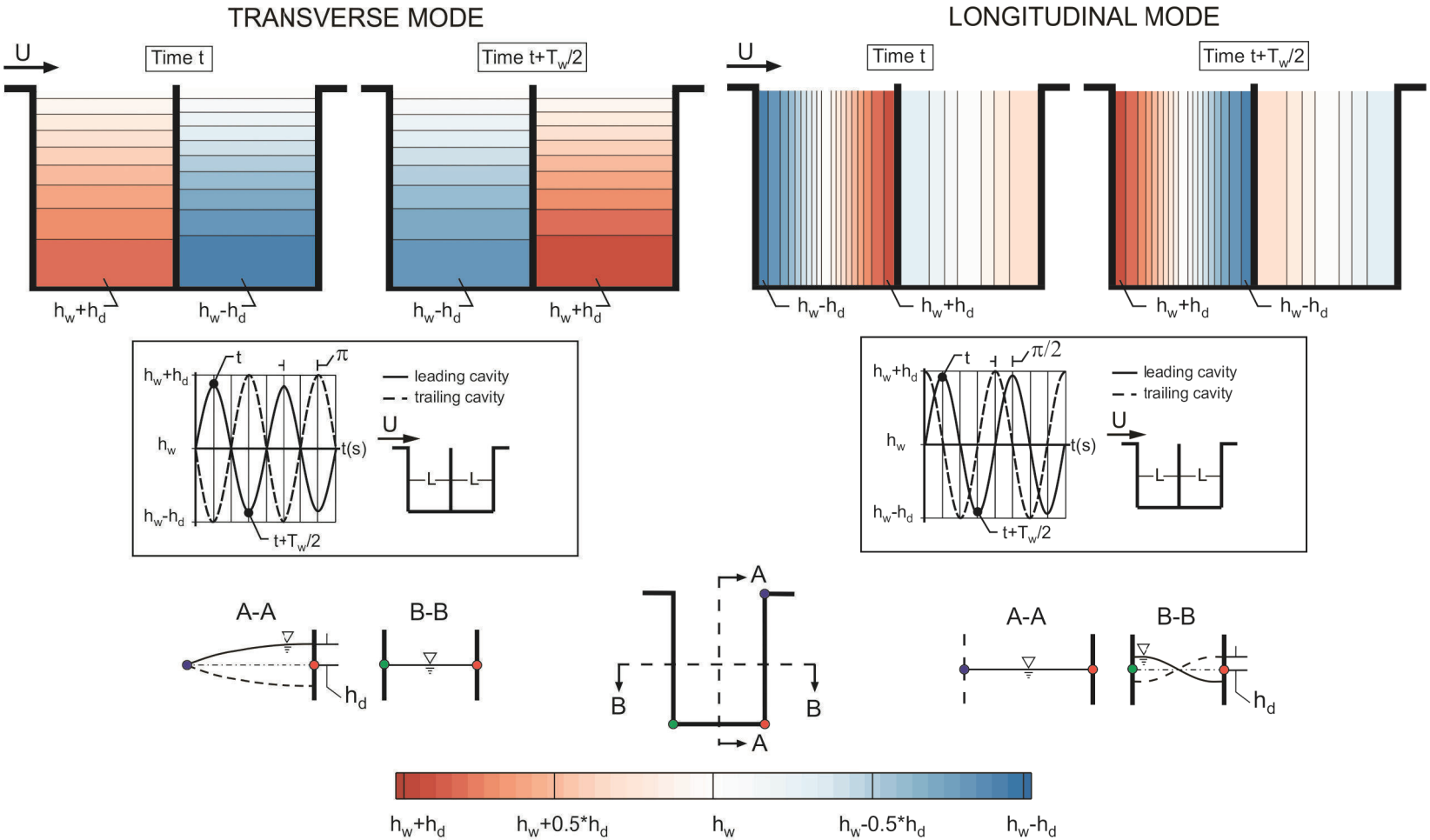

Figure 5.7: Contours of instantaneous water depth inside cavity corresponding to transverse (left) and longitudinal (right) modes of gravity standing waves within cavities. Red contour levels represent values of water depth larger than nominal depth h_w and blue contour levels represent values of water depth smaller than nominal depth h_w; h_d is oscillation amplitude of gravity standing wave.

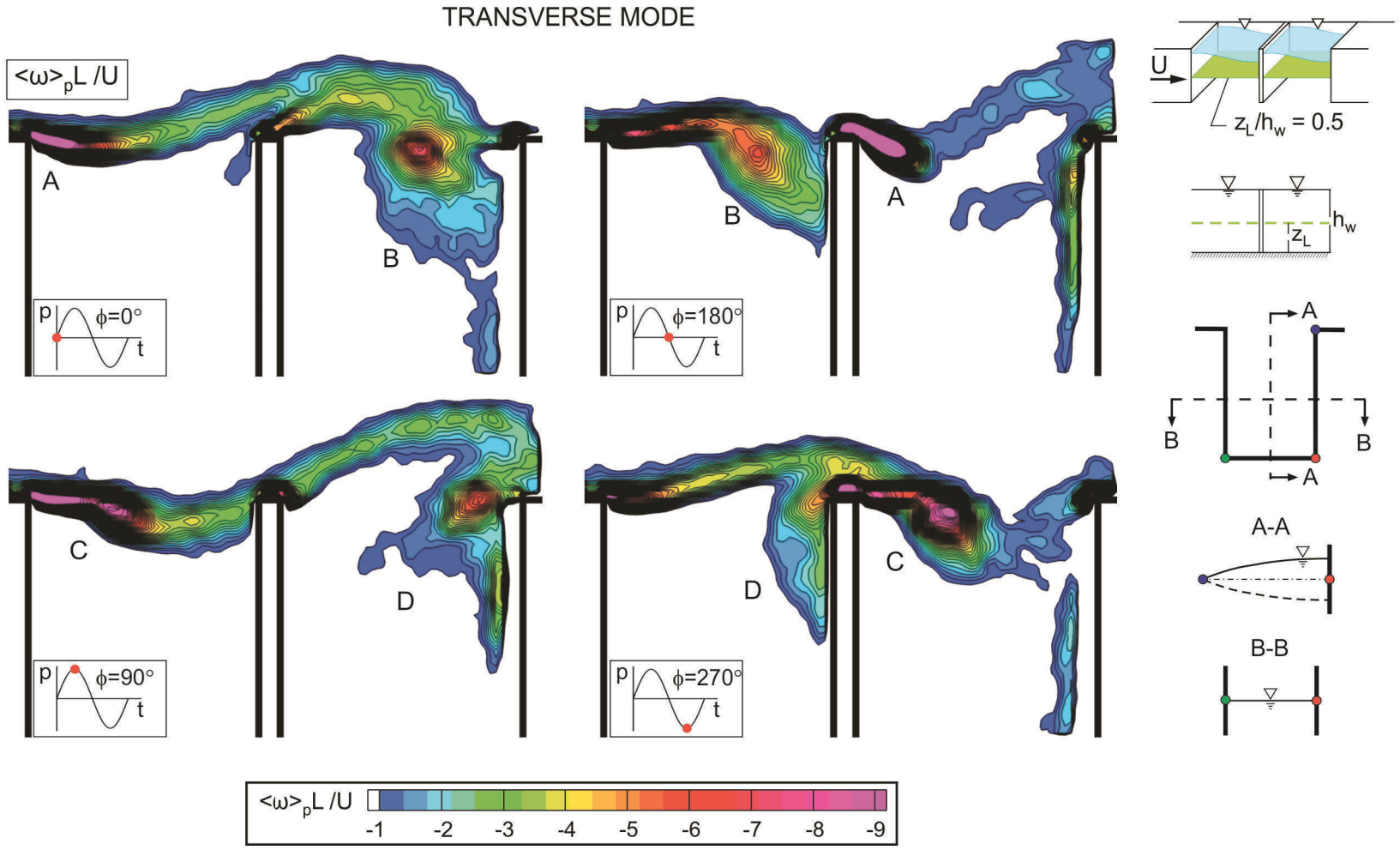

Figure 5.8a: Contours of phase-averaged vorticity $\langle\omega\rangle_p L/U$, for transverse mode of gravity standing waves within cavities.

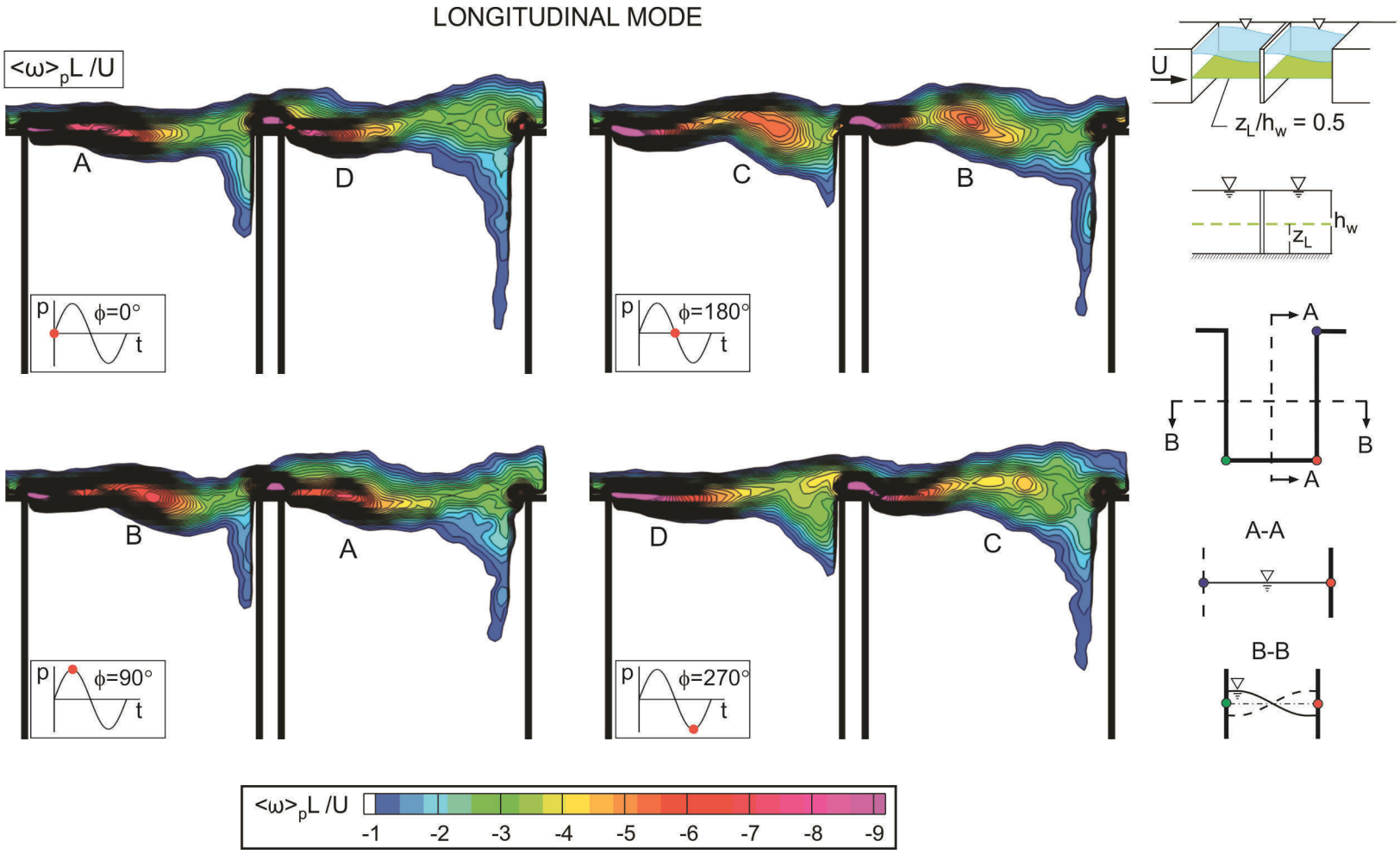

Figure 5.8b: Contours of phase-averaged vorticity $\langle\omega\rangle_p L/U$, for longitudinal mode of gravity standing waves within cavities.

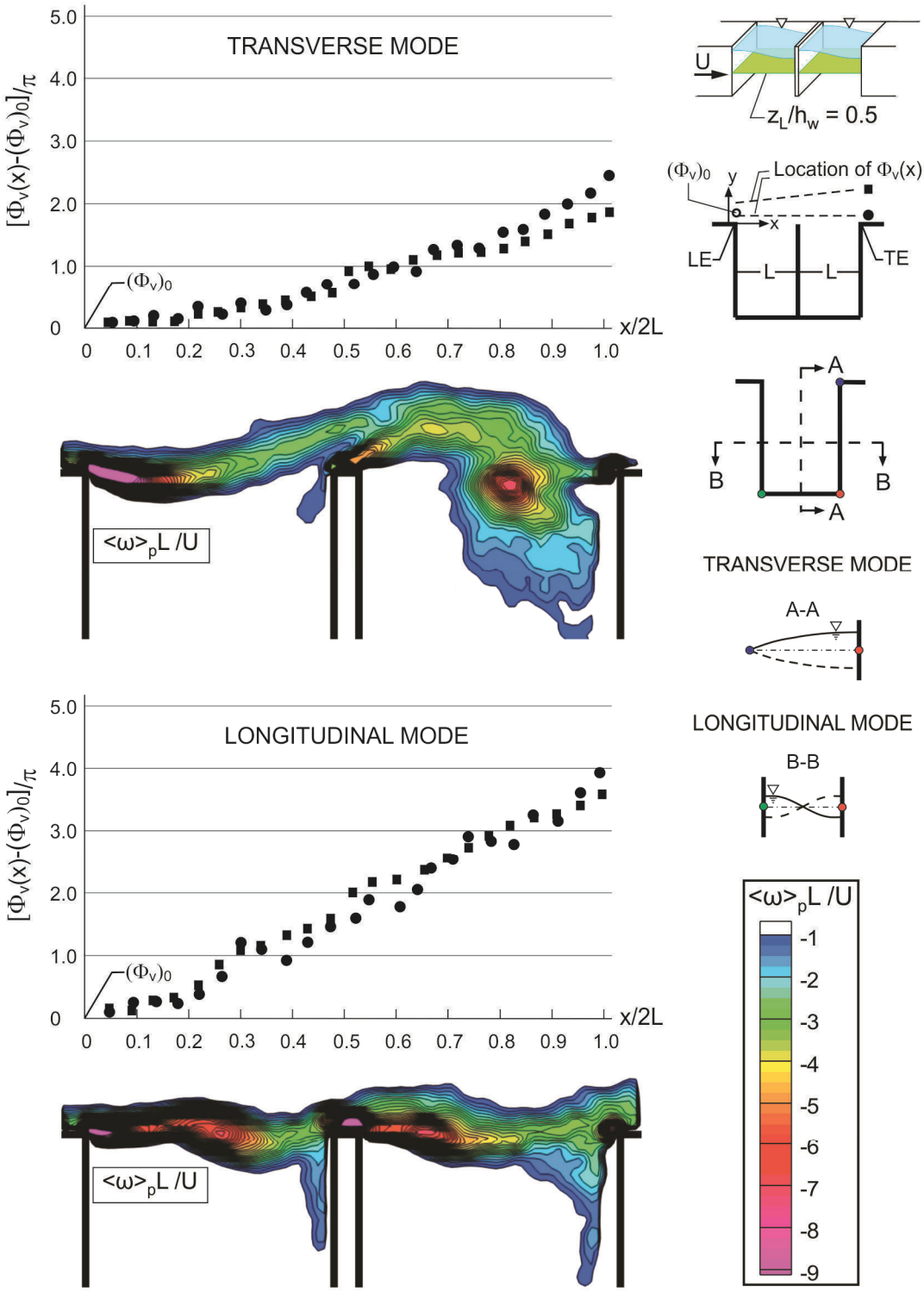

Figure 5.9: Phase variation of transverse velocity $\Phi_v(x)$ with downstream position ($x/2L$) along a horizontal line $y/L = 0.08$ (round symbols) and along a line where $\langle u \rangle / U = 0.9$ (square symbols), for transverse (top row) and longitudinal (bottom row) modes of gravity standing waves within cavities.

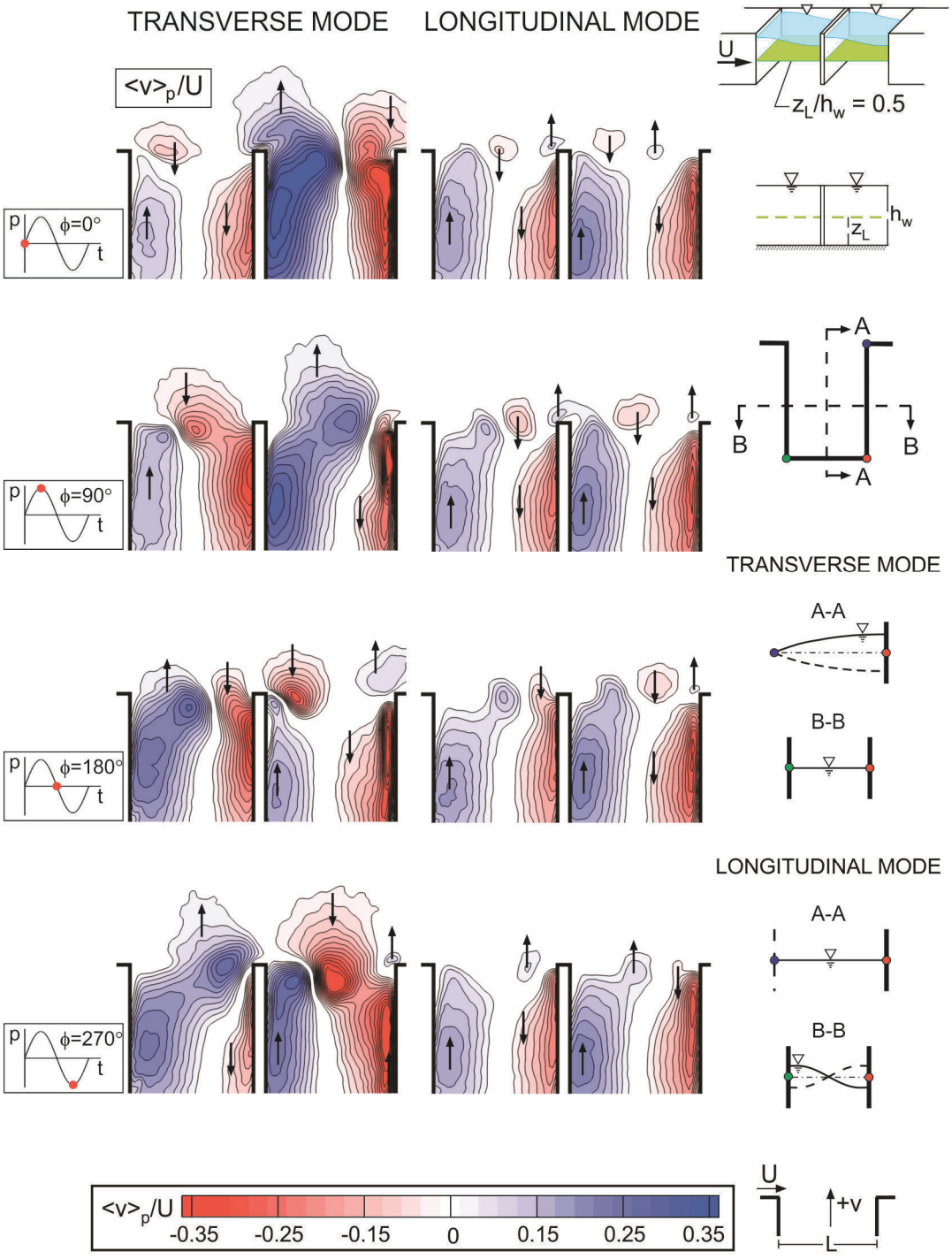

Figure 5.10: Contours of phase-averaged transverse velocity ($\langle v \rangle_p/U$), for transverse and longitudinal modes of gravity standing waves within cavities, are represented respectively by images in left and right columns.

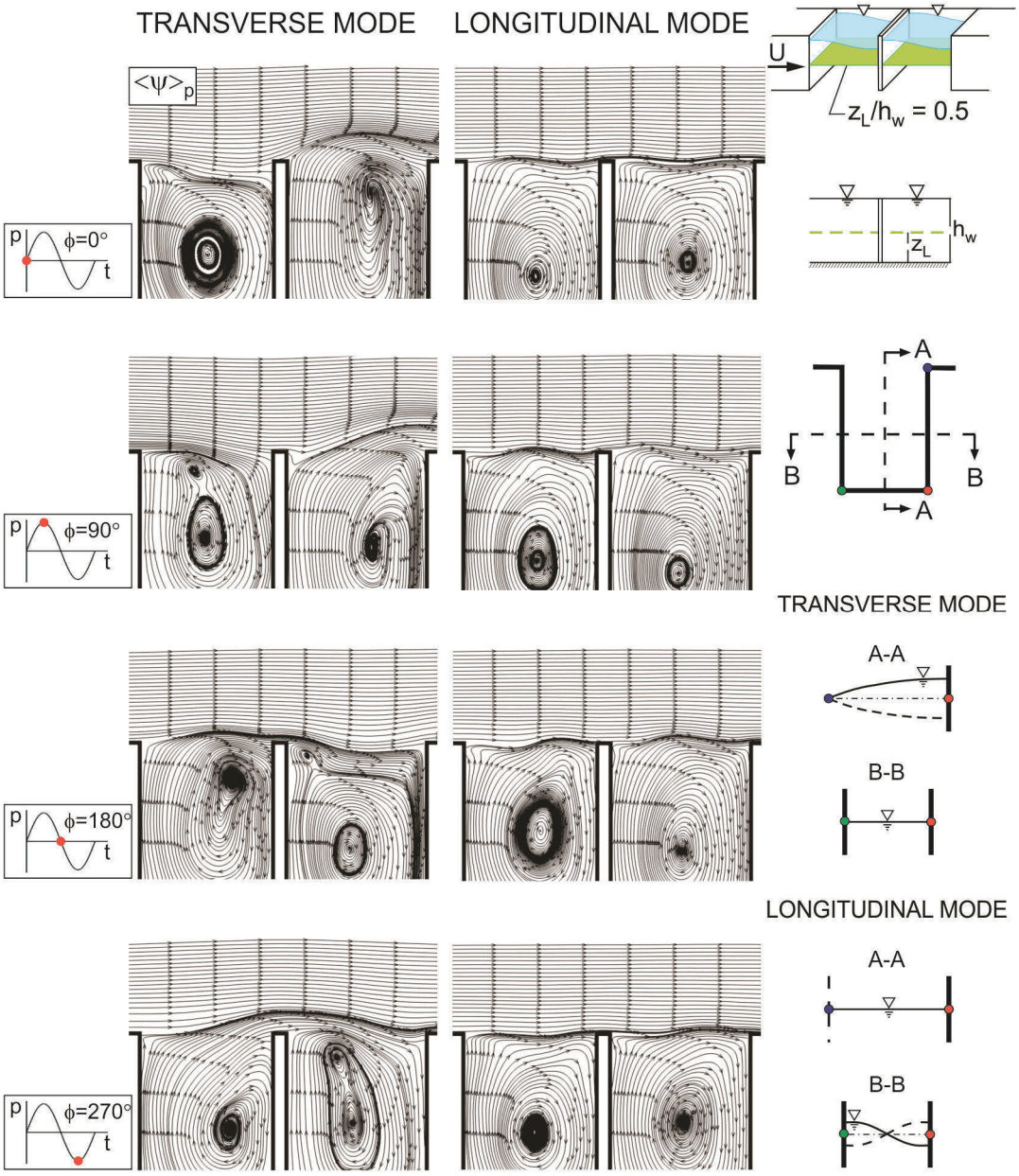

Figure 5.11: Patterns of phase-averaged streamlines ($<\psi>_p$), for transverse and longitudinal modes of gravity standing waves within cavities, are represented respectively by images in left and right columns.

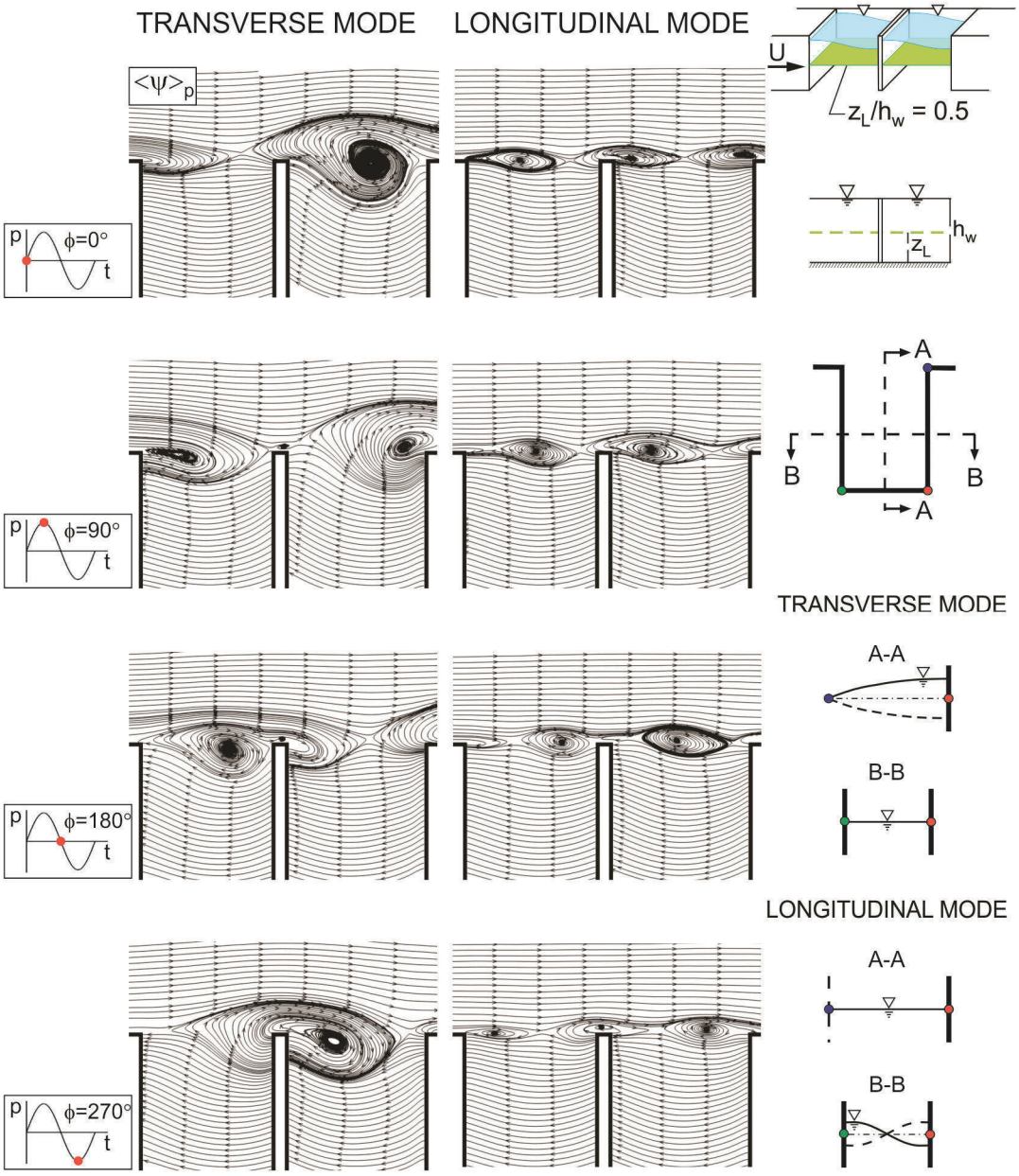

Figure 5.12: Patterns of phase-averaged streamlines ($<\psi>_p$) at a reference plane moving at $0.5U$ where U is the free stream, for transverse and longitudinal modes of gravity standing waves within cavities, are represented by images in left and right columns.

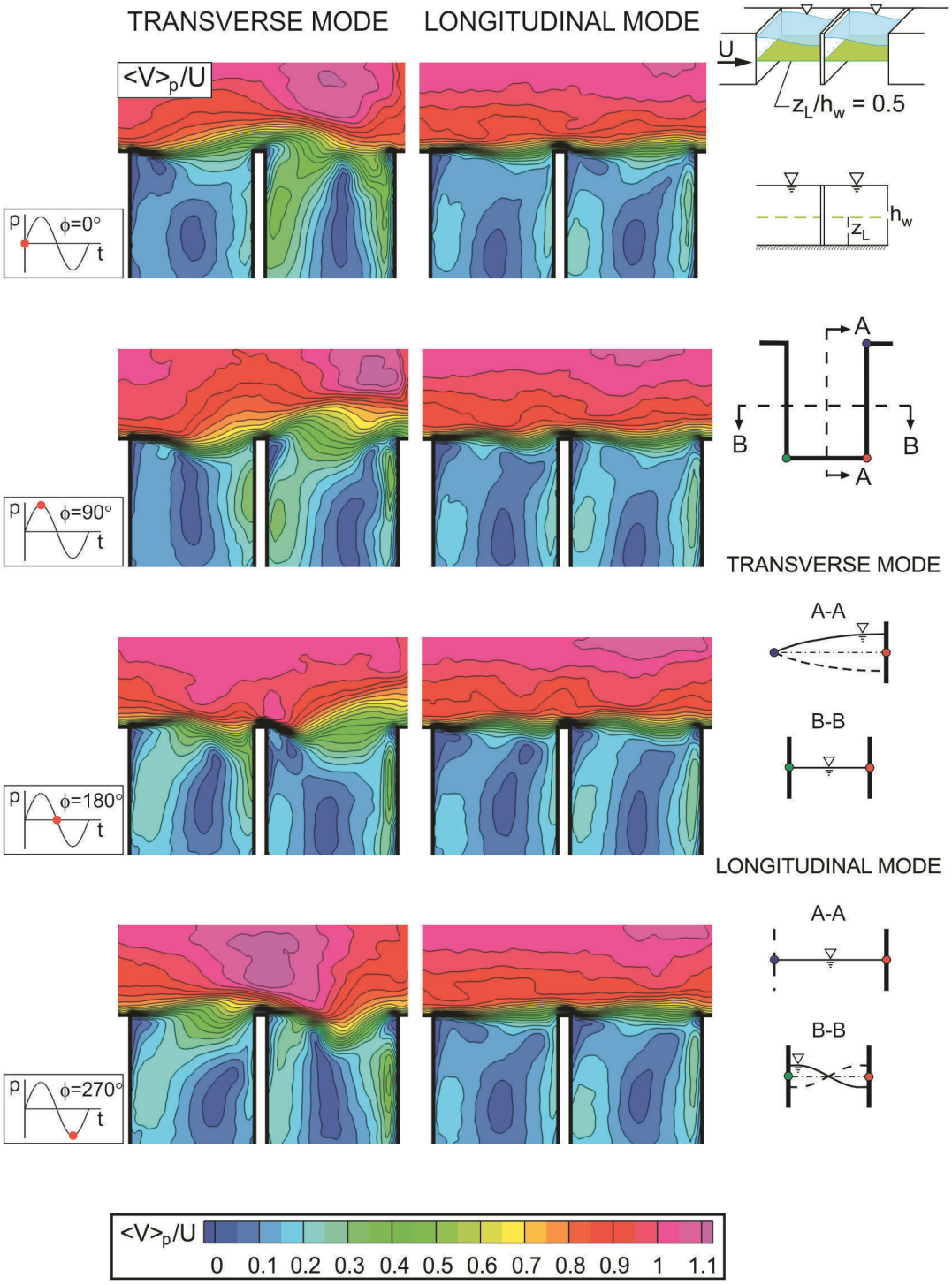

Figure 5.13: Contours of phase-averaged velocity magnitude ($<V>_p/U$) for transverse and longitudinal modes of the gravity standing waves within the cavities, are represented respectively by the images in the left and right columns.

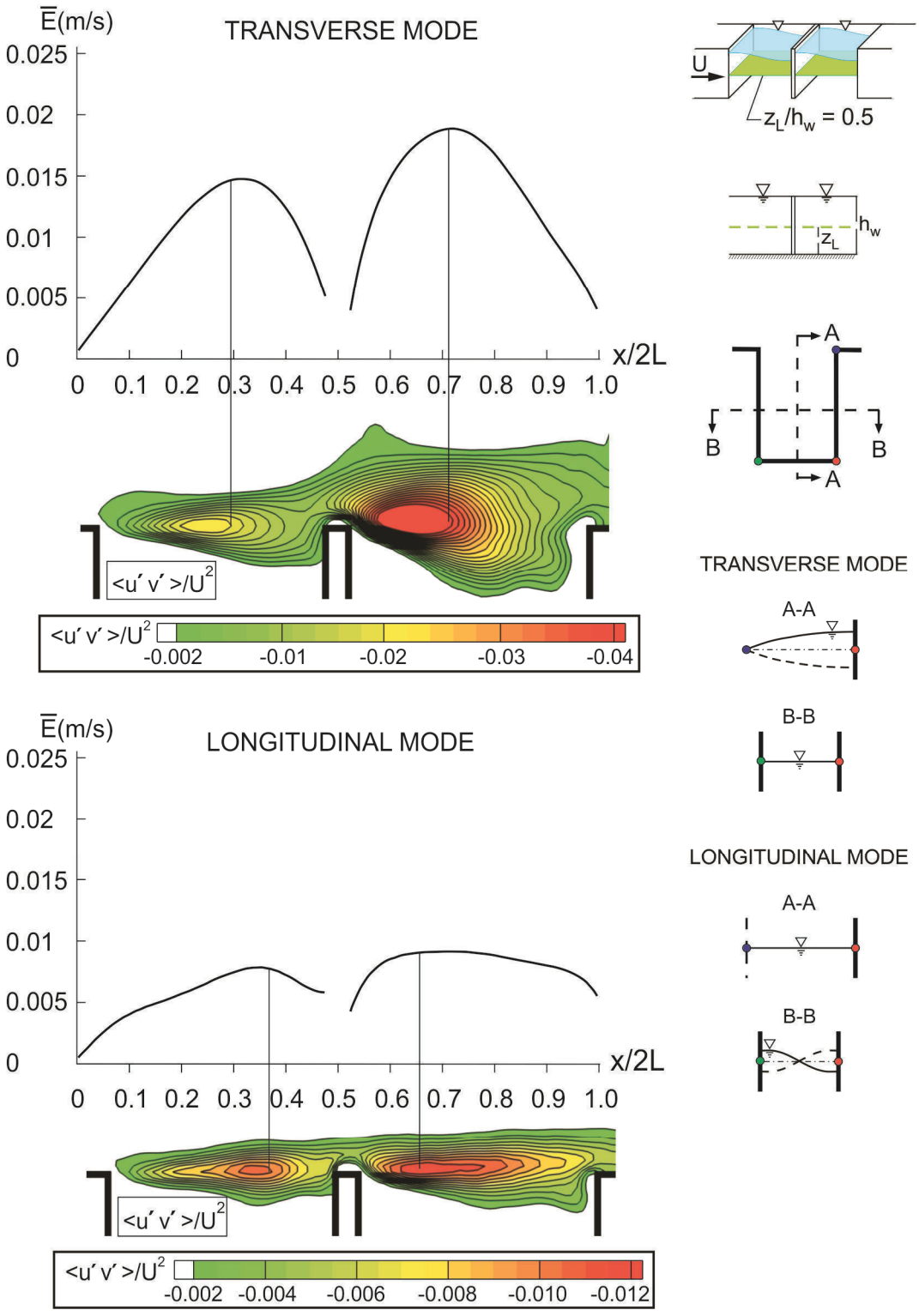

Figure 5.14: Patterns of time-averaged entrainment velocity ($\overline{E}$) and Reynolds stress ($<u'v'>/U^2$) along mouth ($y = 0$) of cavities, for transverse and longitudinal modes of gravity standing waves within cavities, are represented respectively by images in top and bottom rows.

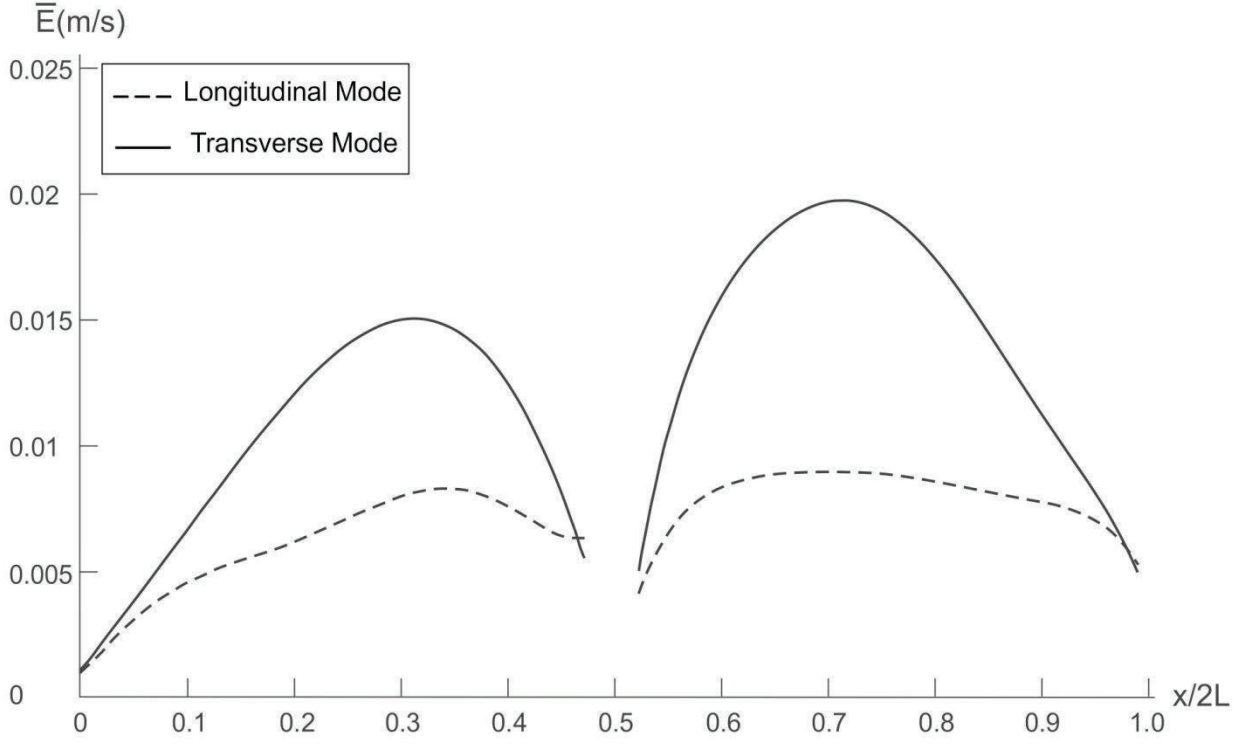

k	Leading Cavity	Trailing Cavity
Longitudinal Mode	0.032	0.035
Transverse Mode	0.048	0.061

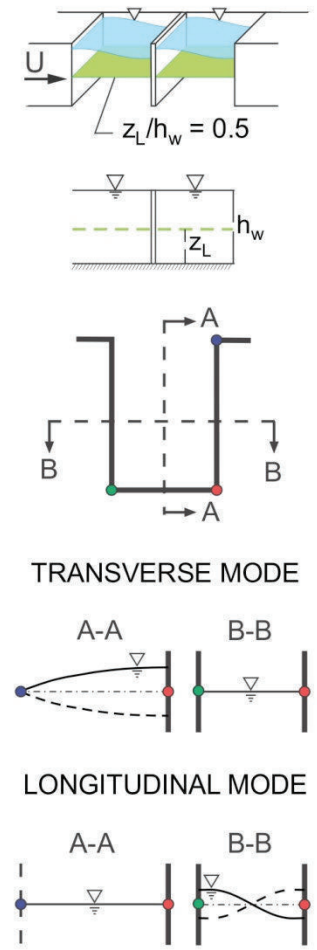

Figure 5.15: Patterns of time-averaged entrainment velocity ($\overline{E}$) along mouth of cavities, for transverse and longitudinal modes of gravity standing waves within cavities, are indicated respectively by solid line and dashed line.

CHAPTER 6

CONCLUDING REMARKS AND RECOMMENDATIONS

A very large number of cavity-like regions in the form of embayments, spur dikes, and jetties are located along rivers, in estuaries, and in coastal regions around the world. The survival and maintenance of living biomass and masses of nutrients, dissolved gases, vegetation, fish, marine life, as well as erosion and transport of sediment are important considerations within these regions and in the main flow exterior to them. This investigation has focused on the detailed flow physics associated with self-sustained oscillations of fully turbulent shallow flow past a cavity and a sequence of cavities, as well as means for their attenuation.

6.1 CONCLUDING REMARKS

A fully turbulent shallow flow past a cavity or a series of cavities gives rise to highly organized oscillations, that is, very large-scale, highly coherent vortex formation in the separated shear layer. This phenomenon involves coupling between the instability/vortex formation in the shallow mixing layer and the modes of the gravity standing wave within the cavity (ies). Quantitative imaging of the

flow structure, in conjunction with unsteady pressure measurements, has provided a description of the detailed physics of this coupled oscillation and its effect on the mass exchange process between the cavity (ies) and the main stream. Techniques for passive control of the oscillations have been characterized in terms of modification of the flow physics, using the same experimental approaches. In the following, a brief summary of the major findings is given.

6.1.1 Depthwise Variations of Flow Structure in Presence of Globally Coupled Shear Layer-Gravity Standing Wave Oscillations

Fully developed turbulent shallow flow past a cavity gives rise to highly ordered flow oscillations due to onset of a gravity standing wave within the cavity. A process of lock-on occurs, whereby the frequency of the vortex formation along the cavity locks-on to, and remains the same as, the eigenfrequency of the gravity standing wave within the cavity. This lock-on is initiated at a critical value of velocity of the turbulent shallow flow. As the velocity is further increased, lock-on is maintained, and the amplitude of the coupled oscillation involving the vortex formation in the shear layer and the gravity standing wave increases until it attains a peak value, which is followed by a decrease. This peak amplitude of the coupled oscillation radically alters the structure of the shear layer along the cavity opening, as well as the recirculation flow within the cavity.

Corresponding phase-averaged patterns of vorticity in presence of the gravity standing wave show: (i) growth of a large-scale coherent vortical structure

in the unsteady shear layer; (ii) travel of this structure in the downstream direction along the opening of the cavity; and (iii) impingement of the large-scale vortical structure at the trailing (downstream)-edge of the cavity. Furthermore, time-averaged patterns of vorticity demonstrate that high level vorticity extends well downstream towards the impingement region during the non-coupled state, but it is rapidly attenuated in streamwise direction during fully-coupled oscillations. Remarkably, the time-averaged streamlines show similar patterns irrespective of whether a gravity standing wave is present within the cavity.

Substantial enhancements of the peak amplitudes of the contours of root-mean-square streamwise and transverse velocity, as well as Reynolds stresses within the separated shear layer along the cavity opening, are associated with the fully-coupled oscillations of the shear layer-gravity standing wave. It is evident that the enhancement of turbulent stresses within the shear layer is directly correlated to the aforementioned streamwise degradation of the peak value of patterns of time-averaged vorticity.

The flow structure in a shallow flow is a function of the elevation of the plane of observation above the bed, i.e., bottom surface. Patterns of time- and phase-averaged transverse velocity, streamlines, and vorticity show that the degree of coherence is decreased as the bed region is approached. This decreased coherence, in turn, leads to attenuation of the Reynolds stress in the separated shear layer during both the non-coupled and fully-coupled states of oscillations.

Furthermore, the aforementioned coupled oscillations of the shear layer and the gravity standing wave have important effects on the mass exchange process. Substantial enhancement of the time-averaged exchange velocity along the cavity opening occurs, which results in larger values of mass exchange coefficient between the cavity and the main stream at elevations extending from the bed to the free-surface.

6.1.2 Attenuation of Oscillations

A small diameter cylinder (bed perturbation) having a height much smaller than the water depth is placed at, and upstream of, the leading edge of the cavity in order to passively control self-sustained oscillations. It has been demonstrated that the bed perturbation (cylinder) results in substantial reductions of the degree of coupling between the inherent instability of the separated shear layer and the gravity standing wave mode within the cavity. However, existence of the cylinder at the leading-edge does not alter the frequency of the oscillation.

The physical origin of the aforementioned attenuation is shown to be largely related to the increase of the shear layer width along the cavity opening, which modifies its stability characteristics; moreover, the streamlines are deflected outward (away) from the cavity. Patterns of time- and phase-averaged transverse velocity and vorticity provide further insight into the underlying physics of the attenuation.

In addition, substantial attenuation of the peak amplitude of Reynolds stress occurs in the separated shear layer, which is associated with a 50% decrease in the value of the mass exchange coefficient.

6.1.3 Self-Sustained Oscillations of Shallow Flow Past a Series of Cavities

Self-excited oscillations can occur in shallow flow past successive cavities, due to resonant coupling between the unsteady shear layer along the cavity opening and one or more modes of the gravity standing wave within the cavities. As the flow velocity is varied, the onset of these highly coherent structures is associated with a resonant peak of the unsteady pressure fluctuation within the cavities for different orientations of the gravity standing wave within the cavities, i.e., transverse or longitudinal.

Two principal elements of this resonant state have been identified: (i) a defined phase shift between the gravity standing wave oscillations within consecutive cavities, i.e., $\pi/2$ for the longitudinal mode and π for the transverse mode; and (ii) a total of π or 2π streamwise phase shift along the undulating shear layer past each individual cavity, depending on the mode of the gravity standing wave. Both of these phase shifts (i) and (ii) are required for occurrence of the self-sustained oscillations.

Patterns of time-averaged velocity magnitude, transverse velocity, streamline patterns, spectral response of the cross-stream velocity fluctuation, root-mean-square of streamwise and transverse velocity fluctuations, as well as

Reynolds stresses define the physics of the oscillation with respect to the orientation of the gravity standing wave within each of the successive cavities. Similar flow patterns and magnitudes of pressure fluctuations occur within each of the sequential cavities, but there are identifiable distinctions.

Corresponding phase-averaged patterns of vorticity define the time-dependent development of the undulating vorticity layer along the openings of the cavities and the phase shift between sequential cavities. In presence of the transverse mode of the gravity standing wave, there is a π phase shift between cavity oscillations. The undulating vorticity layer evolves into a highly coherent single vortex, which eventually impinges upon the downstream corner of the trailing cavity. That is, for the transverse-oriented gravity standing wave system, the vorticity layer resembles a single vortex during part of the oscillation cycle due to the π phase shift along each cavity, thereby mimicking the classical oscillation past a single cavity. On the other hand, for the streamwise-oriented gravity standing wave system, the vorticity layer shows small amplitude transverse undulations about a nominal state due to the 2π phase shift along each cavity.

The aforementioned locked-on oscillations generate large magnitudes of turbulent stresses within the separated shear layer and, in turn, result in higher entrainment demand of the separated shear layer. This phenomenon is associated with the mass exchange between the cavity and the main stream. The magnitude of

the mass exchange is a strong function of orientation and phase of the gravity standing wave.

6.2 RECOMMENDATIONS FOR FURTHER INVESTIGATIONS

The following recommendations address possibilities for future research, in order to gain insight into the underlying physics of shallow flows having a finite streamwise length scale, with eventual application to real-world applications.

(1) It has been shown that the flow structure is sensitive to the elevation within the shallow water layer. Therefore, it would be insightful to acquire three-dimensional representations of the flow field to reveal the flow structure for shallow flow past a single cavity and a series of cavities.

(2) Resonance of a gravity standing wave within a cavity with the unsteady vortex formation along the cavity shear layer has not been simulated with computations. It would be preferable to compute the three-dimensional flow field.

(3) The amplitude of the gravity standing wave oscillation can be attenuated via a passive control device, i.e., a cylinder located upstream of the leading edge. It would be worthwhile to pursue a control device that would be universally effective for various modes of the gravity wave resonance, variable velocity of the main stream of river-like configurations, different

length to width ratios of the cavity (ies), and different bed (bottom surface) topologies representative of those that occur in the field.

REFERENCES

Adamczyk, A. A., & Rimai, L. (1988). 2-Dimensional particle tracking velocimetry (PTV): technique and image processing algorithms. *Experiments in Fluids*, *6*(6), 373-380.

Adrian, R. J. (1984). Scattering particle characteristics and their effect on pulsed laser measurements of fluid flow: speckle velocimetry vs particle image velocimetry. *Applied Optics*, *23*(11), 1690-1691.

Adrian, R. J. (1988). Statistical properties of particle image velocimetry measurements in turbulent flow. In *Laser Anemometry in Fluid Mechanics-III*, Lisbon, Portugal: Ladoan-Instituto Superior Tecnico, pp. 115-129.

Adrian, R. J. (1991). Particle-imaging techniques for experimental fluid mechanics. *Annual review of fluid mechanics*, *23*(1), 261-304.

Adrian, R. J., & Westerweel, J. (2010). *Particle image velocimetry*. Vol. 30, Cambridge University Press.

Alavian, V., & Chu, V. H. (1985). Turbulent exchange flow in shallow compound channel. In *Proceedings of the 21st International Congress of IAHR, Melbourne*, pp. 446-451.

Arunajatesan, S., Shipman, J. D., & Sinha, N. (2002). Hybrid RANS-LES simulation of cavity flow fields with control. *AIAA Paper*, *1130*, 2002.

ASCE Task Force (1963). Friction factors in open channels. *Journal of the Hydraulics Division of the ASCE*, *89*, 97-143.

Babarutsi, S., Ganoulis, J., & Chu, V. H. (1989). Experimental investigation of shallow recirculating flows. *Journal of Hydraulic Engineering*, *115*(7), 906-924.

Babarutsi, S., & Chu, V. H. (1991a). A two-length-scale model for quasi-two dimensional turbulent shear flows. In *Proceedings of the 24th Congress of the IAHR* (pp. 51-60). (CHP 1)

Babarutsi, S., & Chu, V. H. (1991b). Dye-concentration distribution in shallow recirculating flows. *Journal of Hydraulic Engineering*, *117*(5), 643-659. (MS3)

Babarutsi, S., & Chu, V. H. (1993). Reynolds-stress model for quasi-two dimensional turbulent shear flow. *Engineering turbulence modelling and experiments*, *2*, 93-102.

Babarutsi, S., & Chu, V. H. (1998). Modeling transverse mixing layer in shallow open-channel flows. *Journal of hydraulic engineering*, *124*(7), 718-727.

Bendat, J. S., & Piersol, A. G. (1980). Engineering applications of correlation and spectral analysis. *New York, Wiley-Interscience,* 315, 1.

Bian, S., Driscoll, J. F., Elbing, B. R., & Ceccio, S. L. (2011). Time resolved flow-field measurements of a turbulent mixing layer over a rectangular cavity. *Experiments in fluids*, *51*(1), 51-63.

Biggs, C., Nokes, R., & Vennell, R. (2010). The dynamics of a steady shallow turbulent jet. *Proceedings of the 17th Congress of the Asia and Pacific Division of the International Association of Hydraulic Engineering and Research*.

Biron, P. M., Ramamurthy, A. S., & Han, S. (2004). Three-dimensional numerical modeling of mixing at river confluences. *Journal of Hydraulic Engineering*, *130*(3), 243-253.

Booij, R., & Tukker, J. (2001). Integral model of shallow mixing layers. *Journal of Hydraulic Research*, *39*(2), 169-179.

Brevis, W., Niño, Y., & Vargas, J. (2006). Experimental characterization and visualization of mass exchange process in dead zones in rivers. In *Proceedings of 3rd International Conference on Fluvial Hydraulics (RiverFlow 2006)* (pp. 235-242).

Brevis, W., García-Villalba, M., & Niño, Y. (2014). Experimental and large eddy simulation study of the flow developed by a sequence of lateral obstacles. *Environmental Fluid Mechanics*, 1-21.

Cattafesta III, L. N., Song, Q., Williams, D. R., Rowley, C. W., & Alvi, F. S. (2008). Active control of flow-induced cavity oscillations. *Progress in Aerospace Sciences*, *44*(7), 479-502.

Celik, E., Sever, A. C., Kiwata, T., & Rockwell, D. (2007). Oscillations of flow past perforated and slotted plates: attenuation via a leading-edge ramp. *Experiments in fluids*, *42*(4), 639-651.

Chan, F. C., Ghidaoui, M. S., & Kolyshkin, A. A. (2006). Can the Dynamics of Shallow Wakes be Reproduced from a Single Time-Averaged Profile. *Physics of Fluids,* 18:048105.

Chang, K., Constantinescu, G., & Park, S. O. (2007). Assessment of predictive capabilities of detached eddy simulation to simulate flow and mass transport past open cavities. *Journal of Fluids Engineering*, *129*(11), 1372-1383.

Chen, D., & Jirka, G. H. (1993). Mixing Character and Meandering Mechanism of a Plane Jet Bounded in a Shallow Water Layer. In *Hydraulic Engineering* (pp. 2147-2152), ASCE.

Chen, D., & Jirka, G. H. (1995). Experimental Study of Plane Turbulent Wakes in a Shallow Water Layer. *Fluid Dynamics Research*, 16:11.

Chen, D., & Jirka, G. H. (1997). Absolute and Convective Instabilities of Plane Turbulent Wakes in a Shallow Water Layer. *Journal of Fluid Mechanics,* 338:157-172.

Chen, D., & Jirka, G. H. (1998). Linear Stability Analysis of Turbulent Mixing Layers and Jets in Shallow Water Layers. *Journal of Hydraulic Research*, 36:815.

Chen, D., & Jirka, G. H. (1999). LIF study of plane jet bounded in shallow water layer. *Journal of Hydraulic Engineering*, 125(8), 817-826.

Cheney, E., & Kincaid, D. (2012). *Numerical mathematics and computing*. 7th edition, Brooks/Cole: Cengage Learning.

Chu, V. H., Wu, J. H., & Khayat, R. E. (1983). Stability of turbulent shear flows in shallow channel. *Proc. 20th IAHR Congress, Moscow*, 3:128–133. 19, 21, 261.

Chu, V. H., & Babarutsi, S. (1988). Confinement and bed-friction effects in shallow turbulent mixing layers. *Journal of Hydraulic Engineering*, *114*(10), 1257-1274.

Chu, V. H., Wu, J. H., & Khayat, R. E. (1991). Stability of Transverse Shear Flows in Shallow Open Channels. *Journal of Hydraulic Engineering*, 117, 1370-1388.

Constantinescu, G., Sukhodolov, A., & McCoy, A. (2009). Mass exchange in a shallow channel flow with a series of groynes: LES study and comparison with laboratory and field experiments. *Environmental fluid mechanics*, *9*(6), 587-615.

Constantinescu, G. (2013). LE of shallow mixing interfaces: A review. *Environmental Fluid Mechanics*, 1-26.

Cooley, J. W., & Tukey, J. W. (1965). An algorithm for the machine calculation of complex Fourier series. *Mathematics of computation*, *19*(90), 297-301.

Couairon, A., & Chomaz, J. M. (1997). Absolute and convective instabilities, front velocities and global modes in nonlinear systems. *Physica D: Nonlinear Phenomena*, *108*(3), 236-276.

Dracos, T., Giger, M., & Jirka, G. H. (1992). Plane turbulent jets in a bounded fluid layer. *Journal of Fluid Mechanics*, 241, 587–614.

Dudley, J., & Ukeiley, L. (2011). Detached Eddy Simulation of a Supersonic Cavity Flow With and Without Passive Flow Control. *AIAA Computational Fluid Dynamics Conference*, AIAA Paper 2011-3844.

Einstein, A. (1926). *Die Naturwissenschaften*, *A translation can be found in Ideas and Opinions*. Bonanza Books, New York, 1954, pp. 249-253.

Ekmekci, A., & Rockwell, D. (2007). Oscillation of shallow flow past a cavity: Resonant coupling with a gravity wave. *Journal of fluids and structures*, *23*(6), 809-838.

Elwell, F. (2004). *Flushing of embayments*. Ph.D Disseration, Department of Applied Mathematics and Theoretical Physics, Cambridge University.

Engelhardt, C., Krüger, A., Sukhodolov, A., & Nicklisch, A. (2004). A study of phytoplankton spatial distributions, flow structure and characteristics of mixing in a river reach with groynes. *Journal of Plankton Research*, *26*(11), 1351-1366.

Ercan, A., & Younis, B. A. (2009). Prediction of Bank Erosion in a Reach of the Sacramento River and its Mitigation with Groynes. *Water resources management*, *23*(15), 3121-3147.

Fujihara, M., Sakurai, Y., & Okamoto, T. (2011). Hydraulic structure and material transport in an irrigation channel with a side-cavity for aquatic habitat. *Transactions of The Japanese Society of Irrigation, Drainage and Rural Engineering, Volume 78, Issue 1,* pp. 17-22.

Ghidaoui, M. S., & Kolyshkin, A. A. (1999). Linear stability analysis of lateral motions in compound open channels. *Journal of Hydraulic Engineering*, *125*(8), 871-880.

Ghidaoui, M. S., Kolyshkin, A. A., Liang, J. H., Chan, F. C., Li, Q., & Xu, K. (2006). Linear and Nonlinear Analysis of Shallow Wakes. *Journal of Fluid Mechanics,* 548:309.

Giger, M., Dracos, T., & Jirka, G. (1991). Entrainment and mixing in plane turbulent jets in shallow-water. *Journal of Hydraulic Research*, 29 (5), 615–642.

Grubišic, V., Smith, R. B., & Schär, C. (1995). The effect of bottom friction on shallow-water flow past an isolated obstacle. *Journal of the atmospheric sciences*, 52(11), 1985-2005.

Hart, D. P. (1998). High-speed PIV analysis using compressed image correlation. *Journal of Fluids Engineering*, *120*(3), 463-470.

Heller, H. H., & Bliss, D. B. (1975). The physical mechanism of flow-induced pressure fluctuations in cavities and concepts for their suppression. *AIAA paper*, *491*, 1975.

Huerre, P., & Monkewitz, P. (1985). Absolute and convective instabilities in free shear layers. *Journal of Fluid Mechanics*, *159*, 151-68.

Huerre, P., & Monkewitz, P. A. (1990). Local and global instabilities in spatially developing flows. *Annual Review of Fluid Mechanics*, 22(1), 473-537.

Ikeda, S., Yoshike, T., & Sugimoto, T. (1999). Experimental study on the structure of open channel flow with impermeable spur dikes. *Annual Journal of Hydraulic Engineering-JSCE*, *43*, 281-286.

Ingram, G. R., & Chu, V. H. (1987). Flow around Islands in Rupert Bay: An Investigation of the Bottom Friction Effect. *Journal of Geophysical Research,* 92:14,521.

Jamieson, E., Gaskin, S. J. (2007). Laboratory Study of 3D characteristics of recirculating flow in a river embayment. In *Proceedings of the 32st IAHR Congress, Venice, Italy*, paper 539.

Jarrett, E. L., & Sweeney, T. L. (1967). Mass transfer in rectangular cavities.*AIChE Journal*, *13*(4), 797-800.

Jirka, G. H. (1994). *Shallow jets*. In Davies, PA and Neves, MJV (Ed.), Recent Research Advances in the Fluid Mechanics of Turbulent Jets and Plumes, Volume 255 of Nato Advanced Science Institutes Series, Series E, Applied Sciences, Dordrecht, Netherlands, 155–175.

Jirka, G. H. (1998). Large scale flow structures and mixing processes in shallow flows. In *Proc. 2nd Int. Symp. Env. Hydr., Hong Kong*. 15, 202.

Jirka, G. H. (1999). *Environmental fluid mechanics: Its role in solving problems of pollution in lakes, rivers and coastal waters*. In Bianchi G., ed., 'Environmental Applications of Mechanics and Computer Science. CISM Courses and Lectures, No 409,' pp. 49–98. Springer, Berlin. 15, 202.

Jirka, G. H. (2001). Large scale flow structures and mixing processes in shallow flows. *Journal of hydraulic research*, 39(6), 567-573.

Jirka, G. H., & Uijttewaal, W. S. J. (2004). Shallow flows: a definition. *Shallow flows*, 3-11.

Kadotani, K., Fujita, I., Matsubara, T., & Tsubaki, R. (2008). Analysis of water surface oscillation at open channel side cavity by image analysis and large eddy simulation. In *ICHE conference*, Nagoya, Japan, September 8-12.

Kang, J., Yeo, H., & Kim, C. (2012). An Experimental Study on a Characteristics of Flow around Groyne Area by Install Conditions. *Engineering*, *4*(10), pp. 636-645.

Kawamura, T., Mayer, S., Garapon, A., & Sorensen, L. (2002). Large eddy simulation of a flow past free surface piercing circular cylinder. *Journal of Fluid Engineering,* 124:91–101.

Keane, R. D., & Adrian, R. J. (1990). Optimization of particle image velocimeters. I. Double pulsed systems. *Measurement science and technology*,*1*(11), 1202.

Kimura, I., & Hosoda, T. (1997). Fundamental properties of flows in open channels with dead zone. *Journal of Hydraulic Engineering*, *123*(2), 98-107.

Knisely, C., & Rockwell, D. (1982). Self-sustained low-frequency components in an impinging shear layer. *Journal of Fluid Mechanics*, *116*, 157-186.

Kolyshkin, A. A., & Ghidaoui, M. S. (2002). Gravitational and shear instabilities in compound and composite channels. *Journal of Hydraulic Engineering*, *128*(12), 1076-1086.

Kolyshkin, A. A., & Ghidaoui, M. S. (2003). Stability analysis of shallow wake flows. *Journal of Fluid Mechanics*, *494*, 355-377.

Kuo, C. H., & Yang, D. W. (2004). Lock-on phenomena in cavity flows. *Journal of the Chinese Institute of Engineers*, *27*(1), 119-128.

Kurzke, M., Weitbrecht, V., & Jirka, G. H. (2002). Laboratory concentration measurements for determination of mass exchange between groin fields and main stream. In *IAHR Conference,'River Flow', Louvain de la Neuve, Belgium*.

Lakshminarayana, B. (1996). *Fluid Dynamics and Heat Transfer of Turbomachinery*. NY: Wiley Interscience.

Landreth, C. C., & Adrian, R. J. (1988). Electro-optical image shifting for particle image velocimetry. *Applied Optics*, 27, 4216-4220.

Le Coz, J., Brevis, W., Niño, Y., Paquier, A., & Riviére, N. (2006). Open-channel side-cavities: A comparison of field and flume experiments. In *Proceedings of 3rd International Conference on Fluvial Hydraulics, River Flow 2006,* pp. 235-242.

Liang, D. F., Chong, K. J. Y., Thusyanthan, N. I., & Tang, H. W. (2012). Thermal imaging study of scalar transport in shallow wakes. *Journal of Hydrodynamics*, Ser. B, 24(1), 17-24.

Martinez, M. A., & Onorato, M. (2009). Cavity Flow Control by a Rod in Crossflow. *Acc. Sc. Torino, Atti Sc. Fis.* 143.

Martinez, M. A., Di Cicca, G. M., Iovieno, M., & Onorato, M. (2012). Control of cavity flow oscillations by high frequency forcing. *Journal of Fluids Engineering*,*134*(5), 051201.

McCoy, A., Constantinescu, G., & Weber, L. (2006). Exchange processes in a channel with two vertical emerged obstructions. *Flow, turbulence and combustion*, *77*(1-4), 97-126.

McCoy, A., Constantinescu, G., & Weber, L. (2007). A numerical investigation of coherent structures and mass exchange processes in channel flow with two lateral submerged groynes. *Water resources research*, *43*(5), W05445.

McCoy, A., Constantinescu, G., & Weber, L. J. (2008). Numerical investigation of flow hydrodynamics in a channel with a series of groynes. *Journal of Hydraulic Engineering*, *134*(2), 157-172.

McGrath, S., & Shaw, L. (1996). Active control of shallow cavity acoustic resonance. *AIAA paper*, *1949*, 1996.

Meile, T., Boillat, J. L., & Schleiss, A. J. (2011). Water-surface oscillations in channels with axi-symmetric cavities. *Journal of Hydraulic Research*, *49*(1), 73-81.

Mizumura, K., & Yamasaka, M. (2002). Flow in open-channel embayments. *Journal of Hydraulic Engineering*, *128*(12), 1098-1101.

Mongeau, L., Franchek, M. A., & Kook, H. (1999). Control of interior pressure fluctuations due to flow over vehicle openings. *Human Factors*, 2015, pp. 06-22, doi:10.4271/1999-01-1813.

Monkewitz, P. A. (1990). The role of absolute and convective instability in predicting the behavior of fluid systems. *European Journal of Mechanics B Fluids*, *9*, 395-413.

Muto, Y., Imamoto, H., & Ishigaki, T. (2000). Turbulence characteristics of a shear flow in an embayment attached to a straight open channel. In *Proceedings of the 4th International Conference on HydroScience and Engineering, IAHR,* Seoul, Korea, p. 232.

Muto, Y., Baba, Y., & Aya, S. (2002). Velocity measurements in open channel flow with rectangular embayments formed by spur dykes. *Ann. Disas. Prev. Res. Inst. Kyoto Univ*, 45B-2.

Naudascher, E., & Rockwell, D. (1994). *Flow-Induced Vibrations: an engineering guide*. Dover Publications, Inc., New York, USA, pp 71-80.

Nazarovs, S. (2005). Stability analysis of shallow wake flows with free surface. In *Proceedings of the International Conference on Theory and Application of Mathematics and Informatics,* Alba Iulia, Romania, pp. 345-354.

Newland, D. E. (1993). *An introduction to Random Vibrations, Spectral & Wavelet Analysis*, Prentice Hall, Singapore.

Nezu, I., & Nakagawa, H. (1993). Turbulence in open channels. *AA Balkema, Rotterdam, The Netherlands*.

Nezu, I., & Onitsuka, K. (2002). PIV Measurements of side-cavity open-channel flows-Wando model in rivers. *Journal of Visualization*, *5*(1), 77-84.

Oertel Jr, H. (1990). Wakes behind blunt bodies. *Annual Review of Fluid Mechanics*, *22*(1), 539-562.

Ohmoto, T., Hirakawa, R., & Watanabe, K. (2005). Interaction between water surface oscillations and large eddies in an open channel with spur dikes. In *31st IAHR Congress, Seoul, Korea,* pp. 347–348.

Ohmoto, T., Hirakawa, R., & Watanabe, K. (2009). Effects of Spur Dike Directions on River Bed Forms and Flow Structures. In *Advances in Water Resources and Hydraulic Engineering*, pp. 957-962, Springer Berlin Heidelberg.

Panickar, P., & Raman, G. (2008). Understanding the mechanism of cavity resonance suppression using a cylindrical rod in crossflow. *AIAA paper*, *54*.

Perry, A. E., & Chong, M. S. (1987). A description of eddying motions and flow patterns using critical-point concepts. *Annual Review of Fluid Mechanics*, *19*(1), 125-155.

Pickering, C. J., & Halliwell, N. A. (1984). Speckle photography in fluid flows: signal recovery with two-step processing. *Applied Optics*, *23*(8), 1128-1129.

Pope, S. B. (2000). *Turbulent Flows*. Cambridge University Press.

Rhoads, B. L., & Sukhodolov, A. N. (2008). Lateral momentum flux and the spatial evolution of flow within a confluence mixing interface. *Water Resources Research*, 44(8), doi:10.1029/2007WR006634.

Ribi, J. M., Boillat, J. L., & Schleiss, A. J. (2010). Flow exchange between a channel and a rectangular embayment equipped with a diverting structure. In *Proceedings International Conference on Fluvial Hydraulics, IAHR*. ISBN 978-3-939230-00-7, pp. 665-671.

Riviere, N., Garcia, M., Mignot, E., & Travin, G. (2010). Characteristics of the recirculation cell pattern in a lateral cavity. In *Proceedings International Conference on Fluvial Hydraulics, IAHR*. ISBN 978-3-939230-00-7, pp. 673-679.

Rockwell, D., & Naudascher, E. (1978). Review-self-sustaining oscillations of flow past cavities. *ASME Transactions Journal of Fluids Engineering*, *100*, 152-165.

Rockwell, D., & Naudascher, E. (1979). Self-sustained oscillations of impinging free shear layers. *Annual Review of Fluid Mechanics*, *11*(1), 67-94.

Rockwell, D. (1983). Oscillations of impinging shear layers. *AIAA journal*, *21*(5), 645-664.

Rowland, J. C., Stacey, M. T., & Dietrich, W. E. (2009). Turbulent characteristics of a shallow wall-bounded plane jet: experimental implications for river mouth hydrodynamics. *Journal of Fluid Mechanics*, 627, 423-449.

Roy, A. G., Buffin-Belanger, T., Lamarre, H., & Kirkbride, A. D. (2004). Size, shape and dynamics of large-scale turbulent flow structures in a gravel-bed river. *Journal of Fluid Mechanics*, *500*, 1-27.

Sadeque, M. A. F., Rajaratnam, N., & Loewen, M.R. (2009). Shallow turbulent wakes behind bed-mounted cylinders in open channels. *Journal of Hydraulic Research*, 47(6), 727-743.

Sanjou, M., & Nezu, I. (2013). Hydrodynamic characteristics and related mass-transfer properties in open-channel flows with rectangular embayment zone. *Environmental Fluid Mechanics*, *13*(6), 527-555.

Sarno, R. L., & Franke, M. E. (1994). Suppression of flow-induced pressure oscillations in cavities. *Journal of Aircraft*, *31*(1), 90-96.

Sarpotdar, S., Panickar, P., & Raman, G. (2009). Cavity tone suppression using a rod in cross flow–investigation of shear layer stability mechanism. In *Proceedings of the 47th AIAA Aerospace Sciences Meeting Including The New Horizons Forum and Aerospace Exposition. Orlando: AIAA*, pp. 1-32.

Schär, C., & Smith, R. B. (1993). Shallow-water flow past isolated topography. Part I: Vorticity production and wake formation. *Journal of the atmospheric sciences*, 50(10), 1373-1400.

Seabergh, W. C. (2002). *Inner-bank erosion processes and solutions at coastal inlets* (p. 11). US Army Engineer Research and Development Center.

Socolofsky, S. A., & Jirka, G. H. (2004). Large-scale flow structures and stability in shallow flows. *Journal of Environmental Engineering Science*, 3, 451–462.

Stanek, M. J., Ross, J. A., Odedra, J., & Peto, J. (2003). High frequency acoustic suppression- The mystery of the rod-in-crossflow revealed. In *41st AIAA Aerospace Sciences Meeting & Exhibit, Reno, NV*.

Sukhodolov, A., Uijttewaal, W. S. J., & Engelhardt, C. (2002). On the correspondence between morphological and hydrodynamical patterns of groyne fields. *Earth Surface Processes and Landforms*, *27*(3), 289-305.

Sukhodolov, A., Engelhardt, C., Krüger, A., & Bungartz, H. (2004). Case study: Turbulent flow and sediment distributions in a groyne field. *Journal of Hydraulic Engineering*, *130*(1), 1-9.

Sukhodolov, A. N., & Sukhodolova, T. A. (2013). Shallow wake behind exposed wood-induced bar in a gravel-bed river. *Environmental Fluid Mechanics*, 1-13.

Tang, Y. P., & Rockwell, D. (1983). Instantaneous pressure fields at a corner associated with vortex impingement. *Journal of Fluid Mechanics*, *126*, 187-204.

Tennekes, H., & Lumley, J.L. (1977). *A First Course in Turbulence*. Cambridge MIT Press.

Thompson, M., Hourigan, K., & Sheridan, J. (1996). Three-dimensional instabilities in the wake of a circular cylinder. *Experimental Thermal and Fluid Science*, 12(2), 190-196.

Tukker, J., & Booij, R. (1996). The Influence of Shallowness on Large-Scale Coherent Structures. In *Advances in Turbulence VI*. ISBN 978-94-009-0297-8, pp. 141-144. Springer Netherlands.

Tuna, B. A., Tinar, E., & Rockwell, D. (2013). Shallow flow past a cavity: globally coupled oscillations as a function of depth. *Experiments in fluids*, *54*(8), 1-20.

Uijttewaal, W. S. J., & Tukker, J. (1998). Development of quasi two-dimensional structures in a shallow free-surface mixing layer. *Experiments in Fluids*, *24*(3), 192-200.

Uijttewaal, W. S. J. (1999). Groyne field velocity patterns determined with particle tracking velocimetry. In *Proceedings of the 28th IAHR Congress,* Graz, Austria.

Uijttewaal, W. S. J., & Booij, R. (2000). Effects of shallowness on the development of free-surface mixing layers. *Physics of Fluids*, *12*, 392-402.

Uijttewaal, W. S. J., Lehmann, D., & Mazijk, A. V. (2001). Exchange processes between a river and its groyne fields: Model experiments. *Journal of Hydraulic Engineering*, *127*(11), 928-936.

Uijttewaal, W. S. J., & Jirka, G. H. (2003). Experiments on grid induced turbulence in shallow flows. *Journal of Fluid Mechanics*, 489, 325–344.

Uijttewaal, W. S. J. (2005). Effects of groyne layout on the flow in groyne fields: Laboratory experiments. *Journal of Hydraulic Engineering*, *131*(9), 782-791.

Uijttewaal, W. S. J. (2011). Horizontal mixing in shallow flows. In *34th IAHR world congress*, Brisbane, Australia. ISBN 978-0-85825-868-6, pp. 3808-3814.

Ukeiley, L. S., Ponton, M. K., Seiner, J. M., & Jansen, B. (2004). Suppression of pressure loads in cavity flows. *AIAA journal*, *42*(1), 70-79.

USACE (2002). Engineering and design, coastal engineering manual, harbor hydrodynamics. *Report EM* 1110-2-1100. Department of the Army, US Army Corps of Engineers, Washington DC.

v Carmer, C. F., Weitbrecht, V., & Jirka, G. H. (2001). On the genesis and fate of large coherent vortical structures in turbulent shallow wake flows. In *Proc. 3rd Int. Symp. Env. Hydr. Tempe, USA*. 37, 39, 188, 244, 286.

v Carmer, C. F., Rummel, A. C., & Jirka, G. H. (2003). Influence of secondary motion in large-scale coherent structures on the mass transport in a shallow turbulent wake. *Proc. Int. Symp. Shallow Flows, Delft, NL*. 37, 67, 343.

v Carmer, C.F. (2005). *Shallow turbulent wake flows: momentum and mass transfer due to large-scale coherent vortical structures*. Dissertationsreihe am Institut für

Hydromechanik der Universität Karlsruhe (TH), 3-937300-63-5, 1439-4111, Universitätsverlag Karlsruhe, Germany.

Valentine, E. M., & Wood, I. R. (1979). Experiments in longitudinal dispersion with dead zones. *Journal of the Hydraulics Division*, *105*(8), 999-1016.

van Prooijen, B.C., Booij, R., & Uijttewaal, W. S. J. (2000). Measurement and analysis methods of large scale horizontal coherent structures in a wide shallow channel. In *10th international symposium on applications of laser techniques to fluid mechanics.* Calouste Gulbenkian Foundation, Lisbon.

van Prooijen, B. C., & Uijttewaal, W. S. J. (2002). A linear approach for the evolution of coherent structures in shallow mixing layers. *Physics of Fluids*, *14*, 4105-4114.

van Prooijen, B. C., & Uijttewaal, W. S. J. (2009). The relevance of a back-scatter model for depth-averaged flow simulation. *Flow, Turbulence and Combustion*, *82*(1), 73-91.

Wallast, I., Uijttewaal, W. S. J., & van Mazijk, A. (1999). Exchange processes between groyne field and main stream. In *Proceedings from the 28th IAHR Congress,* Graz, Austria.

Weitbrecht, V., & Jirka, G. H. (2001). Flow patterns and exchange processes in dead zones of rivers. In *Proceedings of the Congress-International Association for Hydraulic Research*, pp. 439-445.

Weitbrecht, V., Socolofsky, S. A., & Jirka, G. H. (2008). Experiments on mass exchange between groin fields and main stream in rivers. *Journal of Hydraulic Engineering*, *134*(2), 173-183.

Willert, C. E., & Gharib, M. (1991). Digital particle image velocimetry. *Experiments in fluids*, *10*(4), 181-193.

Williamson, C. H. K. (1996). Vortex dynamics in the cylinder wake. *Annual review of fluid mechanics*, 28(1), 477-539.

Wirtz, C. (2004). Hydromorphologische und morphodynamische Analyse von Buhnenfeldern der unteren Mittelelbe im Hinblick auf eine ökologische Gewässerunterhaltung. *Doktorarbeit-PhD Thesis, Fachbereich Geowissenschaften der Freien Universität Berlin*.

Wolfinger, M., Ozen, C. A., & Rockwell, D. (2012). Shallow flow past a cavity: Coupling with a standing gravity wave. *Physics of Fluids*, *24*, 104103.

Yaeger, M. & Duan, J. (2010). Mean Flow and Turbulence around Two Series of Experimental Dikes. In *World Environmental and Water Resources Congress*, 1692-1701.

Yalin, M. S. (1992). *River mechanics*. Pergamon Press, Oxford, England.

Yossef, M. F., & de Vriend, H. J. (2011). Flow details near river groynes: experimental investigation. *Journal of Hydraulic Engineering*, *137*(5), 504-516.

Young, D. F., Munson, B. R., Okiishi, T. H., & Huebsch, W. W. (2010). *A brief introduction to fluid mechanics*. John Wiley & Sons. 4th Edition, J. Wiley & Sons, New York.

Yu, E., Avital, J., & Williams, J. (2008). Large eddy simulation of flow past free surface piercing circular cylinders. *Journal of Fluid Engineering,*130:101304.1–101304.9.

Zhang, X. (1995). Compressible cavity flow oscillation due to shear layer instabilities and pressure feedback. *AIAA journal*, *33*(8), 1404-1411.

Zhang, H. Q., Fey, U., Noack, B. R., König, M., & Eckelmann, H. (1995). On the transition of the cylinder wake. *Physics of Fluids*, 7, 779-794.

Zhang, X., Chen, X. X., Rona, A., & Edwards, J. A. (1999). Attenuation of cavity flow oscillation through leading edge flow control. *Journal of Sound and Vibration*, *221*(1), 23-47.

APPENDIX A

GLOBALLY COUPLED OSCILLATIONS AS A FUNCTION OF DEPTH

In this Appendix, supplementary images are shown for the case where a gravity standing wave is present within the cavity, which was discussed in Chapter 3. In order to give more details concerning the different stages of the oscillation, each figure includes nine different phases of the oscillation cycle, $\phi = 0°$ to 320°. Moreover, seven different elevations within the shallow water layer are demonstrated to show dependence of flow structure to the elevation above the bed. Figures A.1 through A.7 show patterns of phase-averaged streamlines $<\psi>_p$, Figures A.8 to A.14 give phase-averaged transverse velocity $<v>_p/U$, and Figures A.15 to A.21 represent phase-averaged contours of constant vorticity $<\omega>_p L/U$. These figures provide further insight into the flow physics associated with the onset of the gravity standing wave within the cavity.

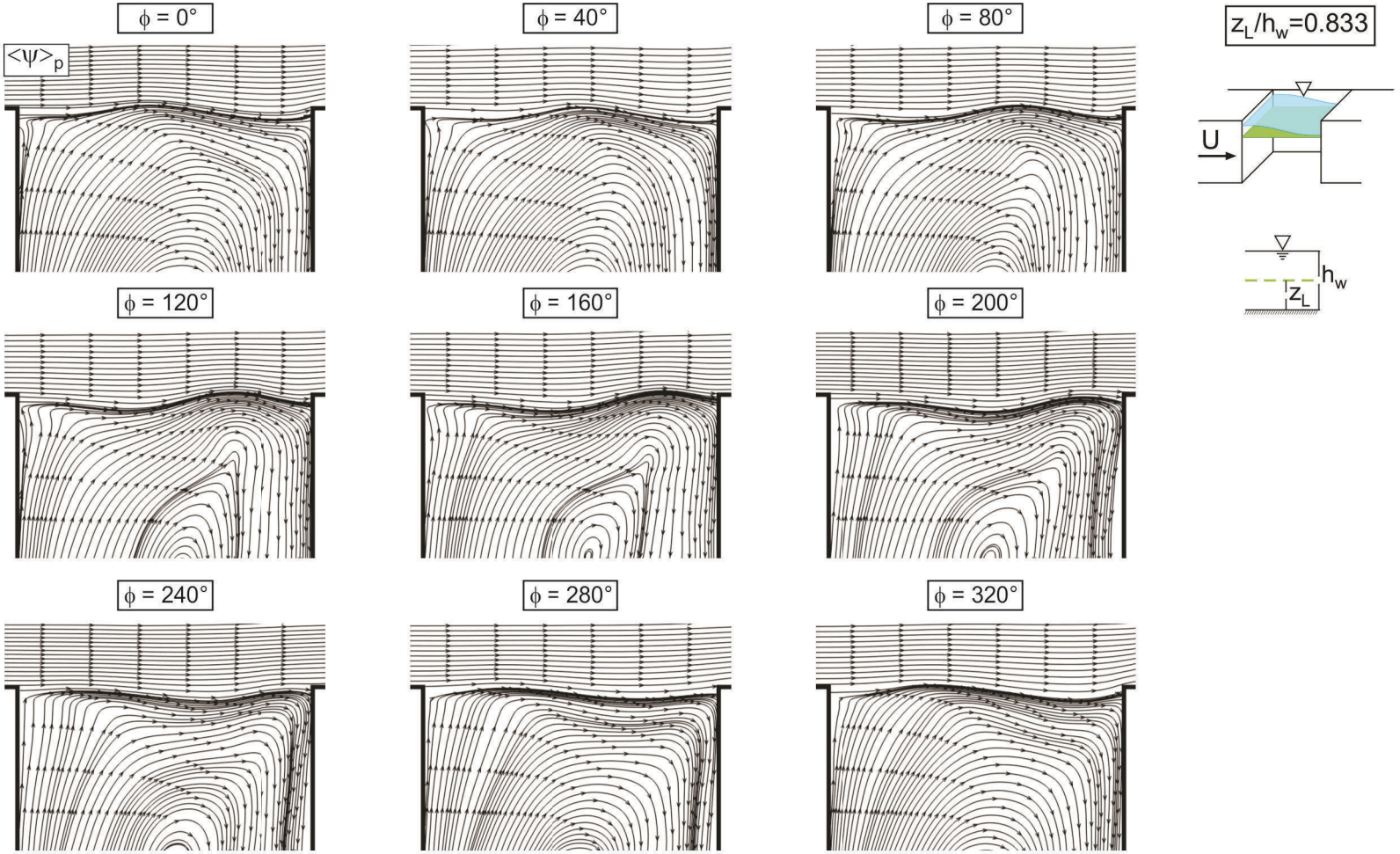

Figure A.1: Phase-averaged patterns of streamlines $<\psi>_p$ at $z_L/h_w = 0.833$ for nine different phases ($\phi = 0°$ to $320°$) of the oscillation cycle in presence of the gravity standing wave within the cavity ($U/f_nL = 1.44$).

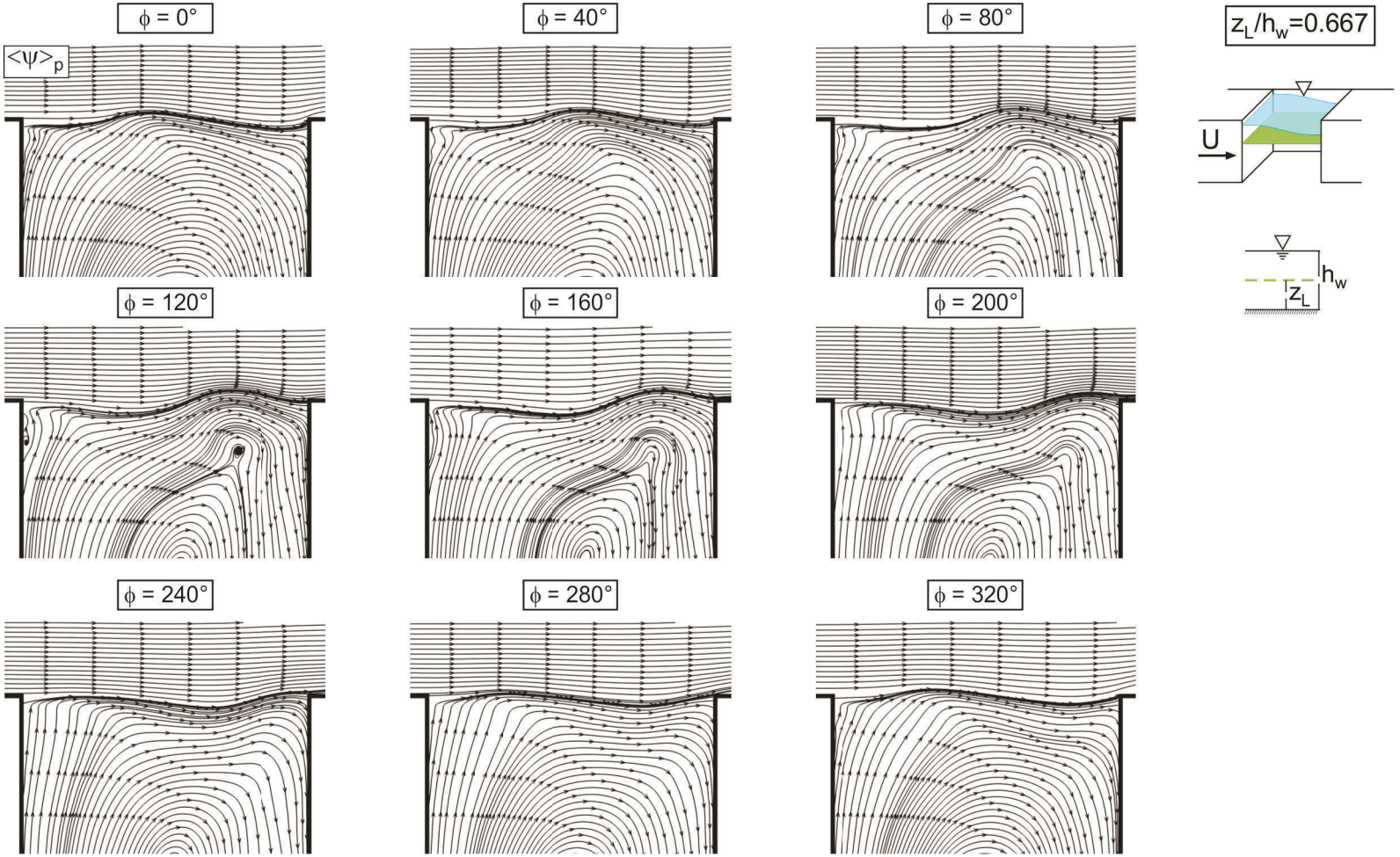

Figure A.2: Phase-averaged patterns of streamlines $<\psi>_p$ at $z_L/h_w = 0.667$ for nine different phases ($\phi = 0°$ to $320°$) of the oscillation cycle in presence of the gravity standing wave within the cavity ($U/f_nL = 1.44$).

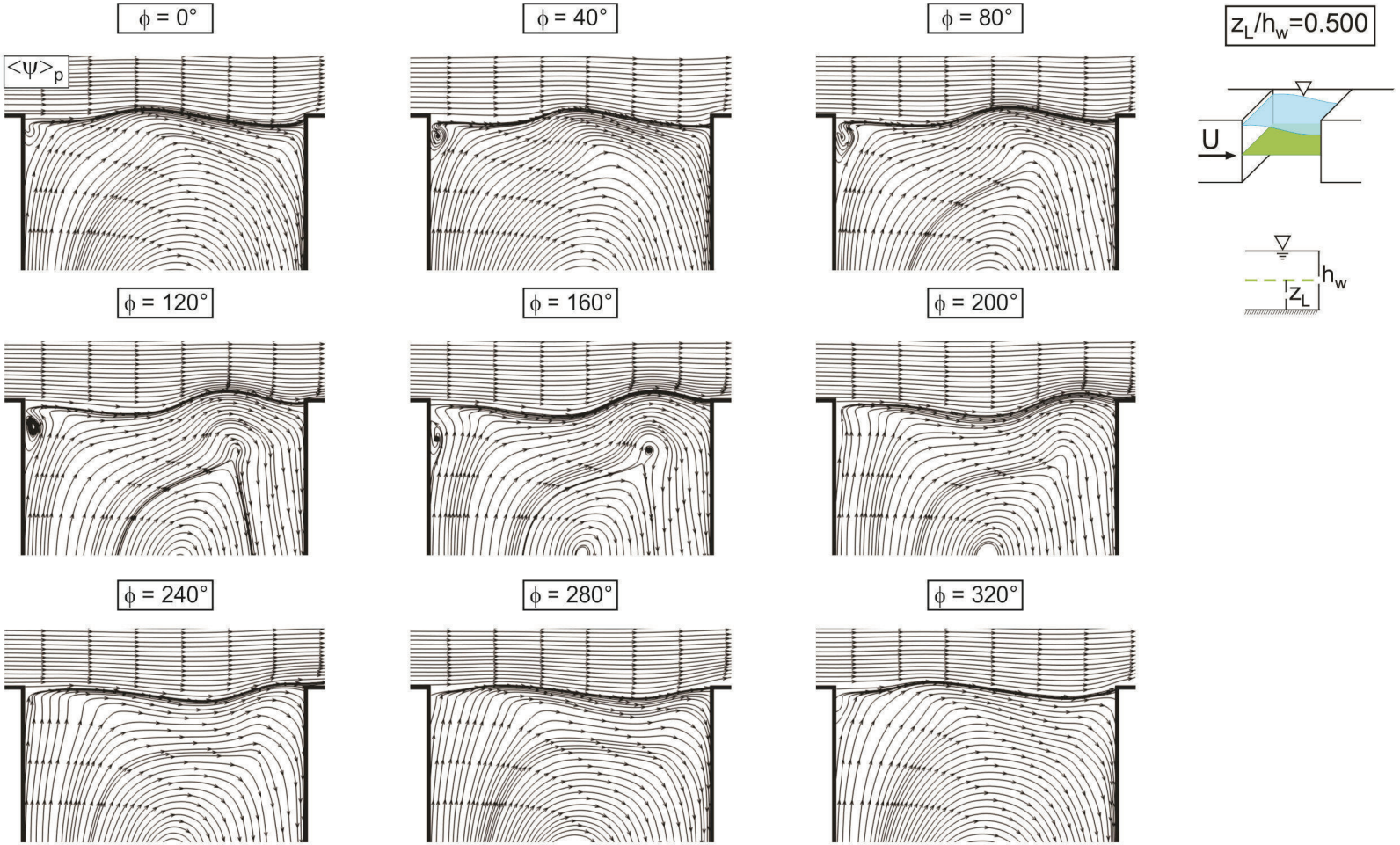

Figure A.3: Phase-averaged patterns of streamlines $\langle\psi\rangle_p$ at $z_L/h_w = 0.500$ for nine different phases ($\phi = 0°$ to $320°$) of the oscillation cycle in presence of the gravity standing wave within the cavity ($U/f_nL = 1.44$).

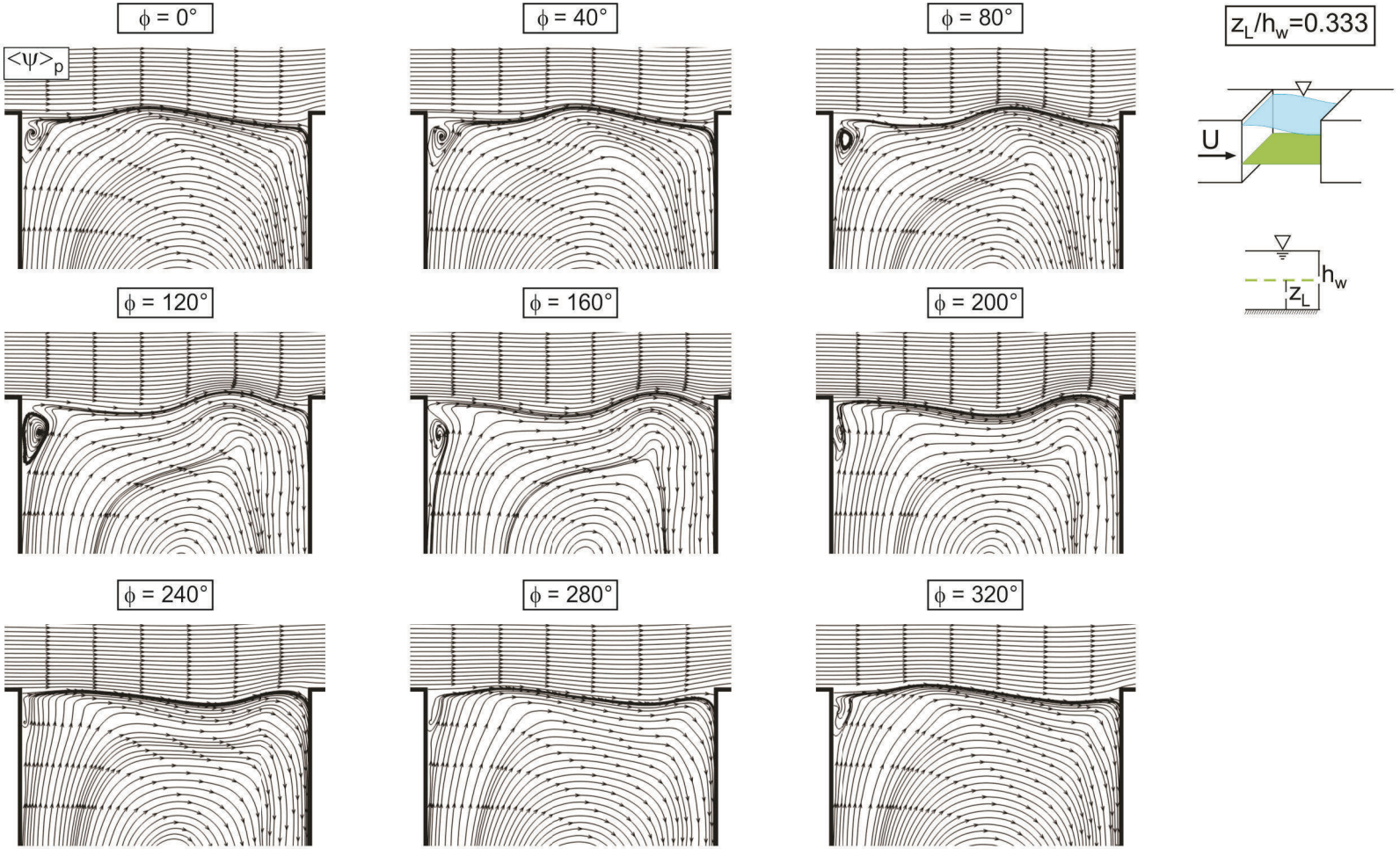

Figure A.4: Phase-averaged patterns of streamlines $<\psi>_p$ at $z_L/h_w = 0.333$ for nine different phases ($\phi = 0°$ to $320°$) of the oscillation cycle in presence of the gravity standing wave within the cavity ($U/f_nL = 1.44$).

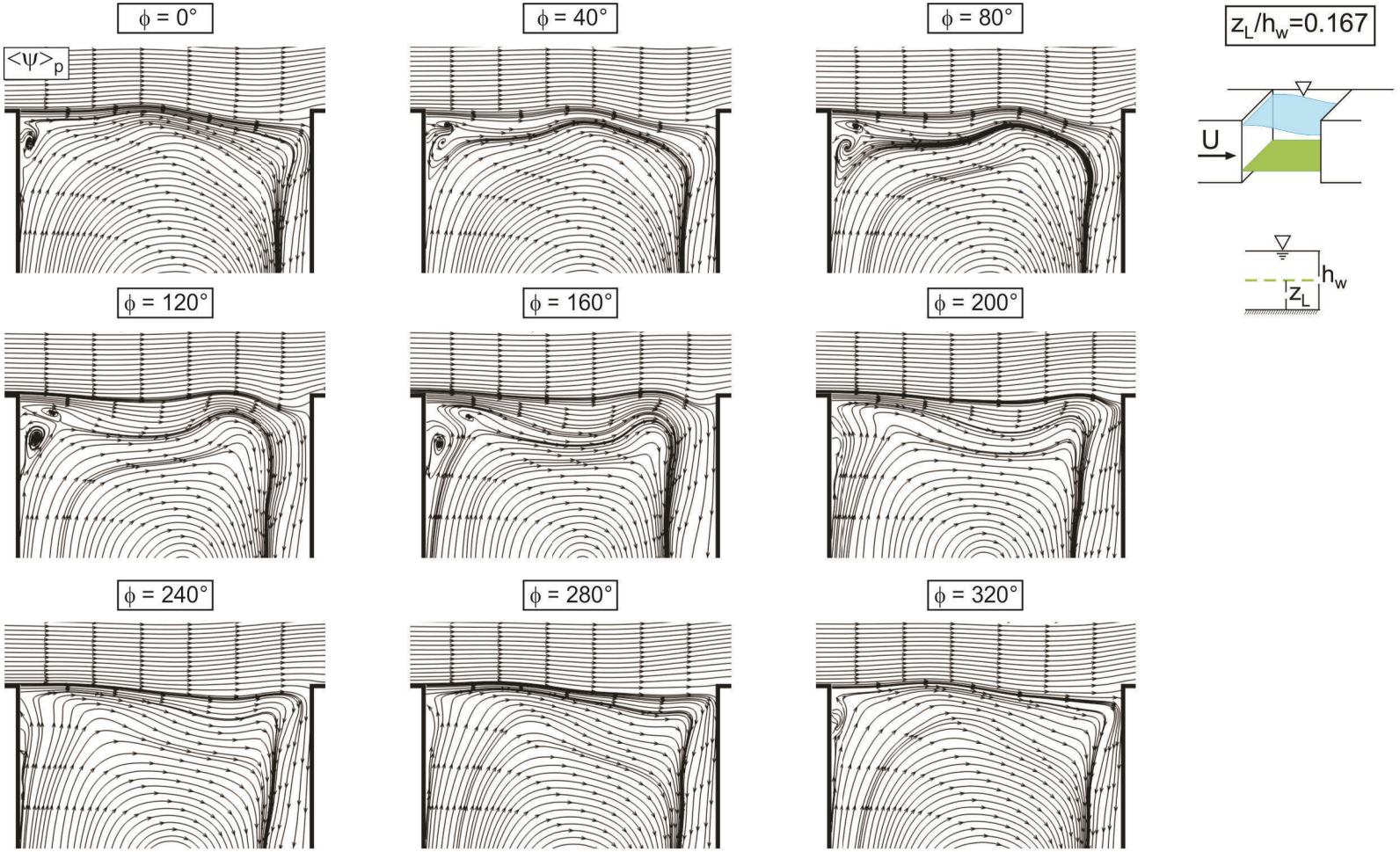

Figure A.5: Phase-averaged patterns of streamlines $<\psi>_p$ at $z_L/h_w = 0.167$ for nine different phases ($\phi = 0°$ to $320°$) of the oscillation cycle in presence of the gravity standing wave within the cavity ($U/f_nL = 1.44$).

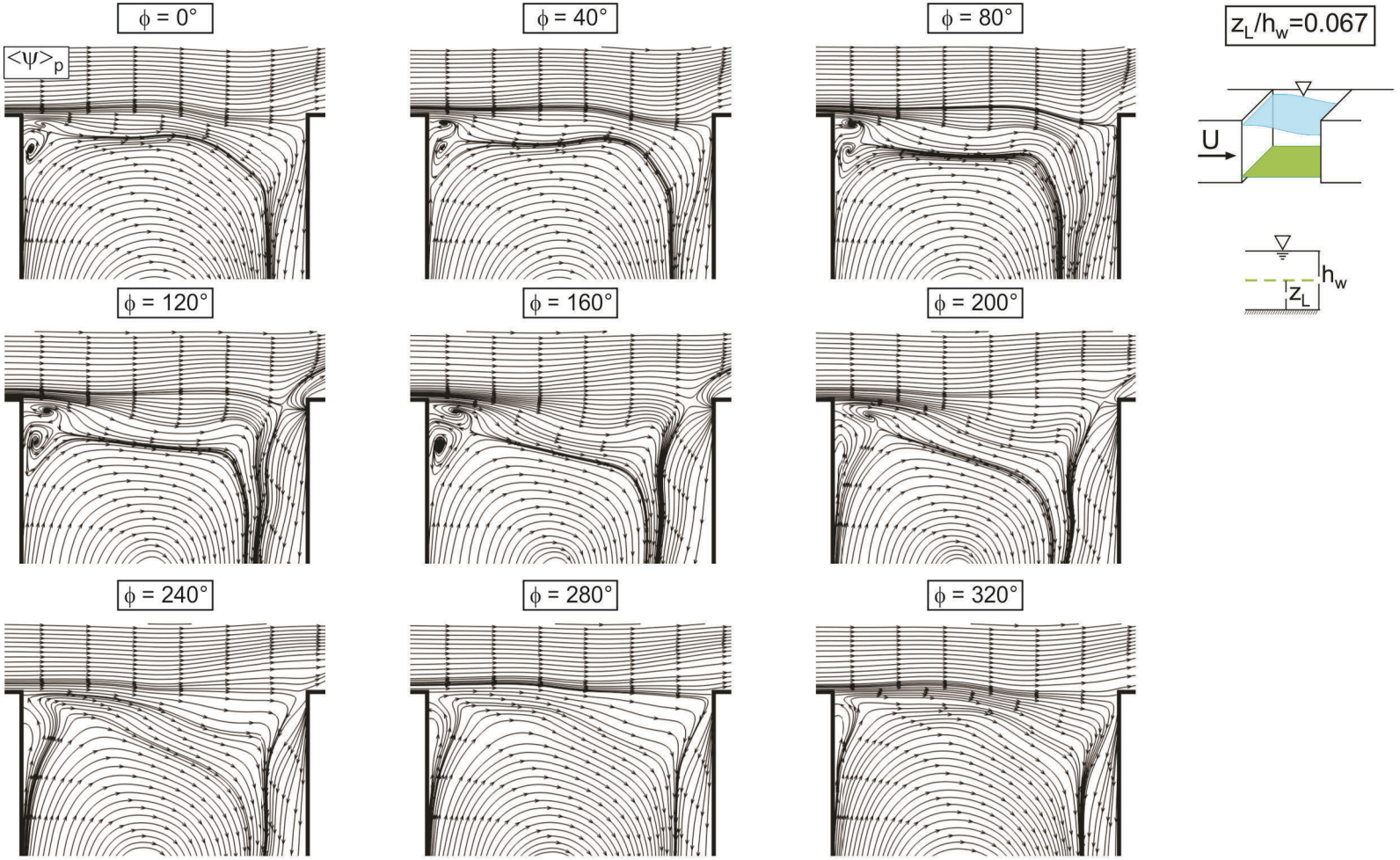

Figure A.6: Phase-averaged patterns of streamlines $\langle\psi\rangle_p$ at $z_L/h_w = 0.067$ for nine different phases ($\phi = 0°$ to $320°$) of the oscillation cycle in presence of the gravity standing wave within the cavity ($U/f_nL = 1.44$).

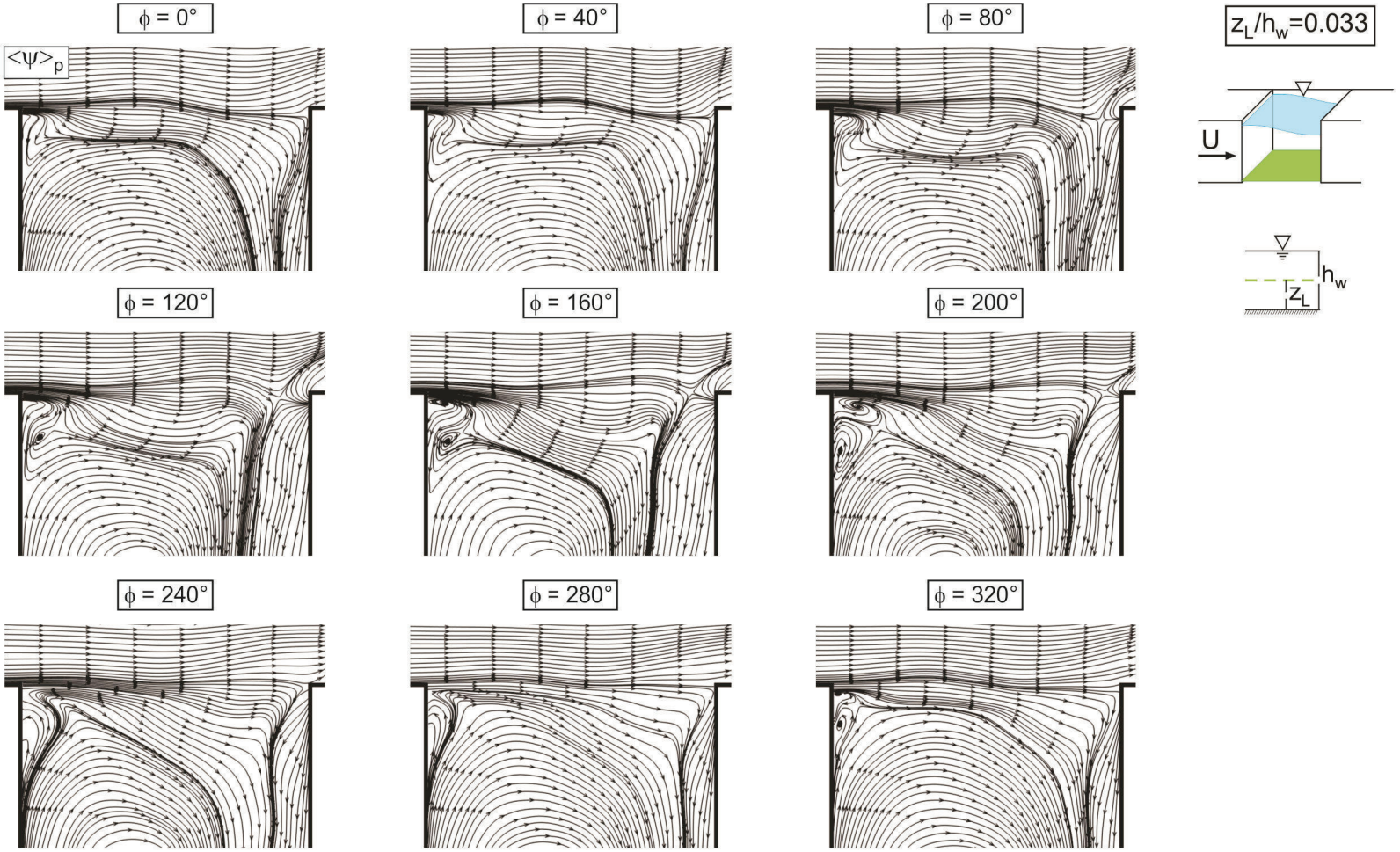

Figure A.7: Phase-averaged patterns of streamlines $<\psi>_p$ at $z_L/h_w = 0.033$ for nine different phases ($\phi = 0°$ to $320°$) of the oscillation cycle in presence of the gravity standing wave within the cavity ($U/f_nL = 1.44$).

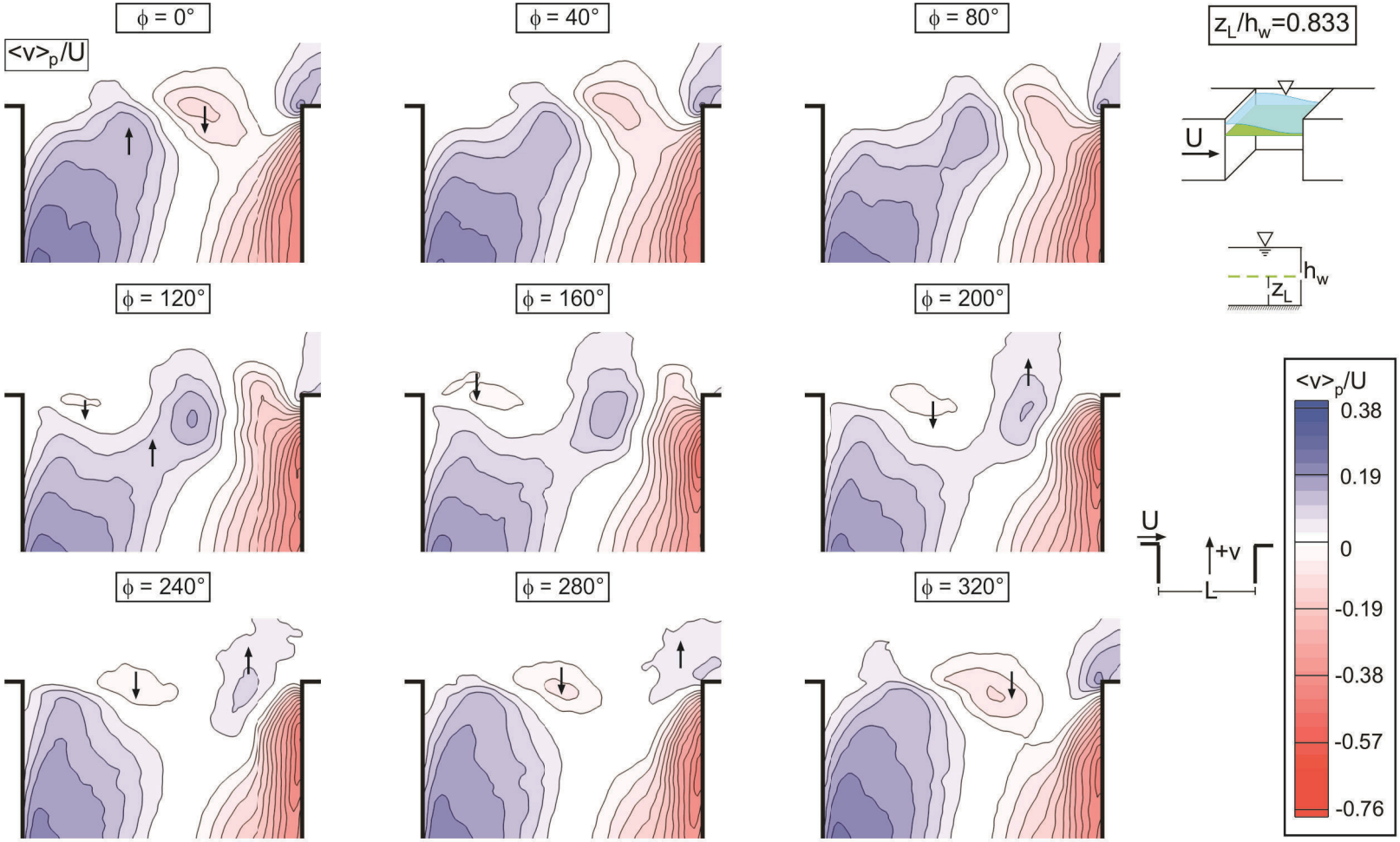

Figure A.8: Contours of phase-averaged transverse velocity $\langle v \rangle_p / U$ at $z_L/h_w = 0.833$ for nine different phases ($\phi = 0°$ to $320°$) of the oscillation cycle in presence of the gravity standing wave within the cavity ($U/f_n L = 1.44$).

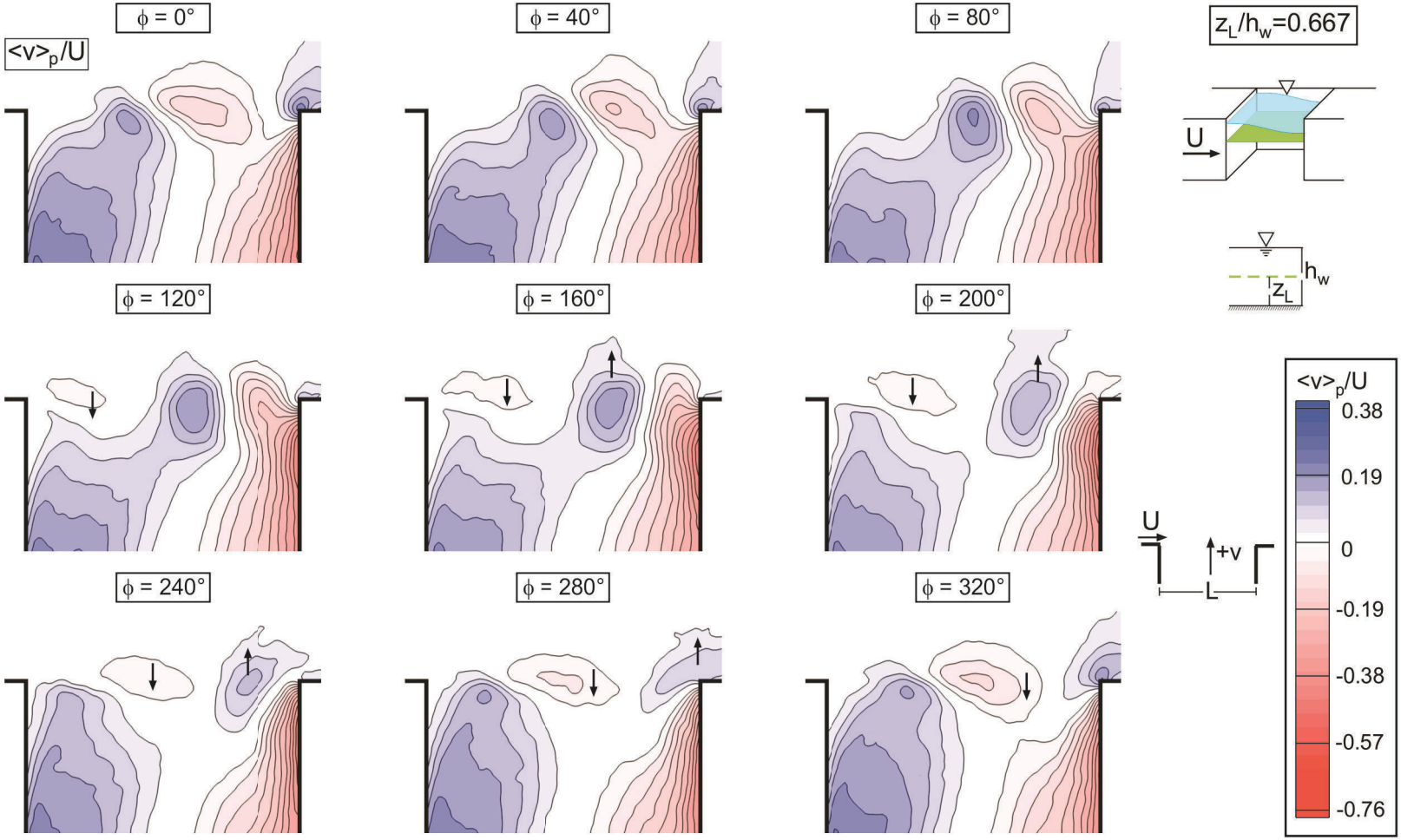

Figure A.9: Contours of phase-averaged transverse velocity $\langle v \rangle_p / U$ at $z_L/h_w = 0.667$ for nine different phases ($\phi = 0°$ to 320°) of the oscillation cycle in presence of the gravity standing wave within the cavity ($U/f_n L = 1.44$).

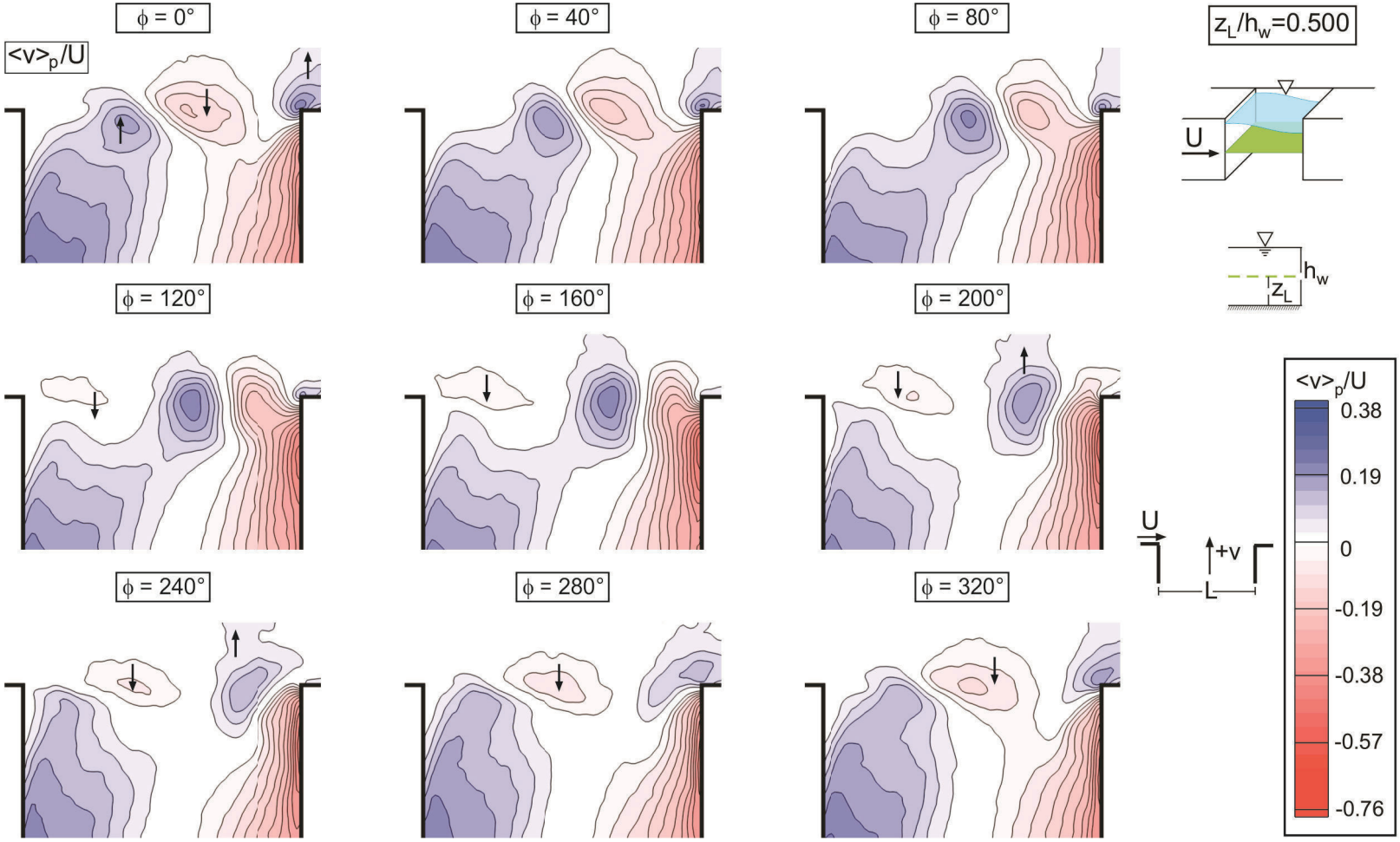

Figure A.10: Contours of phase-averaged transverse velocity $\langle v \rangle_p / U$ at $z_L/h_w = 0.500$ for nine different phases ($\phi = 0°$ to 320°) of the oscillation cycle in presence of the gravity standing wave within the cavity ($U/f_n L = 1.44$).

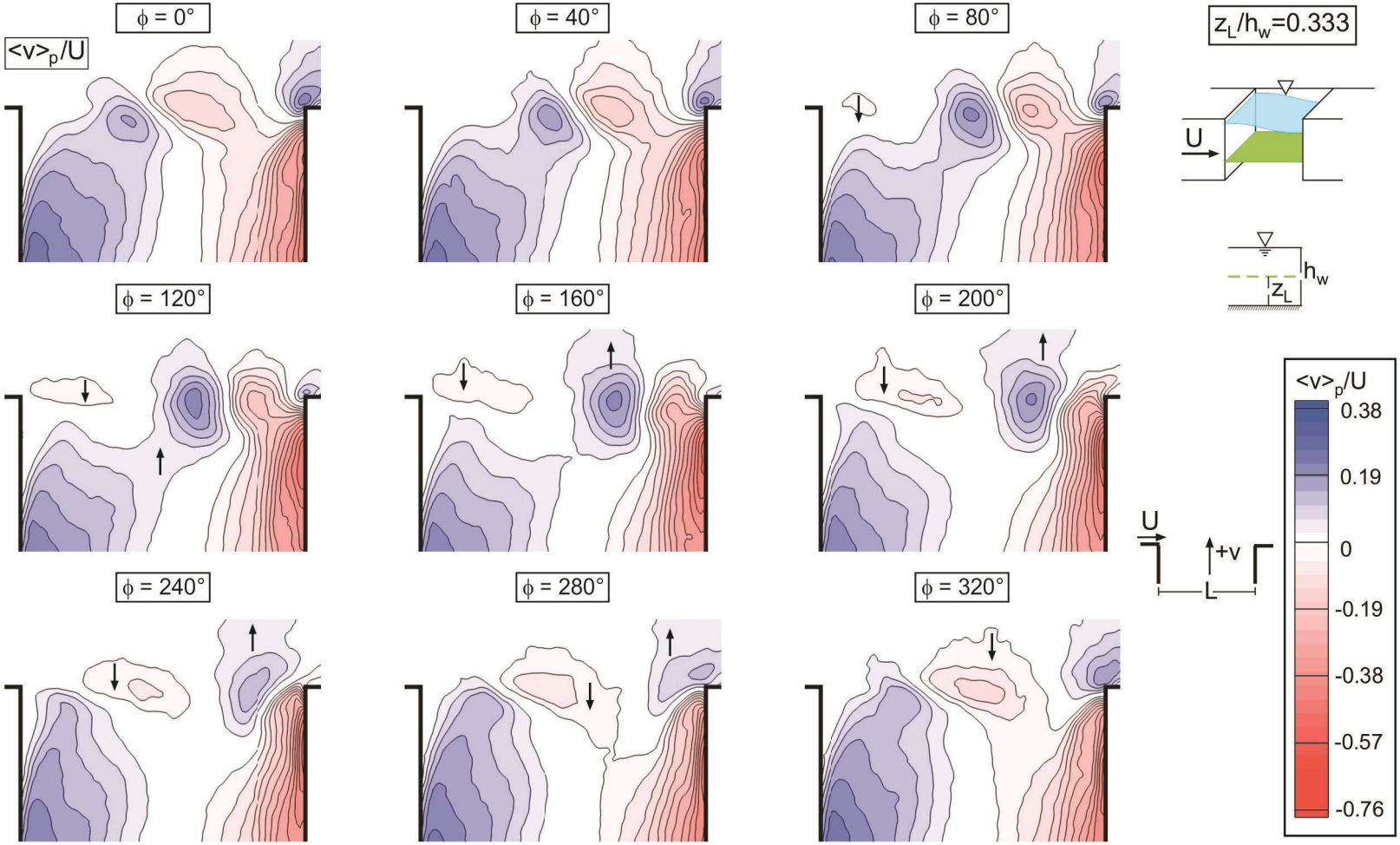

Figure A.11: Contours of phase-averaged transverse velocity $\langle v \rangle_p / U$ at $z_L/h_w = 0.333$ for nine different phases ($\phi = 0°$ to $320°$) of the oscillation cycle in presence of the gravity standing wave within the cavity ($U/f_n L = 1.44$).

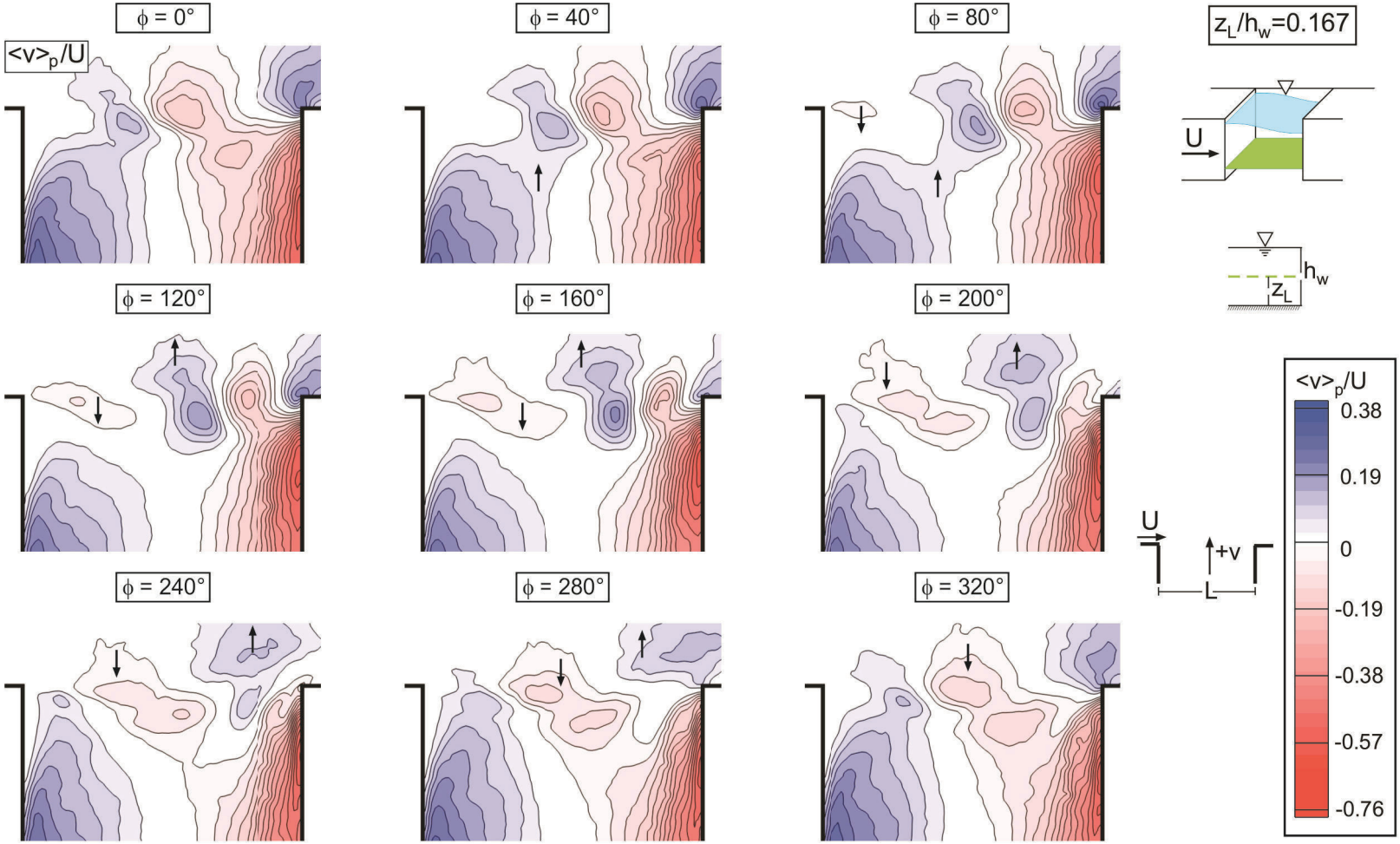

Figure A.12: Contours of phase-averaged transverse velocity $\langle v \rangle_p / U$ at $z_L/h_w = 0.167$ for nine different phases ($\phi = 0°$ to 320°) of the oscillation cycle in presence of the gravity standing wave within the cavity ($U/f_n L = 1.44$).

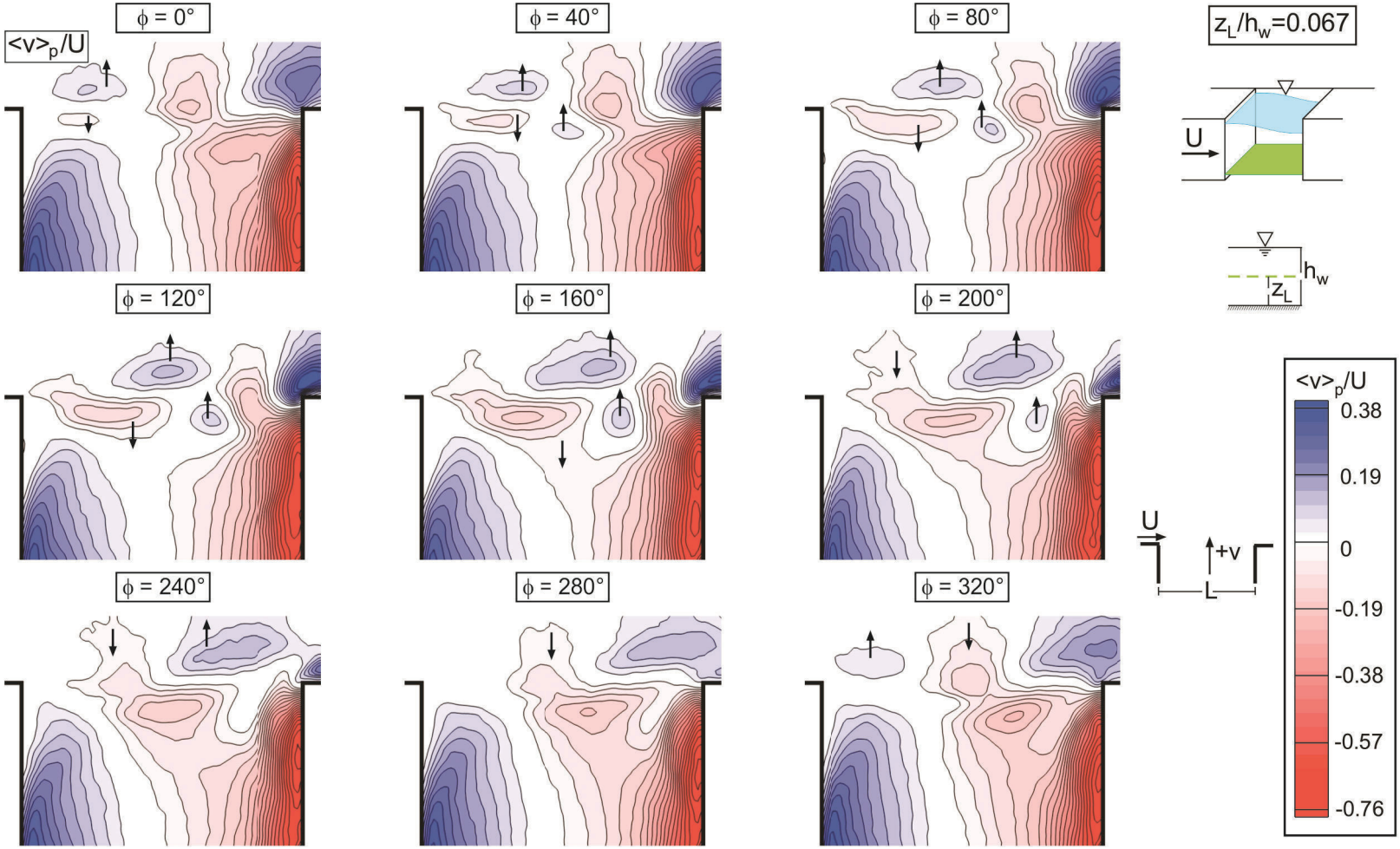

Figure A.13: Contours of phase-averaged transverse velocity $\langle v \rangle_p / U$ at $z_L/h_w = 0.067$ for nine different phases ($\phi = 0°$ to $320°$) of the oscillation cycle in presence of the gravity standing wave within the cavity ($U/f_n L = 1.44$).

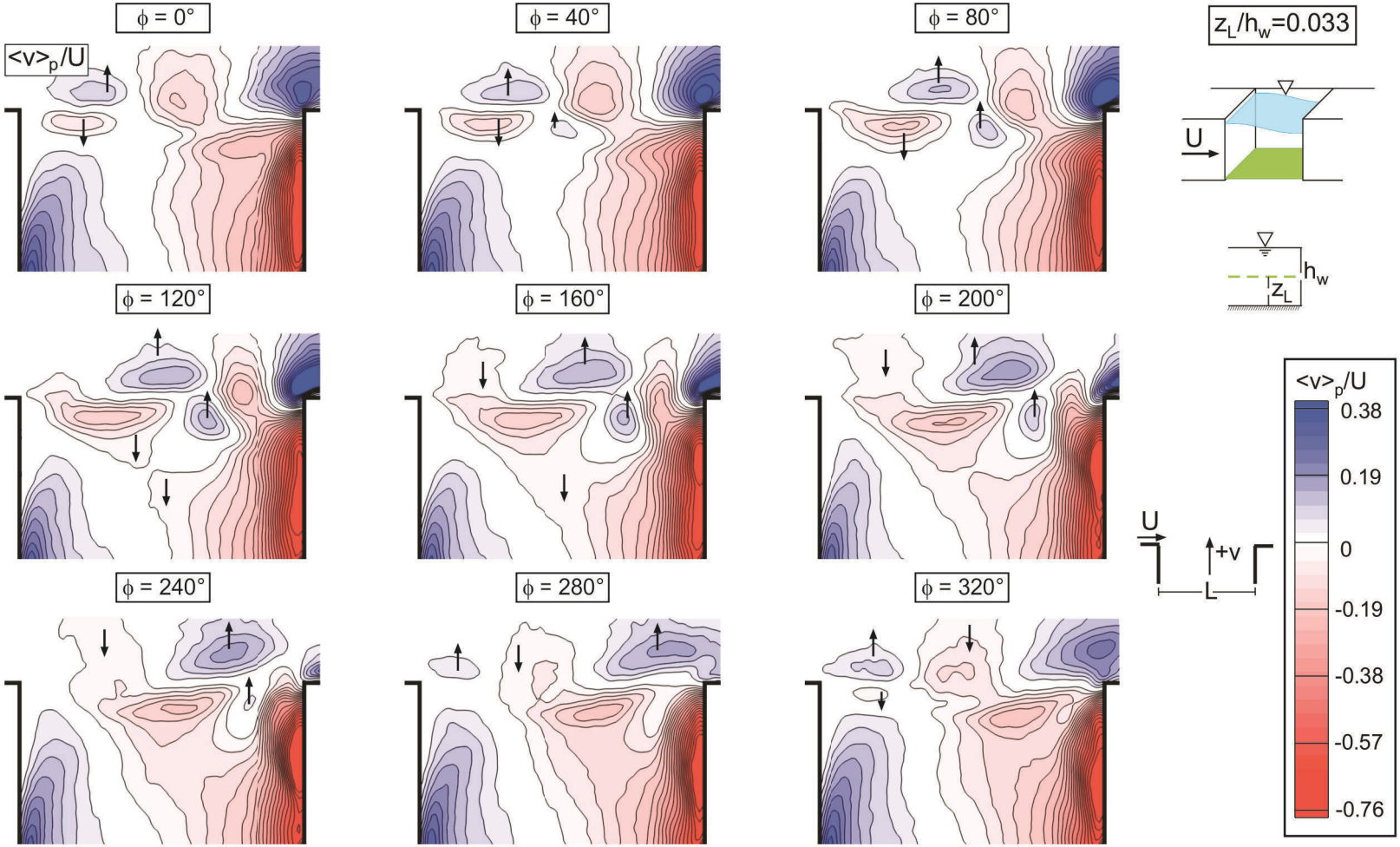

Figure A.14: Contours of phase-averaged transverse velocity $\langle v \rangle_p / U$ at $z_L/h_w = 0.033$ for nine different phases ($\phi = 0°$ to 320°) of the oscillation cycle in presence of the gravity standing wave within the cavity ($U/f_n L = 1.44$).

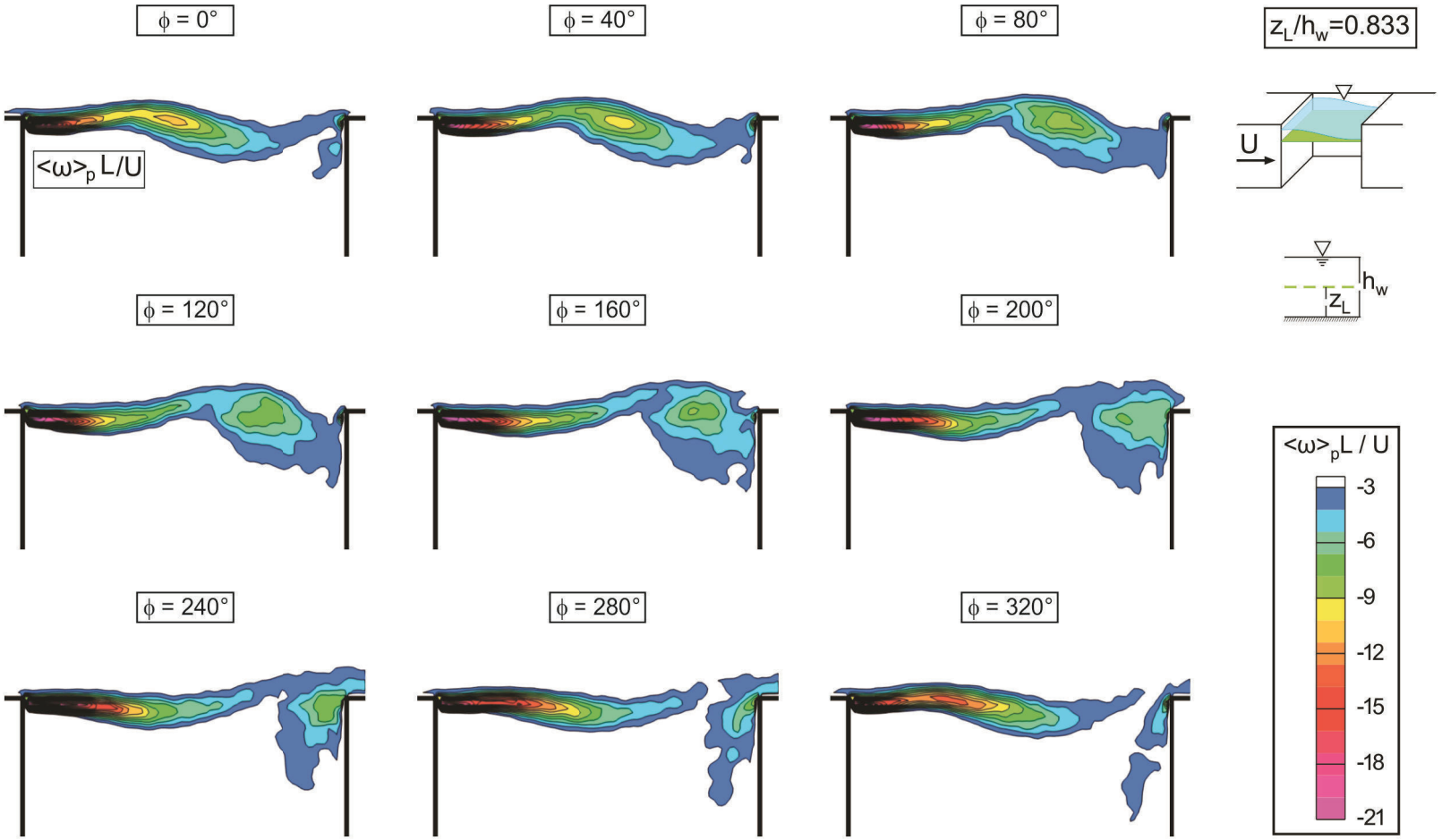

Figure A.15: Contours of phase-averaged vorticity $<\omega>_p L/U$ at $z_L/h_w = 0.833$ for nine different phases ($\phi = 0°$ to $320°$) of the oscillation cycle in presence of the gravity standing wave ($U/f_n L = 1.44$).

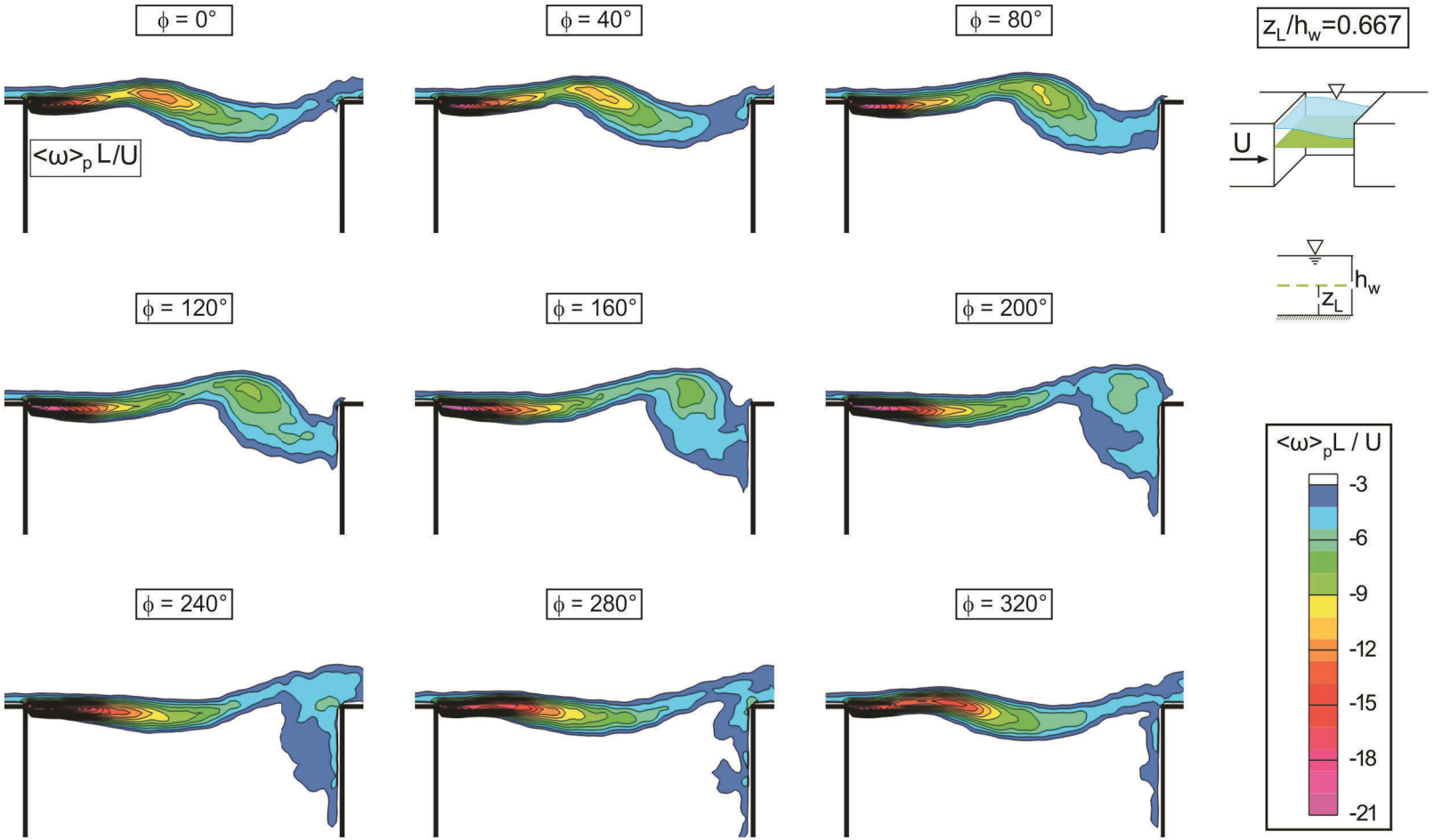

Figure A.16: Contours of phase-averaged vorticity $<\omega>_p L/U$ at $z_L/h_w = 0.667$ for nine different phases ($\phi = 0°$ to 320°) of the oscillation cycle in presence of the gravity standing wave ($U/f_n L = 1.44$).

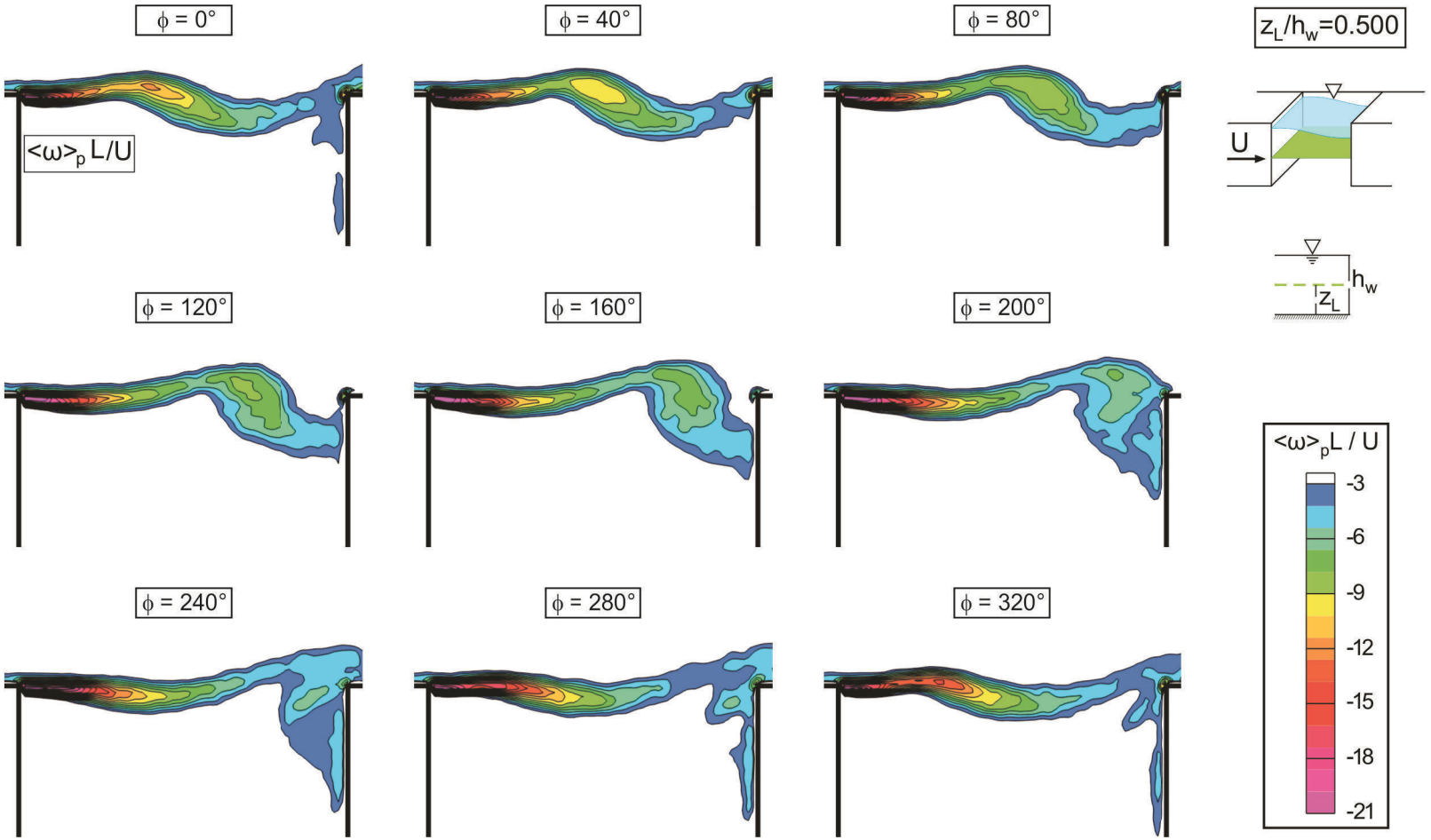

Figure A.17: Contours of phase-averaged vorticity $<\omega>_p L/U$ at $z_L/h_w = 0.500$ for nine different phases ($\phi = 0°$ to 320°) of the oscillation cycle in presence of the gravity standing wave ($U/f_n L = 1.44$).

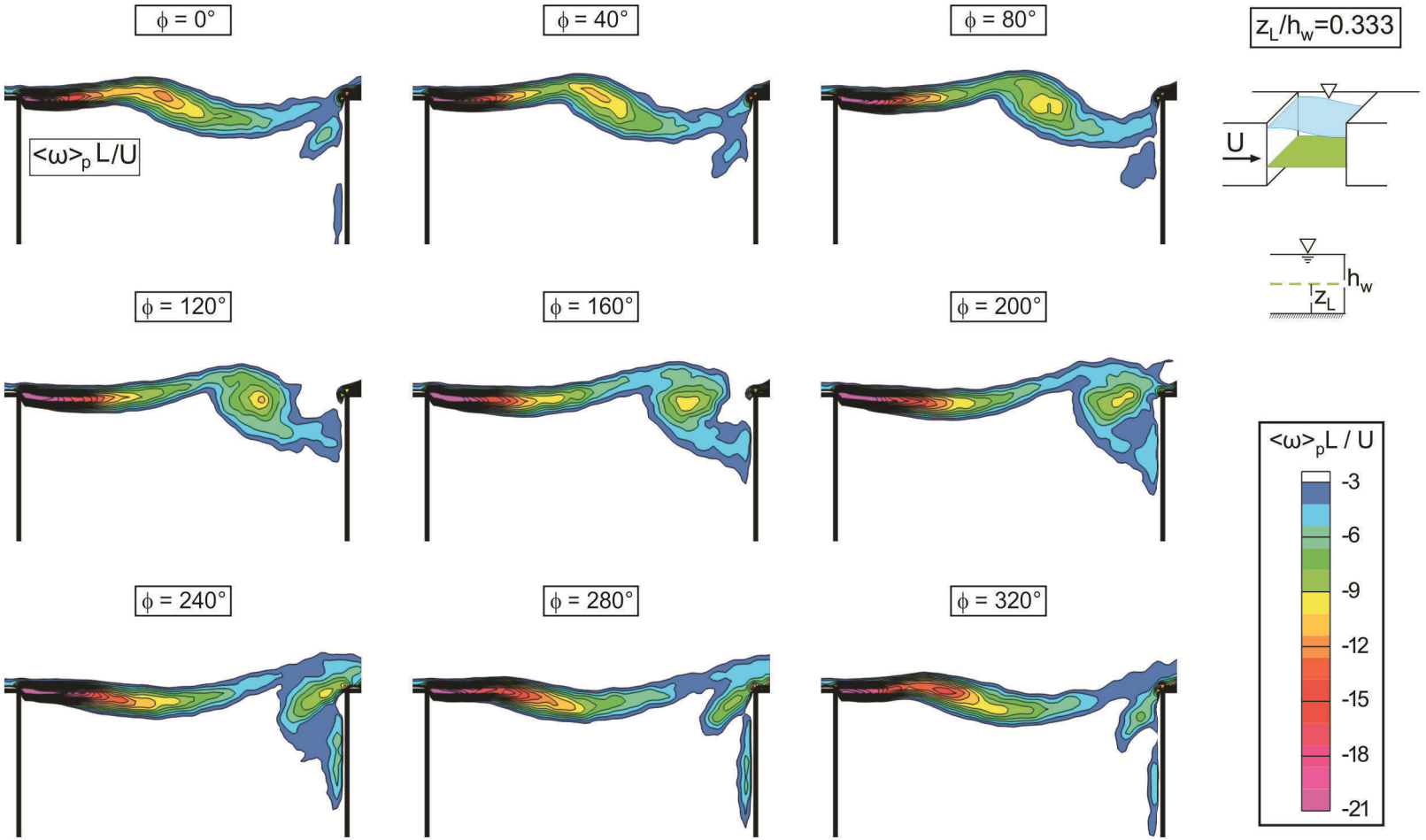

Figure A.18: Contours of phase-averaged vorticity $<\omega>_p L/U$ at $z_L/h_w = 0.333$ for nine different phases ($\phi = 0°$ to $320°$) of the oscillation cycle in presence of the gravity standing wave ($U/f_n L = 1.44$).

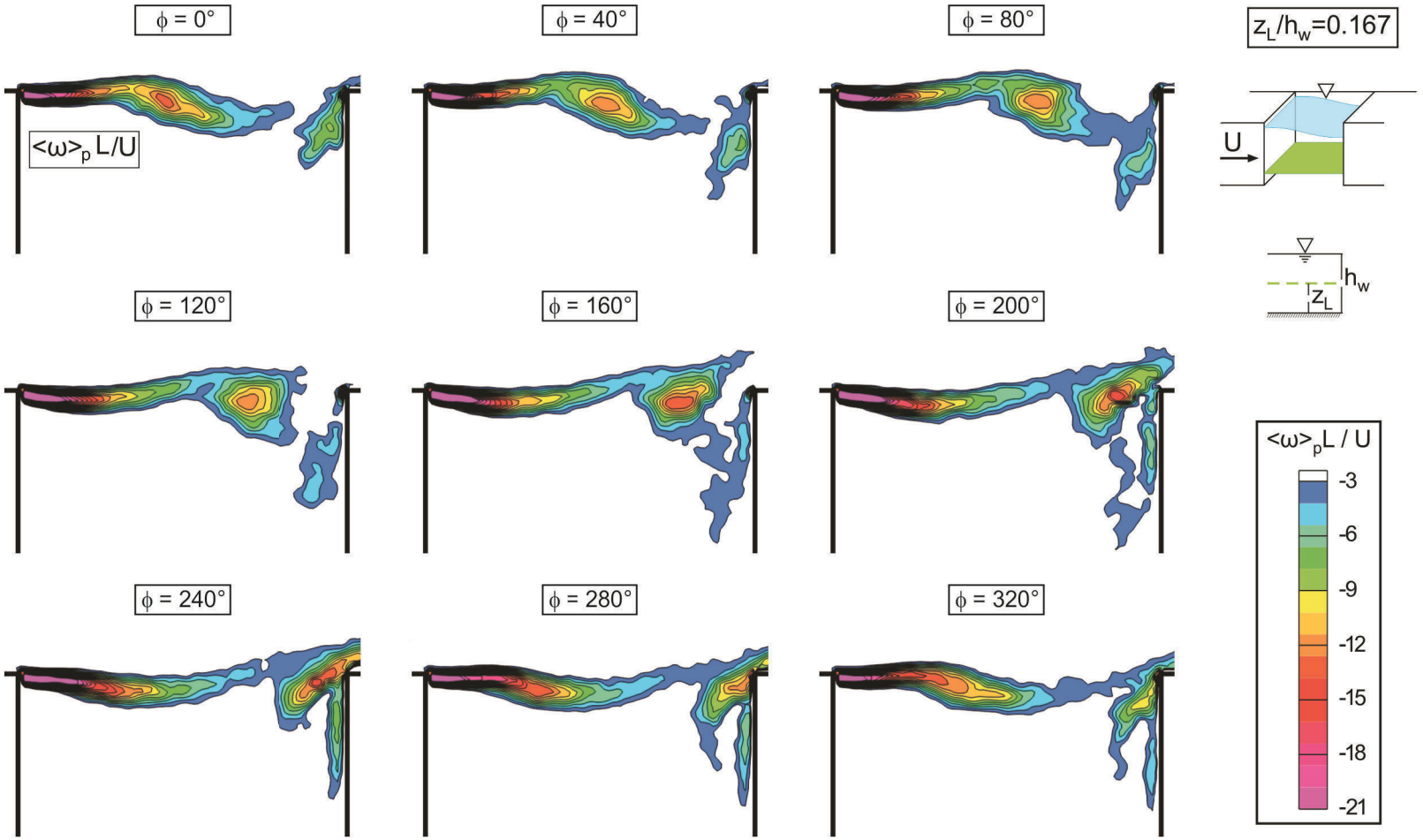

Figure A.19: Contours of phase-averaged vorticity $<\omega>_p L/U$ at $z_L/h_w = 0.167$ for nine different phases ($\phi = 0°$ to 320°) of the oscillation cycle in presence of the gravity standing wave ($U/f_n L = 1.44$).

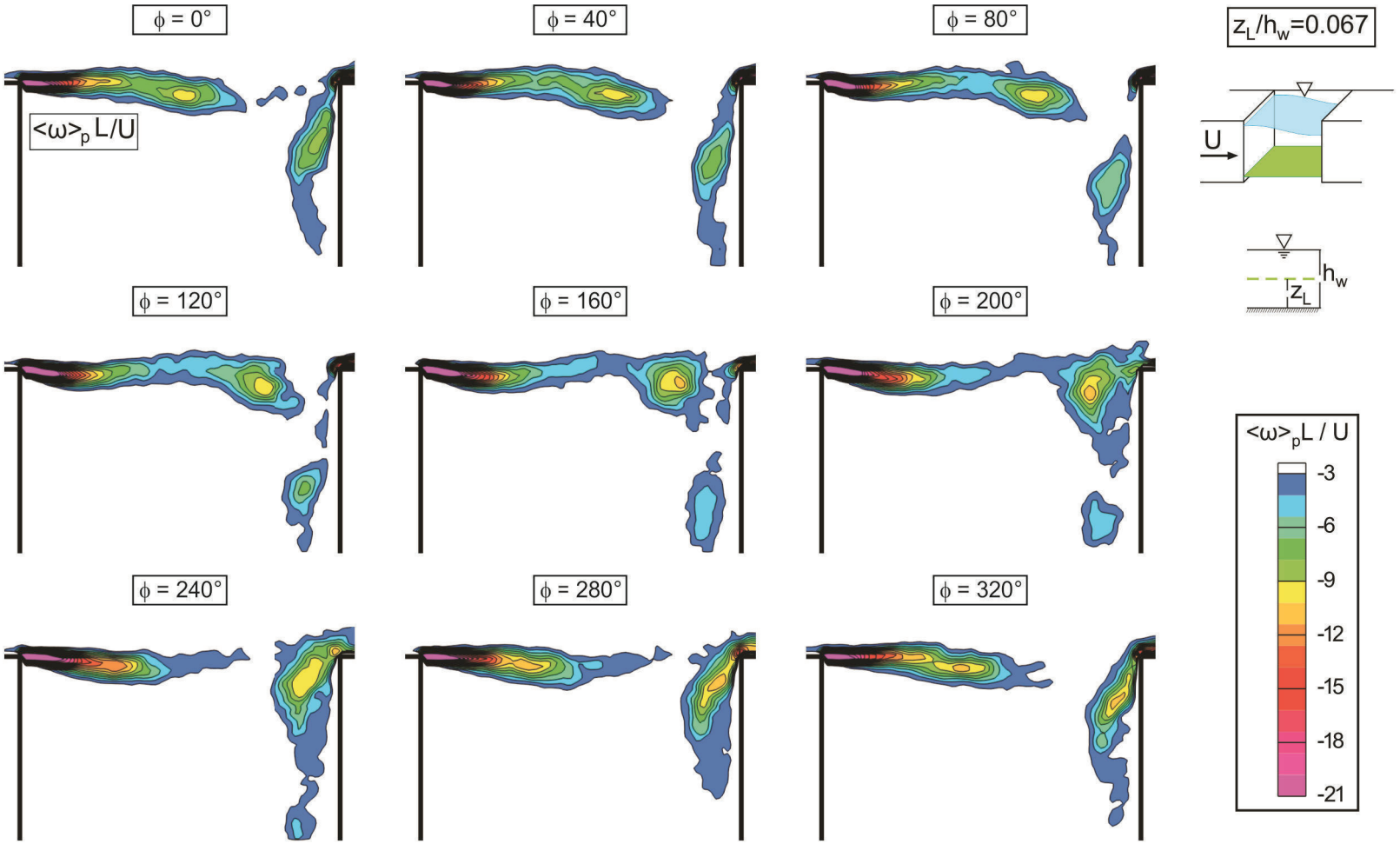

Figure A.20: Contours of phase-averaged vorticity $<\omega>_p L/U$ at $z_L/h_w = 0.067$ for nine different phases ($\phi = 0°$ to $320°$) of the oscillation cycle in presence of the gravity standing wave ($U/f_n L = 1.44$).

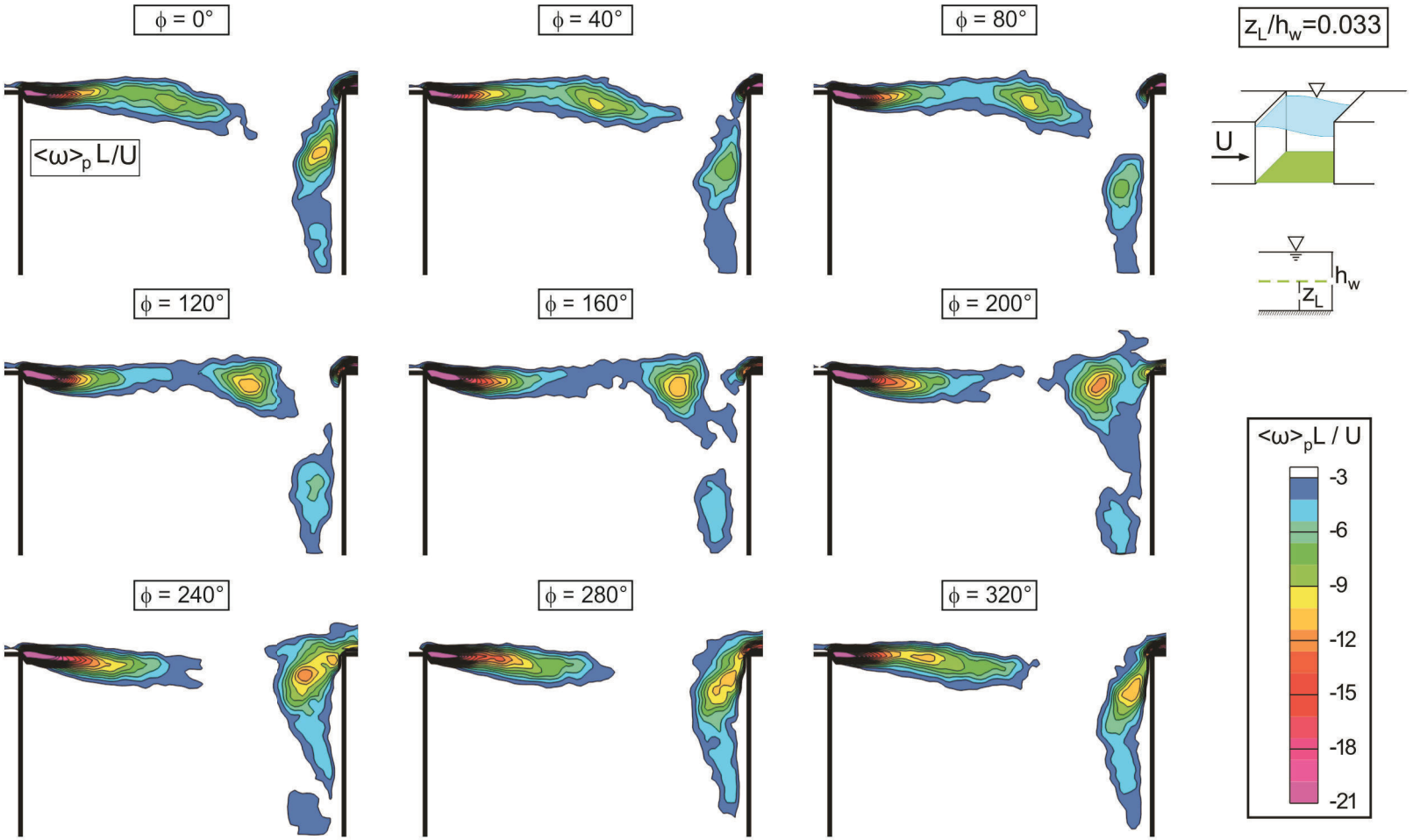

Figure A.21: Contours of phase-averaged vorticity $<\omega>_p L/U$ at $z_L/h_w = 0.033$ for nine different phases ($\phi = 0°$ to $320°$) of the oscillation cycle in presence of the gravity standing wave ($U/f_n L = 1.44$).

APPENDIX B

ATTENUATION OF OSCILLATIONS VIA A BED PERTURBATION

In Chapter 4, phase-averaged images were included at two elevations: well above the bed (z_L/h_w = 0.667) and near the bed (z_L/h_w = 0.067), for two different phases (ϕ = 90° and 270°) of the oscillation cycle. In this Appendix, phase-averaged images are included at four elevations z_L/h_w = 0.667, 0.333, 0.167, and 0.067 for four different phases (ϕ = 0°, 90°, 180°, and 270°). This series of figures further reveals details of the effects of a bed perturbation (cylinder) at elevations above the bed.

Figures B.1 through B.4 show patterns of phase-averaged streamlines $<\psi>_p$, Figures B.5 through B.8 show patterns of phase-averaged streamlines $<\psi>_p$ in a reference frame corresponding to one-half of the free stream velocity U_r, Figures B.9 to B.12 give phase-averaged streamwise velocity $<u>_p/U_r$, Figures B.13 to B.16 demonstrate phase-averaged transverse velocity $<v>_p/U_r$, and Figures B.17 to B.20 show phase-averaged contours vorticity $<\omega>_pL/U_r$.

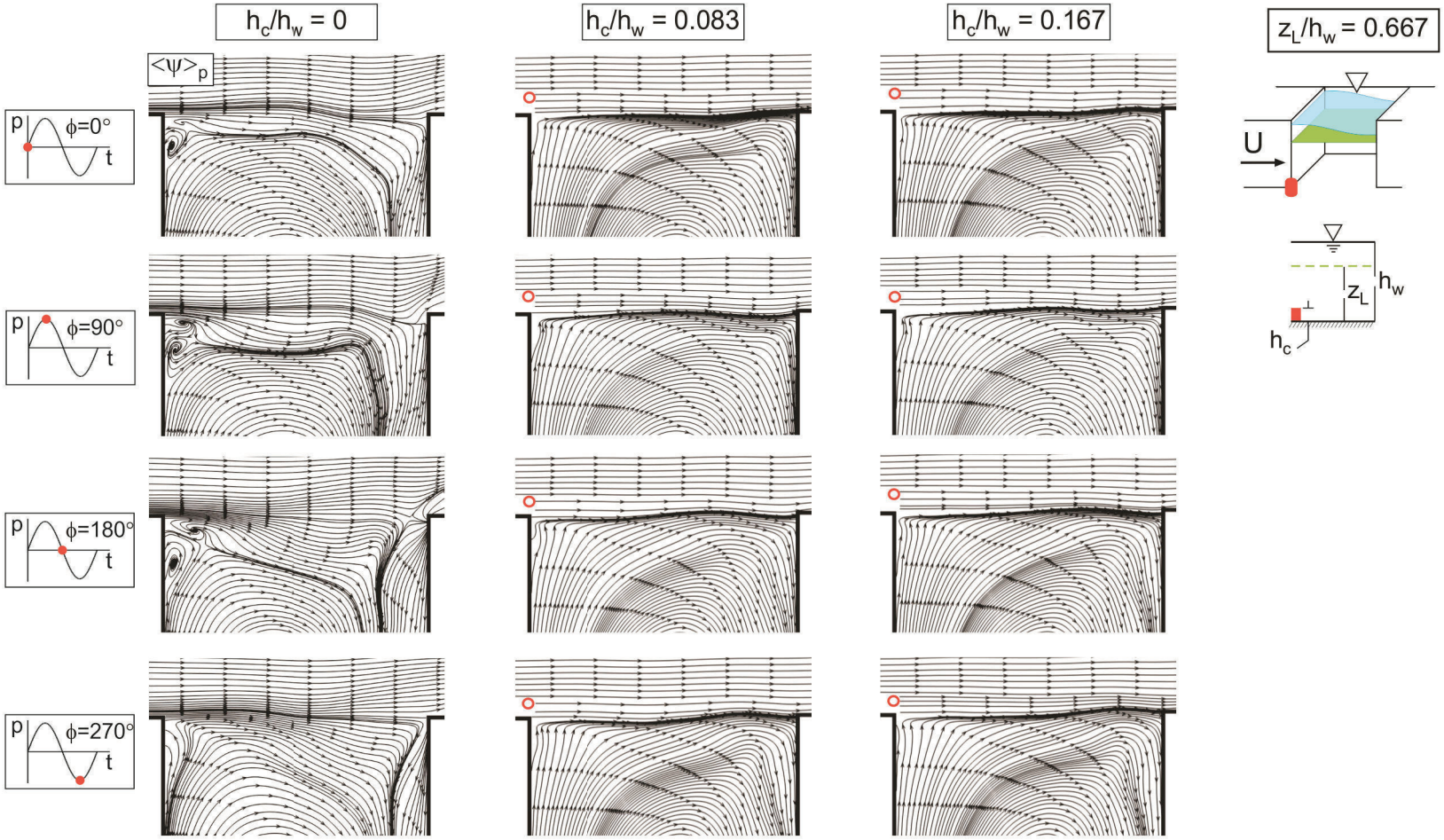

Figure B.1: Phase-averaged patterns of streamlines $<\psi>_p$ at $z_L/h_w = 0.667$ for four different phases $\phi = 0°, 90°, 180°,$ and 270° of the oscillation cycle. Case $h_c/h_w = 0$ corresponds to the non-attenuated oscillation in absence of the control cylinder; $h_c/h_w = 0.083$ and 0.167 correspond to attenuated cases in presence of the control cylinder.

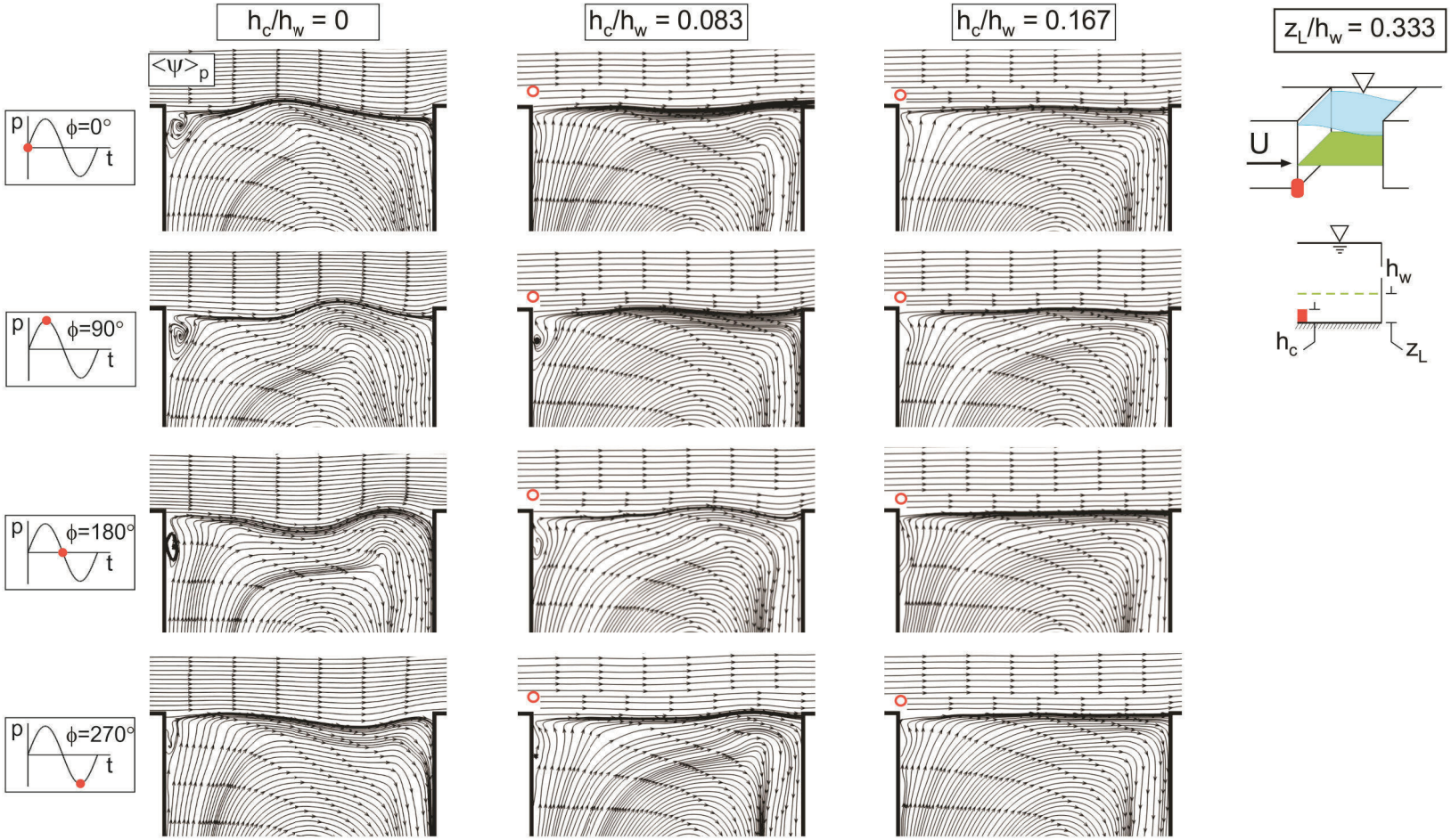

Figure B.2: Phase-averaged patterns of streamlines $<\psi>_p$ at $z_L/h_w = 0.333$ for four different phases $\phi = 0°, 90°, 180°,$ and 270° of the oscillation cycle. Case $h_c/h_w = 0$ corresponds to the non-attenuated oscillation in absence of the control cylinder; $h_c/h_w = 0.083$ and 0.167 correspond to attenuated cases in presence of the control cylinder.

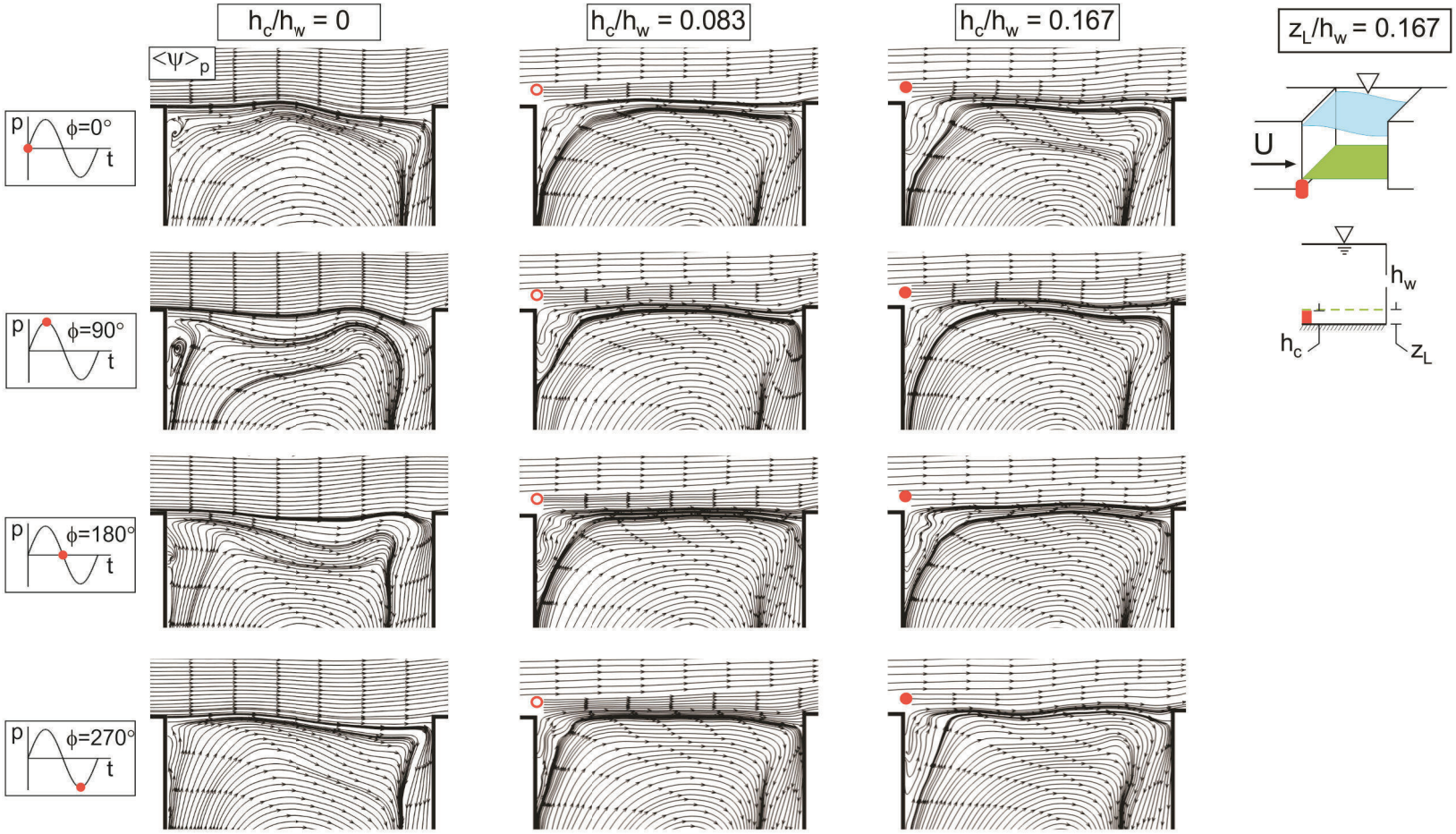

Figure B.3: Phase-averaged patterns of streamlines $<\psi>_p$ at $z_L/h_w = 0.167$ for four different phases $\phi = 0°, 90°, 180°,$ and 270° of the oscillation cycle. Case $h_c/h_w = 0$ corresponds to the non-attenuated oscillation in absence of the control cylinder; $h_c/h_w = 0.083$ and 0.167 correspond to attenuated cases in presence of the control cylinder.

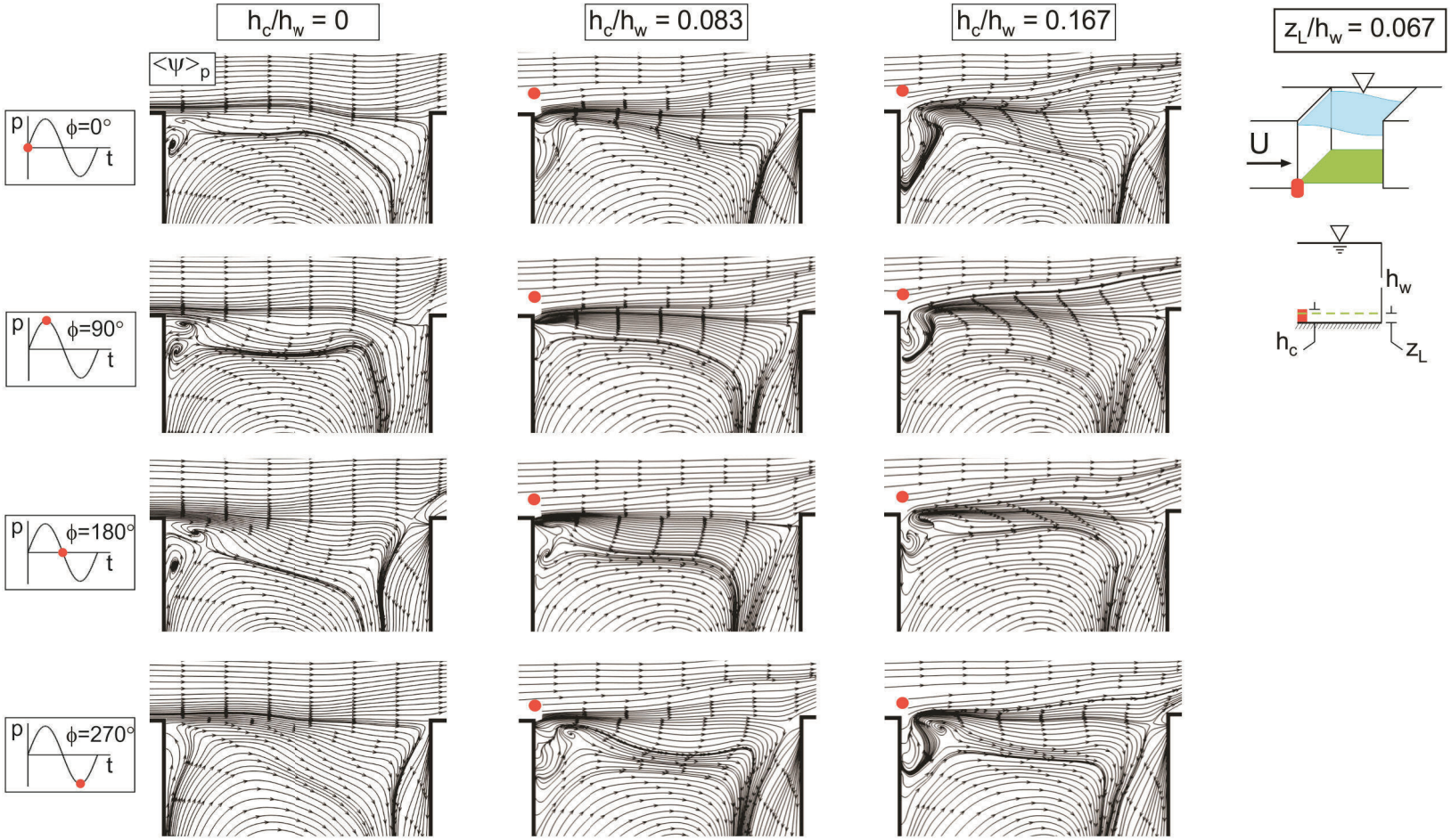

Figure B.4: Phase-averaged patterns of streamlines $<\psi>_p$ at $z_L/h_w = 0.067$ for four different phases $\phi = 0°, 90°, 180°,$ and 270° of the oscillation cycle. Case $h_c/h_w = 0$ corresponds to the non-attenuated oscillation in absence of the control cylinder; $h_c/h_w = 0.083$ and 0.167 correspond to attenuated cases in presence of the control cylinder.

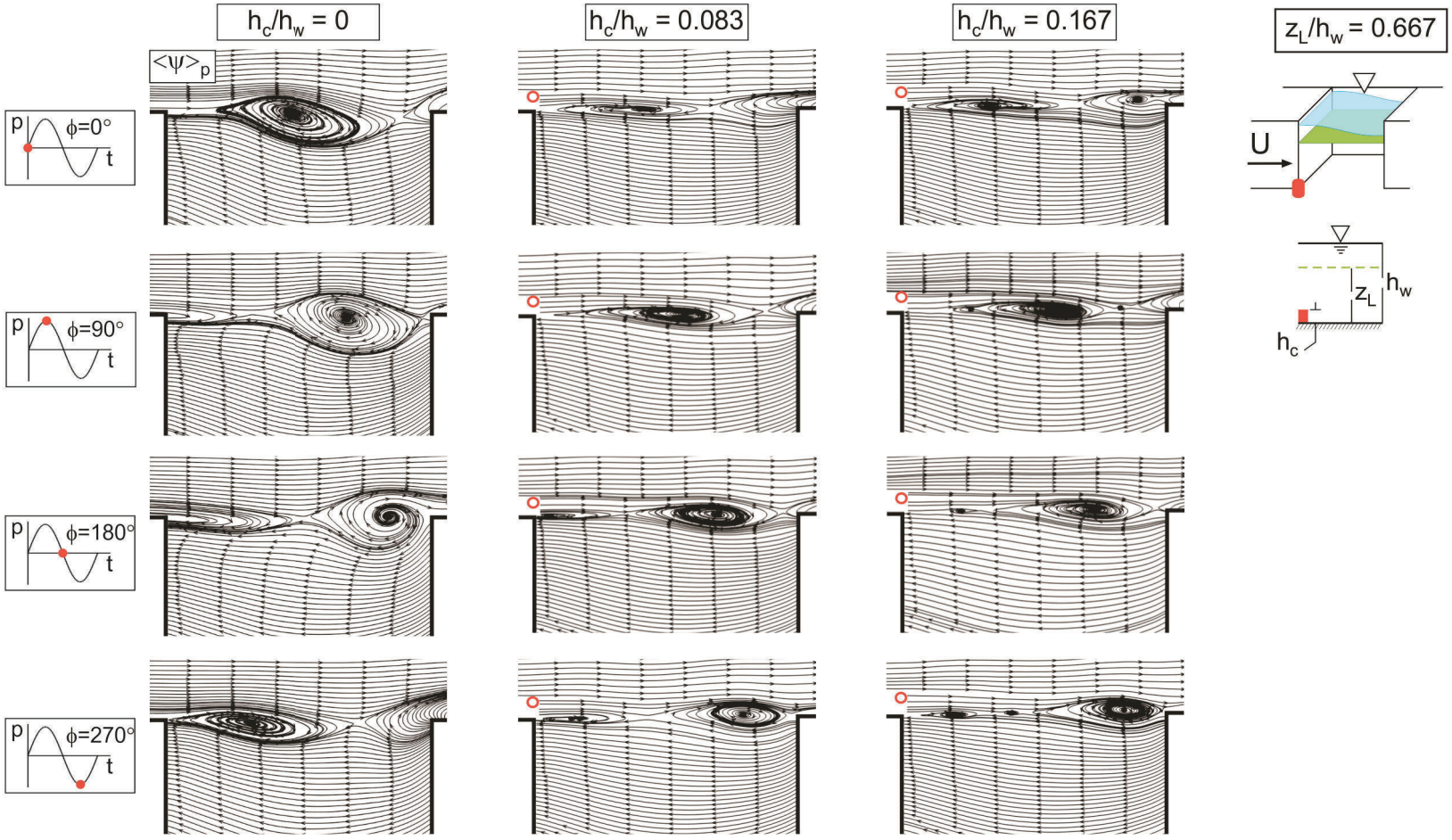

Figure B.5: Patterns of phase-averaged streamlines $<\psi>_p$ in a reference frame moving at $0.5U_r$ where U_r is the free stream velocity at $z_L/h_w = 0.667$ for four different phases $\phi = 0°$, 90°, 180°, and 270° of the oscillation cycle. Case $h_c/h_w = 0$ corresponds to the non-attenuated oscillation in absence of the control cylinder; $h_c/h_w = 0.083$ and 0.167 correspond to attenuated cases in presence of the control cylinder.

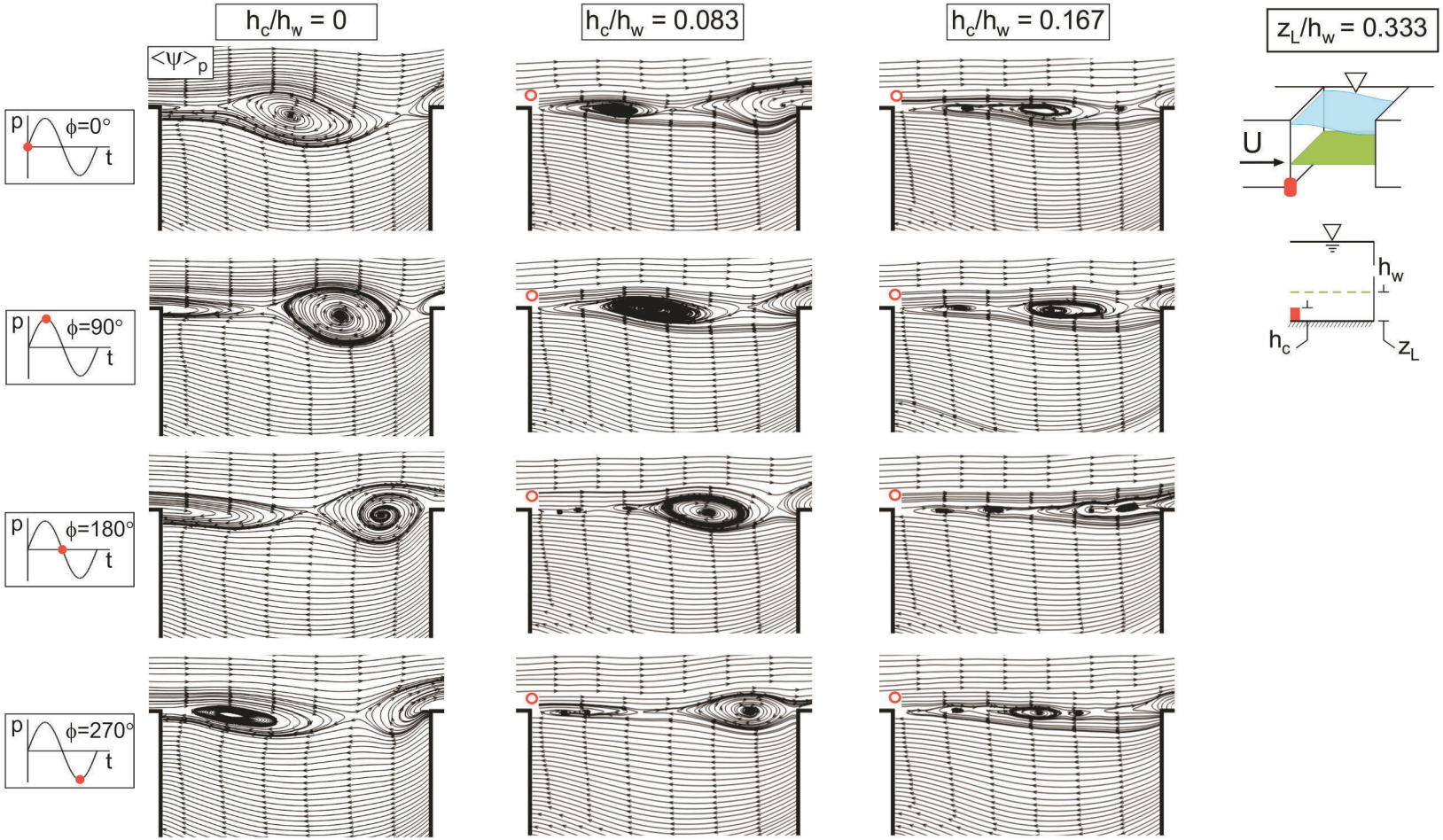

Figure B.6: Patterns of phase-averaged streamlines $<\psi>_p$ in a reference frame moving at $0.5U_r$ where U_r is the free stream velocity at $z_L/h_w = 0.333$ for four different phases $\phi = 0°$, 90°, 180°, and 270° of the oscillation cycle. Case $h_c/h_w = 0$ corresponds to the non-attenuated oscillation in absence of the control cylinder; $h_c/h_w = 0.083$ and 0.167 correspond to attenuated cases in presence of the control cylinder.

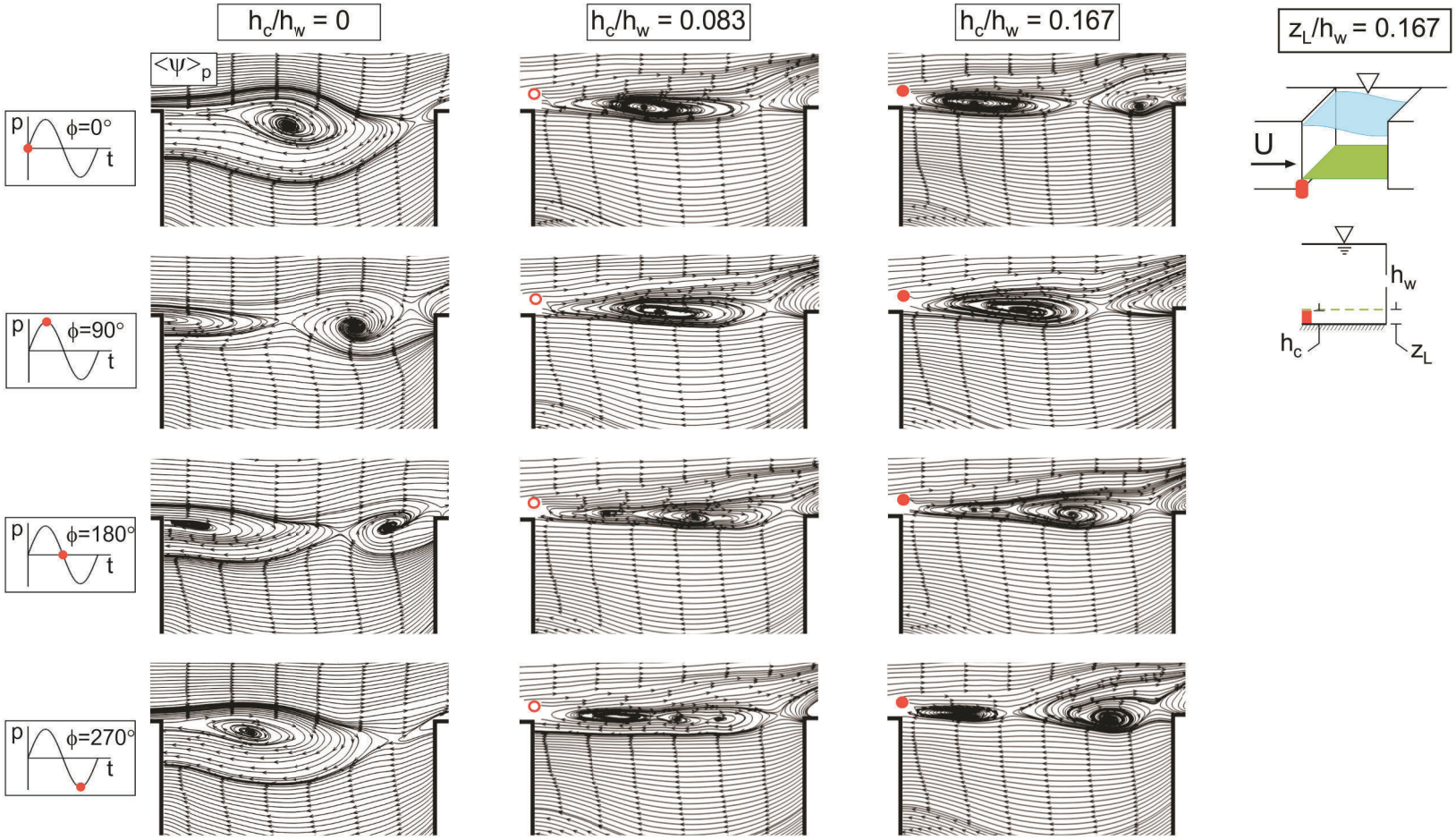

Figure B.7: Patterns of phase-averaged streamlines $<\psi>_p$ in a reference frame moving at $0.5U_r$ where U_r is the free stream velocity at $z_L/h_w = 0.167$ for four different phases $\phi = 0°$, 90°, 180°, and 270° of the oscillation cycle. Case $h_c/h_w = 0$ corresponds to the non-attenuated oscillation in absence of the control cylinder; $h_c/h_w = 0.083$ and 0.167 correspond to attenuated cases in presence of the control cylinder.

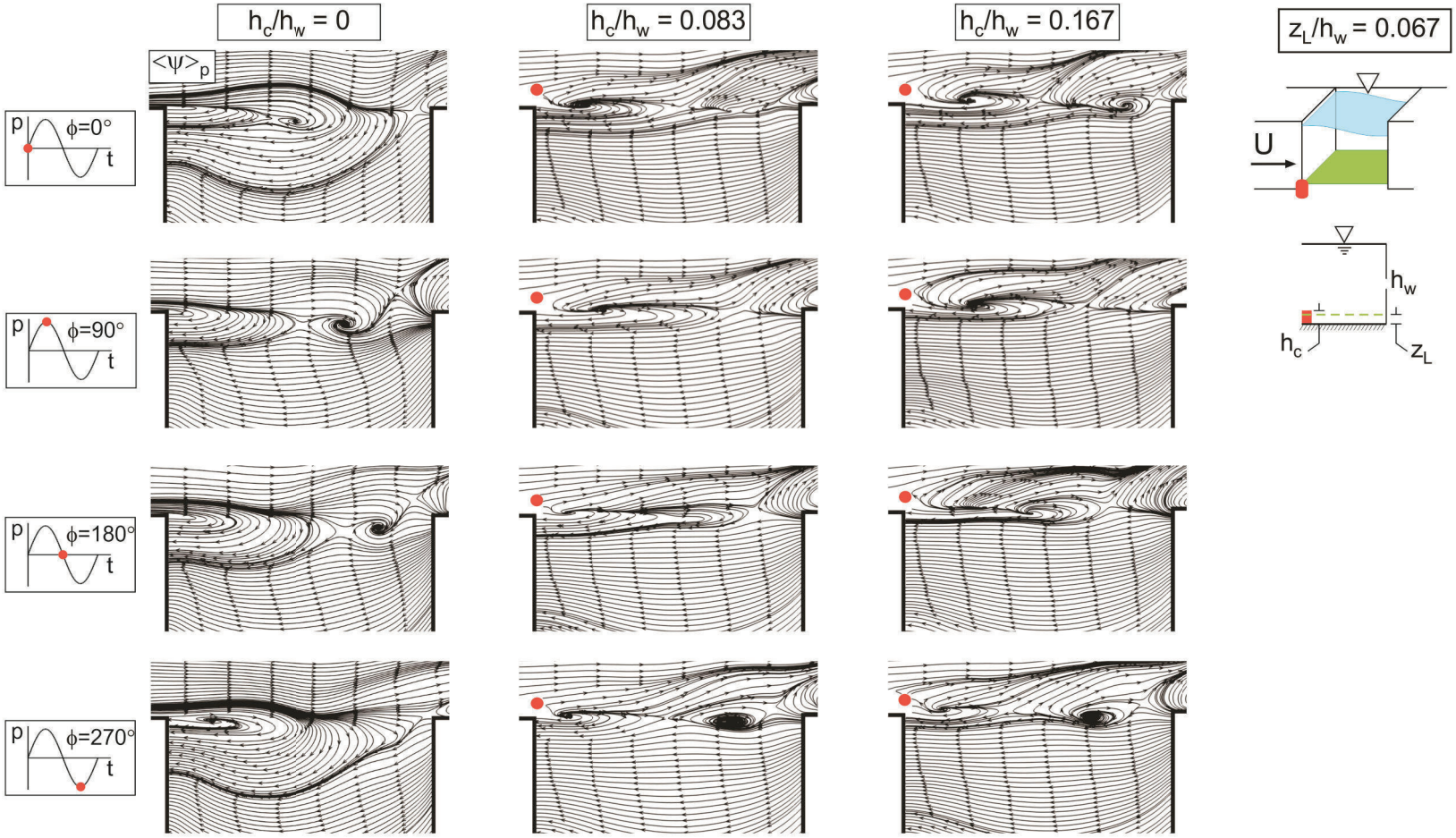

Figure B.8: Patterns of phase-averaged streamlines $<\psi>_p$ in a reference frame moving at $0.5U_r$ where U_r is the free stream velocity at $z_L/h_w = 0.067$ for four different phases $\phi = 0°$, 90°, 180°, and 270° of the oscillation cycle. Case $h_c/h_w = 0$ corresponds to the non-attenuated oscillation in absence of the control cylinder; $h_c/h_w = 0.083$ and 0.167 correspond to attenuated cases in presence of the control cylinder.

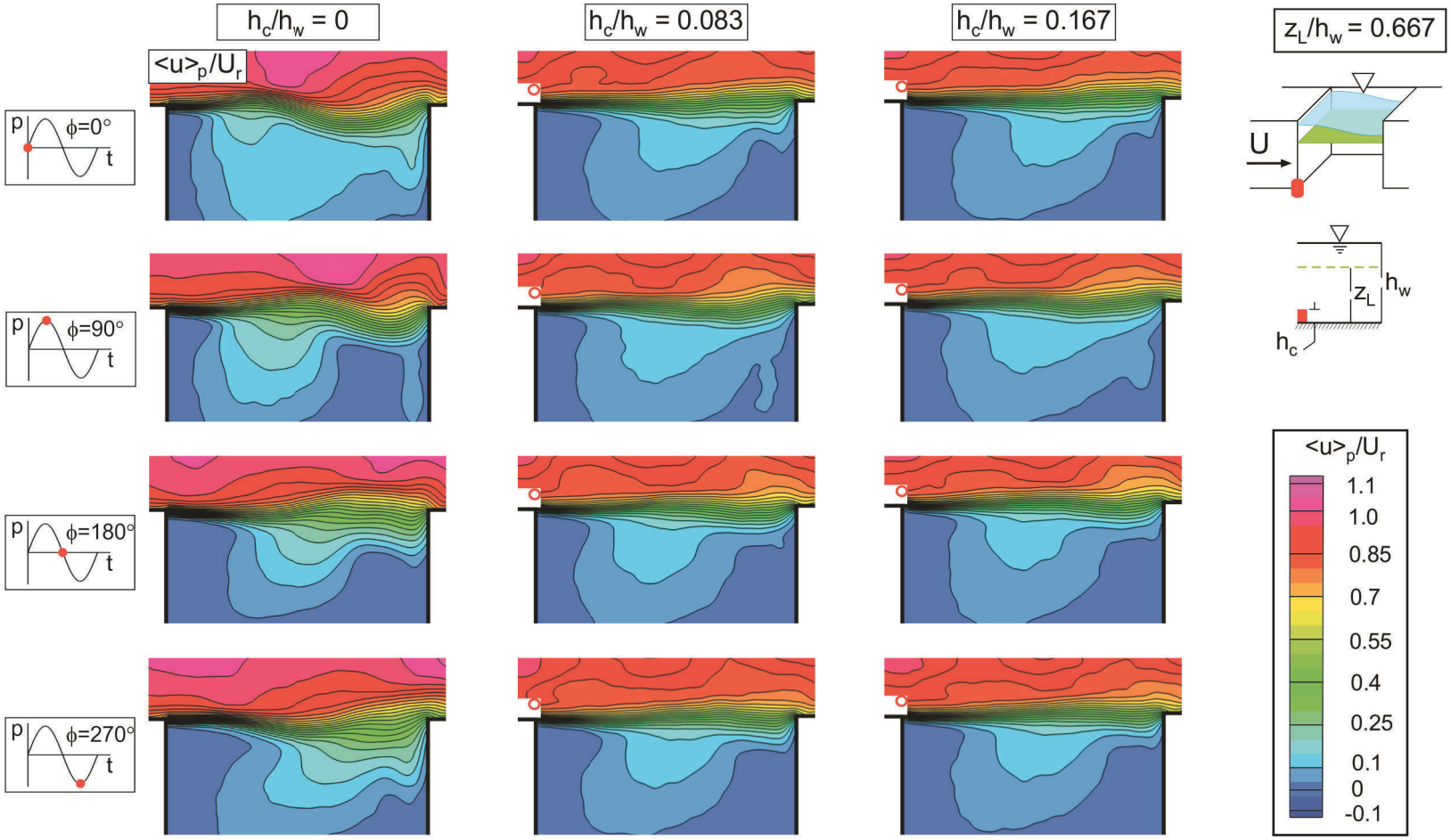

Figure B.9: Phase-averaged patterns of streamwise velocity $\langle u \rangle_p/U_r$ at $z_L/h_w = 0.667$ for four different phases $\phi = 0°$, 90°, 180°, and 270° of the oscillation cycle. Case $h_c/h_w = 0$ corresponds to the non-attenuated oscillation in absence of the control cylinder; $h_c/h_w = 0.083$ and 0.167 correspond to attenuated cases in presence of the control cylinder.

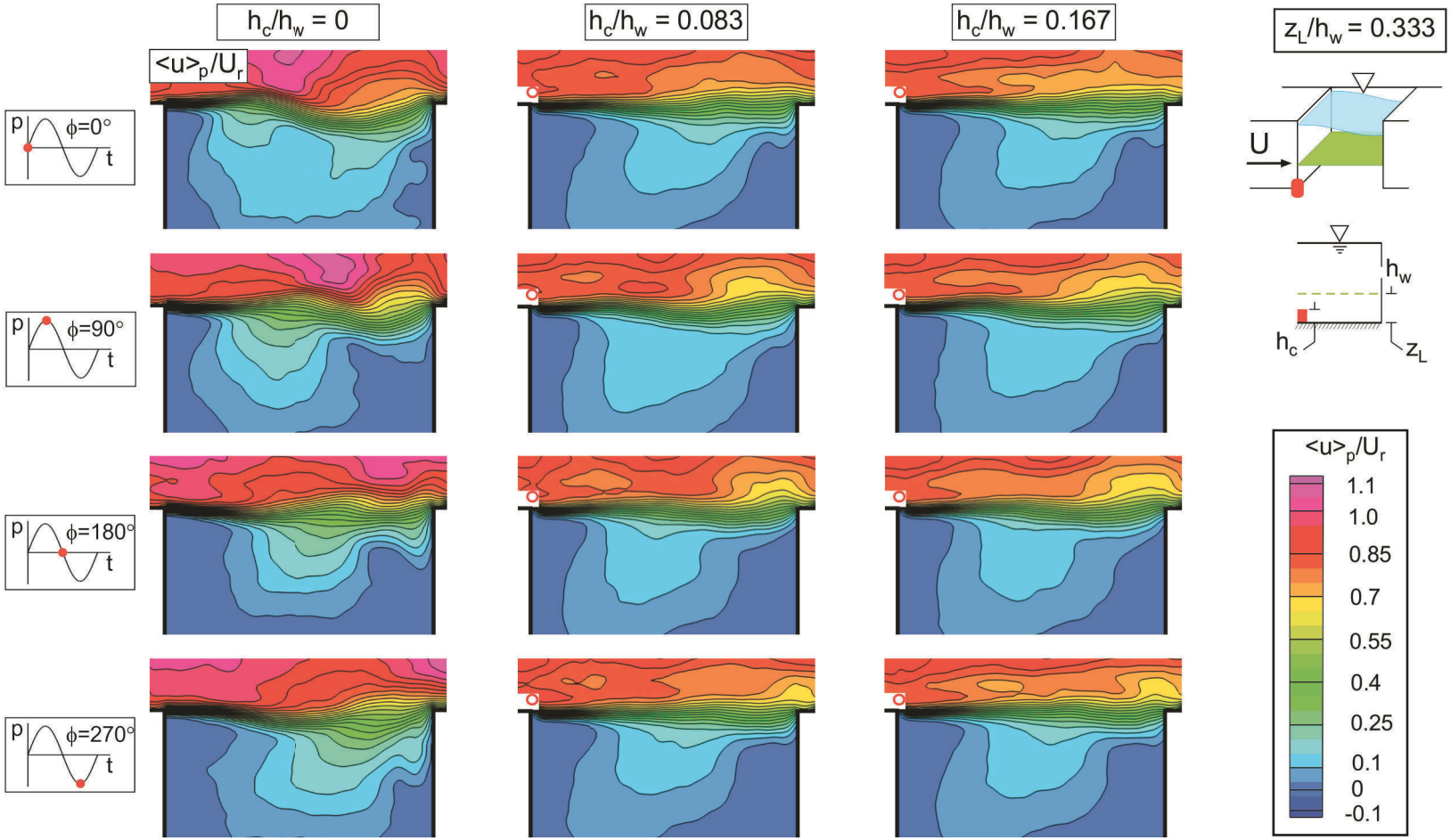

Figure B.10: Phase-averaged patterns of streamwise velocity $\langle u \rangle_p/U_r$ at $z_L/h_w = 0.333$ for four different phases $\phi = 0°$, 90°, 180°, and 270° of the oscillation cycle. Case $h_c/h_w = 0$ corresponds to the non-attenuated oscillation in absence of the control cylinder; $h_c/h_w = 0.083$ and 0.167 correspond to attenuated cases in presence of the control cylinder.

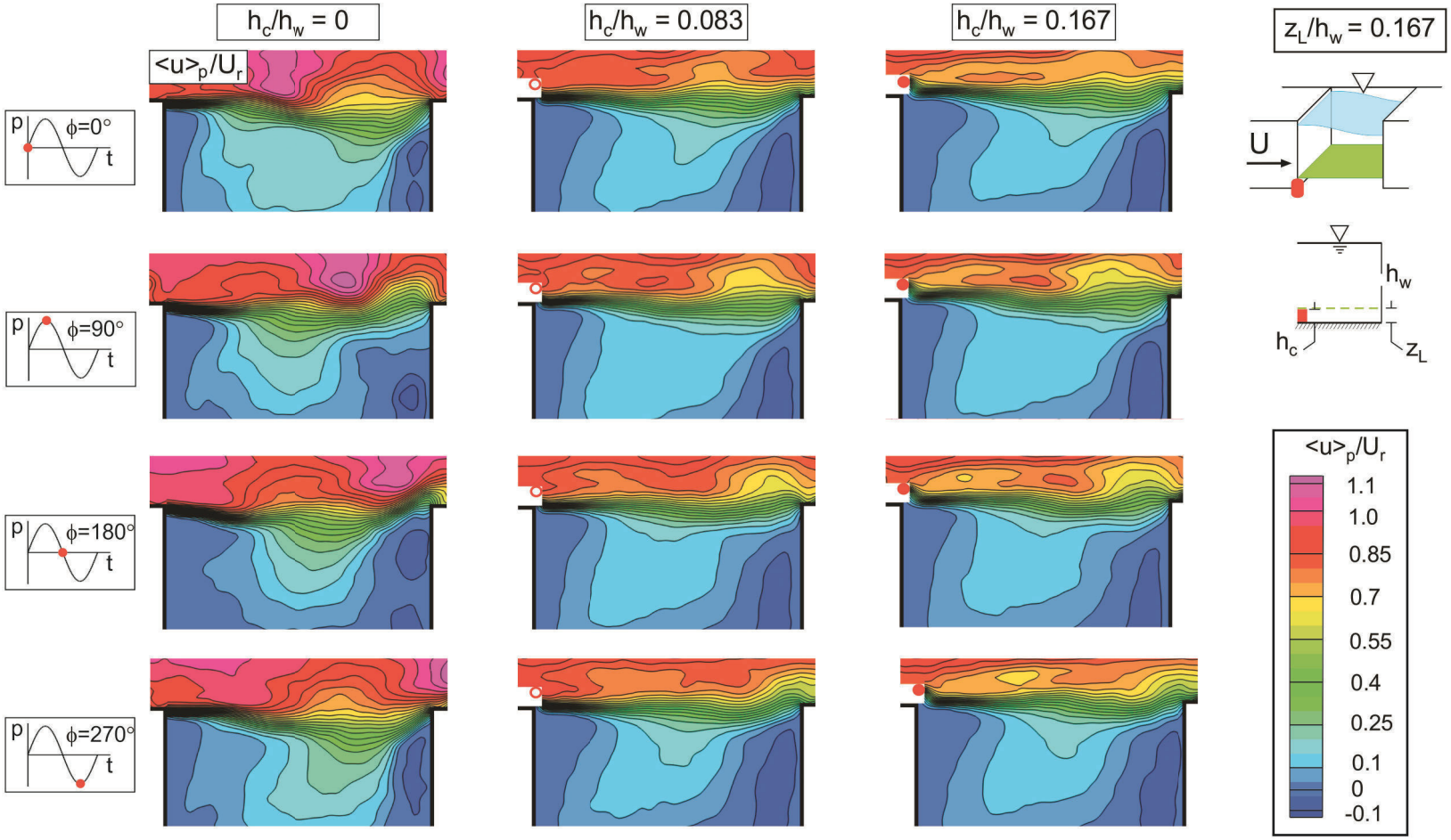

Figure B.11: Phase-averaged patterns of streamwise velocity $\langle u \rangle_p/U_r$ at $z_L/h_w = 0.167$ for four different phases $\phi = 0°$, 90°, 180°, and 270° of the oscillation cycle. Case $h_c/h_w = 0$ corresponds to the non-attenuated oscillation in absence of the control cylinder; $h_c/h_w = 0.083$ and 0.167 correspond to attenuated cases in presence of the control cylinder.

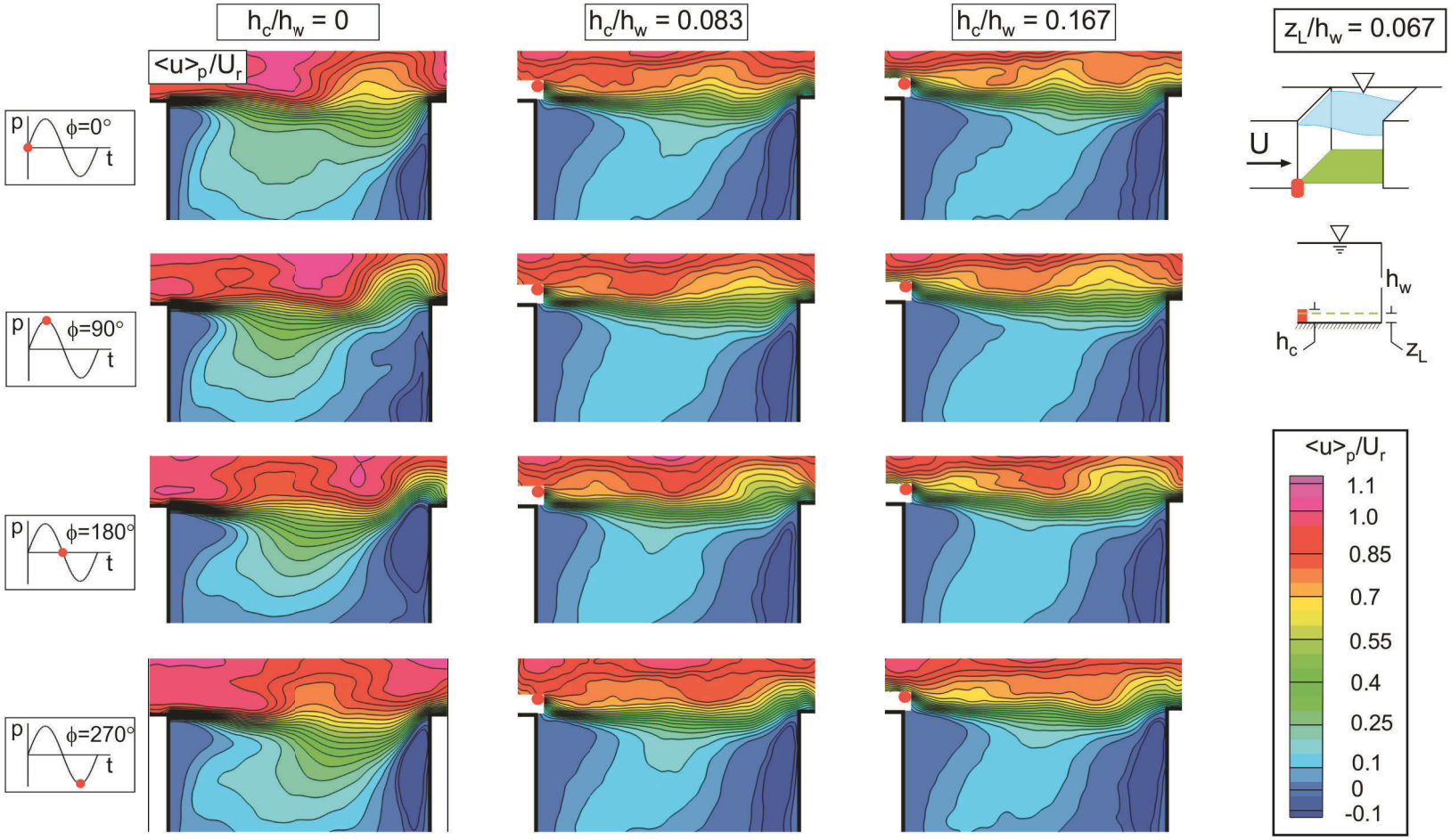

Figure B.12: Phase-averaged patterns of streamwise velocity $\langle u \rangle_p/U_r$ at $z_L/h_w = 0.067$ for four different phases $\phi = 0°$, 90°, 180°, and 270° of the oscillation cycle. Case $h_c/h_w = 0$ corresponds to the non-attenuated oscillation in absence of the control cylinder; $h_c/h_w = 0.083$ and 0.167 correspond to attenuated cases in presence of the control cylinder.

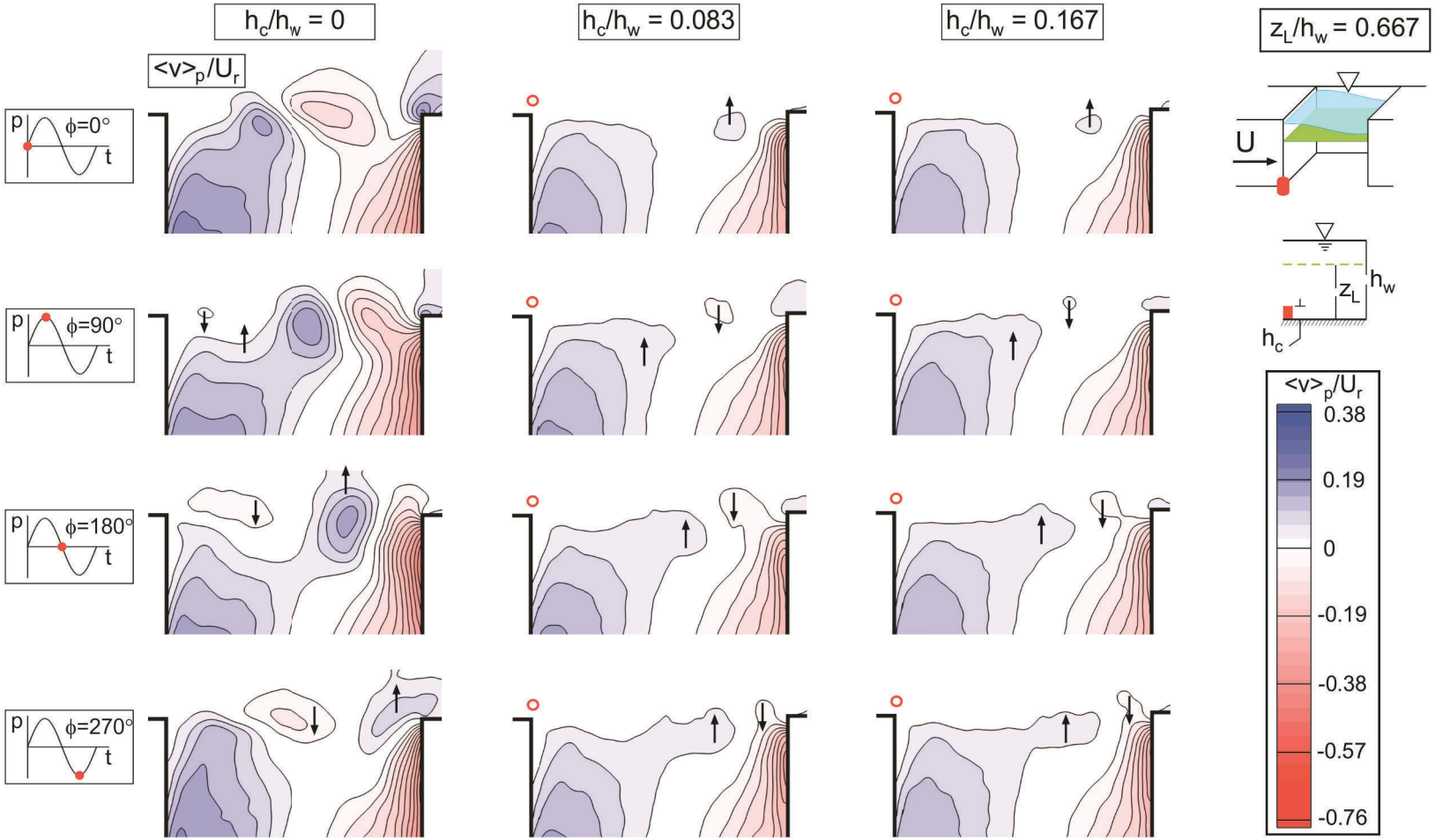

Figure B.13: Patterns of phase-averaged transverse velocity $\langle v \rangle_p/U_r$ at $z_L/h_w = 0.667$ for four different phases $\phi = 0°, 90°, 180°,$ and 270° of the oscillation cycle. Case $h_c/h_w = 0$ corresponds to the non-attenuated oscillation in absence of the control cylinder; $h_c/h_w = 0.083$ and 0.167 correspond to attenuated cases in presence of the control cylinder.

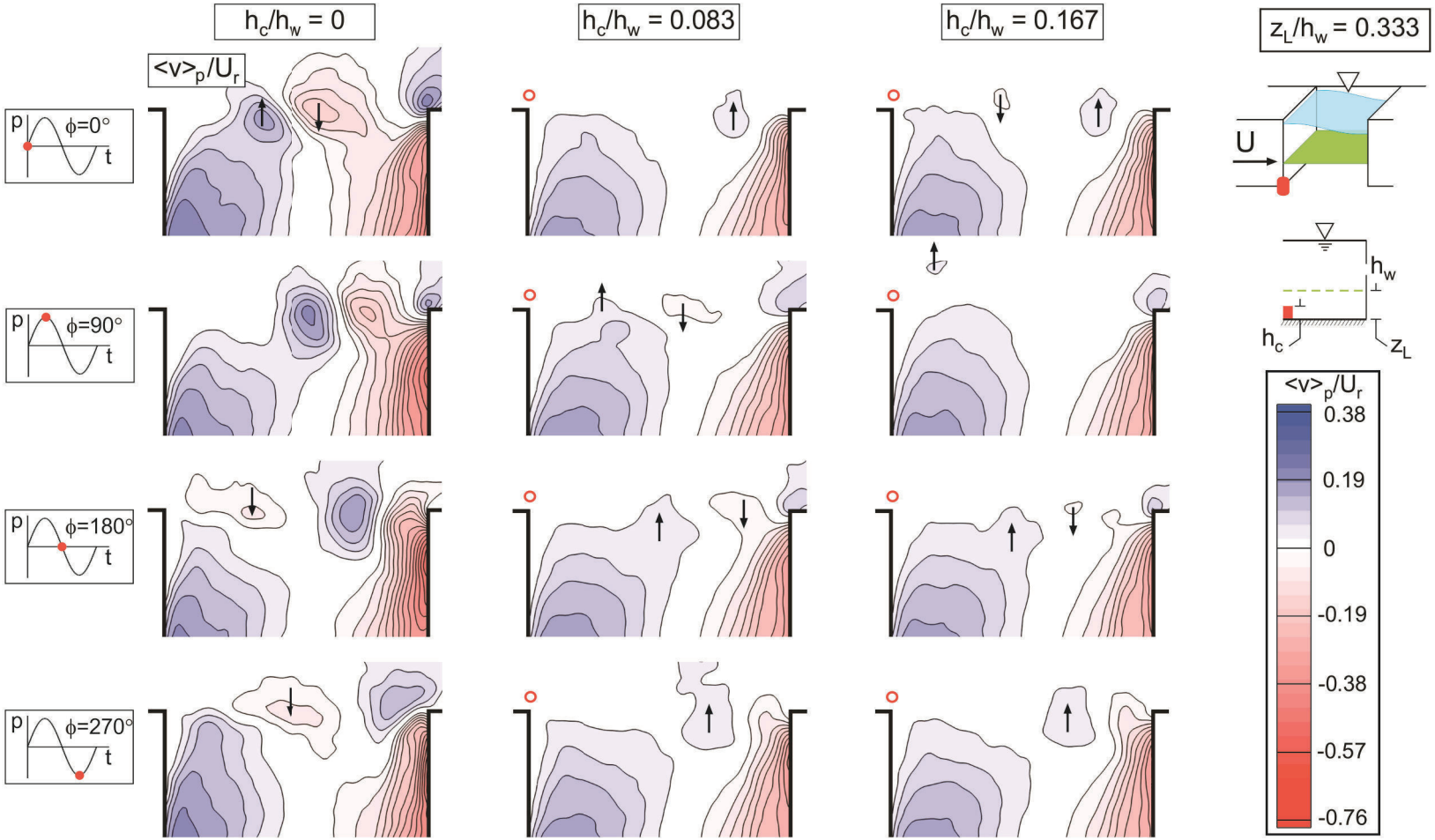

Figure B.14: Patterns of phase-averaged transverse velocity $\langle v \rangle_p/U_r$ at $z_L/h_w = 0.333$ for four different phases $\phi = 0°, 90°, 180°,$ and 270° of the oscillation cycle. Case $h_c/h_w = 0$ corresponds to the non-attenuated oscillation in absence of the control cylinder; $h_c/h_w = 0.083$ and 0.167 correspond to attenuated cases in presence of the control cylinder.

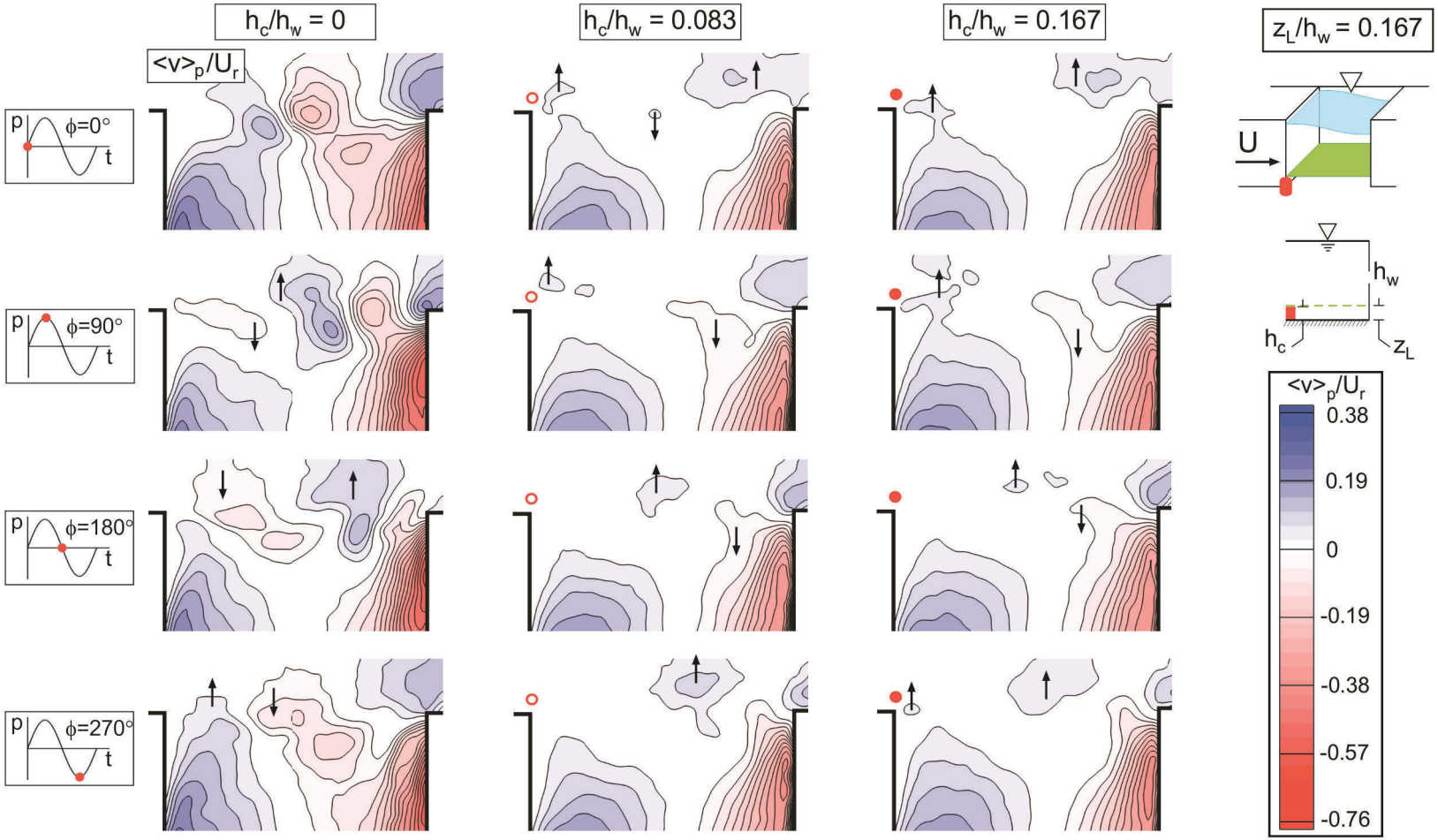

Figure B.15: Patterns of phase-averaged transverse velocity $\langle v \rangle_p / U_r$ at $z_L/h_w = 0.167$ for four different phases $\phi = 0°, 90°, 180°,$ and 270° of the oscillation cycle. Case $h_c/h_w = 0$ corresponds to the non-attenuated oscillation in absence of the control cylinder; $h_c/h_w = 0.083$ and 0.167 correspond to attenuated cases in presence of the control cylinder.

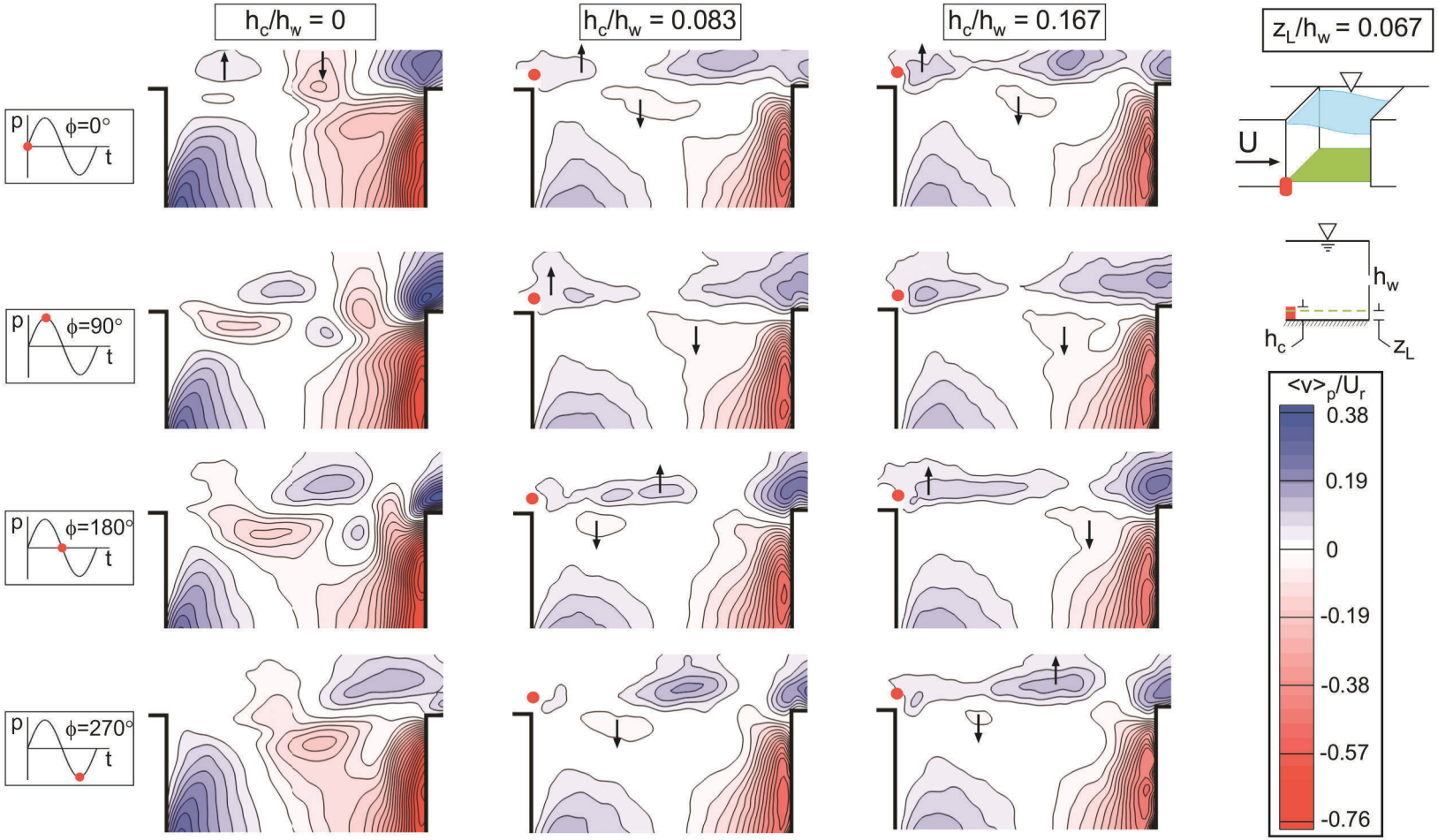

Figure B.16: Patterns of phase-averaged transverse velocity $\langle v \rangle_p/U_r$ at $z_L/h_w = 0.067$ for four different phases $\phi = 0°, 90°, 180°,$ and 270° of the oscillation cycle. Case $h_c/h_w = 0$ corresponds to the non-attenuated oscillation in absence of the control cylinder; $h_c/h_w = 0.083$ and 0.167 correspond to attenuated cases in presence of the control cylinder.

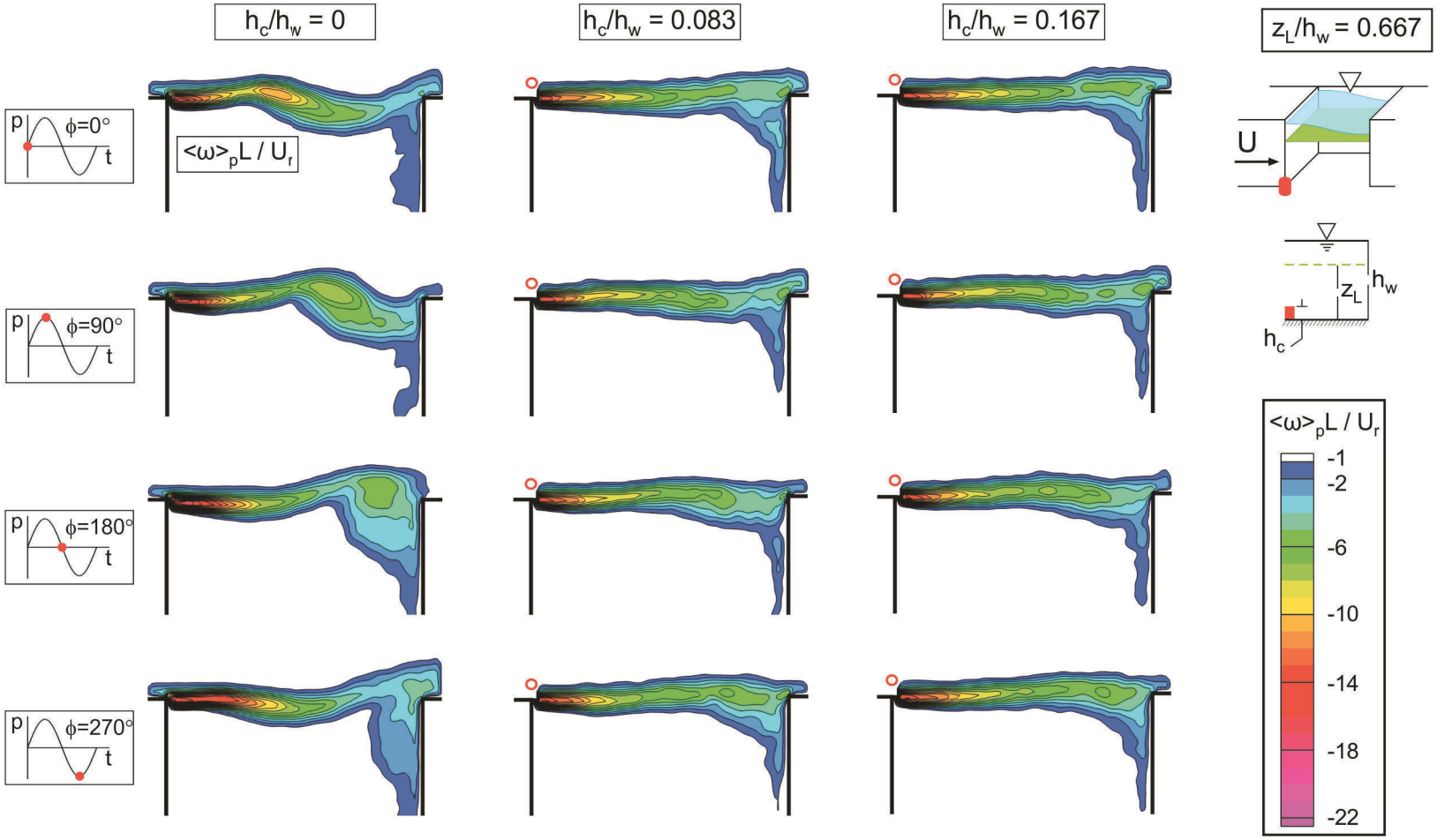

Figure B.17: Patterns of phase-averaged vorticity $\langle\omega\rangle_p L/U_r$ at $z_L/h_w = 0.667$ for four different phases $\phi = 0°$, 90°, 180°, and 270° of the oscillation cycle. Case $h_c/h_w = 0$ corresponds to the non-attenuated oscillation in absence of the control cylinder; $h_c/h_w = 0.083$ and 0.167 correspond to attenuated cases in presence of the control cylinder.

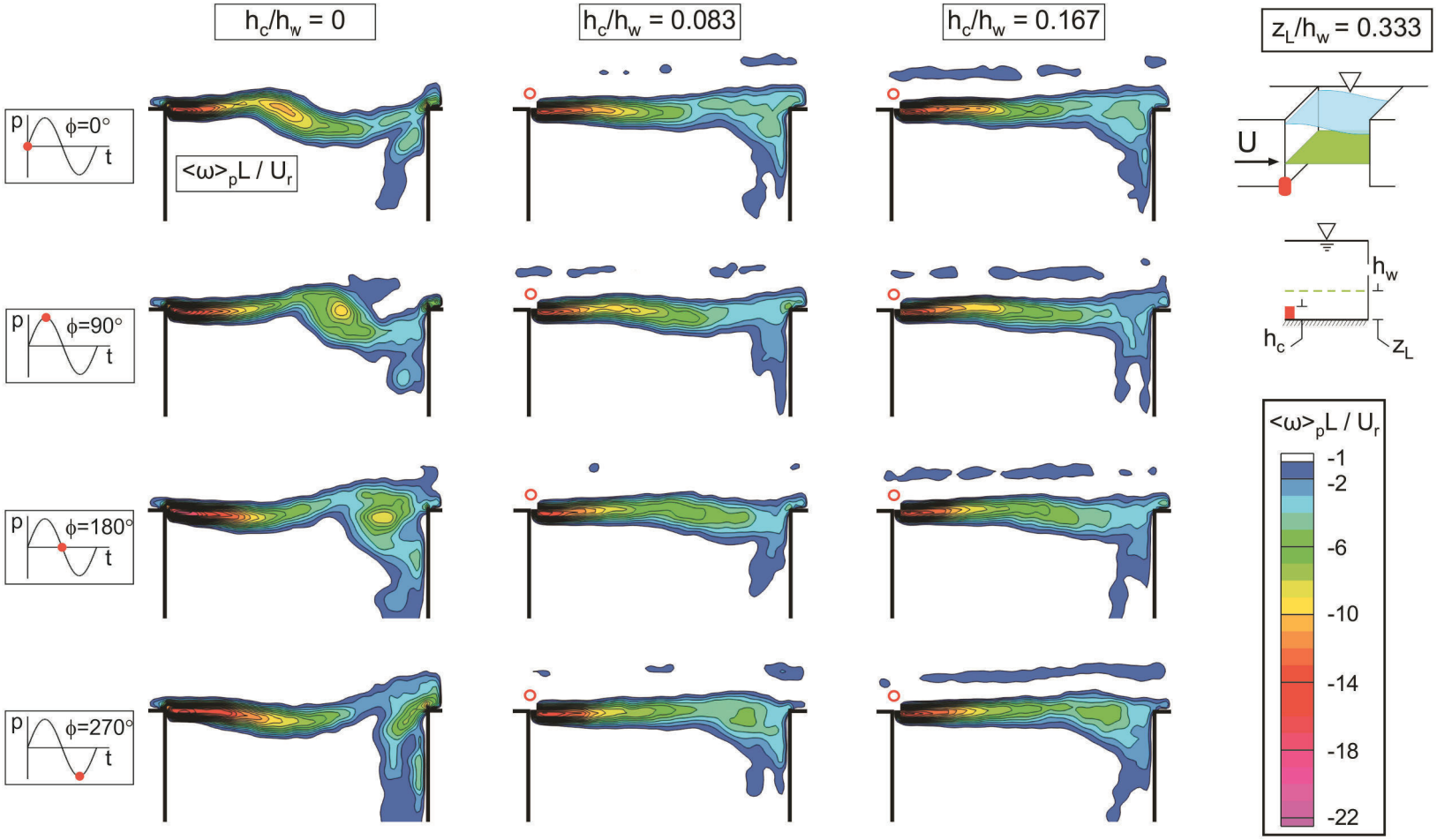

Figure B.18: Patterns of phase-averaged vorticity $\langle\omega\rangle_p L/U_r$ at $z_L/h_w = 0.333$ for four different phases $\phi = 0°$, 90°, 180°, and 270° of the oscillation cycle. Case $h_c/h_w = 0$ corresponds to the non-attenuated oscillation in absence of the control cylinder; $h_c/h_w = 0.083$ and 0.167 correspond to attenuated cases in presence of the control cylinder.

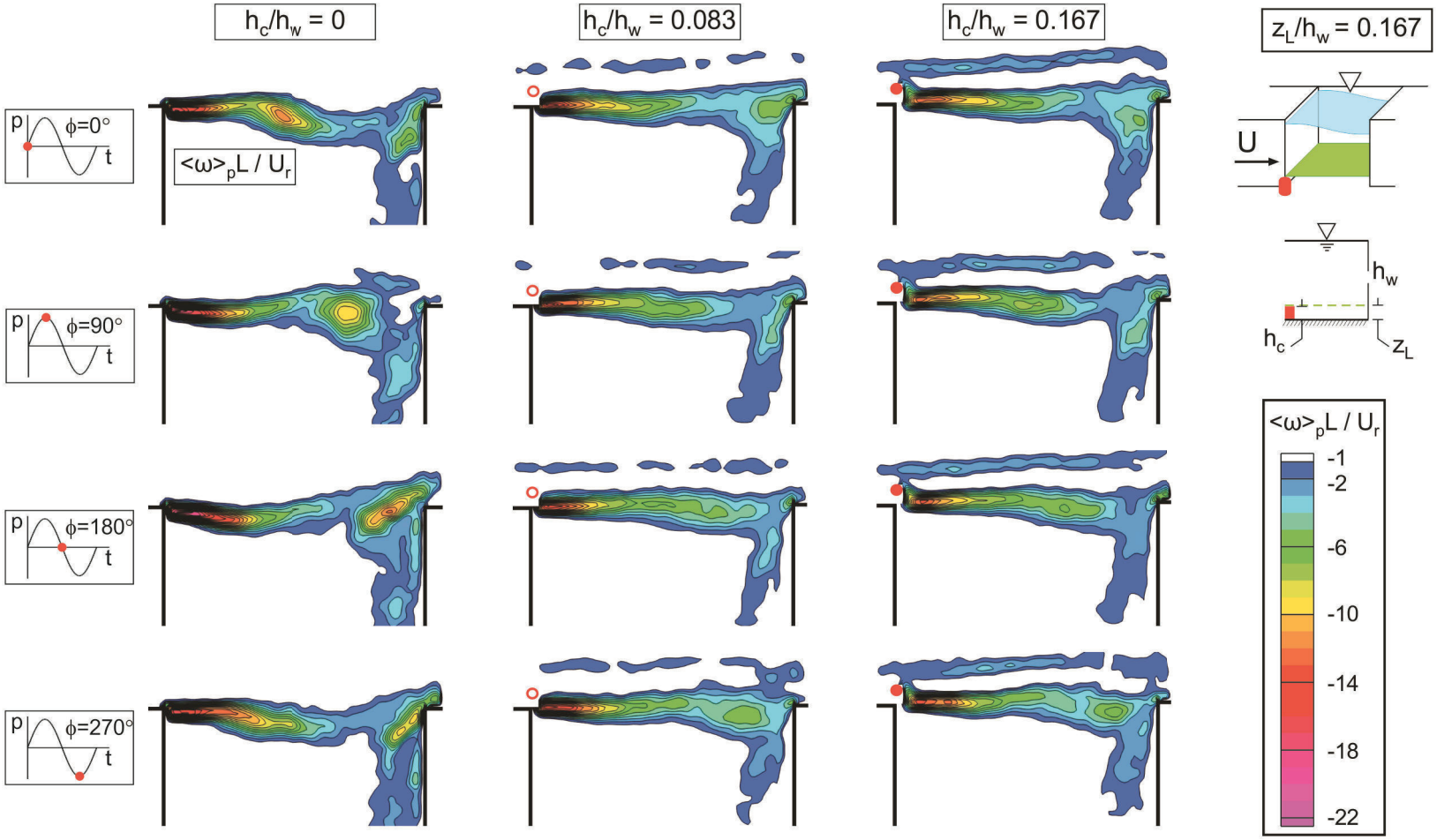

Figure B.19: Patterns of phase-averaged vorticity $<\omega>_p L/U_r$ at $z_L/h_w = 0.167$ for four different phases $\phi = 0°$, 90°, 180°, and 270° of the oscillation cycle. Case $h_c/h_w = 0$ corresponds to the non-attenuated oscillation in absence of the control cylinder; $h_c/h_w = 0.083$ and 0.167 correspond to attenuated cases in presence of the control cylinder.

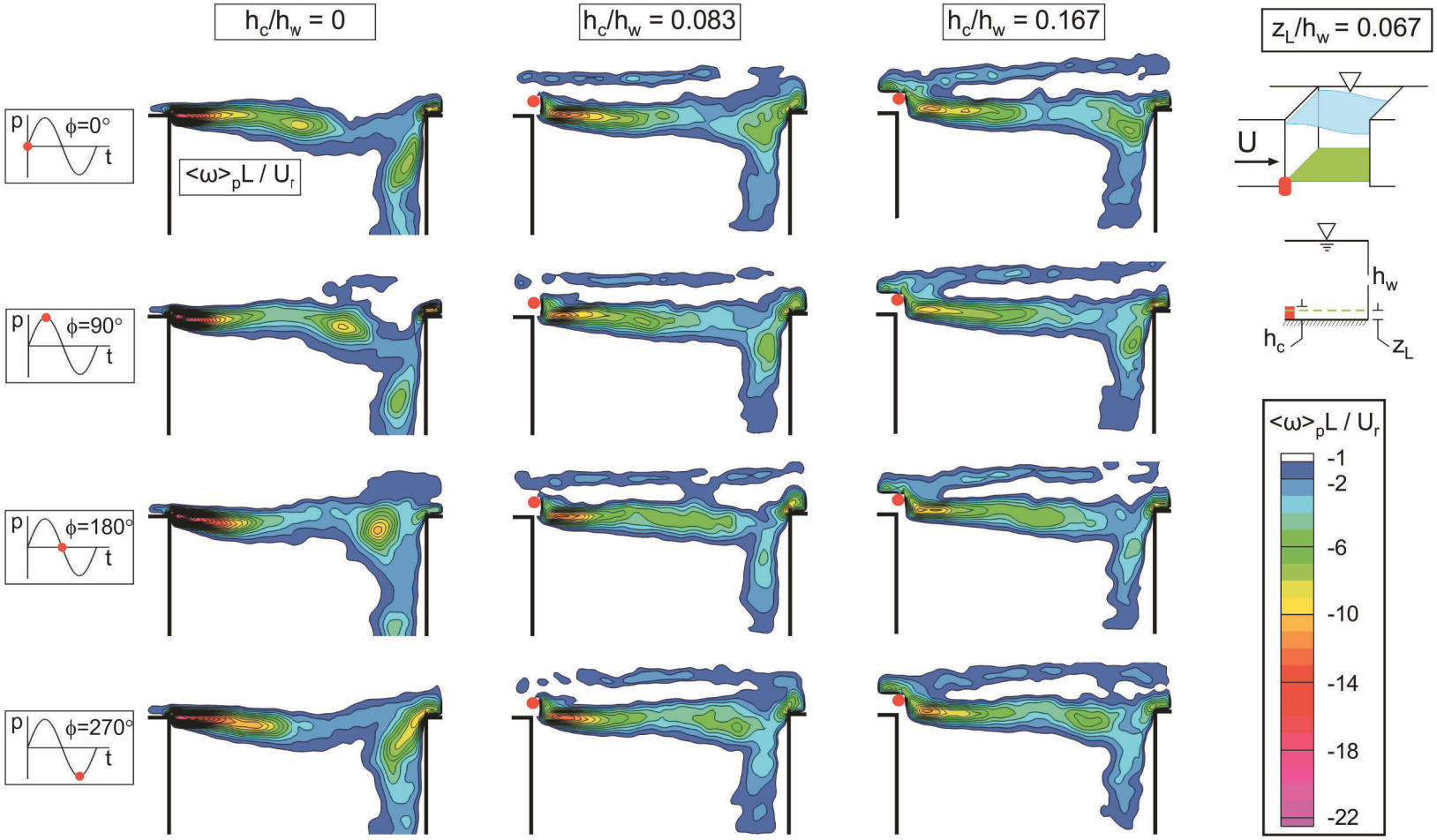

Figure B.20: Patterns of phase-averaged vorticity $\langle\omega\rangle_p L/U_r$ at $z_L/h_w = 0.067$ for four different phases $\phi = 0°$, 90°, 180°, and 270° of the oscillation cycle. Case $h_c/h_w = 0$ corresponds to the non-attenuated oscillation in absence of the control cylinder; $h_c/h_w = 0.083$ and 0.167 correspond to attenuated cases in presence of the control cylinder.

APPENDIX C

SELF-SUSTAINED OSCILLATIONS OF SHALLOW FLOW PAST SEQUENTIAL CAVITIES

The images in this Appendix provide representations of the phase-averaged flow structure at different elevations within the shallow water layer, in order to demonstrate that the phase shift between the flow structure within successive cavities phenomenon, which was shown in Chapter 5, holds for all elevations above the bed. In Figures C.1 thorough C.8, three different elevations z_L/h_w = 0.067, 0.500, and 0.833 within the shallow water layer are shown for four different phases ϕ = 0° to 270° of the oscillation cycle.

Figures C.1 and C.2 show patterns of phase-averaged streamlines $<\psi>_p$, Figures C.3 and C.4 give phase-averaged streamwise velocity $<u>_p/U$, Figures C.5 and C.6 demonstrate contours of phase-averaged transverse velocity $<v>_p/U$, and Figures C.7 and C.8 show contours phase-averaged vorticity $<\omega>_pL/U$. It is evident from Figures C.1 thorough C.8 that the flow structure exhibit a phase shift of either $\pi/2$ or π between leading and trailing cavities depending upon the orientation of the gravity standing wave in each cavity, that is, longitudinal or transverse.

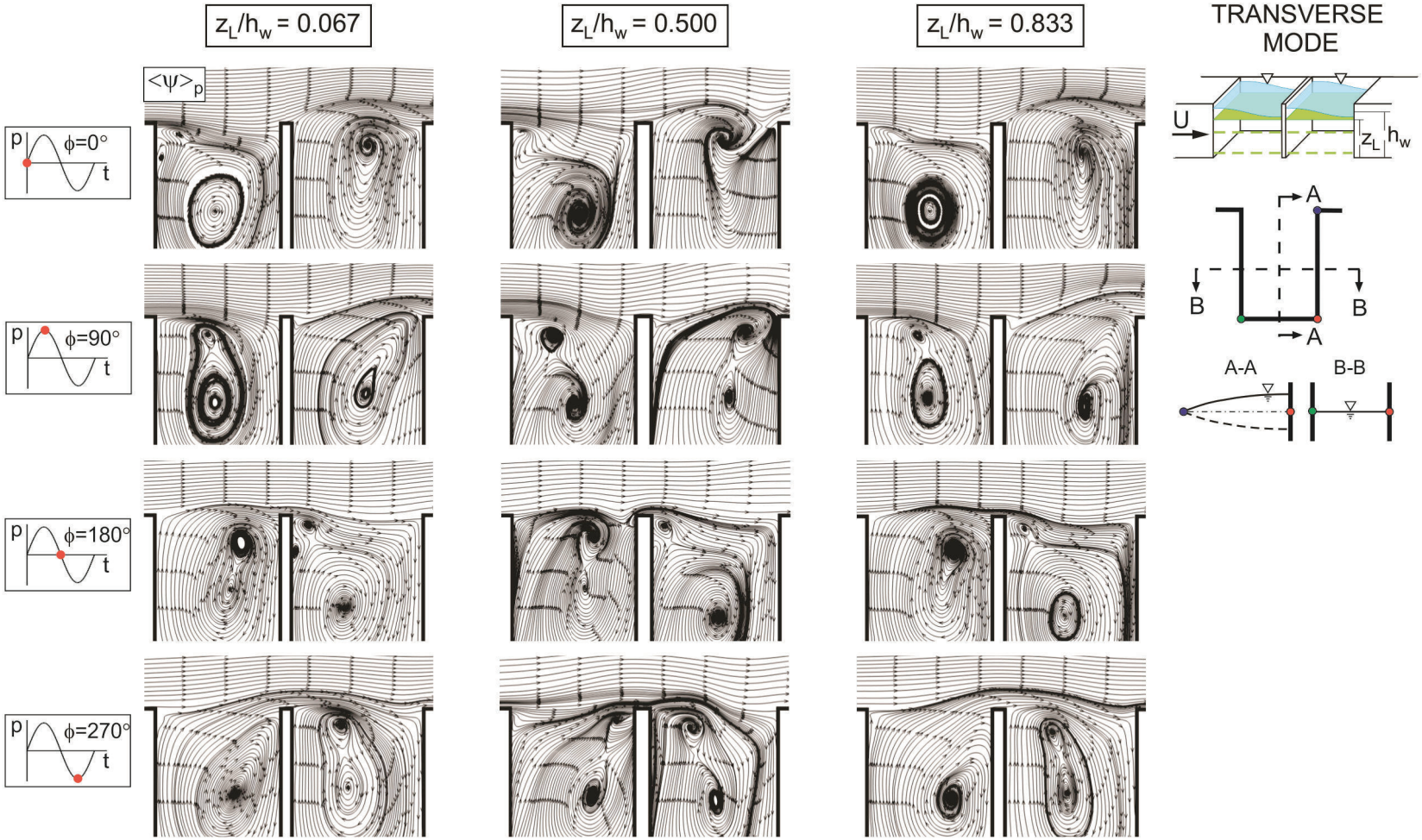

Figure C.1: Phase-averaged patterns of streamlines $\langle\psi\rangle_p$ at $z_L/h_w = 0.067$ (left column), 0.500 (middle column), and 0.833 (right column) for four different phases $\phi = 0°, 90°, 180°,$ and 270° of the oscillation cycle, for transverse mode of gravity standing waves within cavities.

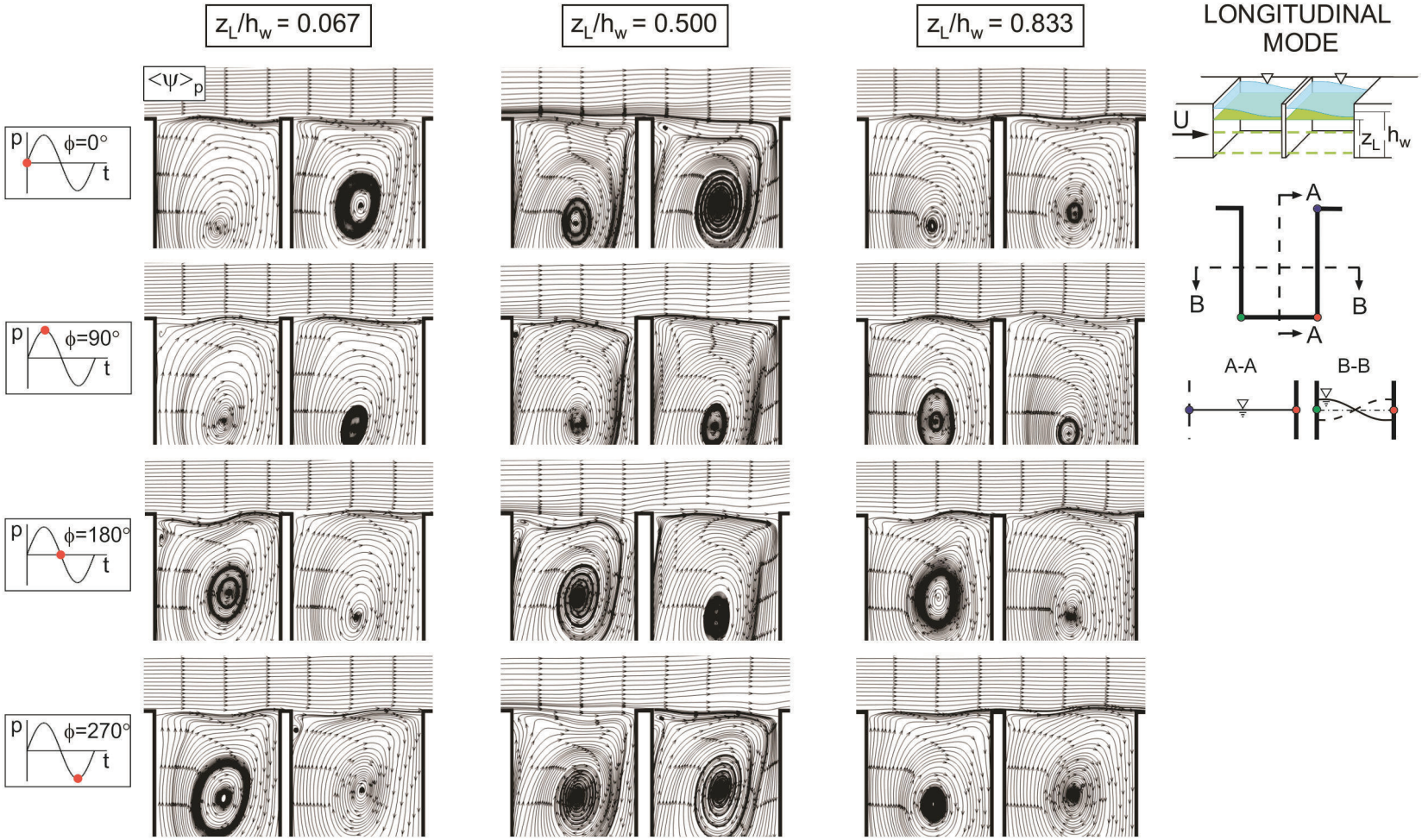

Figure C.2: Phase-averaged patterns of streamlines $<\psi>_p$ at $z_L/h_w = 0.067$ (left column), 0.500 (middle column), and 0.833 (right column) for four different phases $\phi = 0°, 90°, 180°,$ and 270° of the oscillation cycle, for longitudinal mode of gravity standing waves within cavities.

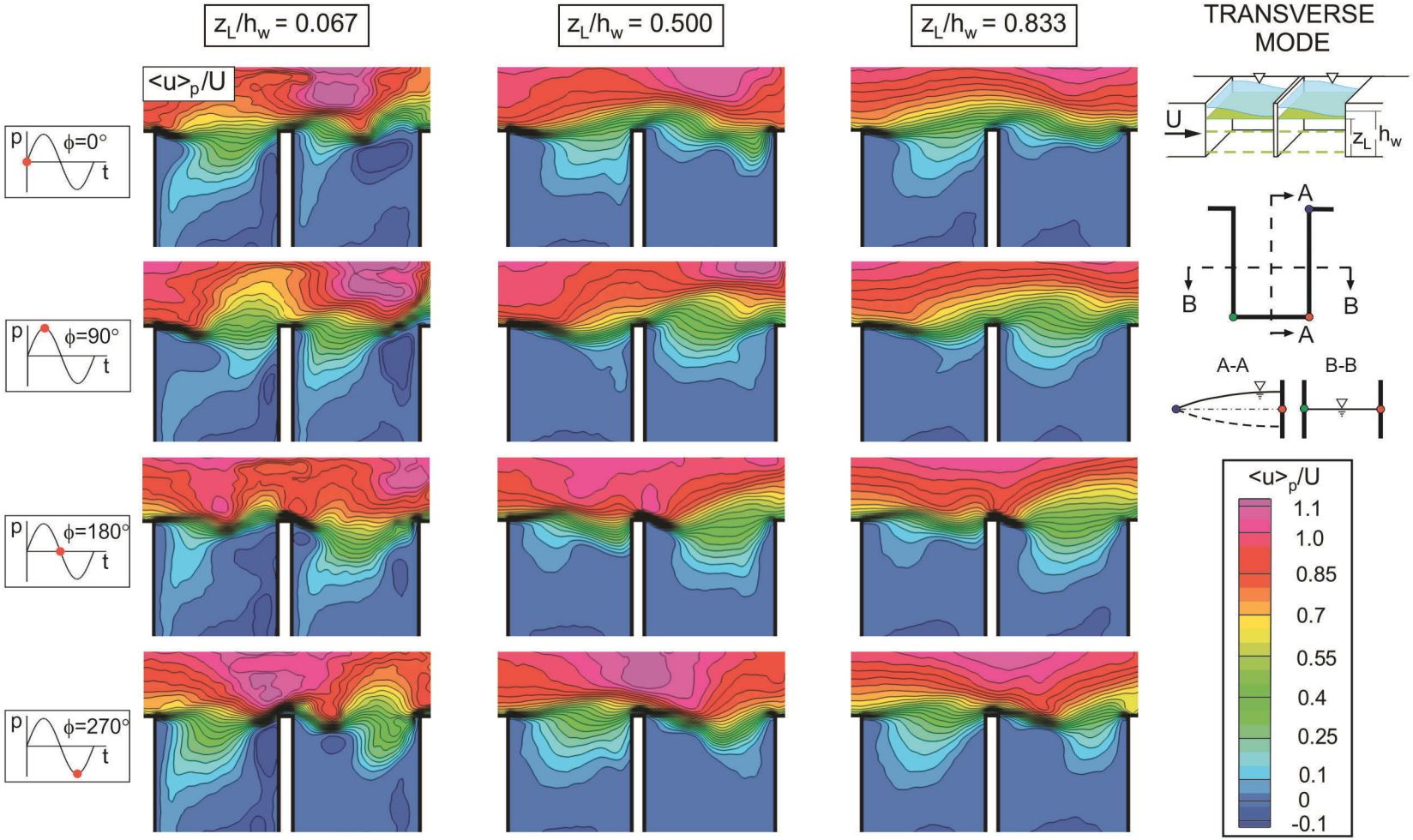

Figure C.3: Contours of phase-averaged streamwise velocity $\langle u \rangle_p / U$ at $z_L/h_w = 0.067$ (left column), 0.500 (middle column), and 0.833 (right column) for four different phases $\phi = 0°, 90°, 180°,$ and $270°$ of the oscillation cycle, for transverse mode of gravity standing waves within cavities.

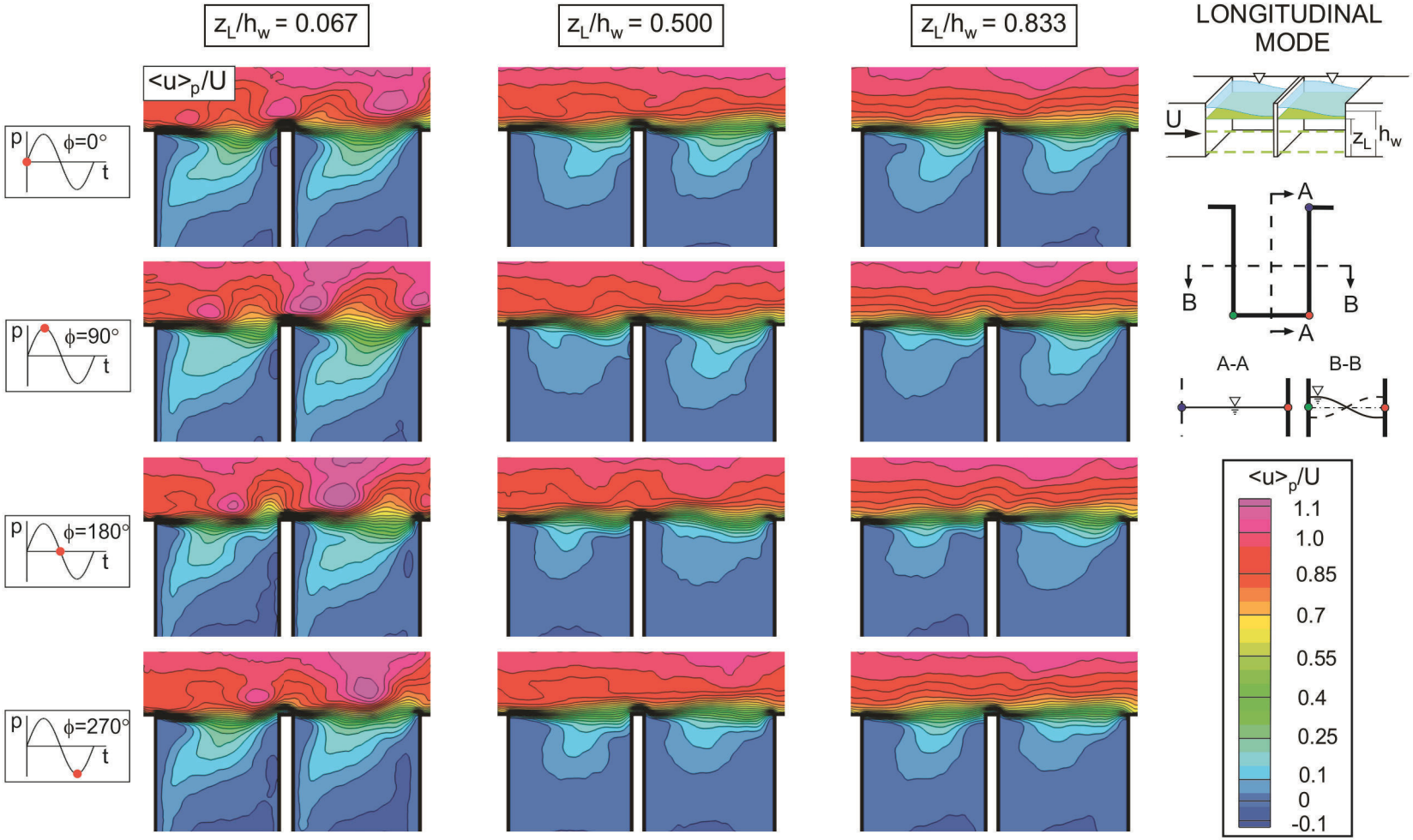

Figure C.4: Contours of phase-averaged streamwise velocity $\langle u \rangle_p / U$ at $z_L/h_w = 0.067$ (left column), 0.500 (middle column), and 0.833 (right column) for four different phases $\phi = 0°, 90°, 180°,$ and $270°$ of the oscillation cycle, for longitudinal mode of gravity standing waves within cavities.

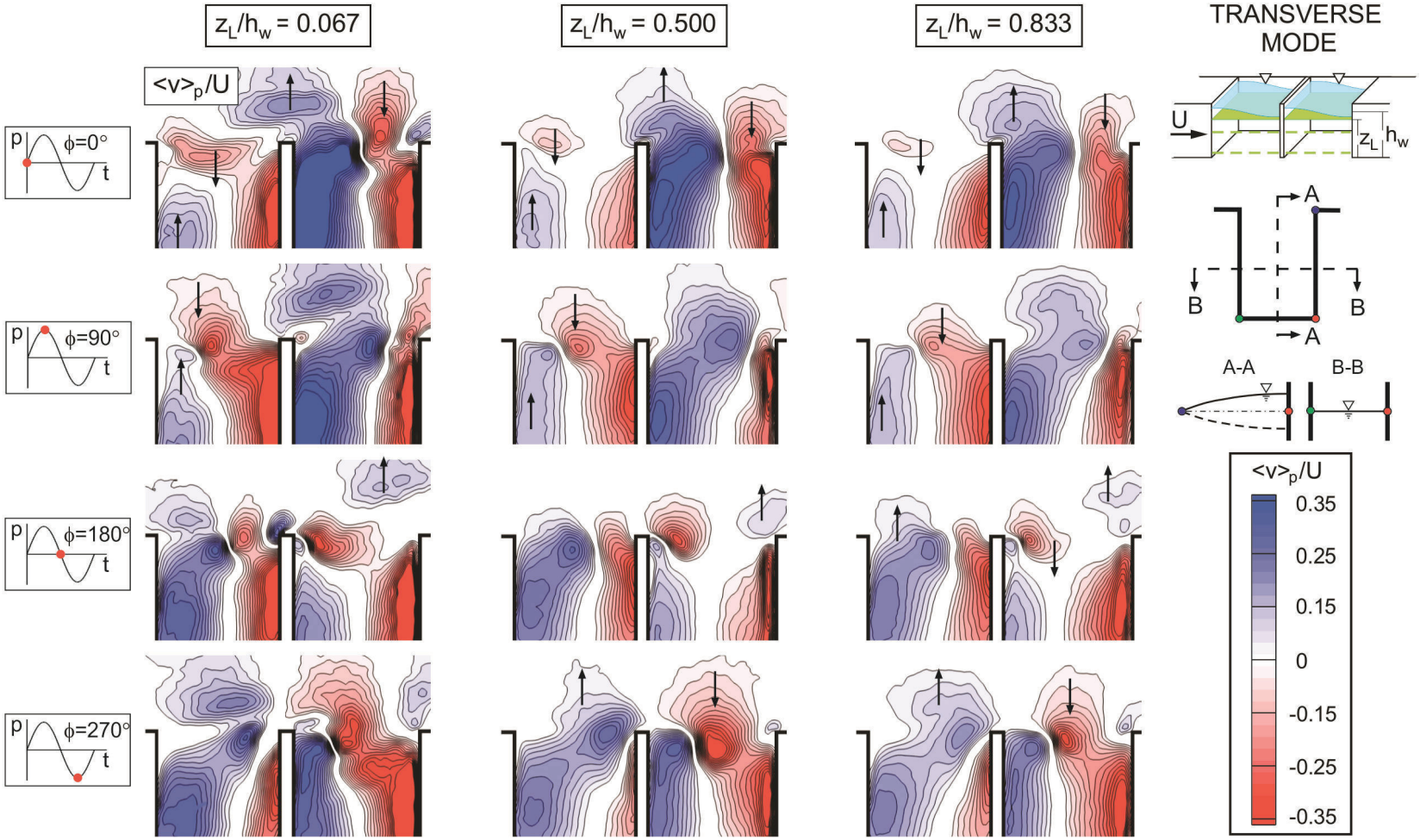

Figure C.5: Contours of phase-averaged transverse velocity $\langle v \rangle_p / U$ at $z_L/h_w = 0.067$ (left column), 0.500 (middle column), and 0.833 (right column) for four different phases $\phi = 0°, 90°, 180°,$ and 270° of the oscillation cycle, for transverse mode of gravity standing waves within cavities.

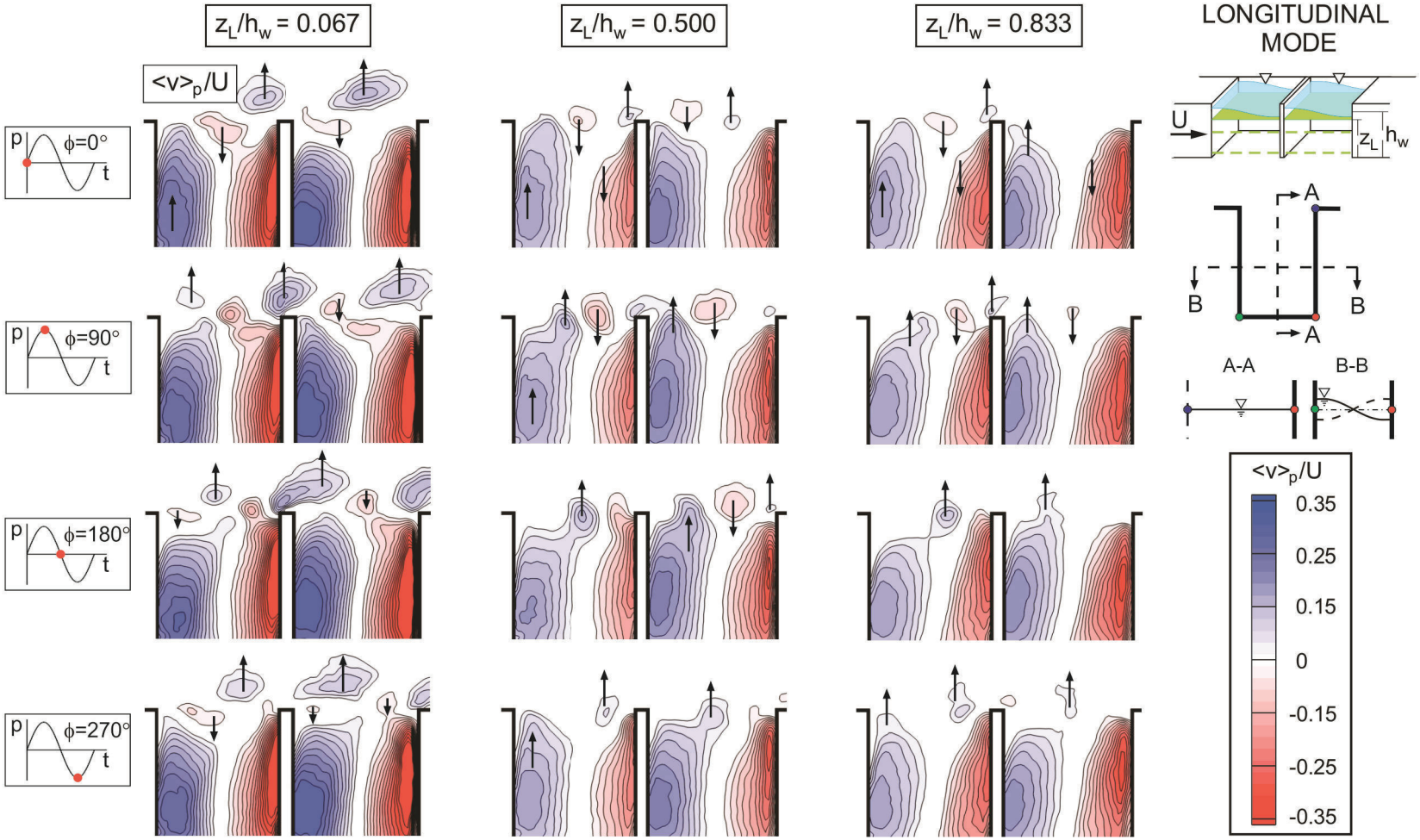

Figure C.6: Contours of phase-averaged transverse velocity $\langle v \rangle_p / U$ at $z_L/h_w = 0.067$ (left column), 0.500 (middle column), and 0.833 (right column) for four different phases $\phi = 0°, 90°, 180°,$ and 270° of the oscillation cycle, for longitudinal mode of gravity standing waves within cavities.

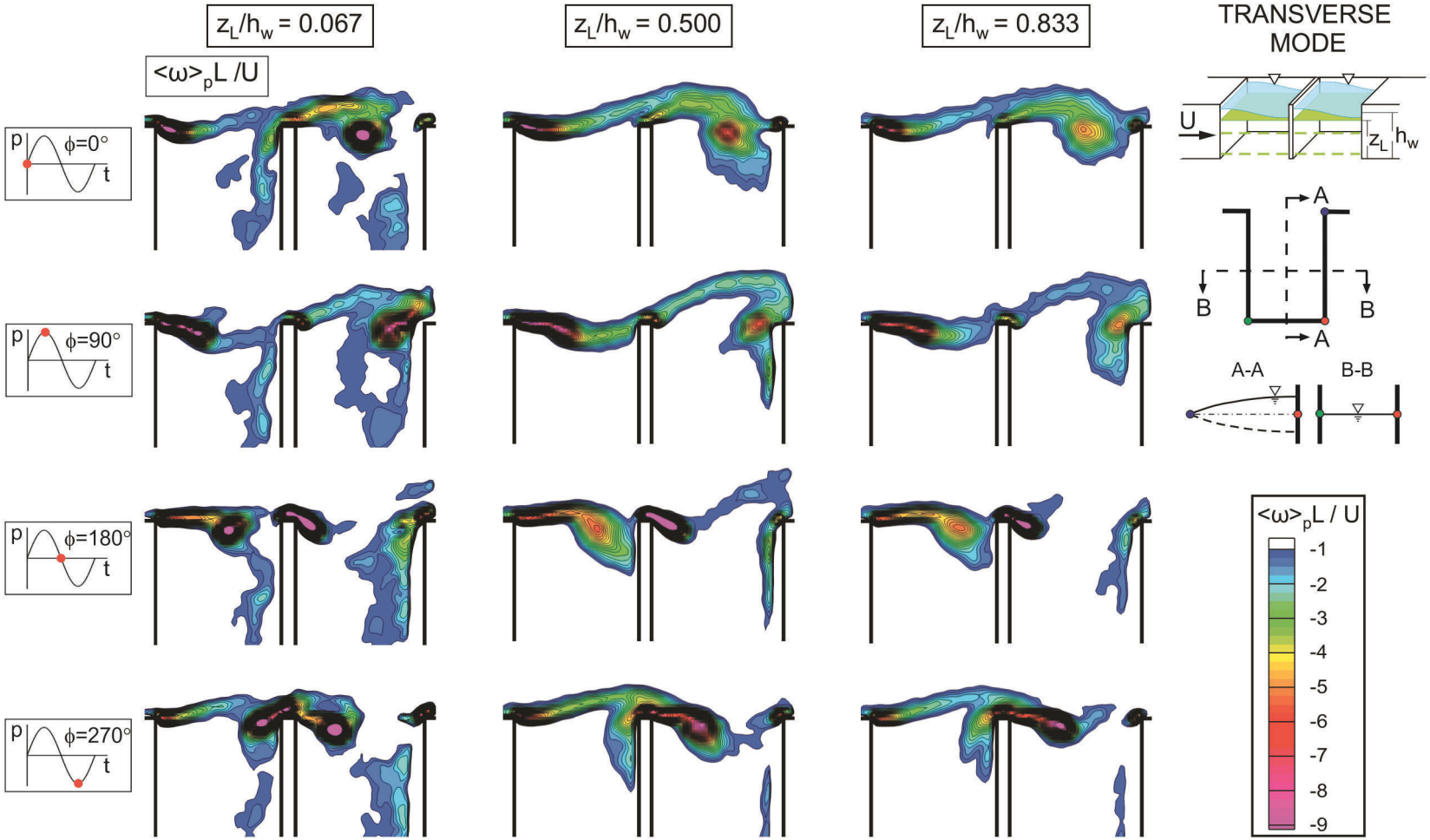

Figure C.7: Contours of phase-averaged vorticity $<\omega>_p L / U$ at $z_L/h_w = 0.067$ (left column), 0.500 (middle column), and 0.833 (right column) for four different phases $\phi = 0°, 90°, 180°,$ and $270°$ of the oscillation cycle, for transverse mode of gravity standing waves within cavities.

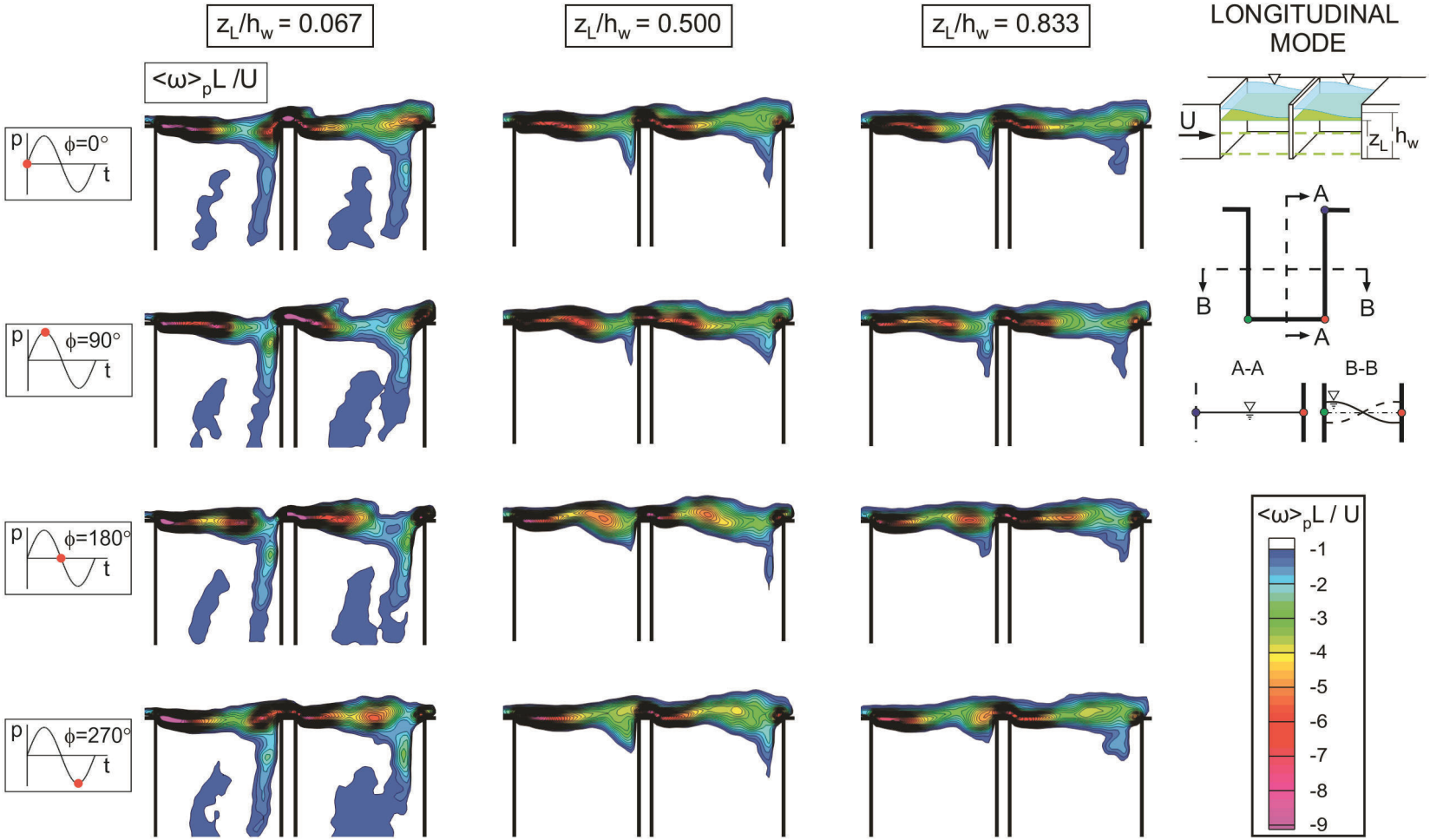

Figure C.8: Contours of phase-averaged vorticity $<\omega>_p L / U$ at $z_L/h_w = 0.067$ (left column), 0.500 (middle column), and 0.833 (right column) for four different phases $\phi = 0°, 90°, 180°,$ and 270° of the oscillation cycle, for longitudinal mode of gravity standing waves within cavities.

VITA

Burak Ahmet Tuna was born in Izmir, Turkey on August 7, 1987 as the son of Sevil and Sukru Tuna. After completing high school education at Buca High School, Izmir, Turkey in 2005, he attended TOBB University of Economics and Technology (TOBB ETU) in Ankara, Turkey, where he received a Bachelor of Science degree in Mechanical Engineering in 2010. Then, he joined the Mechanical Engineering and Mechanics Department at Lehigh University. He received his Master of Engineering degree in Mechanical Engineering in January 2013, and began working toward his Ph.D. degree at the same university. During his graduate study at Lehigh University, he worked under the supervision of Professor Donald Rockwell. He is currently enrolled in Ph.D. program in Mechanical Engineering in the P. C. Rossin College of Engineering at Lehigh University.